Sensors: Technologies and Applications

IFSA

Sensors & Transducers

**International Official Open Access Journal of the
International Frequency Sensor Association (IFSA)
Devoted to Research and Development
of Sensors and Transducers**

Volume 209, Issue 2, February 2017

Editor-in-Chief
Prof., Dr. Sergey Y. YURISH

IFSA

Contents

Research Articles

Authors are encouraged to submit article in MS Word (doc) and Acrobat (pdf) formats
by e-mail: editor@sensorsportal.com. Please visit journal's webpage with preparation instructions:
http://www.sensorsportal.com/HTML/DIGEST/Submition.htm

International Frequency Sensor Association (IFSA).

The 2nd International Conference on Advances in Sensors, Actuators, Metering and Sensing

ALLSENSORS' 2017

19 - 23 March, 2017 - Nice, France

The ALLSENSORS 2017 is an event covering related topics on theory practice and applications of sensor devices, techniques, data acquisition and processing, and on wired and wireless sensors and sensor networks.

The conference is intended to serve as a forum for researchers from the academia and the industry, professionals, standard developers, policy makers, investors and practitioners to present their recent results, to exchange ideas, and to establish new partnerships and collaborations.

The topics suggested by the conference can be discussed in term of concepts, state of the art, research, standards, implementations, running experiments, applications, and industrial case studies. Authors are invited to submit complete unpublished papers, which are not under review in any other conference or journal in the following, but not limited to, topic areas:

* Sensors types
* Quantum sensors and measurements
* Cryogenic sensors and systems
* Biosensors and bio-oriented electronics
* Sensor technologies and materials
* Aerospace sensors and sensor systems

* Sensor-related techniques and methods
* Transducers, actuators
* Metering/Measurements
* Sensing systems
* Sensor-system algorithms, protocols, communication and computation

Important deadlines:

Submission (full paper):
1 December 2016
Notification:
10 January 2017
Registration:
25 January 2017
Camera ready:
5 February 2017

http://www.iaria.org/conferences2017/ALLSENSORS17.html

International Frequency Sensor Association (IFSA) Publishing

Digital Sensors and Sensor Systems: Practical Design

Sergey Y. Yurish

The goal of this book is to help the practicians achieve the best metrological and technical performances of digital sensors and sensor systems at low cost, and significantly to reduce time-to-market. It should be also useful for students, lectures and professors to provide a solid background of the novel concepts and design approach.

Book features include:

- Each of chapter can be used independently and contains its own detailed list of references
- Easy-to-repeat experiments
- Practical orientation
- Dozens examples of various complete sensors and sensor systems for physical and chemical, electrical and non-electrical values
- Detailed description of technology driven and coming alternative to the ADC a frequency (time)-to-digital conversion

Formats: printable pdf (Acrobat) and print (hardcover), 419 pages

ISBN: 978-84-616-0652-8,
e-ISBN: 978-84-615-6957-1

Digital Sensors and Sensor Systems: Practical Design will greatly benefit undergraduate and at PhD students, engineers, scientists and researchers in both industry and academia. It is especially suited as a reference guide for practicians, working for Original Equipment Manufacturers (OEM) electronics market (electronics/hardware), sensor industry, and using commercial-off-the-shelf components

http://sensorsportal.com/HTML/BOOKSTORE/Digital_Sensors.htm

MOSCOW
SEIA'17

3rd International Conference on Sensors and Electronic Instrumentation Advances

20-22 September 2017
Moscow, Russia

IFSA

ASAME

The 3rd International Conference on Sensors and Electronic Instrumentation Advances (SEIA' 2017) is a forum for presentation, discussion, and exchange of information and latest research and development results in both theoretical and experimental research in sensors, transducers and their related fields. It brings together researchers, developers, and practitioners from diverse fields including international scientists and engineers from academia, research institutes, and companies to present and discuss the latest results in the field of sensors and measurements.

The conference is organized by the International Frequency Sensor Association (IFSA) and Asian Society of Applied Mathematics and Engineering (ASAME) in technical cooperation with National Research Center Kurchatov Institute and National Research Nuclear University (both from Moscow, Russia).

The conference is focusing any significant breakthrough and innovation in Sensors, Electronics, Measuring Instrumentation and Transducers Engineering Advances and its applications. Topics of Interest include any aspects of:

- Sensor Technology;
- Instruments and Measuring Technology.

Submission (2-page abstract)	**20 March 2017**
Notification of acceptance	**20 April 2017**
Registration	**20 May 2017**
Camera Ready	**30 June 2017**

Contribution Types:

Regular papers
Posters

One event - three publications !

1. All registered abstracts will be published in the conference proceedings.

2. Selected extended papers will be published in Sensors & Transducers journal.

3. The best full-page papers will be recommended to extend to book chapters for 'Advances in Sensors: Reviews' Book Series.

IFSA Publishing   MEPhI   ostec   Xcelera

http://www.sensorsportal.com/SEIA_2017/

Sensors & Transducers

Water Quality Monitoring using Wireless Sensor Network and Smartphone-based Applications: A Review

[1] **Herlina ABDUL RAHIM,** [1] **Syahidah Nurani ZULKIFLI,**
[1] **Nurul Adilla MOHD SUBHA,** [1, 2] **Ruzairi ABDUL RAHIM**
and [3] **Hafilah ZAINAL ABIDIN**

[1] Department of Control and Instrumentation Engineering, Faculty of Electrical Engineering,
Universiti Teknologi Malaysia, 81310 UTM Johor Bahru, Malaysia
[2] Faculty of Electrical and Electronic Engineering, Universiti Tun Hussein Onn Malaysia (UTHM),
86400 Parit Raja, Batu Pahat, Johor, Malaysia
[3] Language Academy, Universiti Teknologi Malaysia, 81310 UTM Johor Bahru, Malaysia
[1] Tel.: +607-5537804
E-mail: herlina@utm.my

Abstract: A wireless sensor network (WSN) has a huge potential in water ecology monitoring applications. The integration of WSN to a portable sensing device offers the feasibility of sensing distribution capability, on-site data measurements, and remote sensing abilities. Due to the advancement of WSN technology, unexpected contamination events in water environments can be observed continuously. Local Area Network (LAN), Wireless Local Area Network (WLAN) and Internet web-based are commonly used as a gateway unit for data communication via local base computer using standard Global System for Mobile Communication (GSM) or General Packet Radio Services (GPRS). However, WSN construction is costly and a growing static infrastructure increases the energy consumptions. Hence, a growing trend of smartphone-based application in the field of water monitoring is a surrogate approach to engage mobile base stations for in-field analysis that are driven by the expanding adaptation of Bluetooth, ZigBee and standard Wi-Fi routers. Owing to the fact that smartphones are portable and accessible, mobile data collection from WSN in remote locations are achievable. This paper comprehensively reviews the detection of water contaminants using smartphone-based applications in accordance with WSN technologies. In this paper, some recommendations and prospective views on the developments of water quality monitoring will be discussed.

Keywords: Wireless sensor-based network (WSN), Water quality monitoring, Smartphone-based system, WSN construction.

1. Introduction

An expanding group of water contaminants which are constantly changing is responsible for the breakthrough of various contagious diseases, such as diarrhea, hepatitis, SARS, pneumonia, kidney failure, irritations and pulmonary disease [1]. The tremendous amount of waste generated is a major concern in sustaining safe and clean water supply. Waste production imposes a significant change in the quality of water due to a breakdown of various contaminants, chemically and biologically, which contains highly toxic substances. Although raw water or wastewater undergo treatment process before distribution process,

water distribution system (WDS) pipeline are easily exposed to intentional or accidental contamination. Intentional sabotage events have been reported to occur within public drinking water supply in north-east Scotland [2] and tap water in Turkey [3] due to the prevalence of mesophilic Aeromonas bacteria which is the act of terrorism or mischief. As for accidental contamination occurrence, the breakdown of contaminants is commonly through cracks in WDS pipelines that are easily exposed to polluted environments. The derivation of most common non-biological contaminants is ammonia, arsenic, barium, boron, chlorine, chromium, cadmium, lead, mercury, nickel, nitrate and sodium [4]. Based on the Third Contaminants Candidate List (CCL3) reviewed by United States of Environmental Protection Agency (USEPA), the most commonly found microbial contaminants are Adenovirus, Caliciviruses, Campylobacter jejuni, Enterovirus, Helicobacter pylori, Escherichia coli (E. coli), Legionella, Mycobacterium avium, Naegleria fowleri, Salmonella enterica and Shigella sonnei [5]. These contaminants have been significantly presence in aqueous environments such as river, groundwater, wells, water storage, tap and drinking water. Excessive consumption of substance concentration may lead to toxicity and hazardous to human health. Hence, the principal motivation for water quality monitoring is to provide a safe water supply to public, retail and wholesale consumers.

Recently, water monitoring technologies have expanded to a wide variety of directions. Several monitoring technologies have been introduced in order to provide higher detection sensitivity as well as data accuracies. Such improved technologies are sensor placement approach (SPA) [6-8], microfluidic devices [9-11], spectroscopic techniques [12-14] and biosensor array [15-19]. Often these monitoring techniques correlate with chemo-metric analysis which particularly used in analytical chemistry and biology applications. Multivariate analysis using various chemo-metric techniques provide information on chemical substances extracted from sensing devices to obtain qualitative and quantitative data measurements. Despite the meticulous techniques established from previous studies, providing a fast response, sensitive and accurate detection technique is a necessity for the production of threats-free water supply. Therefore, online wireless sensor network-based detection approach was recently established to measure water quality in real-time whilst having the potential to provide an early warning system as well as true/false detection alarms. According to EPA, online water quality sensors should impose three main objectives, which are (1) reproducibility of data measurements at different contaminants concentration level; (2) predicting baseline water quality level at various locations; (3) interpretations of response data analysis, qualitative and quantitative measures [20].

Detection of low concentration contaminants in water sources are a challenging task, especially when for microbiological contaminants [21]. Traditionally,

analysis of water contaminants has been performed in laboratories and water facilities that often utilizes high-end technological instrumentations. Although conventional method, also known as "off-line analytical methods", such as multiple fermentation tube (MTF) [22-25], membrane filtration (MF) [26-28], DNA amplification [29-31] and gas/liquid chromatography-mass spectrometry (MS) [32-35] have been remarkably successful in water contaminants data analysis, several researches review the drawbacks of employing these methods in real-time measurements which are primarily time-consuming, limited detection of specified contaminants, relatively high cost, heavy instrumentation setup and provide small data sets [36-39]. This equipment requires expert guidelines for conducting analytical measurements and procedures.

Since the introduction of wireless sensing mechanism, several studies have been reported to established integration of detection techniques with wireless sensor network (WSN) applications. Online monitoring offers portability, compact, flexible and faster response which are suitable for on-site deployments. A surrogate approach utilizing WSN instrumentations is able to identify unlimited water quality parameter as discussed in [40], which are summarized in Table 1.

Table 1. WSN-based online monitoring instrumentations [40].

Online monitoring instruments	Water Quality Parameter
Physical	Turbidity, color, electrical conductivity (EC), hardness, temperature
Inorganic	pH and DO level, metals, nutrients, fluoride
Organic	Carbon, hydrocarbon, UV absorption, pesticides, disinfectant-by-product (DBP)
Biological	Algae, protozoa, pathogens
Hydraulics	Flow, level, pressure

As seemingly promising, not many researchers considered the detection of contaminants at the point of consumption, which is primarily tap and drinking water supply. Today, hand-held devices such as portable microfluidic devices, miniaturized biosensors and spectroscopy have been commercially available, hence, providing an efficient way for on-site monitoring of water quality assessments. The application of WSN within water distribution system is the simplest way to enable in-field and real-time water contaminants detection. An automated detection system reduces the time limitations of a conventional analytical method, having to work with real-time water samples without the necessity for laboratories usage and able to response faster whenever contaminants are detected. Therefore, a comprehensive review on the state-of-the-art WSN

and smartphone-based monitoring technologies, as well as their applications for the detection of water contaminants are presented in this paper. Limitations and future recommendations for present water quality monitoring system will be extensively elaborated.

2. WSN Design Structure

A wireless sensor network (WSN) is a distributed architecture consisting several subsystems that are able to communicate with one another through an electronic device, commonly known as a transceiver or receiver. There have been a numerous research on the constructions of WSN technology for the detection of water contaminants whilst providing low cost, higher detection sensitivity, sufficient data sets, improved data acquisition and low power consumptions [41]. Typically, a WSN system comprises a number of low power consumption sensing station nodes that enable data acquisition process. The basic system of WSN comprises a sensor distribution system, central data station, and a controller unit which permits data analysis process.

WSN technologies often correlate with real-time automated monitoring system equipped with data acquisition, network transmission, and software data analysis. This intelligent technique enables the monitoring system to characterize water conditions, observing changes in water quality, identifying emerging contaminants and providing water assessments [42-45]. There are several network topologies used for implementation of network nodes, such as the star topology, peer-to-peer (Mesh), and cluster tree topology network [46]. Fig. 1 illustrates the network topology. A star topology is a single hop communication architecture in which the PAN coordinator, also known as the router nodes connects to multiple nodes. In contrast, a MESH topology is a multi-hop communication system in which the router nodes are connected to multiple other nodes while a tree topology is a combination (hybrid) of star-mesh architecture. Referring to [47], the WSN design structure monitoring system consists of three main parts which data are monitoring nodes, data base station and remote monitoring center as shown in Fig. 2.

(a) Star topology	(b) MESH topology	(c) Cluster tree topology
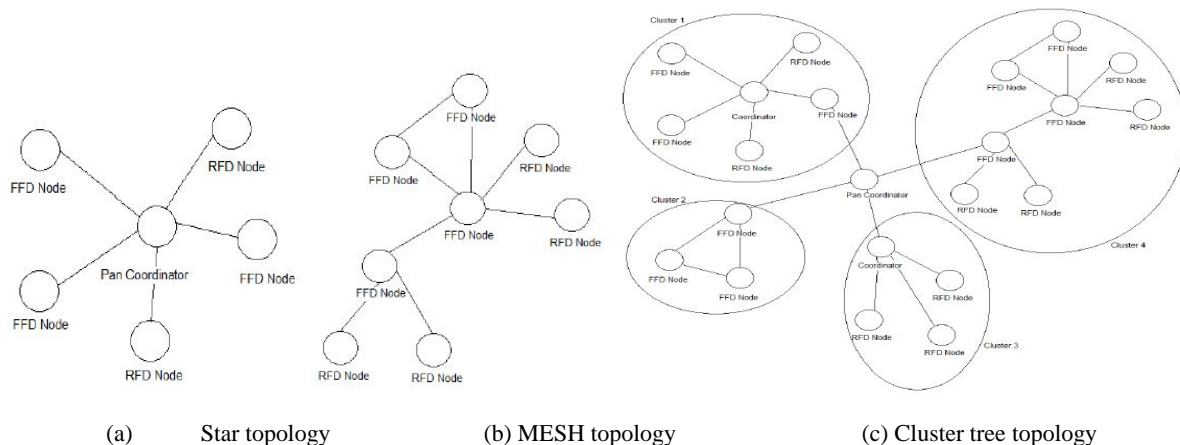
Fig. 1. Wireless sensor-based network (WSN) topologies [46].

Each of the sensing nodes placed at distributed water area does not only assemble parameters such as pH level, dissolved oxygen, EC and temperature, but also capable of obtaining wide coverage of linearization. These collected data measurements are then transmitted to a remote monitoring center from the base station via GPRS network system. The proposed system successfully monitors the temperature and pH level of an artificial lake, obtaining value ranging from 0 to 80 °C and 0 to 12 pH level, respectively. In relation to this, Lindsay et al. [48] have developed the integration of WSN for environmental sensing application in Lakes, which is known as LakeNet. The construction of WSN was embedded onto floating probe consist of waterproof controller unit and sensor nodes. The sensors detect pH level, temperature and dissolved oxygen in water

samples and describe any diurnal fluctuations and photosynthesis. These data are transmitted via a wireless system to relay stations and PC gateway [49]. Similarly, this method has also been applied in Flynn et al. [50] and Yang et al. [51] for the in-situ monitoring of water quality in aqueous environments.

3. Smartphone-based Monitoring System

Recently, smartphones are known as the pocket-sized computer featuring almost any application that interest consumers. WSN applications have been embedded with smartphones due to portability and low-cost devices suitable to be used for on-site monitoring analysis which gives direct information to the users [52, 53].
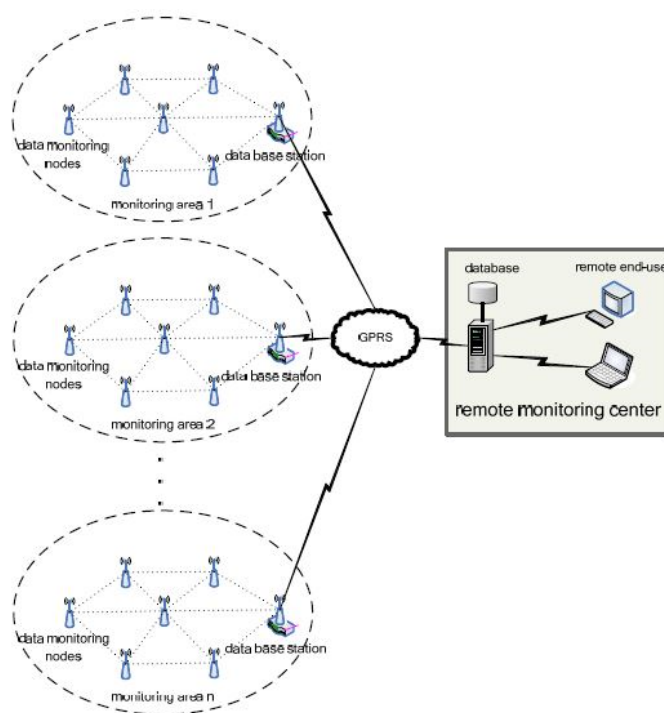
Fig. 2. WSN system consist of three main parts: data monitoring nodes, data base station and remote monitoring center [47].

Smartphones are more accessible and portable in comparison to other laboratory analysis techniques including several in-situ monitoring devices [54]. An expanding development of smartphone-based monitoring apps has increased interest among researchers to fully utilized smartphones as a smart detector. A surrogate approach to exploit smartphones for water monitoring is by integration of RGB camera, Bluetooth, ZigBee, Wi-Fi, GPS, GPRS and GSM communication. Sensing devices capture measurements and smartphones are used to control experimental variables as well as displaying results on a screen that basically resembles the tiny version of a laptop computer. This was illustrated in several studies that developed a sensing device featuring smartphone applications and user interface data analysis for deployment of environmental, nutrition, lab-on-chip diagnostic, point-of-care measurements and biomolecular detections [55-62].

Basically, integration of smartphones is categorized into two applications, which are used as a detector and instrumental interface. Despite the successful developments of mobile sensing and data collection via WSN application, there are very few efforts on the evaluation of smartphones as data collectors in remote locations [63]. The impact of smartphone-based mobility data collection from isolated regions have been investigated by Wu et al. [64], Park and Heidemann [65] and Shepard et al. [66]. As comparison, Zuhal and Murat [67] also studied the feasibility of smartphone-based data collection from wireless sensor networks but in an urban environment. In relation to data collection efficiency, several WSN islands were targeted with various sizes and connection availability resulting in a negative linear relationship between data collection protocols and sizes of islands.

Currently, smartphones have been reported to integrate with conventional analytical devices, such as a biosensor, spectrometer and microfluidic approach. With superior advancement in sensing techniques, simultaneous multiple analysis is feasible due to smartphone-based monitoring applications. Multiple channel diagnostic devices utilizing smartphones are useful for high-throughput in-situ monitoring with minimal size, weight, cost and data transmissions [68].

3.1. Bluetooth Communications

A Bluetooth is an open wireless technology medium that enables connection between devices at a certain specified distance. It operates through a short-range (10 m-100 m) radio waves ad hoc network which is known as the piconet. A piconet is a basic Bluetooth topology technology which only allows a maximum of seven devices interconnected to a master device. A Bluetooth is a low energy consumption device which is capable of long operation timeframe that requires only coin-cell batteries for power supply. Generally, a Bluetooth wireless technology comprises data rates of up to 721 kbit/s, however, a high speed frequency of 2.4 Mbit/s is achievable by using an 802.11 AMP [69, 70].

The application of Bluetooth transceiver embedded in a smartphone-based for the monitoring of water contaminants has been expanding tremendously due to its low power consumption and low operational cost. A smartphone-based portable bacteria detection have been developed by Jing et al.

[71] using a pre-concentrating microfluidic sensor integrated with an impedance sensing system. The low-cost sensors and sensing system are able to identify and quantify bacteria in aqueous environments. The demonstration of fabricated microfluidic smartphone-based platform successfully detects bacteria with a lower limit of detection (LOD) at 10 E. coli cells per milliliter. Data analysis was performed using a well-designed Android application program which allows recording and visualization of data measurements transmitted via Bluetooth circuit module. The schematic diagram of the wireless system is shown in Fig. 3.
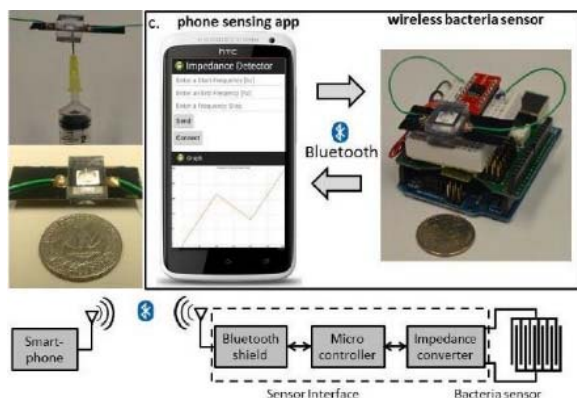
Fig. 3. Schematic of wireless mobile phone bacteria sensing system [71].

Previously, the development of smartphone-based impedance screen-printed electrodes for the detection of 2,4,6-trinitrotuluene (TNT) in water using Bluetooth platform was developed by Diming et al. [72]. The embedded sensing system comprises an alternative current (AC) impedance of 20 kHz, an AD5933 analyzer chip, Arduino microcontroller and a smartphone-based platform. The combined sensing system has a detection limit as low as 10-6 TNT impedance properties. The data transmission was executed using smartphone apps to receive and plot the real-time data. Despite the successful detection of TNT substance in water samples, impedance transducers are dependable to frequencies. Results show that TNT presence is able to be detected at a frequency ranging from 10 kHz to 30 kHz only. Portable smartphone platforms have also been applied to bio-sensing events to receive, analyze and display detected signals. There have been several studies related to bio-detections of bacteria and biomarkers that correlate with the integration of Bluetooth module communication system [73-75].

A similar approach of smartphone-based electrochemical impedance spectroscopy (EIS) was also established for the detection of proteins [76]. A miniaturized biosensor embedded to an EIS detector observes and detects EIS signal measurement of proteins via Bluetooth protocol using a smartphone. With the implementation of smartphone-based protein detection, the system allows fast operational time

responses, cost effective and portability with a detection limit as low as 1.78 µg/ml and 2.97 ng/ml for bull serum albumin (BSA) and thrombin respectively. A mobile sensing for water quality monitoring has also been studied by Anthony and Aloys [77] using integration of water quality sensors (electrical conductivity (EC), pH and oxidation-reduction potential (ORP)) to an Arduino microcontroller unit, a serial Bluetooth module, Android mobile apps and a web-server internet.

Generally, Bluetooth communication modules are among the most favorable wireless communication system via smartphone-based platform due to their relatively low power consumption in comparison to other high data rate system such as Wi-Fi [78-81]. The simplicity of Bluetooth devices and capability to work in a remote location with the absence of the Wi-Fi connection allows the deployments of on-site water monitoring. In addition, Bluetooth is mostly embedded in almost every available smartphones. As reported by Unyoung et al. [82], the detection of bacterial pathogens in water monitoring was investigated using a microfluidic DNA sensor integrated to a mobile interface which allows users to visualize of data results. With the implementation of a wireless interface and electrochemical analyzer unit, the system is able to identify E. coli sequences and map out the signal output via a mobile application which is shown in Fig. 4.

3.2 Smartphone Camera

The application of smartphone camera in water monitoring has been used by interconnecting smartphones with a sensing instrument to detect the output signals. Due to camera's high resolution, often it has been used to perform fluorescence imaging, such as capturing bright-field microscopic bacterial and microorganism morphology [83-88]. The concept could overcome the limitation on the detection of various microbiological activity in remote areas, in which the usage of cellphones is extensive.
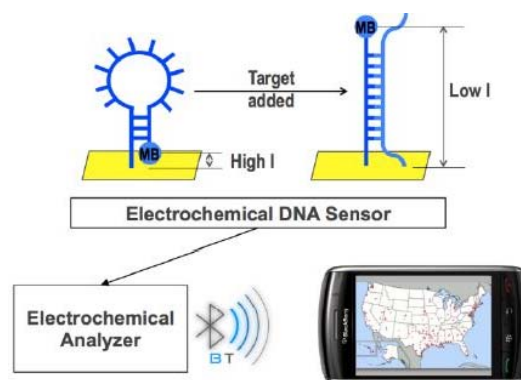
Fig. 4. An overview of microfluidic DNA sensor integrated with mobile interface: an electrochemical sensor provides an electrochemical signal when hybridized to its target pathogen sequence [82].

In addition, a similar concept could also be implemented on a conventional smartphone camera technology without having the necessity to have high-end smartphones. The same concept of lens-free smartphone microscope was also investigated by Tseng et al. [89]. In their study, they used an LED light source excitation to create a hologram of each targeted samples which is then captured by the smartphone camera. The system demonstrates various micro particles images of platelets and parasites. Following this, the detection of analytes concentration based on various fluorescence imaging was reported by Erickson et al. [90] using a portable smartphone camera embedded to a reflectance photometry. Interestingly, the light source used in the system was a built-in smartphone flash which is cost-effective. This adds up the advantages of using smartphone features which do not require additional accessories or instruments setup. A smartphone-based camera was also been used as fluorescence analyzer for the detection of Ochratoxin A, identification of highly pathogenic H5N1 viruses, quantitation of prostate-specific antigen (PSA), detection of E. coli and Salmonella bacteria [91-94]. Since a smartphone camera offers limited functionality, many smartphone-based water monitoring applications often utilize colorimetric and visualization technique to detect analytes concentration. A smartphone camera with a remote server integration is also used as a colorimetric reader for rapid on-site analysis. This was reported by Yu et al. [95] for the detection of catechols in water samples using a 2 x 2 colorimetric sensor array which comprises a pH indicator. In this case, the smartphone is used for data acquisition and processing of the sensor array. A 16-megapixel smartphone camera was used to directly capture the color produced by probe/analytes mixtures. The schematic diagram of overall sensing technique is shown in Fig. 5. The results show the capability of the proposed system to detect 13 different catechols ate 12.5 mM concentration. According to the author, previous cis-diol-containing analytes use numerous amount of instruments setup. In contrast to the proposed design system, the author managed to reduce the design complexity and probes whilst producing a greater number of analytes detected.

The quality feature of current smartphone camera such as high resolution, sensitive motion detection cameras, built-in light source and advanced wireless connectivity has been fully utilized by researchers to develop rapid environmental monitoring. For instance, it has been reported several microscopic imaging and colorimetric detection that demonstrates smartphone camera platforms [96-99]. According to Hasan et al. [100] the first surface plasmon resonance imaging based on a smartphone was developed by the author itself. However, a more feasible technique was established by Liu et al. [101] and Bremer et al. [102] using smartphone-based LED and camera for light emitting source and sensor, respectively. The system differentiates the others by integrating smartphones with optical fibers probe.
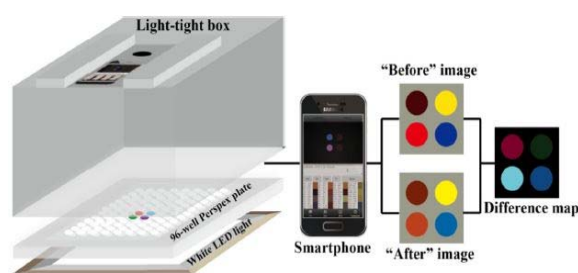
Fig. 5. Schematic diagram of a smartphone-based colorimetric reader [94].

Nevertheless, smartphone camera has limited spatial resolution images due to the pixel size at the sensor, hence providing less accurate data in comparison to a standard microscope. Furthermore, a holographic algorithm is often used to capture the real image, which obviously could not be executed on smartphones because of it high data speed. Despite some potential novelties in utilizing smartphone cameras, its sensitivity is to be questioned since some applications are only able to detect specified analytes or contaminants in medium to high concentration [103]. Since most of the analytes presence in low concentration, hence the lack of device sensitivity is therefore limited.

3.3. ZigBee Protocol

As similar to Bluetooth, ZigBee is a mesh network protocol that enables small data packets transmission over short distances with minimal power consumption. ZigBee operates under a local area network (LAN), hence it is connects to devices with a wider range. The traditional wireless communication technology has limited computing power and bandwidth ranges. The wireless infrastructure contributes to low performances of data transmission from one node to another. An alternative solution was established by Yanan et al. [104] to overcome this issue by implementing WSN gateways via ARM processor, which was constructed using ZigBee and GPRS module. The proposed WSN gateways structure is shown in Fig. 6.

The WSN structure design can improve gateways transmission speed and achieve a long-distance transmission with higher performance.

Previously, a study for real-time groundwater monitoring using wireless network system integrated to a pressure sensor [105]. The remote sensing is based on ZigBee wireless local area (WLAN) IEEE 802.11 network. Following this, Ghaffari et al. [106] introduced a low-cost wireless multi-sensor for the detection of nitrate concentration in water sample via ZigBee transceiver. The ZigBee was used for a short distance communication but it can be extended to a maximum of 150 m by using additional antennas. ZigBee wireless communication protocols have also been used in various environmental monitoring

applications [107]. Another ZigBee-based wireless technology using microelectronic sensor was developed by Xing et al. [108] for the detection of cyto-toxicants in a water supply.
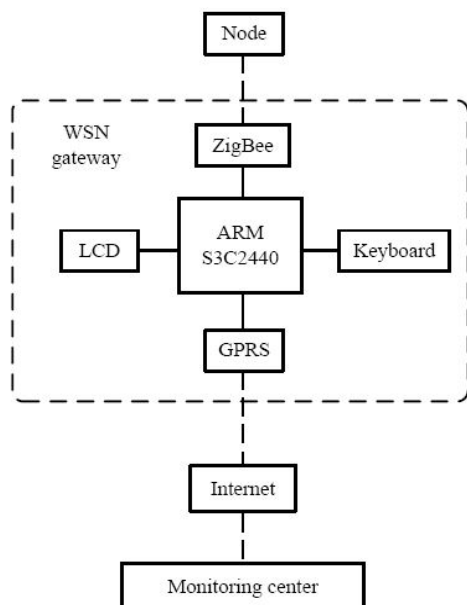
Fig. 6. Structure of WSN Gateways [104].

A ZigBee radio for wireless communication was also being deployed for an on-field measurement of debris in aquatic environments using a smartphone-based robot [109]. A host computer was used to communicate smartphone using Wi-Fi and ZigBee-based fish robot. A PID controller was embedded to the smartphone purposely for the reduction of physical sizes and operational cost. The prototype system integrates a Galaxy smartphone enwrapped with water-proof casing to a robotic fish. The vision-based debris detection does not only improve various dynamic complications but also effectively reduce camera shaking and reflections.

4. Conclusion

Undoubtedly, wireless sensor networks have a huge potential in the field of environmental monitoring sectors due to their advantageous features such as real-time monitoring, ability to operate in remote locations and low power consumption. WSNs application offers a multiple-point of data collection in accordance with a variety of ecological variables. Unexpected contamination events can be monitored and controlled via wireless communication technology. However, exploiting WSN application in rural areas can be a challenging task. Wireless communication is a concept of interconnection between locally based station and station nodes. The construction of WSN may result in global power consumption. In addition, rural areas may have a

limited site for WSN infrastructures. Hence, smartphone-based monitoring technique was introduced for the past few years. In correlation to advanced smartphone applications, water monitoring technologies have been tremendously improved in term of data transmission speed, real-time data collection, low power consumption, system accuracy and operational time responses.

Portable sensing platform is advantageous for multiple detections, semi-quantitative and qualitative analysis, fast operational responses, user- friendly and low cost. It is clear that in order to develop an innovative and effective water monitoring system, the following main criteria must be met: (1) a rapid early detection warning system, (2) the ability to perform continuous real-time data measurements, (3) the ability to respond to the needs and preferences of users, (4) the operational cost reduction with fully utilized devices and (5) the provision of detection abilities in unvisited regions. These requirements are achievable by deploying a smartphone-based water monitoring technology.

There have been many established method utilizing smartphone technology via wireless communication such as GPRS, Bluetooth, and GSM. Since cellular networks have grown linearly over the increment of bandwidth, currently 3G and 4G networks are highly advisable to be fully utilized in water monitoring applications. Up to date, several water monitoring interface with smartphone devices are reported to only display data results rather than performing a qualitative and quantitative analysis. This is obviously due to the lag of data speed and data storage in smartphones which are not suitable to execute a mathematical and statistical algorithm. Hence, it is recommended to use a local hot computer or tablet for data analysis. The disadvantage of using a smartphone to monitor water contaminants is the accessibility and exposure of valuable data to unauthorized personnel if proper precautions are not observed. Cybersecurity and securing wireless system is, therefore, one of the elements that requires further research.

Acknowledgements

References

[1]. Susan, D. R., Environmental Mass Spectroscopy: Emerging Contaminants and Current Issues, *Journal of Analytical Chemistry,* 76, 12, 2004, pp. 3337-3364.

[2]. Gravriel, A. A., Landre, J. P. and Lamb, A. J., Incidence of Mesophilic Aerommonas within a Public Drinking Water Supply in North-East Scotland, *Journal of Applied Microbiology,* 84, 3, 1998, pp. 383-392.

[3]. Kivanc, M., Yilmaz, M. and Demir, F., The Occurrence of Aeromonas in Drinking Water, Tap Water and the Porsuk River, *Brazil Journal of Microbiology,* 42, 1, 2011, pp. 126-131.

[4]. Angelakis, A. N. and Snyder, S. A., Wastewater Treatment and Reuse: Past, Present and Future, *Journal of Water,* 7, 9, 2015, pp. 4887-4895.

[5]. Edswald, J., Water Quality & Treatment: A Handbook on Drinking Water, 6th ed., American Water Works Association, *McGraw-Hill,* 2011.

[6]. Liu, S., Che, H., Smith, K. and Chang, T., A Real Time Method of Contaminant Classification Using Conventional Water Quality Sensors, J*ournal of Environmental Managements,* 154, 2015, pp. 13-21.

[7]. Lambrou, T. P., Anastasiou, C. C., Panayiotou, C. G. and Polycarpou, M. M., A Low-Cost Sensor Network for Real-Time Monitoring and Contamination Detection in Drinking Water Distribution Systems, *Journal of Sensors,* 14, 8, 2014, pp. 2765-2772.

[8]. Che, H., Liu, S., and Smith, K., Performance Evaluation for a Contamination Detection Method Using Multiple Water Quality Sensors in an Early Warning System, *Water,* 7, 4, 2015, pp. 1422–1436.

[9]. Bell, J., Climent, E., Hecht, M., Buurman, M., Rurack K., Combining a Droplet-Based Microfluidic Tubing System with Gated Indicator Releasing Nanoparticles for Mercury Trace Detection, *ACS Sensors,* 1, 4, 2016, pp. 334–338.

[10]. Barbosa, A. I., Gehlot, P., Sidapra, K., Edwards, A. D., Reis, N. M., Portable Smartphone Quantitation of Prostate Specific Antigen (PSA) in a Fluoropolymer Microfluidic Device, *Biosensors and Bioelectronic,* 70, 2015, pp. 5–14.

[11]. Wang, Z., Han, T., Jeon, T.-J., Park, S., & Kim, S. M., Rapid Detection and Quantification of Bacteria Using an Integrated Micro/Nanofluidic Device, *Sensors and Actuators B: Chemica*l, 178, 2013, pp. 683–688.

[12]. Jones, S. L., Tanaka, A., Eastwood, G. M., Young, H., Peck, L., Bellomo, R., and Mårtensson, J., Bioelectrical Impedance Vector Analysis in Critically Ill Patients: A Prospective, Clinician-Blinded Investigation, *Critical Care,* 19, 1, 2015.

[13]. Yu, H., Song, Y., Gao, H., Liu, L., Yao, L., & Peng, J., Applying Fluorescence Spectroscopy and Multivariable Analysis to Characterize Structural Composition of Dissolved Organic Matter and Its Correlation with Water Quality in an Urban River, *Environmental Earth Sciences,* 73, 9, 2015, pp. 5163–5171.

[14]. Puiu, A., Fiorani, L., Menicucci, I., Pistilli, M. and Lai, A., Submersible Spectrofluorometer for Real Time Sensing of Water Quality, *Journal of Sensors,* 15, 6, 2015, pp. 14415-14434.

[15]. Belkhamssa, N., da Costa, J. P., Justino, C. I. L., Santos, P. S. M., Cardoso, S., Duarte, A. C., Rocha-Santos, T. and Ksibi, M., Development of an Electrochemical Biosensor for Alkylphenol Detection, *Talanta,* 158, 30, 2016, pp. 30-34.

[16]. Eltzov, E., Slobodnik, V., Ionescu, R. E. and Marks, R. S., On-Line Biosensor for the Detection of Putative Toxicity in Water Contaminants, *Talanta,* 132, 2015, pp. 583-590.

[17]. Hassan, S. H. A., Van Ginkel, S. W., Hussein, M. A. M., Abskharon, R. and Oh, S-E., Toxicity Assessment Using Different Bioassays and Microbial Biosensors, *Journal of Environmental International,* 92-93, 2016, pp. 106-118.

[18]. Weller, M., 2013, Immunoassays and Biosensors for the Detection of Cyanobacterial Toxins in Water, *Journal of Sensors,* 13, 11, pp. 15085-15112.

[19]. He, X., Liu, Y-L., Conklin, A., Westrick, J., Weavers, L. K. and Dionysiou, D. D., et al., Toxic Cyanobacteria and Drinking Water: Impacts, Detection and Treatment, *Journal of Harmful Algae,* 54, 2016, pp. 174-193.

[20]. John, S. H. and Jeffery, G. S., Distribution System Water Quality Monitoring: Sensor Technology Evaluation Methodology and Results, *United States Environmental Protection Agency,* Article ID: EPA 600/R-09/076, 2009, 60 pages.

[21]. Gonzalez, C., Greenwood, R. and Quevauviller, P. (Eds.), Rapid Chemical and Biological Technique for Water Monitoring, *John Wiley and Sons,* 2009.

[22]. Eckner, K. F., Comparison of Membrane Filtration and Multiple-Tube Fermentation by the Colilert and Enterolert Methods for the Detection of Waterborne Coliform Bacteria, Escherichia Coli and Enterococci Used in Drinking and Bathing Water Quality Monitoring in Southern Sweden, *Applied and Environmental Microbiology,* 64, 1998, pp. 3079-3083.

[23]. Omezuruike, O. I., Damilola, A. O., Adeola, O. T., Fajobi, Enobong, A. and Olufunke, S., Microbiological And Physicochemical Analysis of Different Water Samples Used for Domestic Purposes in Abeokuta and Ojota, Lagos State, Nigeria, *African Journal of Biotechnology,* 7, 2008, pp. 617-621.

[24]. Kimani-Murage, E. W. and Ngindu, A. M., Quality of Water the Slum Dwellers Use: The Case of a Kenyan Slum, *Journal of Urban Health,* 84, 6, 2007, pp. 829-838.

[25]. Brandao, L. R., Medeiros, A. O., Duarte, M. C., Barbosa, A. C. and Rosa, C. A., Diversity and Antifungal Susceptibility of Yeasts Isolated by Multiple-Tube Fermentation from Three Freshwater Lakes in Brazil, *Journal of Water Health,* 8, 2, 2010, pp. 279-289.

[26]. Zidek, Z., Kmonickova, E., Kostecka, P. and Jansa, P., Microfiltration Method of Removal Bacterial Contaminant and Their Monitoring by Nitric Oxide and Limulus Assays, *Journal of Nitric Oxide,* 28, 2013, pp. 1-7.

[27]. Xiong, B., Zydney, A. L. and Kumar, M., Fouling of Microfiltration Membranes by Flowback and Produced Waters from the Marcellus Shale Gas Play, *Water Research,* 99, 2016, pp. 162-170.

[28]. Santos, C. D., Scherer, R. K., Cassini, A. S., Marczak, L. D. F. and Tessaro, I. C., Clarification of Red Beet Stalks Extract By Microfiltration Combined with Ultrafiltration, *Journal of Food Engineering,* 185, 2016, pp. 35-41.

[29]. Bonetta, S., Borelli, E., Bonetta, S., Conio, O., Palumbo, F. and Carraro, E., Development of A PCR Protocol for the Detection of Escherichia Coli O157:H7 and Salmonella spp in Surface Water, *Environmental Monitoring and Assessment,* 177, 1-4, 2011, pp. 493-503.

[30]. Park, S. H., Hanning, I., Jarquin, R., Moore, P., Donoghue, D. J., Donoghue, A. M. and Ricke, S. C., Multiplex PCR Assay for the Detection and Quantification of Campylobacter spp., Escherichia Coli O157:H7, and Salmonella Serotypes in Water

Samples, *FEMS Microbiological Letter*, 316, 1, 2011, pp. 7-15.

[31]. Li, B., Hu, Z. and Elkins, C. A., 2014, Detection of Live Escherichia Coli O157:H7 Cells by PMA-Qpcr, *Journal of Visualized Experiments,* 84, E50967.

[32]. Richardson, S. D. and Postigo, C., A New Technique Helps To Uncover Unknown Peptides and Disinfection-By-Products in Water, *Journal of Environmental Science,* 42, 2016, pp. 6-8.

[33]. Verstraeten, I. M., Fetterman, G. S., Meyer, M. T., Bullen, T. and Sebree, S. K., Use of Tracers and Isotopes to Evaluate Vulnerability of Water in Domestic Wells to Septic Waste, *Ground Water Monitoring and Remediation*, 25, 2, 2005, pp. 107-117.

[34]. Llorca, M., Lucas, D., Ferrando-Climent, L., Badia-Fabregat, M., Cruz-Morato, C., Barcelo, D. and Rodriguez-Mozaz, S., Suspect Screening of Emerging Pollutants and Their Major Transformation Products in Wastewaters Treated With Fungi by Liquid Chromatography Coupled to a High Resolution Mass Spectrometry, *Journal of Chromatography A*, 1439, 2016, pp. 124-136.

[35]. Schaider, L. A., Rudel, R. A., Ackerman, J. M., Dunagan, S. C. and Brody, J. G., Pharmaceuticals, Perfluorosurfactants, and Other Organic Wastewater Compounds in Public Drinking Water Wells in a Shallow Sand and Gravel Aquifer, *Science of Total Environmental*, 468, 2014, pp. 384-393.

[36]. Hall, J., Zaffiro, A., Marx, R. B., Kefauver, P., Krishnan, E. R., Haught, R. and Herrmann, J. G., On-Line Water Quality Parameters as Indicators of Distribution System Contamination 2, *Journal of American Water Works Association,* 99, 2007, pp. 66-77.

[37]. Long, F., Zhu, A. and Shi, H., Recent Advances in Optical Biosensors for Environmental Monitoring and Early Warning, J*ournal of Sensors,* 13, 10, 2013, pp. 13928-13948.

[38]. Richardson, S. D. and Ternes, T. A., Water Analysis: Emerging Contaminants and Current Issues, *Analytical Chemistry*, 83, 12, 2011, pp. 4614-4648.

[39]. Subhas, C. M. and Alex, M., Smart Sensors for Real-Time Water Quality Monitoring, Smart Sensors, Measurement and Instrumentation, 4th ed., *Springer-Verlag Berlin Heidelberg*, New York, 2013.

[40]. Capodaglio, A. G. and Callegari, A., Online Monitoring Technologies for Drinking Water Systems Security, in: Hlavinek P. et al. (Eds.), Risk Management of Water Supply and Sanitation Systems, *Springer Science & Business Media,* 2009, pp. 153-179.

[41]. Akyildiz, L. F., Su, W., Sankarasubramaniam, Y. and Cayirci, E., Wireless Sensor Networks: A Survey, *Journal of Computer Networks*, 38, 4, 2002, pp. 393-422.

[42]. Bughin, J., Chui, M. and Manyika, J., Clouds, Big Data and Smart Assets: Ten Tech-Enabled Business Trends to watch, *McKinsey Q.,* 56, 2010, pp. 75–86.

[43]. Fraternali, P., Castelletti, A., Soncini-Sessa, R., Vaca Ruiz, C. and Rizzoli, A. E., Putting Humans in the Loop: Social Computing For Water Resources Management, *Environmental Modelling and Software,* 37, 2012, pp. 68–77.

[44]. Hasan, R., Raghav, A., Mahmood, S. and Hasan, M. A., Artificial Intelligence in River Quality Assessment, in *Proceedings of the* International Conference on Information Management, Innovation Management and Industrial Engineering (ICIII), Vol. 1, 2011, pp. 491-495.

[45]. Najah, A., El-Shafie, A., Karim, O. A., Jaafar, O. and El-Shafie, A. H., An Application of Different Artificial Intelligences Techniques for Water Quality Prediction, *International Journal of Physics Science*, 6, 2011, pp. 5298–5308.

[46]. Antonio, B., Modelling studies for the detection of bacteria in Biosensor Water Distribution Networks, Master Thesis, *KTH Royal Institute of Technology,* 2012.

[47]. Peng, J., Hongbo, X., Zhiye, H. and Zheming, W., Design of A Water Environment Monitoring System Based on Wireless Sensor Networks, *Journal of Sensors,* 9, 8, 2009, pp. 6411-6434.

[48]. Seders, L. A., Shea, C. A., Lemmon, M. D., Maurice, P. A. and Talley, J. W., 2007, LakeNet: An Integrated Sensor Network for Environmental Sensing in Lakes, *Environmental Engineering Science*, 24, 2, pp. 183–191.

[49]. Manas, R. G., Bjorn, B., Te-Wei, C., Parya, M., Barbara, S. M., Gul, A., Andrzej, W., Laura, L. K. and Gang, L. L., The Microelectronic Wireless Nitrate Sensor Network for Environmental Water Monitoring, *Journal of Environmental Monitoring,* 14, 12, 2012, pp. 3068-3077.

[50]. O'Flynn, B., Martínez-Català, F., Harte, S., O'Mathuna, C., Cleary, J., Slater, C., Regan, F., Diamond, D. and Murphy, H. SmartCoast: A Wireless Sensor Network for Water Quality Monitoring, in *Proceedings of the 32nd IEEE Conference on Local Computer Networks (LCN'07),* Dublin, Ireland, October 15–18, 2007, pp. 815–816.

[51]. Yang, X., Ong, K. G., Dreschel, W. R., Zeng, K., Mungle, C. S. and Grimes, C. A., Design of a Wireless Sensor Network for Long-Term, In-Situ Monitoring of an Aqueous Environment, *Journal of Sensors*, 2, 11, 2002, pp. 455–472.

[52]. Ramanathan, N., Lukac, M., Ahmed, T., Kar, A., Praveen, P., Honles, T., Leong, I., Rehman, I., Schauer, J. and Ramanathan, V., A Cellphone Based System for Large-Scalemonitoring of Black Carbon, *Atmospheric Environment,* 45, 39, 2011, pp. 4481–4487.

[53]. Potyrailo, R. A., Ubiquitous Devices for Chemical Sensing, *Autonomous Sensor Networks,* 2012, pp. 237-264.

[54]. Vashist, S. K., Mudanyali, O., Schneider, E. M., Zengerle, R. and Ozcan, A., Cellphone-Based Devices for Bioanalytical Sciences, *Analytical and Bioanalytical Chemistry*, 406, 14, 2014, pp. 3263-3277.

[55]. Hongying, Z., Oguzhan, Y., Ting-Wei, S., Derek, T. and Aydogan, O., Cost-Effective and Compact Wide-Field Fluorescent Imaging in a Cell-Phone, *Lab on a Chip,* 11, 2, 2011, pp. 315-322.

[56]. David, E., Dakota, O., Li, J., Abdurrahman, G., Seoho, L., Mathew, M. and Saurabh, M., Smartphone Technology Can Be Transformative to the Deployments of Lab-on-Chip Diagnostics, *Lab on a Chip,* 14, 17, 2014, pp. 3159-3164.

[57]. Seoho, L., Vlad, O., Matt, M., Saurabh, M. and David, E., A Smartphone Platform for the Quantification of Vitamin D Levels, *Lab on a Chip,* 14, 8, 2014, pp. 1437-1442.

[58]. Seoho, L., Balaji, S., Sasank, V., Saurabj, M. and David, E., Personalized Nutrition Diagnostics at the Point-of-Need, *Lab on a Chip,* 16, 13, 2016, pp. 2408-2417.

[59]. Seoho, L., Dakota, O., Jessica, H., Susannah, C., Saurabh, M. and David, E., NutriPhone: Vitamin B12 Testing on Your Smartphone, *Proc. SPIE 9699, Optics and Biophotonics in Low-Resource Setting II*, 2016.

[60]. Isa, N., Ahmet, F. C., Justin, W., Saqib, M., Derek, T., Richie, N., Stephen, P. and Aydogan, O., Smart-Phone Based Computational Microscopy Using Multi-Frame Contact Imaging on a Fiber-Optic Array, *Lab on a Chip*, 13, 20, 2013, pp. 4015-4023.

[61]. Liu, X., Lin, T. and Ann, P. B., Smartphones for Cell and Biomolecular Detection, *Annals of Biomedical Engineering*, 42, 11, 2014, pp. 2205-2217.

[62]. Yanzhi, D., Zhineng, J., Wangping, D., Jing, S., Shixing, C., Haiyun, S., Ali, A., Xiaolei, Z., Shiping, S., Jiye, S. and Chunhai, F., Portable Detection of Clenbuterol Using a Smartphone-Based Electrochemical Biosensor with Electric Field-Driven Acceleration, *Journal of Electroanalytical Chemistry*, Vol. 781, 2016, pp. 339–344.

[63]. Wu, X., Brown, K. N. and Sreenan, C. J., Data Pre-Forwarding For Opportunistic Data Collection in Wireless Sensor Networks, *ACM Transactions on Sensor Networks*, 11, 1, 2014, pp. 1-33.

[64]. Wu, X., Brown, K. N. and Sreenan, C. J., Analysis of Smartphone User Mobility Traces for Opportunistic Data Collection in Wireless Sensor Networks, *Pervasive and Mobile Computing*, 9, 6, 2013, pp. 881-891.

[65]. Park, U. and Heidemann, J., Data Muling With Mobile Phones for Sensornets, in *Proceedings of the 9th ACM Conference on Embedded Networked Sensor Systems (SenSys '11)*, New York, 2011, pp. 162-175.

[66]. Shepard, C., Rahmati, A., Tossell, C., Zhong, L. and Kortum, P., Livelab: Measuring Wireless Networks and Smartphone Users in the Field, *ACM SIGMETRICS Performance Evaluation Review*, 38, 3, 2011, pp. 15-20.

[67]. Zuhal, C. and Murat, D., Smartphone-Based Data Collection from Wireless Sensor Networks in an Urban Environment, *Journal of Network and Computer Applications*, 58, 2015, pp. 208-216.

[68]. Li-Ju, W., Yu-Chung, C., Rongrong, S. and Lei, Li., A Multichannel Smartphone Optical Biosensor for High-Throughput Point-Of-Care Diagnostics, *Biosensors and Bioelectronics*, 87, 2017, pp. 686-692.

[69]. Dean, A. G., (Ed.), The Handbook of Personal Area Networking Technologies and Protocols, *Cambridge University Press*, 2013.

[70]. Yan, Z., Jun, Z. and Miao, M. (Eds.), Handbook of Research on Wireless Security, *Idea Group Inc. (IGI)*, 2008.

[71]. Jing, J., Xinhao, W., Ran, C., Yukun, R., Chengpeng, H., Zhida, X. and Gang, L. L., Smartphone Based Portable Bacteria Pre-Concentrating Microfluidic Sensor and Impedance Sensing System, *Sensors and Actuators B: Chemical*, 193, 2014, pp. 653-659.

[72]. Diming, Z., Jing, J., Junye, C., Qian, Z., Yanli, L., Yao, Y., Shuang, L., Gang, L. L. and Qingjun, L., Smartphone-based Portable Biosensing System using Impedance Measurement with Printed Electrodes for 2, 4, 6-trinitrotoluene (TNT) Detection, *Biosensors and Bioelectronics*, 70, 2015, pp. 81-88.

[73]. Rajendran, V. K., Bakthavathsalam, P. and Jaffar Ali, B. M., Smartphone Based Bacterial Detection using Bio functionalized Fluorescent Nanoparticles, *Microchimica Acta*, 181, 15-16, 2014, pp. 1815-1821.

[74]. Roda, A., Michelini, E., Cevenini, L., Calabria, D., Calabretta, M. M. and Simoni, P., Integrating Biochemiluminesence Detection on Smartphones: Mobile Chemistry Platform for Point-of-Need Analysis, *Analytical Chemistry*, 86, 15, 2014, pp. 7299-7304.

[75]. Souza, F. C., Lima, A. and Neff, H., Smartphone-based Portable Optical Biosensor Utilizing Surface Plasmon Resonance, in *Proceedings of the IEEE International Instrumentation and Measurement Technology Conference*, 2014, pp. 890-895.

[76]. Diming, Z., Yanli, L., Qian, Z., Lei, L., Shuang, L., Yao, Y., Jing, J., Gang, L. L. and Qingjun, L., Protein Detecting with Smartphone-controlled Electrochemical Impedance Spectroscopy for Point-of-Care Applications, *Sensors and Actuators B: Chemical*, 222, 2016, pp. 994-1002.

[77]. Anthony, F. and Aloys, N. M., Ubiquitous Mobile Sensing for Water Quality Monitoring and reporting within Lake Victoria Basin, *Wireless Sensor Network*, 6, 2014, pp. 257-264.

[78]. Lee, J., Su, Y. and Shen, C., A Comparative Study of Wireless Protocols: Bluetooth, UWB, ZigBee, and Wi-Fi, in *Proceedings of the 33rd Annual Conference on Industrial Electronics Society*, 2007, pp. 46–51.

[79]. Dave, U. A., and Samant, R. M., Overview of Smartphone Application Development Using Cross-Platform Framework, in *Proceedings of the International Conference & Workshop on Emerging Trends in Technology (ICWET '11)*, 2011.

[80]. Aram, S., Troiano, A., Rugiano, F. and Pasero, E., Low Power and Bluetooth-Based Wireless Sensor Network for Environmental Sensing Using Smartphones, *Artificial Intelligence Applications and Innovations*, 2012, pp. 332–340.

[81]. Aram, S., Toriono, A., Rugiano, F. and Pasero, E., Mobile Environmental Sensing Using Smartphones, in Measurement, Instrumentation, and Sensors Handbook, Second Edition, *CRC Press*, 2014, pp. 1–12.

[82]. Kim, U., Ravikumar, A., Seubert, J., and Figueira, S., Detection of bacterial pathogens through microfluidic DNA sensors and mobile interface toward rapid, affordable, and point-of-care water monitoring, in *Proceedings of the IEEE Point-of-Care Healthcare Technologies (PHT)*, 2013.

[83]. Breslauer, D. N., Maamari, R. N., Switz, N. A., Lam, W. A. and Fletcher, D. A., Mobile Phone Based Clinical Microscopy for Global Health Applications, *PLoS ONE*, 4, 7, 2009, pp. E6320.

[84]. Switz, N. A., D'Ambrosio, M. V. and Fletcher, D. A., Low-Cost Mobile Phone Microscopy with a Reversed Mobile Phone Camera Lens, *PLoS ONE*, 9, 5, 2014, pp. E95330.

[85]. Zhu, H., Yaglidere, O., Su, T.-W., Tseng, D. and Ozcan, A., Cost-effective and compact wide-field fluorescent imaging on a cell-phone, *Lab on a Chip*, 11, 2, 2011, pp. 315-322.

[86]. Zhu, H., Mavandadi, S., Coskun, A. F., Yaglidere, O. and Ozcan, A., Optofluidic Fluorescent Imaging Cytometry on a Cell Phone, *Analytical Chemistry*, 83, 17, 2011, pp. 6641-6647.

[87]. Navruz, I., Coskun, A. F., Wong, J., Mohammad, S., Tseng, D., Nagi, R., Stephen, P. and Ozcan, A., Smart-Phone Based Computational Microscopy Using Multi-Frame Contact Imaging on a Fiber-Optic Array, *Lab on a Chip*, 13, 20, 2013, pp. 4015.

[88]. Bishara, W., Sikora, U., Mudanyali, O., Su, T.-W., Yaglidere, O., Luckhart, S., and Ozcan, A., Holographic Pixel Super-Resolution In Portable Lensless On-Chip Microscopy Using A Fiber-Optic Array, *Lab on a Chip*, 11, 7, 2011, pp. 1276.

[89]. Tseng, D., Mudanyali, O., Oztoprak, C., Isikman, S. O., Sencan, I., Yaglidere, O., and Ozcan, A., Lensfree Microscopy on a Cellphone, *Lab on a Chip,* 10, 14, 2010, pp. 1787.

[90]. Erickson, D., O'Dell, D., Jiang, L., Oncescu, V., Gumus, A., Lee, S., Matthew, M. and Mehta, S., 2014, Smartphone Technology Can Be Transformative to the Deployment of Lab-On-Chip Diagnostics, *Lab on a Chip,* 14, 17, pp. 3159.

[91]. Diana, B., Roberto, M. and Jean, L. M., Fluorescence Analyzer Based on Smartphone Camera and Wireless for Detection of Ochratoxin A, *Sensors and Actuators B: Chemical*, 232, 2016, pp. 462-468.

[92]. Yeo, S.-J., Choi, K., Cuc, B. T., Hong, N. N., Bao, D. T., Ngoc, N. M., et al., Smartphone-Based Fluorescent Diagnostic System for Highly Pathogenic H5N1 Viruses, *Theranostics,* 6, 2, 2016, pp. 231–242.

[93]. Barbosa, A. I., Gehlot, P., Sidapra, K., Edwards, A. D., and Reis, N. M., Portable Smartphone Quantitation of Prostate Specific Antigen (PSA) in a Fluoropolymer Microfluidic Device, *Biosensors and Bioelectronics*, 70, 2015, pp. 5–14.

[94]. Nicolini, A. M., Fronczek, C. F., and Yoon, J.-Y., Droplet-Based Immunoassay On A, Sticky, Nanofibrous Surface for Multiplexed and Dual Detection of Bacteria Using Smartphones, *Biosensors and Bioelectronic,* 67, 2015, pp. 560–569.

[95]. Yun, W., Yuanyuan, L., Xu, B., Juan, H., Jinchen, X., Xiaoyu, T. and Liang, N., A Smartphone-Based Colorimetric Reader Coupled with a Remote Server for Rapid On-site Catechols Analysis, *Talanta,* 160, 2016, pp. 194-204.

[96]. Zhu, H., Mavandadi, S., Coskun, A. F., Yaglidere, O. and Ozcan, A., Optofluidic Fluorescent Imaging Cytometry on a Cell Phone, *Analytical Chemistry*, 83, 17, 2011, pp. 6641–6647.

[97]. Shen, L., Hagen, J. a. and Papautsky, I., Point-of-Care Colorimetric Detection with a Smartphone, *Lab on a Chip,* 12, 21, 2012, pp. 4240.

[98]. Gallegos, D., Long, K. D., Yu, H., Clark, P. P., Lin, Y., George, S., Pabitra, N. and Brian, T. C., Label-Free Biodetection Using a Smartphone, *Lab on a Chip,* 13, 11, 2013, pp. 2124–2132.

[99]. Dutta, S., Saikia, K. and Nath, P., Smartphone Based LSPR Sensing Platform Forbio-Conjugation Detection and Quantification, *RSC Adv.,* 6, 26, 2016, pp. 21871–21880.

[100]. Hasan, G., Erol, O., Guzin, K., Mehmet, C., Elif, E., Ahmet, E. T., Sencer, A., Yildiz, U., Caglar, E. and Aykutlu, D., A Smartphone Based Surface Plasmon Resonance Imaging (SPRi) Platform for On-site Biodetection, *Sensors and Actuators B: Chemical,* 239, 2017, pp. 571-577.

[101]. Liu, Y., Liu, Q., Chen, S., Cheng, F., Wang, H. and Peng, W., Surface Plasmon Resonance Biosensor Based on Smart Phone Platforms, *Scientific Report,* 5, 2015, pp. 12864.

[102]. Bremer, K. and Roth, B., Fibre Optic Surface Plasmon Resonance Sensor System Designed For Smartphones, *Optics Express,* 23, 13, 2015, pp. 17179–17184.

[103]. Preechaburana, P., Suska, A., and Filippini, D., Biosensing with Cell Phones, *Trends in Biotechnology,* 32, 7, 2014, pp. 351–355.

[104]. Yanan, W., Lingling, S. and Shuo, L., The Design of Wireless Sensor Network Gateway based on ZigBee and GPRS, *International Journal of Future Generation Communication and Networking,* 7, 2, 2014, pp. 47-58.

[105]. Anumalla, S., Ramamurthy, B., Gosselin, D. C., and Burbach, M., Ground Water Monitoring using Smart Sensors, in *Proceedings of the IEEE International Conference on Electro Information Technology,* 2005.

[106]. Ghaffari, S. A., Caron, W., Loubier, M., Rioux, M., Viens, J., Gosselin, B. and Messaddeq, Y., A Wireless Multi-Sensor Dielectric Impedance Spectroscopy Platform, *Journal of Sensors,* 15, 9, 2015, pp. 23572-23588.

[107]. Xiao, Y., Zhang, J., Liu, T., and Gao, X., An Environmental Monitoring System Based on ZigBee for Emergency Applications, in *Proceedings of the 5th International Conference on Wireless Communications,* Networking and Mobile Computing, 2009.

[108]. Xing, J. Z., Zhu, L., Jackson, J. A., Gabos, S., Sun, X. J., Wang, X. B. and Xu, X., Dynamic Monitoring of Cytotoxicity on Microelectronic Sensors, *Chemical Research in Toxicology,* 18, 2, 2005, pp. 154-161.

[109]. Wang, Y., Tan, R., Xing, G., Wang, J., Tan, X., Liu, X., and Chang, X., Monitoring Aquatic Debris Using Smartphone-Based Robots, *IEEE Transactions on Mobile Computing*, 15, 6, 2016, pp. 1412–1426.

Sensors & Transducers

Image Reconstruction of Metal Pipe in Electrical Resistance Tomography

**[1] Suzanna RIDZUAN AW, [2, 3, *] Ruzairi ABDUL RAHIM,
[2] Yusri MOHD YUNUS, [3] Mohd Hafiz FAZALUL RAHIMAN,
[4] Yasmin WAHAB, [2] Fazlul Rahman Mohd YUNUS,
[5] Elmy Johana MOHAMED, [6] Azian ABDUL AZIZ, [2] Chiew Loon GOH,
[2] Jayasuman PUSPPANATHAN, [7] R. G. GREEN and [8] Zhen Cong TEE**

[1] Faculty of Electrical & Automation Engineering Technology, TATiUC, Jalan Panchor,
Telok Kalong, Kemaman, Terengganu, 24000, Malaysia
[2] Process Tomography and Instrumentation Engineering Research Group (PROTOM-i), Innovative
Engineering Research Alliance, Faculty of Electrical Engineering, Universiti Teknologi Malaysia,
Johor, 81310, Malaysia
[3] School of Mechatronic Engineering, Universiti Malaysia Perlis, Pauh Putra Campus,
Arau, Perlis, 02600, Malaysia
[4] Department of Instrumentation & Control Engineering (ICE), Faculty of Electrical & Electronics
Engineering, Universiti Malaysia Pahang, Pekan, Pahang, 26600, Malaysia
[5] Department of Mechatronics and Robotics, Faculty of Electrical and Electronic Engineering,
Universiti Tun Hussein Onn Malaysia, Johor, 86400, Malaysia
[6] Language Academy, Universiti Teknologi Malaysia, Johor Bahru, 81310, Malaysia
[7] School of Engineering, Sheffield Hallam University, Sheffield, United Kingdom
[8] Logo Solution Sdn. Bhd. Johor, 81200, Malaysia
[2] Tel.: +60197104000, fax: +607-4537150
E-mail: ruzairi@fke.utm.my, ruzairi@uthm.edu.my

Abstract: This paper demonstrates a Linear Back Projection (LBP) algorithm based on the reconstruction of conductivity distributions to identify different sizes and locations of bubble phantoms in a metal pipe. Both forward and inverse problems are discussed. Reconstructed images of the phantoms under test conditions are presented. From the results, it was justified that the sensitivity maps of the conducting boundary strategy can be applied successfully in identifying the location for the phantom of interest using LBP algorithm. Additionally, the number and spatial distribution of the bubble phantoms can be clearly distinguished at any location in the pipeline. It was also shown that the reconstructed images agree well with the bubble phantoms.

1. Introduction

Tomography offers a unique opportunity to reveal the complexities of internal structure of an object without the need to invade the object. One of the most extensive modalities of tomography is the Electrical Resistance Tomography (ERT). ERT is an accepted diagnostic technique for imaging the interior of

opaque systems. It is relatively safe, inexpensive to operate and is relatively fast, thus enabling real-time monitoring of processes. This technique has found applications in many areas, including medical imaging, environmental monitoring, and industrial processes. Electrical Resistance Tomography (ERT) has become a promising technique in monitoring and analysing various industrial flows due to its diverse advantages, such as high speed, low cost, suitability for various sizes of pipes and vessels, having no radiation hazard, and being non-intrusive [1-3, 20, 21]. It provides cross sectional images of conductivity distribution within its sensing region. For a system employing ERT on a metallic or conducting vessel pipe, the electrodes need to be insulated from the pipe wall. In addition, the conducting boundary strategy needs to be applied to overcome the grounding effect [4, 5].

Since the ERT model is nonlinear and difficult to be solved analytically, the finite element method (FEM) is preferable in solving forward modeling. From the solution, the data is interpolated to generate the sensitivity distribution. Later, the sensitivity distribution obtained is used with linearized method to solve inverse problems.

In this paper, simulations were used in reconstructing the image of bubble phantoms in a metal wall using conducting measurement techniques in ERT. FEM was used to solve the forward model and the data obtained were then interpolated in MATLAB to obtain the sensitivity distribution for every possible injection-measurement electrode pair and the total sensitivity distribution. Then, every projected voltage measurements for both the homogeneous and nonhomogeneous systems were recorded. Lastly, an image reconstruction was developed using the Linear Back Projection (LBP) algorithm. Goals of the current research and development efforts involved verifying the feasibility and effectiveness of the sensitivity maps developed in reconstructing the image for the system under investigation.

2. System Configuration

Sixteen rectangular electrodes of 12 mm × 100 mm were utilized in this research. The electrodes were mounted at the center of a stainless steel column and evenly spaced along the circumference. The system was modelled in 2D planes using COMSOL Multiphysics 4.2®, a finite element analysis tool. The settings of the parameter used in the simulation are shown in Table 1. For an invasive ERT, the electrodes must be in continuous contact with the medium inside the column. Hence, in this research, it is assumed that the electrodes make electrical contact with the fluid inside the column but do not affect the normal mass transfer within the system.

A flexible circuit board was used as the electrode in the research. It is to be noted that metal electrodes for electrically-conducting (metallic) column differ

slightly from a non-conducting (insulating) column in which the electrodes need to be insulated from the conducting column. Fig. 1 shows the design of the electrode fabrication using flexible circuit board of the proposed system for the ERT system deploying a conducting vessel.

Table 1. Simulation parameters with COMSOL 4.2a.

Parameter	Value
Column's Inner radius	50 mm
Column's Outer radius	51 mm
Column Height	300 mm
Number of electrodes (N)	16
Electrode's material	Gold
Insulator's material	FR4
Electrode's width (w) x height (h)	12 × 100 mm
Current excitation	5 mA
σ_{water}	8.3×10^{-3} S/m
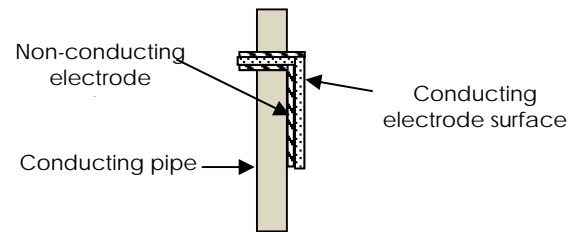
Fig. 1. Electrode Fabrication using flexible circuit board.

A 2D physical model has been developed such that it mimics the real ERT system being developed in the laboratory for experimental purposes. Sixteen electrodes that were insulated from the column wall were placed equidistantly inside the column. The materials for each related domain in the model were defined such that they also resemble the real ERT system. The domain for the column was set to be of stainless steel material and the main medium inside the column was tap water with a conductivity of 8.3 mS/m. The electrodes utilized were from a flexible gold coated printed circuit board (PCB). FR4 material was chosen as the material for the insulating part of the electrodes. FR, which stands for Flame Retardant, is a glass fiber epoxy laminate that is most commonly used in PCB materials. All boundary and initial conditions were set to produce an electrical field, solving any electrical potential distribution. The cross section view of the COMSOL model is shown in Fig. 2.

For the ERT system that uses a metal pipe, the adjacent strategy, which is the most commonly used measurement method in ERT is unsuitable for application to the conducting vessel since much of the electrical current from the injection electrode would travel to the ground through the wall material rather than through the multiphase mixture. This greatly reduces the sensitivity of the system. This is called the grounding effect of the vessel. To overcome the grounding effect of the vessel, a conducting boundary strategy was implemented on the model. The strategy

involved each electrode acting sequentially as a current source whilst the whole of the conducting vessel behaved as a grounded current sink. This is illustrated in Fig. 3.
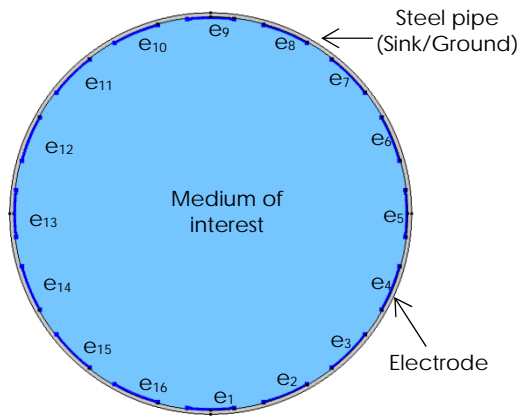
Fig. 2. ERT Model using Metal Pipe.
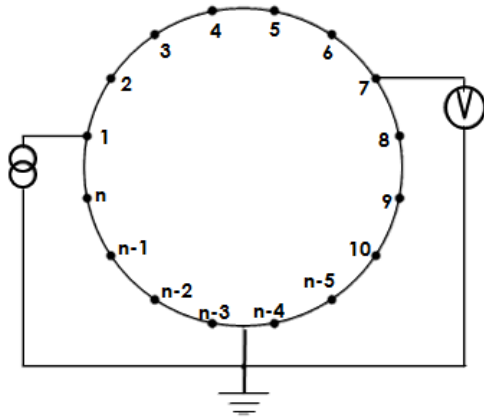
Fig. 3. Conducting Boundary Strategy [6].

A constant current of 5 mA was injected initially at the source electrode, namely electrode 1, e1. In this strategy, all the voltage measurements were referenced to the same earth potential of the conducting boundary which is the pipe itself [7]. This procedure is repeated for all possible pairs of electrodes until a full rotation of the electrical field was obtained. The current density streamline when the metal pipe is grounded is shown in Fig. 4 resulting electrical field when one electrode acted as the source electrode and the others acted as the measurement electrodes, conditioned by the material distribution within the domain of interest is shown in Fig. 5.

3. Image Reconstruction

The sensing field of an ERT system is spread over the entire volume due to its "soft-field" characteristics [8-10]. The paths of electric currents in an ERT system are nonlinear. Current diffuses all over the target, and the current distribution depends on the material's internal conductivity distribution $\sigma = \sigma(r)$ [11]. The image reconstruction problem of conductivity distribution in ERT is an ill-posed and ill-conditioned inverse problem. To solve this inverse problem, a forward model that relates to the dependency between conductivity distribution and boundary voltages need to be solved first. The ERT tomogram, which is the cross sectional image is developed by solving the conductivity distribution in the area of interest.
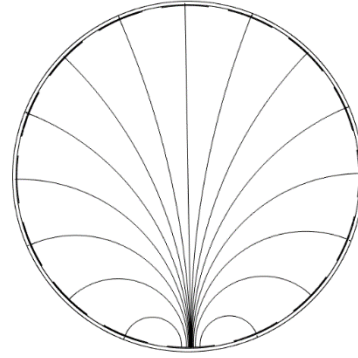
Fig. 4. Current Density Streamline of Metal Pipe using Conducting Strategy.
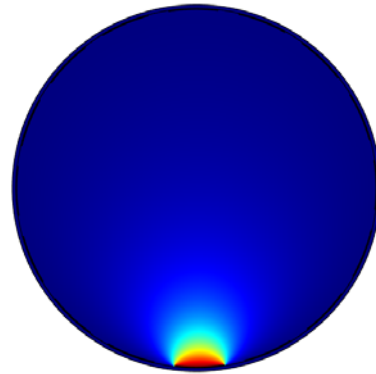
Fig. 5. Electrical Field for Single Injection Electrode.

3.1. Forward Problem

In ERT, the forward problem computes the electrical potentials in the boundary by utilising the initial estimation of the conductivity distribution. The forward problem can be represented by equation (1), where $Y, v,$ and c denote the global conductance matrix, the nodal voltage vector, and the nodal current vector respectively.

$$Y \cdot v = c \qquad (1)$$

Maxwell's law is used in this forward problem to model the distribution of the electrical field of the ERT system. The sensitivity distribution is solved in forward problems using the analytical approach. The sensitivity distribution of a homogeneous conductivity

medium can be acquired by solving the forward model using both analytical and numerical method. Since it is difficult to obtain the analytical solutions of the equation, the numerical solvers, i.e., the finite element methods (FEM) are preferable and the most commonly used method to solve the forward problem. COMSOL Multiphysics 4.2, has been utilized in this work to solve the forward problem of an ERT system of a conducting vessel pipe.

3.2. Sensitivity Distribution using Conducting Strategy

The sensitivity theorem or lead theorem which analysed the boundary of mutual impedance experienced by the changes of conductivity within the sensing region has been introduced by Geselowitz and later refined by Lehr. It is based on Green's theorem and the divergence theorem [12]. By adapting the two theorems to a conducting volume as shown in Fig. 6, the reciprocity theorem (Equation 2) and lead theorem of mutual impedance Z (Equation 3) can be deduced as [13]:

$$I_\phi \psi_{AB} = I_\psi \phi_{CD} \qquad (2)$$

$$Z = \phi_{CD}/I_\phi = \psi_{AB}/I_\varphi, \qquad (3)$$

where ψ_AB and ϕ_CD are the voltage potentials measured between terminal AB and CD due to the injection currents I_ψ and I_ϕ respectively. From the divergence and reciprocity theorem, Geselowitz and Lehr derived a relationship between the mutual impedance changes, ΔZ and the conductivity changes [14].

$$\Delta Z = \frac{\Delta \varphi_{CD}}{I_\varphi} = - \int_v \Delta \sigma \frac{\nabla \varphi}{I_\varphi} \cdot \frac{\nabla \psi}{I_\psi} dv \qquad (4)$$
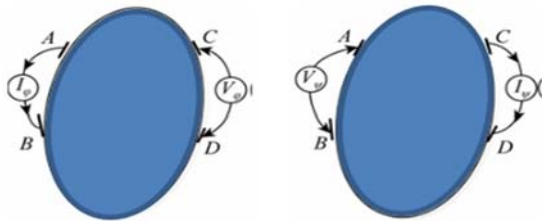
Fig. 6. Mutual Impedance Relation between Terminal AB and CD [15].

Solving for Equation 4, the sensitivity theorem to solve the inverse problem of ERT can be simplified to:

$$S_{ij} = \frac{\Delta R}{\Delta \sigma} = - \int_v \frac{\nabla \varphi_i}{I_i} \cdot \frac{\nabla \varphi_j}{I_j} dv \qquad (5)$$

where S_{ij} is the sensitivity distribution when the i-th and j-th electrode pair is in excitation and measurement respectively, R is the mutual resistance that is a special case of mutual impedance, Z, φ_i is the potential distributions within the medium when the i-th electrode is excited by current I_i, φ_j is the potential distributions within the medium when the j-th electrode is excited by current I_j.

Assuming that the conductivity distribution is composed of k small uniform pixels, the sensitivity coefficient of each pixel can be deduced as [15].

$$S_{i,j}(k) = - - \int_{\Omega_k} \frac{\nabla \varphi_{ik}}{I_i} \cdot \frac{\nabla \varphi_{jk}}{I_j} d\Omega_k, \qquad (6)$$

where Ω_k is the discrete 2D area of the k-th pixel, $s_{i,j}(k)$ is the sensitivity coefficient at the k-th pixel when the i-th and j-th electrode pairs are in excitation and measurement respectively, φ_{ik} is the potential distributions at the k-th pixel when the i-th electrode is excited by current I_i, φ_{jk} is the potential distributions at the k-th pixel when the j-th electrode is excited by current I_j.

The procedure of attaining the sensitivity distribution is only complete when all electrodes are used for injection, such that the cycle has all the possible projections. The sensitivity matrix can then be expressed by [15].

$$S =$$
$$= \begin{bmatrix} S_{1,2}(1) & S_{1,2}(2) & \cdots & S_{1,2}(k) & \cdots & S_{1,2}(M) \\ S_{1,3}(1) & S_{1,3}(2) & \cdots & S_{1,3}(k) & \cdots & S_{1,3}(M) \\ \vdots & \vdots & \cdots & \vdots & \cdots & \vdots \\ S_{i,j}(1) & S_{i,j}(2) & \cdots & S_{i,j}(k) & \cdots & S_{i,j}(M) \\ \vdots & \vdots & \cdots & \vdots & \cdots & \vdots \\ S_{n-2n}(1) & S_{n-2n}(2) & \cdots & S_{n-2n}(k) & \cdots & S_{n-2n}(M) \end{bmatrix}$$
$$(7)$$

The sensitivity theorem is also applicable to the conducting vessel because the electrical field within the vessel still obeys Greens' and the reciprocity theorem. Here, 128×128 pixels which equals to 16384 pixels is implemented to attain the sensitivity distribution. The electric potential, φ and the electric field distribution, E is governed by equation 8.

$$-\nabla \varphi = E \qquad (8)$$

Thus, Equation (8) that denotes the sensitivity of the electrode pair i-j (i for excitation and j for measurement) to the conductivity change in a pixel at position k-th can be rewritten as:

$$s_{i,j}(k) = \int_{\Omega k} (E_{ik}/I_i) \cdot (E_{jk}/I_j) d\Omega_k, \qquad (9)$$

where E_{ik} and E_{jk} are the electric field strength at k-th pixel when the i-th and j-th electrode pairs are injected with currents I_i and I_j respectively in turn[16]. Practically, it is assumed that the electric field is the same at every point of the area Ω_k since the pixels are so small. Assuming a unit current, Equation (9) can be deduced to equation 10.

$$s_{i,j}(k) = E_{ikc} \cdot E_{jkc} A_{\Omega_k} \qquad (10)$$

where E_{ikc} and E_{ikc} are the electric field intensities at the centre of k-th pixel when the i-th electrode pair is in excitation mode and the j-th electrode pair is in measurement mode. A_{Ω_k} is the area of the k-th pixel. Finally, the sensitivity coefficient of each pixel is also obtained. The sensitivity coefficient for each electrode pair at a spatial location k-th is obtained by the dot product of the two electric fields. The sensitivity matrix is represented by the sensitivity map.

The sensitivity map for each configuration of electrode 1, showing the excitation of the ERT system that was fitted with 16 electrodes on a stainless steel pipe modelled in COMSOL is illustrated in Fig. 7.

From the map, it is observed that the sensitivity field is non-uniformly distributed over the medium of interest. The sensitivity is higher within the area close to both excitation and measurement electrode pair. When it is away from the active injection electrode pair, the sensitivity is lower. The combination of all independent projection of the electrode pair configurations is as shown in Fig. 8. It is also known as the weight balance map (WBM).

The surface matrix of the WBM is as presented in Fig. 9 below.
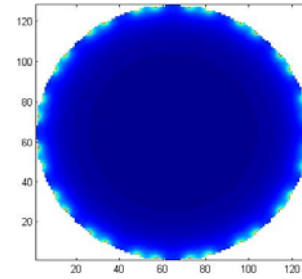
Fig. 8. Weight Balance Map.
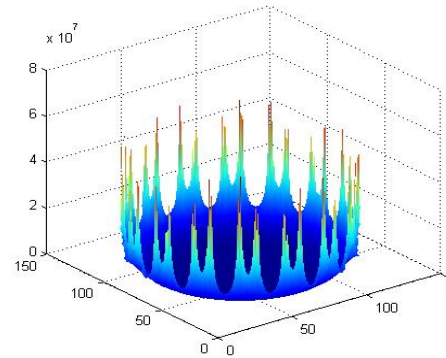
Fig. 9. Surface Matrix of the WBM.

3.3. Inverse Problem

As for the inverse problem, the conductivity distribution is reconstructed based on the electric potentials measured in the boundary, through the use of an adequate mathematical procedure [17]. One needs to solve the forward problem for some assumed conductivity before solving the inverse problem, so that the expected voltages can be compared with the measured data. Furthermore, the interior electric fields are normally required for the calculation of a Jacobian. Typically, FEM is used to compute the boundary voltages for a known conductivity distribution. Only in cases of a very simple geometry, and homogeneous in nature, or at least with very simple conductivity, could the forward problem be solved analytically [18].

There are numerous methods to reconstruct the ERT images which can be broadly divided into three classes: linear (single step and iterative methods); non-linear iterative methods; and heuristic multivariate
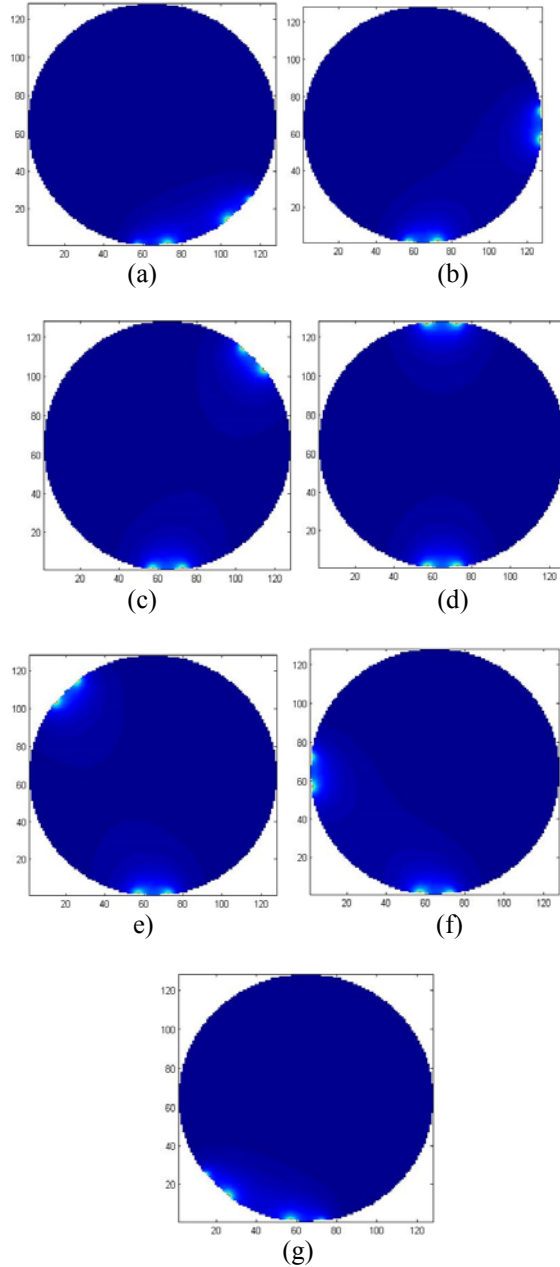

Fig. 7. Sensitivity Map Distribution of: (a) electrodes 1 and 3, (b) electrodes 1 and 5, (c) electrodes 1 and 7, (d) electrodes 1 and 9, (e) electrodes 1 and 11, (f) electrodes 1 and 13, (g) electrodes 1 and 15.

methods. However, the linear method has been chosen in this research since it is the most quick and simple. The linear methods are fast since the images are produced by simply multiplying the measurements by a single, pre-calculated matrix. In the linear method, Linear Back Projection (LBP) is the most extensively applied by researchers. The matrix in LBP is the transposal of an estimated solution to the forward problem, based upon either field gradients or more commonly, sensitivity maps (where the area in the measuring volume is divided into sensitivity areas). LBP is known as the non-iterative linear method [17].

LBP algorithm is a type of back projection algorithm and is essentially based on the linearization of a normalized form of the original problem. The projection data from each sensor with its sensitivity maps is combined to generate a concentration profile in LBP. Theoretically, given by the corresponding sensitivity map, LBP can be viewed as a weighted back projected or "smearing" of each one of the normalized measurements along its sensing zone [19].

The principle of this back-projection in ERT is that a relative change of the boundary measurement, $\Delta V\_(i,j)/V\_(i,j)$ with its sensitivity at each pixel as its weight factor is back-projected to the whole domain as relative changes of the conductivity at each pixel in the i,j projection. Because of its linear approach and fixed weight factors, LBP could not provide an accurate image. Nonetheless, it provides a fast on- line view or preview for initial visualization [12].

3.3.1. Implementation of LBP

For the LBP implementation in this research, the first step was the calibration for a homogeneous system. The homogeneous flow for this research was a full flow of tap water with a conductivity of $8.33 \times 10\text{-}3$ S/m. Later, the system was used to reconstruct the cross-sectional image of the region of interest based on Equation 11 that represents the LBP algorithm.

$$\text{BP}(x, y) = \sum_{Tx=0}^{n} \sum_{Rx=0}^{n} A_{Tx,Rx} \times \bar{S}_{Tx,Rx}(x, y) \qquad (11)$$

where $\text{LBP}(x, y)$, is the profile showing the concentration image obtained using the LBP algorithm in $n \times n$ (128×128) matrix where n equals to the dimension of the sensitivity matrix; $\bar{S}_{Tx,Rx}(x, y)$ is the normalized sensitivity map for the view of transmitter Tx to receiver Rx, and $A_{Tx,Rx}$ is the sensor loss value which refers to the difference of the homogeneous and non-homogeneous flow for the projection of transmitter Tx to receiver Rx. Non-homogeneous flow refers to the flow condition when a phantom or object exists inside the pipe. $A_{Tx,Rx}$ is represented in Equation 12 below:

$$A_{Tx,Rx} = \frac{V_{homo}(Tx,Rx) - V_{non-homo}(Tx,Rx)}{V_{homo}(Tx,Rx)}, \qquad (12)$$

where $V_{homo}(Tx, Rx)$ is the electric potential measured when Tx acts as source electrode and Rx acts as the receiver electrode in the condition of full water flow; while $V_{non-homo}(Tx, Rx)$ is the electric potential measured when Tx acts as the source electrode and Rx acts as the receiver electrode in the condition of a non-homogeneous flow.

The algorithm is then applied in a programming environment along with the sensor loss data and sensitivity maps to be computed and programmed to generate the image. The authors used the MATLAB programming environment to reconstruct the image.

4. Results and Discussions

In the simulation of the two-phase flow model using COMSOL, the properties for each material under investigation are based on their real properties. Based on the sensor loss and sensitivity maps obtained, MATLAB was used to reconstruct the image diameter of bubble phantom placed close to each other.

From the results presented in Table 2, the reconstructed images produced successfully displayed the location of phantoms of interest correctly using the LBP algorithm. It is observed that the sensor loss value is higher when there is existence of an object in between the source electrode and receiver electrode. This causes the concentration profile to become higher and denser at the located object. For a single phantom, the location of the bubble image resembles the real location of the phantom.
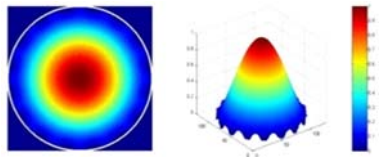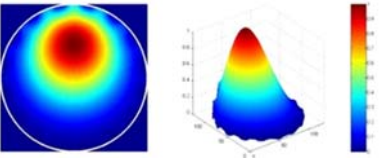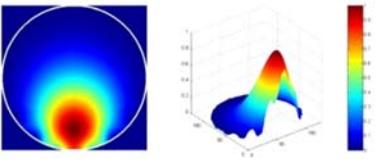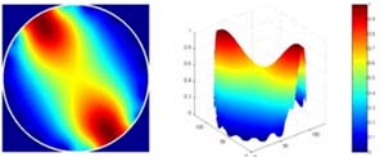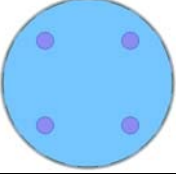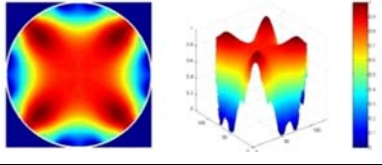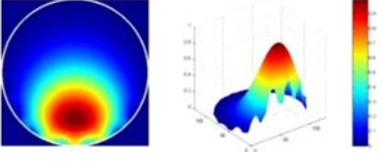
As for the images when there exist more than one phantom such as illustrated in the 4th and 5th results, it is shown that LBP is still sufficient to produce the correct location of the image even though the shapes of the phantoms are not 100% accurate. This is caused by the smearing effect in LBP due to its linear approach and fixed weight factor. Bubbles located at the center of the pipe, could lead to artefacts in the image. When the bubble is located near the boundary of the pipe, the grounded wall will introduce much more artefact and blurring to the boundary or even distort the reconstructed image. Although it is proven that LBP is still adequate enough to be implemented for initial visualization and verification of the study, LBP is not good enough to obtain the image of bubbles which are located close to one another. The conductivity distribution changes too much when two bubbles are located too near to each other. The sensitivity values decreases when the excitation using LBP algorithm. A number of bubble phantoms were tested to justify the research. In order to verify the efficiency and feasibility of the research as well as the sensitivity based image reconstruction algorithm, the reconstructed image of six phantoms for the two-phase flow (water/gas) displayed in Table 2 were analyzed.

The first one shows the image acquired when a bubble phantom of 20 mm diameter was located at the center of the pipe. The second result is the image generated when a 20 mm diameter of bubble was

located at 90º. The third result shows the image of a phantom of bubble with 20 mm diameter located at 270º. Next, the image of two bubble phantoms of 20 mm diameter each was shown with the bubbles located at 135º and 315º respectively. The fifth result shows four 10 mm diameter bubble phantoms with their LBP image located at 45º, 135º, 225º and 315º respectively. The last one shows the image attained for a 10 mm electrode is located farther from the measurement electrode.

Table 2. Results of LBP.

Phantom	Reconstructed Image

7. Conclusions

Linearization remains a widespread choice in ERT image reconstruction. Eventhough it could not provide an accurate image due to its linear approach; it does provide a fast on-line view for initial visualization. Generating a sensitivity distribution or also known as a sensitivity map of a homogeneous medium is a very important step in the linearization method. A correct sensitivity map is crucial in solving any inverse problems towards producing a correct image reconstruction. Upon solving the sensitivity distribution, the electrical potentials obtained will be fed to an inverse algorithm to obtain the previously unknown conductivity distribution. Simulation results of six bubble phantoms demonstrated that the invasive ERT sensor in a metal pipe applying conductivity boundary strategy together with the sensitivity based reconstruction algorithm is feasible to provide the cross sectional images of the water/gas two-phase flow. The locations of the bubbles can also be well distinguished. However, the exact shape of the conductivity distribution was not obtained due to the imperfection of the linear method approximations in the algorithm used since the method is linear and has fixed weighting factor.

Acknowledgements

References

[1]. Jin, H., Yang, S., He, G., Wang, M. and Williams, R. A., The effect of gas-liquid counter-current operation on gas hold-up in bubble columns using electrical resistance tomography, *Journal of Chemical Technology and Biotechnology*, 85, 9, 2010, pp. 1278-1283.

[2]. Xu, Y., Wang, H., Cui, Z. and Dong, F., Application of electrical resistance tomography for slug flow measurement in gas/liquid flow of horizontal pipe, *IEEE Computer Society*, 2009.

[3]. Dyakowski, T., Jeanmeure, L. F. C. and Jaworski, A. J., Applications of electrical tomography for gas–solids and liquid–solids flows — a review, *Powder Technology*, 112, 3, 2000, pp. 174-192.

[4]. Wang, M., Dickin, F. J. and Williams, R. A., Electrical resistance tomography of metal walled vessels and pipelines, *Electronics Letters*, 30, 10 1994, pp. 771-773.

[5]. Aw, S. R., Rahim, R. A., Rahiman, M. H. F., Yunus, F. R. M. and Goh, C. L., Electrical resistance tomography: A review of the application of conducting vessel walls, *Powder Technology*, 254, 2014, pp. 256-264.

[6]. Grieve, B. D., On-line Electrical Impedance Tomography for Industrial Batch Processing, *UMIST Manchester*, UK, 2002.

[7]. Davidson, J. L., Ruffino, L. S., Stephenson, D. R., Mann, R., Grieve, B. D. and York, T. A., Three-dimensional electrical impedance tomography applied to a metal-walled filtration test platform, *Measurement Science and Technology*, 15, 11 2004, p. 2263.

[8]. Fan, W. R. and Wang, H. X., Maximum entropy regularization method for electrical impedance tomography combined with a normalized sensitivity map, *Flow Measurement and Instrumentation*, 21, 3, 2010, pp. 277-283.

[9]. Seppanen, A., Karhunen, K., Lehikoinen, A., Kaipio, J. P. and Monteiro, P. J. M., Electrical resistance tomography imaging of concrete, *CRC Press*, 2009.

[10]. Yong Song, K. and et al., Sensitivity map generation in electrical capacitance tomography using mixed normalization models, *Measurement Science and Technology*, 18, 7, 2007, p. 2092.

[11]. Karhunen, K., Seppanen, A., Lehikoinen, A., Blunt, J., Kaipio, J. P. and Monteiro, P. J. M., Electrical resistance tomography for assessment of cracks in concrete, *ACI Materials Journal*, 107, 5 2010, pp. 523-531.

[12]. Wang, M., Dickin, F. J. and Mann, R., Electrical Resistance Tomographic Sensing Systems for Industrial Applications, *Chemical Engineering Communications*, 175, 1 1999, pp. 49-70.

[13]. Huang, S., Wang, Z. and Jin, Y., Studies on gas-solid-solid circulating fluidized-bed reactors, *Chemical Engineering Science*, 54, 13-14, 1999, pp. 2067-2075.

[14]. Lehr, J., A Vector Derivation Useful in Impedance Plethysmographic Field Calculations, *IEEE Transactions on Biomedical Engineering,* BME-19, 2, 1972, pp. 156 - 157.

[15]. Zhou, H., Xu, L., Cao, Z., Hu, J. and Liu, X., Image reconstruction for invasive ERT in vertical oil well logging, *Chinese Journal of Chemical Engineering*, 20, 2, 2012, pp. 319-328.

[16]. Sun, J. and Yang, W., Evaluation of fringe effect of electrical resistance tomography sensor. *Measurement*, 53, 2014, pp. 145-160.

[17]. Rasteiro, M. G., Silva, R., Garcia, F. A. P., Faia, P., Electrical Tomography: a review of Configurations and Applications to Particulate Processes, *KONA Powder and Particle Journal*, 29, 2011, pp. 67 - 80.

[18]. William, L., Nicholas, P. and Andrea, B., The reconstruction problem, *Taylor & Francis*, 2004.

[19]. Mohd Hafiz Fazalul Rahiman, Zulkarnay Zakaria, Ruzairi Abdul Rahim, Wei Nyap Ng, Ultrasonic tomography imaging simulation of two-phase homogeneous flow, *Emerald Sensor Review*, 29, 3 2009, pp. 266 - 276.

[20]. Z. Zakaria, R. Abdul Rahim, M. S. B Mansor, S. Yaacob, N. M. Nor Ayob, S. Z. Mohd. Muji, M. H. fazalul Rahiman, S. M. K. Syed Aman, Advancements in transmitters and sensors for biological tissue imaging in magnetic induction tomography, *Sensors,* 2012, 12, 6, pp. 7126-7156.

[21]. M. H. Fazalul Rahiman, R. Abdul Rahim and N. M. Nor Ayob, The Front-End Hardware Design Issue in Ultrasonic Tomography, *IEEE Sensor Journal,* Vol. 10, No. 7, pp. 1276 -1281.

Sensors & Transducers

Properties of Spray Pyrolysied Copper Oxide Thin Films

[1] S. S. Roy and [2] A. H. Bhuiyan

[1] Department of Physics, Dwarika Paul Mohila Degree College, Sreemongal-3210
[2] Department of Physics, Bangladesh University of Engineering and Technology
Dhaka-1000, Bangladesh

Abstract: Copper oxide (CuO) thin films were deposited on well cleaned glass substrates by spray pyrolysis technique (SPT) from cupric acetate ($Cu(CH_3COO)_2.H_2O$) precursor solutions of 0.05 – 0.15 M molar concentrations (MC) at a substrate temperature of 350 °C and at an air pressure of 1 bar. Effect of varying MC on the surface morphology, structu6ral optical and electrical properties of CuO thin films were investigated. XRD patterns of the prepared films revealed the formation of CuO thin films having monoclinic structure with the main CuO (111) orientation and crystalline size ranging from 8.02 to 9.05 nm was observed. The optical transmission of the film was found to decrease with the increase of MC. The optical band gap of the thin films for 0.10 M was fond to be 1.60 eV. The room temperature electrical resistivity varies from 31 and 24 ohm.cm for the films grown with MC of 0.05 and 0.10 M respectively. The change in resistivity of the films was studied with respect to the change in temperature was shown that semiconductor nature is present. This information is expected to underlie the successful development of CuO films for solar windows and other semi-conductor applications including gas sensors.

Keywords: Spray pyrolysis, CuO, Band gap, Substrate temperature.

1. Introduction

Due to the emerging applications of metal oxides in technology, it is essential to characterize the physical and chemical properties of metal oxides. The application of metal oxide semiconductor sensors in toxic and inflammable gas detection leads to advanced research in this area. Current research in the field of gas sensors has been focused on the fabrication of sensors which are low cost with rapid response, high sensitivity and good selectivity. [1-3].

Thin films, such as titanium oxide (TiO_2), zinc oxide (ZnO), cadmium oxide (CdO), indium oxide (InO_x), copper oxide (Cu_2O, CuO), nickel oxide (NiO), tin oxide (SnO_2), etc. known as transparent conducting oxide (TCO) have been investigated for several applications such as, photo detectors, gas sensor, solar cell, optoelectronic devices, transistor, etc [4-10].

Copper oxide thin films were deposited by vacuum evaporation on silicon substrates in temperatures varying from 150 °C up to 450 °C X-ray diffraction (XRD) patterns showed that in the copper oxide films two phases coexist: CuO and Cu_2O. Substrate temperatures up to 225 °C, Cu and Cu_2O are formed while above this temperature CuO forms. Pure Cu_2O was obtained at 225 °C while pure CuO was found above 350 °C [11]. CuO is a p-type semiconductor with a bandgap of 1.5 to 1.8 eV [12]. CuO thin films have been synthesized by a sol–gel method using cupric acetate Cu (CH_3COO) as a precursor, and XRD patterns of CuO thin films showed that all the films were nanocrystallized in the monoclinic structure, and the crystallite size increase from 40 to 45 nm with increasing annealing temperature. The room temperature DC electrical conductivity was increased from 10^{-6} to 10^{-5} $(\Omega\ cm)^{-1}$ [13]. Copper oxide thin films were prepared by reactive RF magnetron sputtering for a pure copper target in an oxygen-argon atmosphere. XRD studies show that by controlling the oxygen partial pressure single phase Cu_2O and CuO can be

obtained and the resistivity of the film was 43 Ω-cm [14]. There are various established ways of fabricating thin films like spray pyrolysis technique (SPT) system [4, 9], thermal evaporation [6], Dc magnetron sputtering [7], SILAR [15], sol-gel [16], etc. The extensive application of copper oxide thin films in various devices needs low optical band gap, low resistivity films deposited at low temperature from aqueous solution. SPT is one of the methods satisfying these requirements because it is inexpensive, simple, and suitable for mass production among all of these. In this paper, preparation of copper oxide thin films by SPT is discussed and surface morphology, crystal size, optical transmittance and band gap, refractive index, resistivity, activation energy, and Figure of merit of these prepared films are also investigated.

2. Experimental Details

CuO thin films have been deposited on glass substrates by the method of SPT with different molar concentrations (MC) of cupric acetate $(Cu(CH_3COO)_2.H_2O)$ for 0.05, 0.075 0.10, 0.125, and 0.15 3 M. To prepare 100 ml of precursor solution, the required quantity of precursor salt was made to dissolve in distilled water by continuous stirring by a magnetic stirrer for 1 hr. Before deposition, substrates were cleaned well. The deposition parameters of the spray pyrolysis setup such as substrate to nozzle distance, substrate temperature, air pressure and precursor solution flow rate were optimized and was kept constant to obtain well adherent films. For each concentration the reproducibility of the films were verified by repeating the experiments several times. The precursor solution was sprayed using a glass jet nozzle using air as the carrier gas on to the pre-heated, cleaned glass substrates (2×1.5 cm). The possible chemical reaction that takes place on the heated substrate to produce CuO thin film when the droplets of the solution reached the heated substrate is given below.

$$Cu(CH_3COO)_2.H_2O + H_2O \longrightarrow CuO + 2CH_3COOCH_3$$
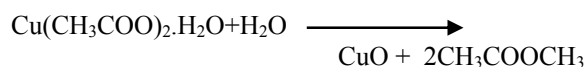
Thickness of the thin films was determined by Fizeau fringe interferometric method. The thickness was found to be about 200 nm. Scanning Electron Microscope (SEM) model HITACHI, S-3400N JAPAN, was used to see the surface morphology. The transmission and absorption spectra for the as-deposited films were recorded using a UV-1631spectrophotometer (SHIMADZU) as a function of wavelength ranging from 290 to 1100 nm. The electrical resistivity was measured using a Van der Pauw method in the range of 300~475 K. Chemical reaction of the copper acetate water solution takes place under stimulated temperature as shown below and provides the formation of CuO film.

3. Results and Discussion

3.1. Surface Morphological and Elemental Analysis

The surface morphology of the CuO thin films of the four MCs observed by SEM is shown in Fig. 1. The microstructure of the thin film prepared at 0.05 M shows needle like appearance and it is interesting to note that the microstructures for thin films prepared at 0.10 M is seen porous structure. As shown in the figure, CuO films with 0.10 M were composed of aggregated particles with porous structure and it is clear that the amount of pores increases as the molar concentration increases and is highest for 0.10 M film.

It is seen that the surface of the prepared samples with 0.10 M is comparatively well aggregated and less rough. These could be the result of the chemical reaction during the deposition. SEM micrographs reveal the formation of particles with different shapes and sizes, it seems appropriate to consider that the particles which appear in SEM images are, in fact, grain agglomerates. Fig.2 shows EDX spectra of 0.10 M of CuO thin film proves that synthesized samples are composed of Cu and O elements by the representation of different copper and oxygen peaks. The atomic percentage of Cu and O is 62.57/37.43 for 0.05 M, for 0.10 M it is 69.23/31.69 and for 0.15 M it is 71.28/31.25. The elemental composition analysis shows that the surface of the samples was rich in copper for molar concentrations 0.10 and 0.15 M.

3.1. X-ray Diffraction Analysis

XRD patterns of CuO thin films synthesized from five MCs are shown in Fig. 2. XRD analysis shows that the CuO thin films have monoclinic crystal structure with some shifts in the position of characteristic peaks. The diffraction peaks observed at different 2θ values correspond to the (110), (002), (111), (200), (-202), and (020) planes of the end-centered monoclinic structured CuO (JCPDS card No. 89-5895). It is expected that the structural properties of the prepared films would be different, since the composition and morphology of pyrolysed films are governed by the spraying conditions on to heated substrate. It is observed from Fig. 2 that the diffraction peak positions are identical for all the CuO thin films, obtained for different MCs, indicating the formation of monoclinic phase CuO in all the cases. Although (111) and (200) reflections are present, no other phases are present for Cu_2O. The lattice constants of the CuO thin films are found to be: a = 4.6623 Å, b = 3.4431 Å and c = 5.1345 Å, and are in good agreement with the standard JCPDS data for monoclinic structured CuO. For peak (111) the calculated values of the crystallite size (D) for the CuO thin films are presented in Table 2. The (111) surface of CuO thin film is energetically the most stable and the predominant crystal face found in polycrystalline samples. It is seen

in the Table 1, the crystallite size increases MC of 0.10 M and then to decreased. For CuO there are many dangling bonds related to the copper and/or oxygen defects at the grain boundaries. As a result, these defects are favorable to the merging process to form larger CuO grains while increasing MC. It implies that the crystallinity of the CuO thin films is improved at higher MC. This may be due to gaining enough energy by the crystallites to orient in proper equilibrium sites at high T_s of 350 °C, resulting in the improvement of crystallinity and degree of orientation of the CuO thin films [17-19]. The peak positions and 'D' values (Table 2) of the diffraction peaks for CuO are in good

agreement with the earlier reports of the spray deposited CuO thin films using $CuCl_2.2H_2O$ [20]. For the spray solution with low MC of 0.05 M, the net heat absorbed by the droplet, may not sufficient enough to vaporize the entire droplet due to fast travel of droplet to the substrate. As a result precipitation and sublimation has taken place on the substrate. So, the reaction appears to be of homogeneous one and the film had low crystalline. When the molar concentration was increases to o.1o M, the intensities of the peaks of CuO got enhanced which indicates that the crystallinity of crystallites had been improved.

(a) (b) (c) (d)
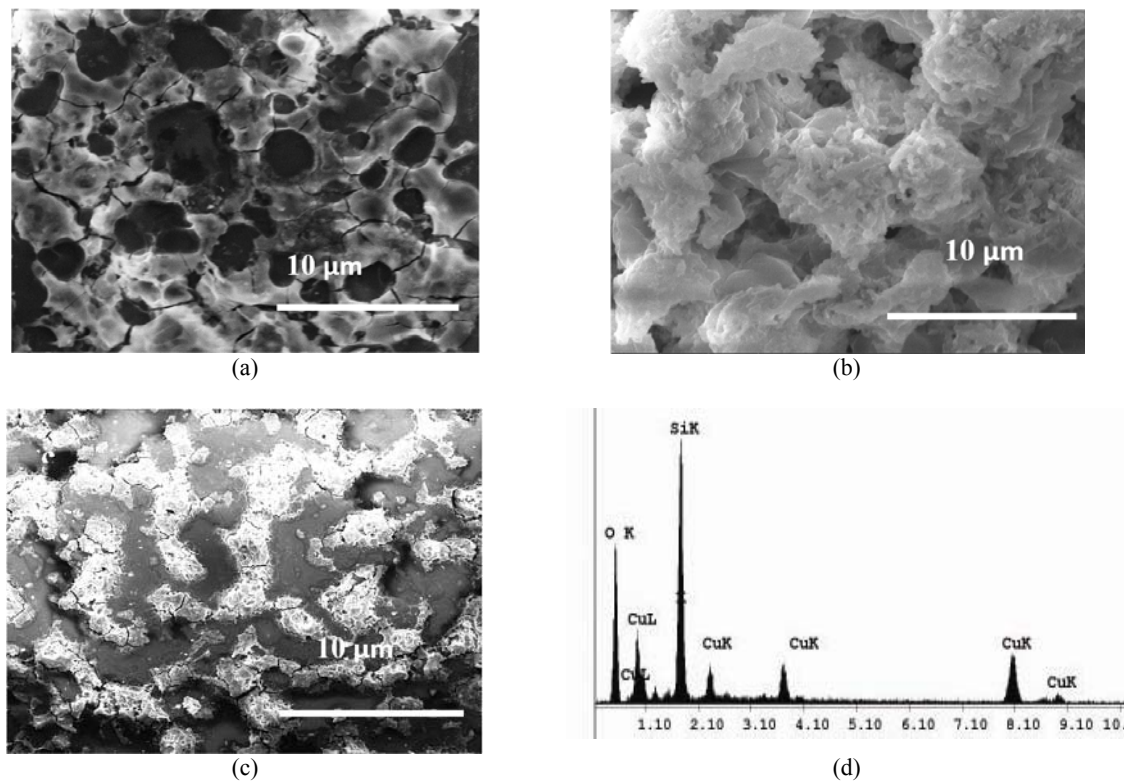
Fig. 1. SEM image of CuO thin films for MC of (a) 0.05 M, (b) 0.10 M, (c) 0.15 M (d) EDX spectrum.
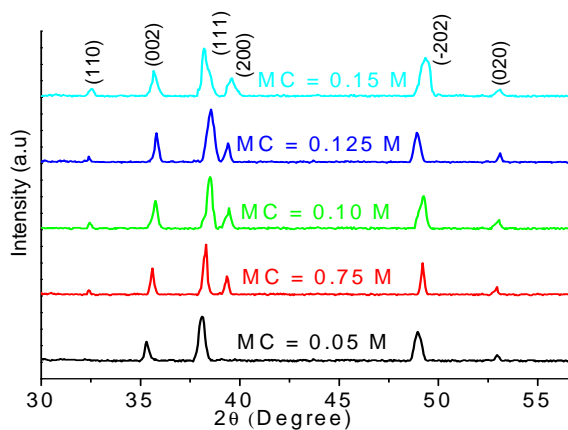
Fig. 2. XRD patterns of CuO thin film synthesized from various solutions of MCs.

Table 2. Crystallite size of the CuO thin films for various MCs.

MC (M)	0.05	0.075	0.10	0.125	0.15
D (nm)	8.0257	8.9341	9.5743	9.6232	9.0532

3.3 Optical Properties

3.3.1. Transmittance and Optical Band Gap

The variation of transmittance T of CuO thin films for MC of 0.05 - 0.15 M, with wavelength is shown in Fig. 3.
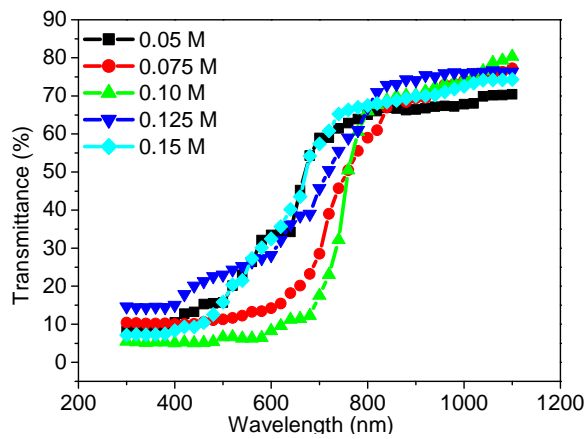
Fig. 3. Optical transmittance vs. wavelength for various MCs.

It is seen that the transmittance is high in the visible and near infrared regions and minimum at wavelength ~ 300 nm. An average 60 to 80 % transmittance are observed in the wavelength range of 800-1100 nm and below 800 nm transmittance decreases rapidly. The transmittance is high about 80 % for CuO thin films grown with MC of 0.10 M. The increase in transmittance may be due to the transition of the CuO films from amorphous to polycrystalline structure. A relatively high transmittance value for the thin film deposited for MC of 0.10 M, may be attributed to less scattering due to the decrease in the degree of irregularity in the grain size distribution [21].The transmittance values are decreased for the next MC of 0.15 M. This suggests that the decrease in the transmittance of CuO thin films with increasing in MC may lead to increase in the degenerate (metallic) nature of the films, which results in light absorption.

The optical band gap for the direct band gap semiconductors is determined using the Tauc model and parabolic bands [22], $(\alpha h\nu)^2 = A(h\nu - E_g)$, where A is a proportionality constant, $h\nu$ is the incident photon energy, α is the absorption coefficient, and E_g is the optical band gap. Fig. 4 shows the absorption coefficient squared $(\alpha h\nu)^2$ as a function of, $h\nu$ for the CuO thin films deposited for various MCs. The α was found in the order of 10^6 m^{-1} which may be suitable for a transparent conducting film. The variation of E_g with MC of the CuO thin films is plotted in Fig. 5. The optical band gap is found to be 2.40 eV for MC of 0.05 M and then a minimum value 1.60 eV for MC of 0.10 M. It can be seen that a band gap tuning of 0.80 eV occurs when the MC is changed by about 0.05 M. The value of the α and E_g decrease as the MC increases gradually up to 0.10 M whereas it starts to increase with further increasing of MC. It may be due to the removal of defects and disorderness in the as-deposited film by increasing of MC.

The variations of refractive index, n for CuO thin films increases with MC, as seen in Fig. 6. The n of CuO thin film is obtained to be 2.82 at MC 0.05 M and it became lowest 2.52 at MC of 0.10 M. This value is very close to the reported values 2.65 of CuO thin film

[23] and it is lower than that of bulk CuO and this low value of refractive index may probably due to the smaller density of the films.
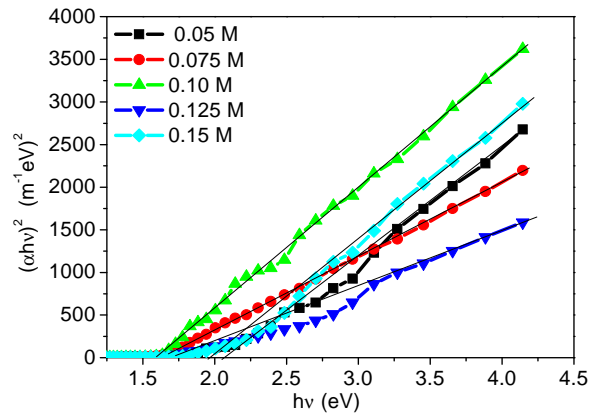
Fig. 4. Variation of $(\alpha h\nu)^2$ with $(h\nu)$ for various MCs.
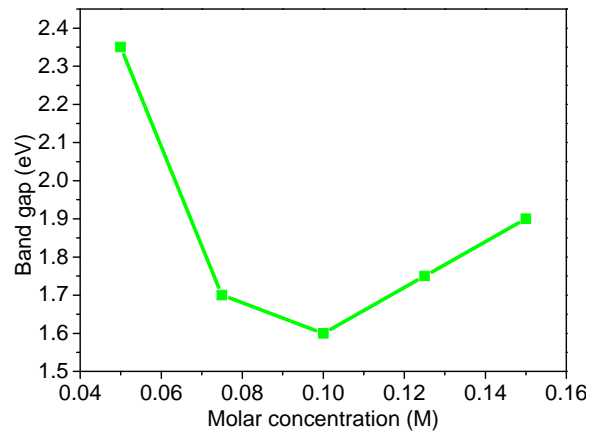
Fig. 5. Band gap vs. MC of CuO thin films.
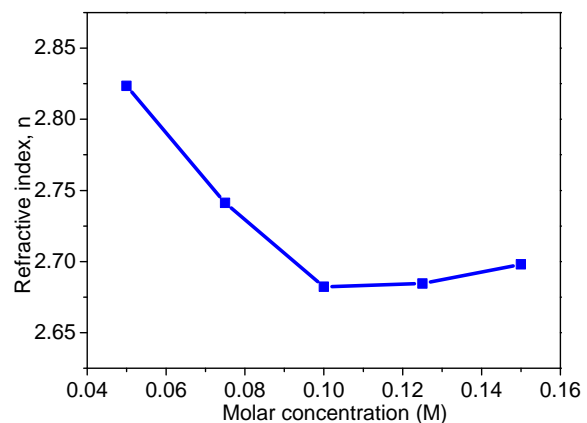
Fig. 6. Variation of refractive index with MC.

The variation of extinction coefficient, k with $h\nu$ is shown in Fig. 7. It is observed that the k increases with the increase of MC. The rise and fall in k is directly related to the absorption of light. The k about 0.1 in the range of wavelength 800-1100 nm (1-1.6 eV)

which is lower than that of CuO thin films prepared by RF magnetron sputtering [23] and is very close to the reported value of CuO thin films prepared on to ITO glass substrates from an aqueous electrolytic bath containing $CuSO_4$ and tartaric acid [24]. The k of CuO thin films increases rapidly for photon energies above 1.6 eV for better crystallization and tends to decrease above 2.3 eV for scattering of phonons dominant with electrons.
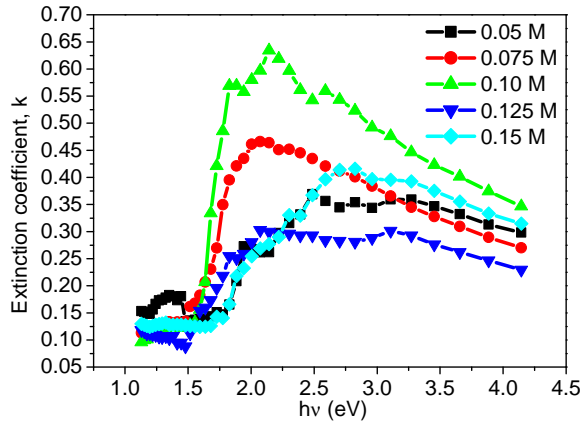
Fig. 7. Variation of extinction coefficient with hυ for various MCs.

3.4. Electrical Properties

The film electrical resistivity (ρ), may be due to combination of three mechanisms, namely (i) due to scattering by phonon, and point defects, etc. (ii) from film surface, (iii) from grain boundaries. Third one be predominant in poly crystalline films. ρ of CuO thin films were measured by van der Pauw method [25]. Fig. 8 present the variation of ρ of CuO thin films with temperature and Fig. 9 display variation of room temperature ρ with different MC. ρ of the films was found to vary from 30 Ohm.cm to 18 Ohm.cm for MC of 0.05 to 0.10 M and it is 25 Ohm.cm for films prepared with 0.15 M. This variation in the electrical resistivity of the films with deposition conditions has been explained in terms of stoichiometric changes induced by copper or oxygen ion vacancies and neutral defects. Increases of the oxygen concentration on the films during deposition led to a peak in electrical resistivity value, which was identified with the formation of stoichiometric CuO.

Fig. 10 reports in lnσ vs. 1000/T curves for CuO thin films with MC of 0.05 - 0.15 M. The variation in conductivity (σ) with temperature indicates the semiconducting behavior of the films suggesting a thermally activated conduction mechanism. The reduction in resistivity with the increase in MC may be due to the increase of carrier concentrations of CuO, lower scattering of excess conduction electrons, and increase in the free path of carrier concentration. Further increases in MC during deposition was observed to result in a high airing of the film resistivity, which was explained as resulting from the

MC of the films with excess oxygen i.e. effectively producing more copper ion vacancies and a p-type semiconductor CuO. This study reveals that MC increases has a considerable effect on the electrical properties of CuO thin films. Generally, the electrical conductivity in semiconductor is caused by thermal excitation of electron, impurities and lattice defects such as dislocation, stacking faults and micro twines [26]. The formation of conductivity increases or decreases, these defects depends on the sticking coefficient, nucleation rates and the migration of impinging copper and oxygen species on the substrate during deposition. In the present study 0.10 M film has the highest electrical conductivity and lowest electrical resistivity. This may be due to the highest grain size of 0.10 M film. The increase of grain size may be due to the improved crystallinity of 0.10 M film. The growth in grains leads to the reduction of grain boundary scattering which decreases the resistivity for the films and eventually the increase in the conductivity of the films [27].

The activation energy (E_a) is calculated from the slope of a curve lnσ vs. (1/T) using the equation given by

$$E_a = -\frac{\ln \sigma}{1/T} 2k \,, \qquad (1)$$

where, σ is the conductivity, k is the Boltzmann constant, and T is the absolute temperature.

From the slope of plots in Fig. 10, E_a for CuO thin film at different MC was calculated and is shown in Fig. 11. The nonlinear nature of the plots exhibit two types of conductivity mechanism. The activation energy in two temperature ranges is calculated from the graphs. E_a is 2.20 eV for 0.10 M film is greater than reported value 1.58 eV [28].

The activation energy E_1 at low temperature range is related to the intrinsic generation process and E_2 at high temperature range to the impurity scattering [29-30]. The low value of activation energy may be associated with the localized levels hopping due to the excitation of carriers from donor band to the conduction band. A low activation energy of 0.14 eV was reported for sputtered CuO thin films [31]. This low value of activation energy was assumed due to the nonstoichiometry of the CuO thin film but in the present case the higher values of activation energy may suggest that the prepared sample is stoichiometric. The electrical conductivity as well as the activation energy was increased after increasing MC. From SEM and EDX observations, it is also found that CuO thin films are stoichiometric. It is observed that metallic like conduction on films produced at low oxygen partial pressures, which they attributed to a high copper content of the films produced under this condition.

The Figure of merit is well-known as an index for evaluating the performance of transparent conducting films, and it is given by the equation $F=(-\rho \ln T)^{-1}$ where ρ is the electrical resistivity and T is the average transmittance in the wavelength range of 800-1100 nm

[32]. Fig. 12 shows the figure of merit values of CuO thin films deposited at various T_s. The figure of merit for the CuO thin films deposited with MC (0.05 - 0.15 M) was found to be 0.13, 0.14 and 0.142 Ω^{-1}cm^{-1}, respectively. The increase in the figure of merit of the CuO thin films is mainly due to the increase in the optical transmittance with increasing MC.
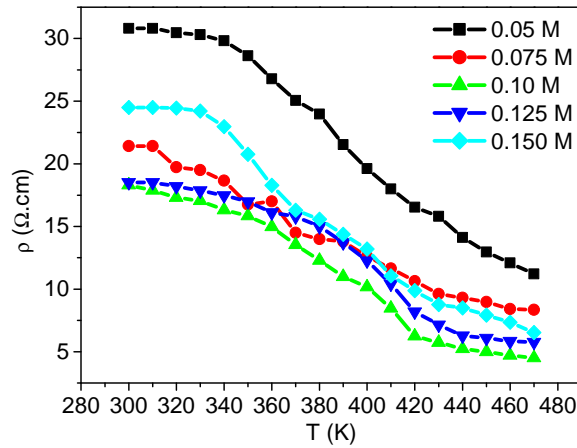
Fig. 8. Variation of resistivity with temperature.
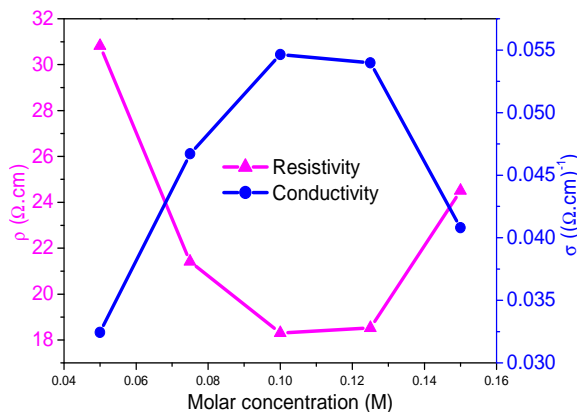
Fig. 9. Variation of resistivity/conductivity at room with MC.
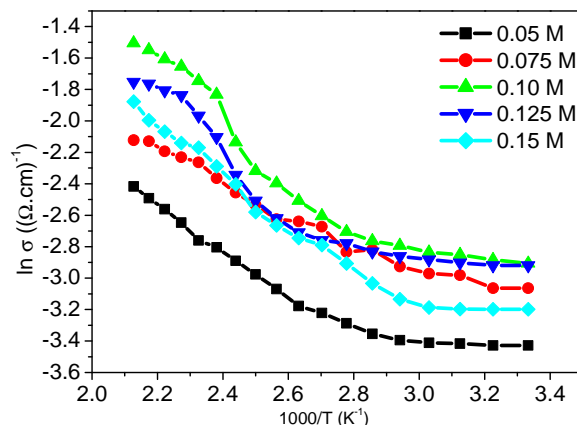
Fig. 10. Variation of lnσ with respect to inverse of temperature for various MC.
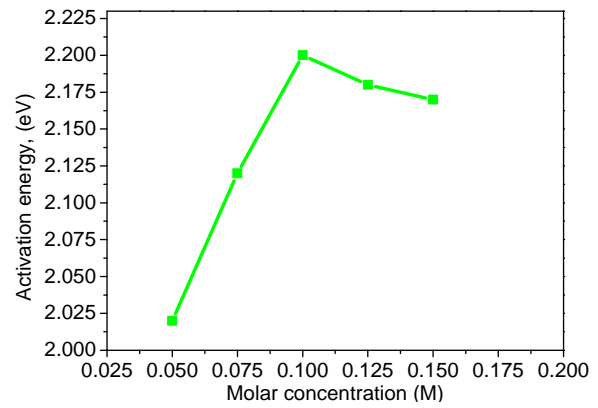
Fig. 11. Variation of activation energy with MC.
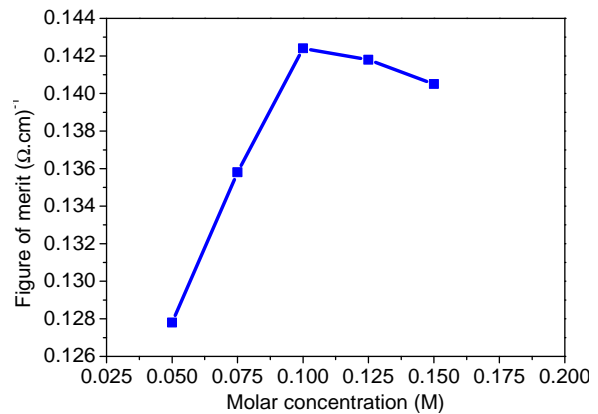
Fig. 12. Variation of Figure of merit with MC.

4. Conclusions

CuO thin films were prepared by a homemade and inexpensive spray pyrolysis technique and reported the synthesized polycrystalline films. The as deposited CuO thin films were characterized structurally, by using SEM, EDX, XRD, optically by UV-visible spectroscopy and electrically by four probe method. The deposited films are found to be stoichiometric CuO thin film. Structural analysis confirmed that prepared films were monoclinic structure with plane as (110), (002), (111), (200), (-202), and (020) where as the peak (111) reveals that strong peak for CuO thin film. The average crystallite size and the average transmittance of the film deposited at 350 °C were about 9.57 Å and 70 % in the wavelength range of 800-1100 nm respectively. The optical band gap varies from 1.90 to 1.65 eV. The lowest value of refractive index is 2.52 for thin film prepared with 0.10 M at T_s of 350 °C. The extinction coefficient increases with the increase of MC of the prepared CuO then films. The minimum resistivity is found to be 18 Ω-m for CuO thin film deposited with MC of 0.10 M. The electrical measurement reveals the semi conducting behavior of the films. The highest figure of merit occurred for the film grown with an optical transmittance about 76% in the wavelength range of 800-1100 nm. This synthesized alloy compound could

be environmental friendly and suitable as a potential buffer layer in the fabrication of heterojunction solar cells and optoelectronic devices.

Acknowledgement

References

[1]. Ueda, N., H. Maeda, H. Hosono and H. Kawazoe, Band-gap widening of CdO thin films, *J. Applied Phys.,* 84, 1998, pp. 6174-6177.

[2]. Maruyama, T., Copper oxide thin films prepared from copper dipivaloylmethanate and oxygen by chemical vapor deposition, *Japanese J. Applied Phys.*, 37, 1998, pp. 4099-4102.

[3]. Wang, C. X., L. W. Yin, L. Y. Zhang, D. Xiang and R. Gao, Metal oxide gas sensors: Sensitivity and influencing factors, *Sensors*, 10, 2010, pp. 2088-2106.

[4]. Masayuki O., Katsuyuki S., Nobuyuki H., Tsuyoshi K., Kumaraa G. R. A., Janos M., Shoji K., Gyorgy P., Porous TiO$_2$ thin films Prepared by spray pyrolysis deposition (SPD) technique and their application to UV sensors, *Solid State Ionics,* 172, 2004, pp. 527–531.

[5]. J. F. Chang, H. H. Kuo, I. C. Leu, M. H. Hon, The effects of thickness and operation temperature on ZnO:Al thin film CO gas sensor, *Sensors and Actuators B: Chemical,* Vol. 84, Issues 2–3, 15 May 2002, pp. 258–264.

[6]. N. E. Makori, I. A. Amatalo, P. M. Karimi, W. K. Njoroge, Optical and Electrical Properties of CdO: Sn Thin Films for Solar Cell Applications, *International Journal of Optoelectronic Engineering,* 4, 1, 2014, pp. 11-15.

[7]. G. Kiriakidis, N. Katsarakis, M. Bender, E. Gagaoudakis and V. Cimalla, InO$_X$ Thin Films, Candidates for Novel Chemical and Optoelectronic Applications, *Mater. Phys. Mech.,* 1, 2000, pp. 83-97.

[8]. Kosuke Matsuzaki, Kenji Nomura, Hiroshi Yanagi, Toshio Kamiya, Masahiro Hirano, and Hideo Hosono, Epitaxial growth of high mobility Cu$_2$O thin films and application to p-channel thin film transistor, *Appl. Phys. Lett.,* 93, 2008, p. 202107-3.

[9]. J. Morales, L. Sanchez, F. Martin, J. R. Ramos-Barrado, M. Sanchez, Use of low-temperature nanostructured CuO thin films deposited by spray-pyrolysis in lithium cells, *Thin Solid Films,* 474, 2005, pp. 133– 140.

[10]. Verma M., Gupta V., A highly sensitive SnO$_2$–CuO multilayered sensor structure for detection of H$_2$S gas, *Sensors & Actuators B,* Vol. 166-167, 2012, pp. 378-385.

[11]. Papadimitropoulos G., Vourdas N, Vamvakas V. E. and Davazoglou D, Deposition and characterization of copper oxide thin films, *J. Phys: Conf. Ser,* 10, 2005, pp. 182–185.

[12]. Marabelli F., Parraviciny G. B, Orioli F. S, Optical gap of CuO, *Phys. Rev. B.,* 52, 1995, pp. 1433–1436.

[13]. Jundale D. M., Joshi P. B., Sen S., Patil V. B., Nanocrystalline CuO thin films: synthesis, microstructural and optoelectronic properties, *J. Mater Sci: Mater Electron,* 23, 2012, pp. 1492-1499.

[14]. A. Parretta. M. K. Jayaraj, A. DI Nocera, S. Loreti, L. Quercia, A. Agati, Electrical and Optical Properties of Copper Oxide Films Prepared by Reactive RF Magnetron Sputtering, *Phys. Stat. Sol. (a),* 155, 1996, pp. 399-403.

[15]. Mageshwari K. and Sathyamoorthy R., Physical properties of nanocrystalline CuO thin films prepared by the SILAR method, *Mat. Sci. Semicon. Proc.,* 16, 2013, pp. 337–343.

[16]. L. L. Hench and J. K. West, The Sol-Gel process, *Chemical Reviews,* Vol. 90, No. 1, 1990, pp. 33–72.

[17]. Akkari F. C., Kanzaria M., and Rezig B., Preparation and characterization of obliquely deposited copper oxide thin films, *Eur. Phys. J. Appl. Phys.,* Vol. 40, 2007, pp. 49–54.

[18]. Ghosh P. K., Maity R., Chattopadhyay K. K., Electrical and optical properties of highly conducting CdO:F thin film deposited by sol–gel dip coating technique, *Sol. Energy Mater. Sol. Cells.,* Vol. 81, Issue 2, February 2004, pp. 279-289.

[19]. Gurumurugan K., Mangalaraj D., Narayandass S. K., Nakanishi Y., DC Reactive Magnetron Sputtered CdO Thin Films, *Mater. Lett.,* Vol. 28, No. 4-6, 1996, pp. 307-312.

[20]. C. Ravi Das, Dinu Alexander, A. Jennifer Christy, L. Jeyadheepan, A. Moses Ezhil Raz, C. Sanjeevi Raza, Preparation and Characterization of CuO Thin Films Prepared by Spray Pyrolysis Technique for Ethanol Gas Sensing Application, *Asian Journal of Applied Sciences,* 7, 2014, pp. 671-684.

[21]. Ghosh M., Rao C. N. R., Solvothermal synthesis of CdO and CuO nanocrystals, *Chem. Phys. Lett.,* Vol. 393, Issue 4-6, August 2004, pp. 493-497.

[22]. J. Tauc, Optical properties and electronic structure of amorphous Ge and Si, *Mat. Res. Bull.* 3, 1968, pp. 37–46.

[23]. Parretta A., Jayaraj M. K., Nocera A. D., Loreti S, Quercia L., and Agati A, Electrical and Optical Properties of Copper Oxide Films Prepared by Reactive RF Magnetron Sputtering, *Phys. Stat. Sol.,* 155, 1996, pp. 399-404.

[24]. Dhanasekaran V., Mahalingam T., Electrochemical and Physical Properties of Electroplated CuO Thin Films, *Journal of Nanoscience and Nanotechnology,* Vol. 13, No. 1, 2013, pp. 250-259.

[25]. I. J. van der Pauw, A method of measuring specific resistivity and Hall effect of discs of arbitrary shape, *Philips Research Reports,* Vol. 13, No. 1, 1958, pp. 1-9.

[26]. N. Revathi, P. Prathap and K. T. R. Reddy, Synthesis and physical behaviour of In$_2$S$_3$ films, *Appl. Surf. Sci.,* 254, 2008, p. 5291-5298.

[27]. Mustafa, O. Influence of grain size on electrical and optical properties of InP films, *Chin. Phys. Lett,* Vol. 25, 2008.

[28]. C. Ravi Das, Dinu Alexander, A. Jennifer Christy, L. Jeyadheepan, A. Moses Ezhil Raz, C. Sanjeevi Raza, Preparation and Characterization of CuO Thin Films Prepared by Spray Pyrolysis Technique for Ethanol Gas Sensing Application, *Asian Journal of Applied Sciences,* 7, 2014, pp. 671-684.

[29]. N. Revathi, P. Prathap, Y. P. V. Subbaiah and R. K. T. Ramakrishna, Growth and characterization of ZnSxSe1-x films deposited by close-spaced evaporation *J. Phys. D, Appl. Phys.,* 41, 2008.

[30]. N. Revathi, P. Prathap and K. T. R. Reddy, Thickness dependent physical properties of close space evaporated In₂S₃ films *Solid State Sci.,* 11, 2009.

[31]. Drobny V. F. and L. Pulfrey, Properties of reactively-sputtered copper oxide thin films, *Thin Solid Films,* Vol. 61, Issue 1, July 1979, pp. 89-98.

[32]. Cho S., Structural, Optical and Electrical Properties of RF- sputtered Indium Oxide Thin Films, *J. Korean Phys. Soc.,* Vol. 60, No. 12, 2012, pp. 2058-2062.

Sensors & Transducers

Study of GeSn Alloy for Low Cost Monolithic Mid Infrared Quantum Well Sensor

Prakash PAREEK and Mukul K. DAS

UGC SAP Research Laboratory, Department of Electronics Engineering
Indian Institute of Technology (Indian School of Mines) Dhanbad, Dhanbad-India
Tel.: +917549028379
E-mail: ppareek1@gmail.com

Abstract: This paper focuses on theoretical study of Tin incorporated group IV alloys particularly GeSn and design of quantum well sensor for mid infrared sensing applications. Initially, the physics behind the selection of material for midinfrared sensor is explained. The importance of controlling strain in GeSn alloy is also explained. The physical background and motivation for incorporation of Tin(Sn) in Germanium is briefly narrated. Eigen energy states for different Sn concentrations are obtained for strain compensated quantum well in Γ valley conduction band (ΓCB), heavy hole (HH) band and light hole (LH) band by solving coupled Schrödinger and Poisson equations simultaneously. Sn concentration dependent absorption spectra for HH- ΓCB transition reveals that significant absorption observed in mid infrared range (3-5 μm). So, $Ge_{1-x} Sn_x$ quantum well can be used for mid infrared sensing applications.

Keywords: GeSn, Strain, Midinfrared, Quantum well, Tin incorporated group IV alloy.

1. Introduction

In last few years, mid infrared sensors (MIR) have drawn attention of researchers from all over the world due to their vast applications. They found their presence in defence, surveillance, medical, information security applications [1]. Group III-V based MIR have already proven their worth by showing excellent performance in past. However, III-V material like GaAs is too expensive for commercial uses. They are also incompatible to Silicon to realize a monolithic sensor. Thus, researchers compelled to look for a new class of material which can enable the design of low cost single chip mid infrared photosensitive devices. Both Silicon (Si) and Germanium (Ge) are two obvious choice to realize low cost MIR. This is due to their compatibility with microelectronics technology, and low cost which can made design of low cost single chip MIR feasible.

Unfortunately due to their indirect band gap nature both Si and Ge are not suitable to be used in active optoelectronic devices like MIR. So, it is necessary to employ some band engineering techniques in Si and Ge to induce direct band gap in them. Between these two, Germanium is the most appropriate material for implementation of band engineering due to the reason as follows. In Ge, the direct bandgap EΓ is only 140 meV larger than the indirect bandgap at L valley [2].

The most important approach of band structure engineering in Ge is incorporation of Tin (Sn) in the Germanium. With incorporation of small amount of Tin into Ge, L and Γ valley decreases. Decrement of Γ is faster than that of L valley and hence direct bandgap can be obtained at a particular value of mole fraction of Tin [3]. Thus GeSn alloy can enable the design of low cost group IV photonic sensors which are as efficient as their III-V group counterpart. However,

due to larger lattice mismatch between Ge and Sn, strain plays a critical role in physics of GeSn alloy. So, it needs to be addressed in a proper manner. Strain balanced structures are suggested to be the best way to tackle excessive strain in multiple layer structure like Quantum well [4]. It not only protects the active layer from excessive strain but also provide an opportunity to maximize its thickness, which is a good thing for photosensitive devices.

This paper focuses on the potential of Tin doped group-IV alloys specially GeSn to be used as an active layer in photosensitive devices like detector. It is the extension of our work reported elsewhere which highlighted potential of Tin incorporated quantum well application as a sensor in brief [5]. Here we give a detailed physical background of Tin incorporated group IV alloy. It highlights the recent progress and challenges in the research and fabrication of these alloys. This work primarily focuses on the use of these alloys in photo detectors. Absorption coefficient is a significant performance parameter in these devices. In this study, Sn content dependent absorption coefficient is evaluated in strain balanced SiGeSn/GeSn strain balanced quantum well. Eigen energy states for different Sn contents in GeSn layer are obtained in the well for Γ valley conduction band (ΓCB), heavy hole (HH) band and light hole (LH) band separately by solving coupled Schrödinger and Poisson equations self consistently. The absorption characteristics are evaluated for different Sn contents in well. The result revealed that HH-ΓCB transition observes high absorption coefficient within 3-5 µm range of wavelength. Thus this well structure can be used as an infrared sensor in various applications.

2. Tin Incorporated Group IV Alloy-Physical Background and Brief Review

Tin, the element that lies below germanium in the periodic table, can crystallize in the diamond structure (α-Sn) as well as in its more familiar metallic form (α-Sn). Only relatively poor specimens of this grey α-Sn had been prepared, however, as it is only formed rather slowly from metallic tin and at temperatures below 13 °C. (and retransforms back to α-Sn above that critical transformation temperature) [6]. The best specimens of α-Sn were in fact obtained by recrystallizing from solution in mercury [7], but such material probably was never of very high crystal perfection, although it could apparently be prepared in relatively pure form (about 10^{15} donors/cm3). The pioneer of inducing the idea of Tin based direct band gap semiconductor was Prof. Goodman who on the basis of theoretical grounds and substrate stabilization effect proved that an alloy of α-Sn and Ge solution can show a directness in its bandgap [6]. Soref and Perry have predicted the direct band gap of Sn based group IV semiconductor (SiGeSn) in year 1991 [8].

$Ge_{1-x}Sn_x$ alloys have attracted a great deal of interest in recent years due to their potential to become the first group IV direct band gap alloys. Diamond cubic Sn (or α-Sn) is a semimetal with a conduction band minimum at the Γ point sitting 0.41 eV below the valence band [9]. By alloying Sn and Ge, the conduction band extrema at both L and Γ valleys are predicted to decrease in energy with increasing Sn composition, but the Γ valley is predicted to decrease more rapidly than the L valley. Tight-binding [9] and pseudopotential [10] electronic structure calculations in virtual crystal approximation predict that $Ge_{1-x}Sn_x$ alloys would undergo an indirect to direct transition with a continuously tunable direct energy bandgap from 0.55eV to 0eV for Sn composition of x=0.2 to 0.6. Due to some difficulties in growing GeSn, Energy bandgap and Sn composition relation was not published until 1997 in which the indirect to direct band gap transition was estimated to occur near x=0.1 which is much lower than the theoretical prediction [11]. The critical concentration for the crossover for germanium for transition from indirect to direct was found as x=0.11 for relaxed $Ge_{1-x}Sn_x$ [12]. For different composition ratios, this alloy can be divided into two main branches first one is α- Sn film with Ge doping (dilute GeSn alloy) which has been reported by Farrow et. al. in 1981 [7], Goodman in 1982 [6], Vnuk et. al. in 1983 [13] and Ge rich $Ge_{1-x}Sn_x$ alloy was reported by [14-16]. Already in the 1980s and 1990s, several groups were studying the fabrication of α-Sn [17-19] or GeSn alloys [14, 20-22]. However several challenges for the single crystalline growth of GeSn alloys were found. Ragan et. al. [16] had given several problems that hindered the utilization of GeSn alloy. They highlighted the three main challenges to overcome:

(i) Minor solid solubility of Sn in Ge < 0.5 %

(ii) A large lattice mismatch between Ge and Sn (~15 %)

(iii) Sn has low surface free energy which causes surface segregation.

All investigations from the 1980s and 1990s showed that growth conditions far away from the thermodynamic equilibrium have a chance to produce monocrystalline GeSn alloys. $Ge_{1-x}Sn_x$ alloys with x<0.2 (x=mole fraction of tin) had been grown on silicon by ultrahigh vacuum chemical vapour deposition. By experimental investigation it had been proved that significant changes occurs in optical constants and redshifts in the interband transition energy as x varied [23, 24]. Suyog Gupta et. al. [25] addressed the challenges mentioned above and presented a first principles based simulation method to estimate lattice and electronic properties of GeSn alloy. They used low temperature molecular beam epitaxy (MBE) to obtain high quality crystalline GeSn layers. Modern semiconductor technology requires epitaxial layers with a prescribed band gap and lattice constant. This dual requirement cannot be implemented via 'one dimensional' binary A_xB_{1-x} or pseudo binary $A_xB_{1-x}C$ alloys. So it has motivated the quest for 'two-dimensional' ternary ($A_xB_yC_{1-x-y}$), pseudo-ternary ($A_xB_yC_{1-x-y}$ D), or quaternary

($A_x B_{1-x} C_y D_{1-y}$) materials whose band gaps and lattice constants can be tuned independently [26, 27].

Group III –V quaternary semiconductors were so successful in decoupling strain and band structure effects gave an impression that ternary group IV semiconductor such as SiGeC and SiGeSn should play similar role in group IV regime. SiGeC was reviewed at least for a decade and it was find out that only a limited amount of carbon can be incorporated and carbon induces a perturbation that make the band structure explanation extremely difficult even by virtual crystal approximation method [28, 29]. Tensile strain on Ge can be produced by growing this material on relaxed $Ge_{1-x}Sn_x$ as reported by Soref and Friedman [30]. However the direct bandgap (Γ valley) of $Ge_{1-x}Sn_x$ decreases very rapidly as a function of x. The solution to this problem is the incorporation of Si, which raises the energy of the alloy band gap. Si also reduces tensile strain on the Ge layer but a compromise can be achieved in such a way that the direct bandgap in Ge is also the lowest band gap in $Ge/Ge_{1-x-y}Si_x Sn_y$ multilayer [31]. Advances in CVD growth technology [32, 33] propels work in SiGeSn horizon.

Thus several studies have carried out for fabrication of high quality GeSn layers but the role of strain should be considered. Therefore, strain balanced structure is becoming very vital. In next section strain compensated structure and its used in implementation of photosensitive device is highlighted in brief.

3. GeSn MIR Sensor

3.1. Model Description

The Quantum well structure considered in our analysis consists of tensile strained SiGeSn barriers and compressively strained GeSn well which ensures the strain balanced condition for quantum well. The growth axis of the structure is assumed along (001) axis. A 76Å thick $Ge_x Sn_{1-x}$ layer is sandwiched between two tensile strained $Si_{0.09} Ge_{0.8} Sn_{0.11}$ layers to form a type-I single quantum-well (SQW) as shown in Fig. 1.

| $Si_{0.09}Ge_{0.8}Sn_{0.11}$ |
| $Ge_{1-x}Sn_x$ **(well)** |
| $Si_{0.09}Ge_{0.8}Sn_{0.11}$ |
| **Strain relaxed buffer** |
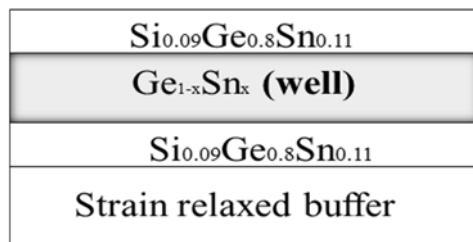
Fig. 1. Schematic of Strain balanced GeSn/SiGeSn Quantum well.

The thickness of barrier is computed as 35 Å by using strain compensate condition [4]. The dimension of the well is chosen in such a way that only one bound state formed in each of the conduction band and valence band. The Sn composition (x) in QW is required to obtain three condition simultaneously, (i) Type I SiGeSn/GeSn quantum well for better quantum carrier confinement, (ii) direct band gap in GeSn layer and (iii) a higher value of HH band offset than that of LH band (to be calculated later) for TE mode operation, which features HH-ΓCB dominant transition. A fully relaxed GeSn layer is used as a buffer layer. The composition of buffer layer should be selected to maintain strain balanced condition in the QW.

3.2. Band Alignment Calculations

Accurate band profile and band discontinuities of the proposed QW structure is the vital requirement for precise modeling of the direct band interband absorption. The strain plays an important role in calculation of band structure and then band discontinuities at the interface of proposed multilayer structure. Our primary concern is to investigate direct interband transition which involves obtaining bandstructure at band edge (Γ-valley conduction band) in GeSn QW by evaluating strain dependent band profile. Moreover, we have also assumed no coupling between the conduction band and valence bands, which is an appropriate estimation for group IV alloys. In this context, model solid theory suggested by Van de Walle, is well suited to our proposed model [34]. Model solid theory is said to be one of the most reliable method to calculate band line ups and their alignment at zone center (Γ-valley) in a strained heterostructure. So we followed this theory to calculate band profile in ΓCB conduction band, HH band and LH band for both well and barrier.

3.3. Coupled Schrodinger Poisson Selfconsistent Solution

After obtaining band profile, Eigen state energy of each band is required in order to evaluate direct absorption characteristics of QW. We obtained quantized energy states for Γ-CB, LH and HH band in QW by solving coupled Schrödinger and Poisson equation self consistently. Self–consistent solution is required to study the quantum confinement effect of carriers in QW more accurately considering variation in charge density of carriers. The Schrödinger equation with effective mass approximation and considering the strain effect is considered in our analysis and is given as [35]:

$$\left[\frac{-\hbar^2}{2} \frac{\partial}{\partial z} \frac{1}{m_j} \frac{\partial}{\partial z} + \frac{\hbar^2 K_t^2}{2m_j} + V_j(z) \right] \psi = E_j \psi , \quad (1)$$

where ħ is the Planck's constant, z is the position variable, K_t is the transverse wave vector, ψ is the wave function, E is the Eigen energy, m and V are the

effective mass and band profile respectively. Suffix X stands for type of band e.g., j=c for Γ conduction band, j=hh for HH valence band and j=lh for LH band. As the Γ valley is of only interest here, the transverse wave vector, K_t is taken as zero. The equation is solved using Finite Difference Method (FDM) to obtain Eigen energies and wave function in the well [36]. The whole region of interest is divided into N number of small elements of equal width, and the equation is solved for each of the elements.

After obtaining Eigen energies and their corresponding wavefunctions, the position dependent charge density of carriers in well is calculated by summing the square of the wave function at each spatial element (Δz) and multiplying this quantity by the number of carriers in each bound state. The expression for electron density (n(z)) and hole density (p(z)) in well is given as [37]:

$$n(z) = \sum_n N_n \left| \psi_n^{CB\Gamma}(z) \right|^2 ;$$
$$p(z) = \sum_m N_m \left| \psi_m^{HH/LH}(z) \right|^2 , \qquad (2)$$

where n and m are the number of subbands in ΓCB, valence band (LH and HH) respectively, N_n is the number of electrons in n^{th} sub-band in conduction band and N_m is number of holes in mth subband of HH band and LH band.

The obtained position dependent carrier charge densities (n(z) and p(z)) are then used in Poisson equation. Poisson equation relates the potential to the charge density distribution as given in eqn.3 [37].

$$\frac{d^2 V}{dz^2} = -\frac{q}{\varepsilon} \left(n(z) - p(z) + N_A - N_D \right) \qquad (3)$$

where n(z) and p(z) are the electrons and holes charge density distribution as obtained above. N_A and N_D are the acceptor and doping impurities in QW respectively and V is the spatial electrostatic potential in QW. Dirichlet and Neumann boundary conditions are also considered while solving the Poisson equation. Poisson equation was also solved by using finite difference numerical technique. In order to obtain self-consistent Eigen state energies both Poisson equation and Schrödinger equations are solved simultaneously until their solutions are converged [38].

3.4. Evaluation of Absorption Coefficient

After calculating Eigen energies and wavefunctions for Γ-CB, HH band LH band, direct interband transition characteristic of the QW structure is studied. Absorption coefficient is evaluated for QW with the help of Fermi golden rule and using the following mathematical expression, for absorption coefficient α [35]:

$$\alpha(\hbar\omega) = \frac{\pi q^2}{n_r c \varepsilon_0 m_0^2 \omega} \sum_{n,m} \left| I_m^n \right|^2 \cdot \left| P_{CV} \right|^2 \cdot \rho_{r2D} \cdot$$
$$\frac{1}{\sigma\sqrt{2\pi}} \exp\left[-\frac{\left(\hbar\omega - E_0 + E_{cn} - E_{vm} \right)^2}{\left(2\sigma \right)^2} \right] (f_v - f_c), \qquad (4)$$

where, ω is the photon frequency, q is the electronic charge, c is the speed of light, n_r is the refractive index of well, ϵ_0 is the static dielectric constant, m_0 is the electron rest mass. E_0 is the direct band gap of $Ge_{1-x}Sn_x$ which is calculated by linear interpolation of direct band gap of Ge and Sn considering bowing parameter. E_{cn} and E_{vm} are the bound state Eigen energies for n_{th} subband in Γ conduction band, and for m_{th} subband in valence band (v=hh for HH band, v=lh for LH band) respectively. I is the overlap integral of the Γ conduction subband wave function and valence subband wavefunction given by following equation.

ρ_{r2D} is reduced joint density of states in QW. QW is assumed to be undoped in this work (ideal case), only valence band is filled with carriers so carrier probability occupancy of conduction band is taken as zero ($f_c=0$, $f_v=1$). Gaussian line shape function is also considered for inhomogeneity in GeSn alloy. P_{cv} is momentum matrix element between conduction band and valence band for Bloch state. It is a key parameter to evaluate absorption in both bulk and nanostructures. Indeed, its magnitude value indicates the strength of the interaction between photon with electron. Moreover under compressive strain TE mode is dominant than TM mode. Hence, TE polarization which parallel to the plane of QW layer is assumed in present study. In TE mode momentum matrix element of HH-Γ-CB transition is much greater than that of LH- ΓCB Γ transition at $K_t=0$.

4. Results and Discussions

In this study, Sn concentration in $Ge_{1-x}Sn_x$ quantum well layer is varied from 0.15 to 0.18 to obtain quantum mechanical characteristic of strain balanced quantum well and then direct absorption characteristic. As for compressive strained GeSn direct band gap nature induced in GeSn layer for $x \geq 0.15$ [39]. Thus the required concentration of Sn should be at least 15% in $Ge_{1-x}Sn_x$ layer. Moreover, beyond 0.18, the inter layer strain increases and it is intolerable and infeasible in actual situations.

The calculated band profile (band offset of Γ conduction band and heavy hole band) with Eigen state energies (E_{c1} for ΓCB, E_{HH} for HH band and E_{LH} for LH band) for QW at different Sn concentration is shown in Fig. 2. It is clearly observe that HH band (E_{HH}) is up shifted in comparison to light hole band profile. This is attributed due to compressive strain in the well. The band offsets of Γ conduction band and heavy hole band are sufficient large to cause quantum confinement effect of carriers. With increasing in Sn concentration, the shifting of E_{HH} in upward direction increases and bad gap also decreases subsequently. It

can be also observed that Eigen wave function of LH band is weakly confined in the well. This is due to a very small negligible band offset for LH band. It also ensure that only HH-ΓCB (E_{HH}-E_{c1}) transition will be dominated in this case. Absorption coefficient spectra (α) for different x are plotted as a function of wavelength and is shown in Fig. 3. Due to higher optical matrix element of HH to ΓCB transition for TE mode, LH-ΓCB transition is ignored in this study.
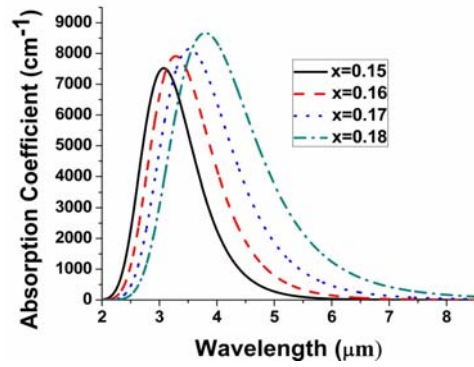
Fig. 3. Plot of absorption coefficient (α) for HH- ΓCB direct transition. versus wavelength for different values of x.

The figure clearly reveals that significant absorption for HH to ΓCB transition is observed in infrared range of wavelength (3-5μm). With increasing in Sn concentration peak absorption wavelength shifted to higher wavelength region. This red shifting is due to the lowering of the energy band gap of GeSn with increasing Sn concentration. It is also observed that with increasing Sn concentration, absorption increases.

4. Conclusions

This works throws light on the potential of Tin Incorporated Group IV alloy. It gives more emphasis on GeSn allys. Initially the motivation behind incorporation of Tin is briefly explained by explaining the basic reason and need behind this concept.

Then a detailed review and background of Tin incorporated Group IV alloy especially GeSn is elaborated along with recent advancement in its fabrication. In addition the origin of Tin and the initial work of Tin incorporation are also highlighted in this section. Also, In this section the various challenges regarding fabrication of GeSn alloy from very beginning is provided. The concept of strain can also play a very crucial role in deciding the structure of the proposed device. The importance of strain balanced structure is also briefly explained.

Later on, this paper explores the potential of GeSn quantum well layer to be used in low cost monolithic photosensitive devices for mid infrared sensing applications. Direct interband absorption is plotted for different Sn content of well for dominant HH- ΓCB transition. Sn content is selected in range of 15% to 18% to provide a direct band gap in the active layer as well as free the proposed structure from defect like dislocation, imperfection due to decrement of critical thickness at higher Sn content.

The result depicts a significant absorption in 3-5 μm range of wavelength. In addition, increment in absorption with Sn concentration is also observed. Thus this quantum well structure is viable to be used as a low cost mid-infrared sensor.
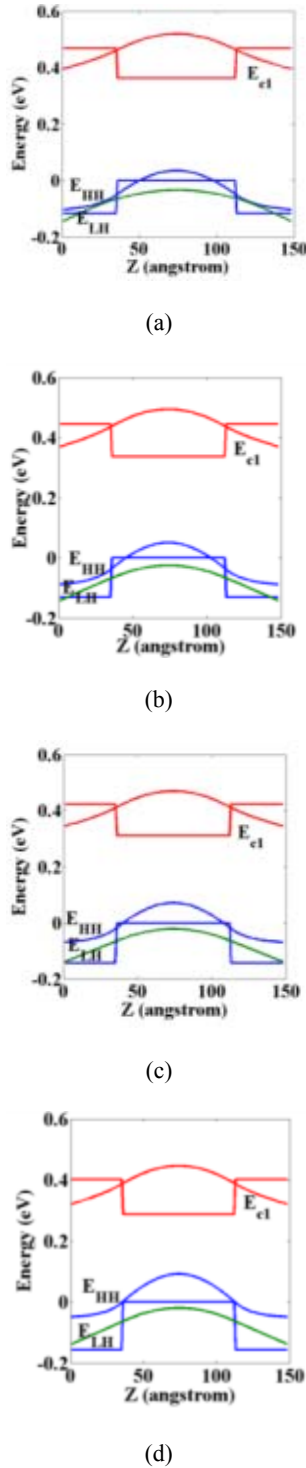

(a)

(b)

(c)

(d)

Fig. 2. Plot of band profile, Eigen energies and wave functions for different values of x. (a) x=0.15, (b) x=0.16, (c) x=0.17, (d) x=0.18.

References

[1]. Roelkens, G. et. al., Silicon-Based Photonic Integration Beyond the Telecommunication Wavelength Range, *IEEE Journal of Selected Topics in Quantum Electronics*, Vol. 20, Issue 4, 2014, Article No. 8201511.

[2]. Pallab Bhattacharya, Semiconductor optoelectronic devices, *Pearson Education Inc.,* Second ed., New Jersey, 1994.

[3]. J. Kouvetakis, J. Menendez and A. V. G. Chizmeshya, Tin based group IV semiconductors: new platforms for opto and micro electronics and silicon, *Annual Review of Material Research*, Vol. 36, 2006, pp. 497-554.

[4]. Ekin Daukes, K. Kawaguchi and J. Zhang, Strain-Balanced Criteria for Multiple Quantum Well Structures and Its Signature in X-ray Rocking Curves, *Crystal growth and design*, Vol. 2, 4, 2002, pp. 287-292, .

[5]. Prakash Pareek, Mukul K. Das, Sn-Concentration Dependent Absorption in Strain Balanced GeSn/SiGeSn Quantum Well, *in Proceedings of the 1st International Conference on Advancement of Computer Communication & Electrical Technology(ACCET'16)*, Murshidabad College of Engineering & Technology, Berhampore, Murshidabad, West Bengal, India, 21-22 October, 2016.

[6]. C. H. L. Goodman, Direct-gap group IV semiconductors based on tin *IEEE Proceedings I: Solid State and Electron Devices,* Vol. 129, 1982, pp. 189-192.

[7]. R. F. C. Farrow, D. S. Robertson, G. M. Williams, A. G. Cullis, G. R. Jones, I. M. Young and P. N. J. Dennis, The growth of metastable, heteroepitaxial films of α-Sn by metal beam epitaxy, *Journal of Crystal Growth*, Vol. 54, 1981, pp. 507-518.

[8]. R. A. Soref and C. H. Perry, Predicted bandgap of the new semiconductor SiGeSn, *Journal of Applied Physics*, Vol. 69, 1991, p. 539.

[9]. D. W. Jenkins and J. D. Dow, Electronic properties of metastable GexSn1-x alloys, *Physical Review B*, Vol. 36, 1987, pp. 7994-8000.

[10]. K. A. Mäder, A. Baldereschi and H. von Känel, Band structure and instability of $Ge_{1-x}Sn_x$ alloys, *Solid State Communication*, Vol. 69, 1989, pp. 1123-1126.

[11]. G. He and H. A. Atwater, Interband transitions in SnxGe1-x alloys, *Physical Review Letters*, Vol. 79, 1997, pp. 1937-1940.

[12]. Vijay R. D'costa, Optical critical points of thin-film $Ge_{1-y}Sn_y$ alloys:a comparative $Ge_{1-y}Sn_y/Ge_{1-x}Si_x$ study, *Physical Review B*, Vol. 73, 2006, p. 125207.

[13]. F. Vnuk, A. DeMonte and R. W. Smith, The composition dependence of the grey tin --> white tin transition in dilute tin-germanium alloys, *Material Letters*, Vol. 2, 1983, pp. 67-70.

[14]. S. I. Shah and J. E. Greene, Growth of single-crystal metastable Ge1-xSnx alloys on Ge(100) and GaAs(100) substrates, *Journal of Crystal Growth*, Vol. 83, 1987, pp. 3–10.

[15]. O. Gurdal P. Desjardins, J. R. A. Carlsson, and N. Taylor H. H. Radamson and J.-E. Sundgren and J. E. Greene, Low-temperature growth and critical epitaxial thicknesses of fully strained metastable Ge1-xSnx (x<0. 26) alloys on Ge(001)2×1, *Journal of Applied Physics*, Vol. 83, 1998, pp. 162-170.

[16]. R. Ragan Kyu S. Min and Harry A. Atwater, Direct energy gap group IV semiconductor alloys and quantum dot arrays in SnxGe1 - x/Ge and SnxSi1 - x/Si alloy systems, *Material Science and Engineering B: Solid-State Material For Advance Technology*, Vol. 87, 2001, pp. 204-213.

[17]. J. D. Sau and M. L. Cohen, Possibility of increased mobility in Ge-Sn alloy system, *Physical Review B*, Vol. 75, 2007, p. 045208.

[18]. A. Harwit, P. R. Pukite, J. Angilello and S. S. Iyer, Properties of diamond structure SnGe films grown by molecular beam epitaxy, *Thin Solid Films*, Vol. 184, 1990, pp. 395–401.

[19]. M. T. Asom A. R. Kortan, L. C. Kimerling, and R. C. Farrow, Structure and stability of metastable alpha-Sn, *Applied Physics Letters*, Vol. 55, 1989, pp. 1439–1441.

[20]. P. R. Pukite, Alex Harwit, and S. S. Iyer, Molecular beam epitaxy of metastable, diamond structure SnxGe1−x alloys, *Applied Physics Letters*, Vol. 54, 1989, pp. 2142–2144.

[21]. M. T. Asom, E. A. Fitzgerald, A. R. Kortan, B. Spear, and L. C. Kimerling, Epitaxial growth of metastable SnGe alloys, Applied Physics Letters, Vol. 55, 1989, pp. 578–579.

[22]. W. Wegscheider, K. Eberl, U. Menczigar, and G. Abstreiter, Single-crystal Sn/Ge superlattices on Ge substrates: growth and structural properties, *Applied Physics Letters*, Vol. 57, 1990, pp. 875–877.

[23]. J. Tolle, Radek Roucka, Andrew V. G. Chizmeshya, and John Kouvetakisa) Vijay R. D'Costa and José Menéndez, Compliant tin-based buffers for the growth of defect-free strained heterostructures on silicon, *Applied Physics Letters*, Vol. 88, 2006, p. 252112.

[24]. C. S. Cook, Stefan Zollnerb, Matthew R. Bauera, Pavan Aellaa, John Kouvetakisa and Jose Menendezc, Optical constants and interband transitions of Ge1−xSnx alloys (x<0. 2) grown on Si by UHV-CVD, *Thin Solid Films*, Vol. 455-456, 2004, pp. 217-221.

[25]. Suyog gupta et. al., GeSn Technology: Extending the Ge Electronics Roadmap, *2011 IEEE IEDM*, 2011, pp. 16.6.1 - 16.6.4.

[26]. A. W. Bett, F. Dimroth, G. Stollwerck and O. V. Sulima, III-V compounds for solar cell applications, *Applied Physics A*, Vol. 69, 1999, pp. 119-129.

[27]. I. Vurgaftman, J. R. Meyer and L. R. Ram-Mohan, Band parameters for III–V compound semiconductors and their alloys, *Journal of Applied Physics*, Vol. 89, 2001, pp. 5815-5876.

[28]. K Brunner et. al., SiGeC: band gaps, band offsets, optical properties, and potential applications, *Journal of Vacuum Science and Technology B*, Vol. 16, 1998, pp. 1701–1706.

[29]. JD Lorentzen, G. H. Loechelt, M. Meléndez-Lira, J. Menéndez, S. Sego, R. J. Culbertson, W. Windl, O. F. Sankey A. E. Bair and T. L. Alford, Photoluminescence in Si1−x−yGexCy alloys, *Applied Physics Letters*, Vol. 70, 1997, pp. 2353–2355,.

[30]. R. A. Soref and L. Friedman, Direct-gap Ge/GeSn/Si and GeSn/Ge/Si heterostructures, *Superlattices and Microstrucures*, Vol. 14, 1993, p. 189.

[31]. J. Menedez and J. Kouvetakis, Type I Ge/Ge1-x-ySixSny strained layer heterostructures with a direct Ge bandgap, *Applied physics Letters*, Vol. 85, 2004, pp. 1175-1177.

[32]. M. Bauer J. Taraci, J. Tolle, A. V. G. Chizmeshya, S. Zollner, David J. Smith, J. Menendez, Changwu Hu, and J. Kouvetakis, Ge–Sn semiconductors for band-gap and lattice engineering, *Applied Physics Letters*, Vol. 81, 2002, pp. 2992-2995.

[33]. M. R. Bauer et. al., Tunable band structure in diamond–cubic tin–germanium alloys grown on silicon substrates, *Solid State Communication*, Vol. 127, 2003, pp. 355-359.

[34]. Chris G. Van de Walle, Band lineups and deformation potentials in the model-solid theory, *Physical Review B*, Vol. 39, 1989, pp. 1871-1883.

[35]. Chuang, Shuan Lien, Physics of optoelctronic devices, *John Wiley & Sons,* New York, 1995.

[36]. Datta, Supriyo, Quantum transport: atom to transistor, *Cambridge University Press*, New York, 2005.

[37]. I. H. Tan, G. L. Snider, L. D. Chang and E. L. Hu, A selfconsistent solution of Schrödinger–Poisson equations using a nonuniform mesh, *Journal of Applied Physics*, Vol. 68, 1990, pp. 4071-4076.

[38]. Frank Stern, Iteration methods for calculating self-consistent fields in semiconductor inversion layers, *Journal of Computational Physics*, Vol. 6, 1970, pp. 56-67.

[39]. Prakash Pareek, Mukul K. Das, Theoretical Analysis of Direct Transition in SiGe/GeSn Strained Quantum Well Structure by Finite Difference Method, *Springer In Proceedings of the Phys.,* Vol. 166, *Advances in Optical Science and Engineering*, 2015, pp. 613-619.

Performance and Analysis of an Asynchronous Motor Drive with a New Modified Type-2 Neuro Fuzzy Based MPPT Controller Under Variable Irradiance and Variable Temperature

Pakkiraiah B. and Durga Sukumar G.

Department of Electrical and Electronics Engineering,
Vignan's Foundation for Science Technology and Research University,
Guntur, A.P, India-522213
E-mail: pakki1988@gmail.com, durgasukumar@gmail.com

Abstract: In the present research, we have developed a new modified Type 2 neuro fuzzy (T2NF) based MPPT controller, which combines the advantages of fractional open circuit voltage (FCV), variable step and optimized P&O algorithm. It leads to a faster and better tracking and lower oscillations around the MPP to contribute higher efficiency. The simulation result shows an efficiency of 96.41 %, an improvement of 2 ms is observed in the starting characteristics. The above concept has been extended to single phase AC photovoltaic system with improvement of 15 % in its performance. It has benefits of high efficiency and low harmonic distortion at output voltage waveform. Here DC-DC boost converter and space vector modulation based inverter are used to provide the required supply to the load. The proposed T2NF based MPPT improves the system efficiency even at abnormal weather conditions. Here a lot of reduction in torque and current ripple contents is obtained with the help of T2NF based MPPT for an asynchronous motor drive. Also the better performance of an asynchronous motor drive is analyzed with the comparison of conventional and proposed MPPT controller using Matlab-simulation results. Practical validations are also carried out and tabulated.

Keywords: Photovoltaic (PV) system, Maximum power point tracking (MPPT) controller, Type 2 neuro fuzzy (T2NF) system, DC-DC boost converter, Space vector modulation (SVM), Abnormal weather conditions, Asynchronous motor (ASM) drive and harmonic distortion.

1. Introduction

The PV power and voltage characteristics are nonlinear and affected by the irradiance and temperature variations. The applied MPPT uses a type of control and logic to look for the knee, which in turn allows the converter to extract the maximum power from the PV array. The tracking method provides a new reference signal for the controller and extracts the maximum power from the PV array. The hill climbing method has slow response especially under varying weather conditions because the MPPT gives the decision directly for the duty cycle declaring a controller of error signal [1-3]. The voltage based MPPT method uses the fact that the ratio between the maximum power voltage and the open circuit voltage under different weather conditions, which are linearly proportional [4]. Perturbation and observation method are commonly used due to its ease of implementation, also works effectively under varying weather

conditions where it can reach to the error signal due to its separation between the MPPT method that controls the reference signal and duty cycle resulting of changing the reference signal [5-6].

Among different intelligent controllers, fuzzy logic is the simplest to integrate with the systems. Recently, fuzzy logic controller has received an increasing attention to researchers for converter control, motor drives and other process control as it provides better responses than other conventional controllers [7]. The imprecision of the weather variations that can be reflected by PV arrays also addressed accurately using fuzzy controller. Here Type 2 fuzzy based technique is implemented for PV system which is involved in the operation of fuzzification, inference and output processing. This output processing consists of type reduction and defuzzification to provide the better performance. The T2FLC deals with the variable step size to increase or decrease the reference voltage. Therefore the tracking time becomes short and the system performance during steady state conditions is much better than other conventional techniques [8-10].

Intelligent controls using artificial intelligence, fuzzy logic and neural networks, these systems are introduced as major sources to improve the performance of motor drives. Intelligent controls with adaptive network techniques are creating an interest research for practical implementation and control of motor drives. Earlier sinusoidal pulse width modulation (SPWM) was majorly used technique for industrial applications, because it reduces the harmonics. SPWM is suitable up to 0.7855 modulation indices for linear modulation index and above it gives more ripples in voltage [11-13]. To overcome this third harmonic injected pulse width modulation SVPWM techniques are used to improve the total harmonic distortion in voltage and current. Also it increases the modulation index up to 0.907 with increasing the fundamental value compared to SPWM [14-16]. Here the speed of the induction motor can also be controlled by direct torque control with PIC. But it cannot give good transient and steady state responses [17]. To overcome this, a new technique with type-2 fuzzy logic systems has been introduced as an upgrading of ordinary fuzzy logic set which is called type-1 fuzzy set. The characterization of type-2 fuzzy set is that the membership value for each element of this set is a fuzzy set in [0,1], not a crisp set like type-1 fuzzy. Type-2 fuzzy set can handle linguistics as well as numerical uncertainties. Because it can be modeled with reducing their effects [18-19].

Unfortunately, type-2 fuzzy sets are more difficult to use and understand than traditional type-1 fuzzy sets. Though it has few difficulties, it being used for many applications like coded video streams, co-channel interference elimination from nonlinear time-varying communication channels, connection admission control, extracting knowledge from questionnaire surveys, forecasting of time-series, function approximation, pre-processing radiographic images and transport scheduling with some control applications [20-21]. A comparison of adaptive neuro

fuzzy based space vector modulation with neural network and conventional based system has been presented [22-23]. Here type-2 neuro fuzzy logic controller based MPPT method is proposed with boost converter to regulate the PV output voltage and track the MPP of PV modules and also to determine the system operation point which varies with load, solar irradiation and temperature variations.

So this paper proposes a novel type 2 neuro fuzzy based MPPT controller which takes variable irradiance and variable temperature into the consideration in order to get performance better than the existed methods. The advantage of this proposed MPPT algorithm is used to control the MPP even under abnormal weather conditions compared to other conventional algorithms. In section 2 mathematical modeling of PV array is discussed. Section 3 & 4 explains about the type 2 neuro fuzzy system and a novel type 2 neuro fuzzy based MPPT controller. Mathematical modeling of asynchronous motor drive is noted in section 5. Section 6 states a brief note on proposed space vector modulation technique. Using the proposed MPPT along with DC-DC converter to boost up the PV output and to feed asynchronous motor drive is detected in section 7. Matlab-simulation results with the comparison of conventional and proposed MPPT techniques are presented in section 8. The concluding remarks are stated in section 9.

2. Mathematical Modeling of PV Array

Solar PV system is made of photovoltaic cells. Cells are grouped to form panels and panels are grouped to form array. The basic mathematical equations describes the ideal PV cell and those are clearly mentioned in equations (1) and (2)

$$I_M = I_{PVCELL} - I_{OCELL} \left[\frac{\exp\left(\frac{QV_M}{KNT_{AP}}\right)}{I_d} - 1 \right], \qquad (1)$$

where I_{PVCELL} is the incident light generated current, I_{OCELL} is the diode reverse saturation current, Q is the charge of an electron at 1.602×10^{-19} C, K is the Boltzmann's constant at 1.381×10^{-23} J/K, T_{AP} is the temperature at the junction in Kelvin, N is the diode identity constant, V_{PVCELL} is the voltage across the PV cell and I_{PVCELL} is the current of the ideal PV model as illustrated in Fig. 1.
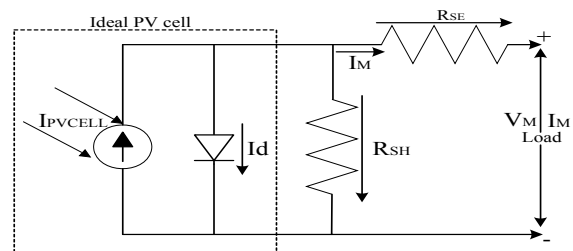
Fig. 1. Practical PV cell equivalent circuit.

PV system basic equation does not represent I-V characteristics, as a practical PV module consists of various PV cells which require additional parametric values as series and parallel resistances (R_{SE} & R_{SH}) as shown in Fig. 1. PV module modeling is based on mathematical equation of the solar cell which is given by Eq. 2.

$$I_M = I_{PVCELL} - I_{OCELL}\left[exp^{\frac{Q(V_M+I_MR_{SE})}{N_TKNT_{AP}}} - 1\right] - \frac{V_M+I_MR_{SE}}{R_{SH}} \quad (2)$$

where I_M = PV module current in Amps, I_{PVCELL} = Photocurrent or light generated current in Amps, I_{OCELL} = Reverse saturation current of a diode in Amps, Q = Electron charge in Coulombs, N = Ideality factor (taken from data sheet), K = Boltzmann constant in J/°K, T_{AP} = Applied temperature for the PV module in Kelvin, V_M = Module voltage in Volts, R_{SE} = Series resistance in ohms, R_{SH} = Parallel resistance in ohms and Current generated by light (I_{PVCELL}) depends linearly on solar radiation and also on temperature is given by Eq. (3)

$$I_{PVCELL} = \frac{P_{AP}[I_{SCR}+T_{SCI}(T_{AP}-T_{REF})]}{P_{REF}} \quad (3)$$

where P_{AP} = Applied solar irradiance in W/m² (applied to the module during the experiment), P_{REF} = Reference irradiance in W/m² (1000 W/m² is taken under STC), I_{SCR} = Module short circuit current (taken from the data sheet), T_{SCI} = Temperature coefficient of short circuit current in A/°K (taken from data sheet), T_{AP} and T_{REF} are applied and reference temperatures in Kelvin. The practical calculated $I_{PV\ CELL}$ values for different irradiance and different temperature are tabulated in Table. 1.

Table 1. The Practical Calculated $I_{pv\ Cell}$ Values for Different Irradiance and Different Temperature.

Irradiance in (W/m²)	Temperature (in °C)				
	20 °C	*30 °C*	*40 °C*	*50 °C*	*60 °C*
1000	8.661	8.678	8.695	8.712	8.729
800	6.929	6.942	6.956	6.97	6.983
500	4.330	4.339	4.347	4.356	4.364
250	2.165	2.169	2.173	2.178	2.182
100	0.866	0.867	0.869	0.871	0.872
50	0.433	0.433	0.434	0.435	0.436
10	0.086	0.086	0.086	0.087	0.087

Modules reverse saturation current (I_{RS}) at nominal condition and reference temperature is given by Eq. (4)

$$I_{RS} = \frac{I_{SCR}}{exp^{\left(\frac{QV_{OC}}{N_TKNT_{AP}}\right)} - 1} \quad (4)$$

where I_{RS} = Reverse saturation current in Amps, and N_T = total no. of cells in a module. Here module voltage decreases as the applied temperature goes on increases which can be calculated by Eq. (5)

$$V_M = \frac{N_TKNT_{AP}}{Q} \times \ln\left[\frac{I_{PVCELL}-I_{RS}}{I_{RS}}\right] \quad (5)$$

On the other hand saturation current (I_{SAT}) is given as

$$I_{SAT} = I_{RS} \times \left(\frac{T_{AP}}{T_{REF}}\right)^3 \times exp^{\left\{\frac{QE_{GO}}{NK}\left(\frac{1}{T_{REF}} - \frac{1}{T_{AP}}\right)\right\}} \quad (6)$$

where E_{GO} = is the semiconductor band gap energy of the module in J/C. The resistance R_{SH} is inversely proportional to leakage current and a small variation of series resistance will affect the PV output power. A PV cell will produce less than 2 watts at approximately 0.5 V. The cells must be connected in series and parallel to get required power. Array basic output current of single diode module is calculated by Eq. (7)

$$I_A = N_{PV}\ I_{PVCELL}$$
$$-N_{PR}I_{OCELL}\left[exp^{\frac{Q}{N_{SE}KNT_{AP}}\left(\frac{V_M}{N_{SE}} + \frac{I_MR_{SE}}{N_{PR}}\right)} - 1\right] -$$
$$\frac{1}{R_{SH}}\left[\frac{N_{PR}V_M}{N_{SE}} + I_MR_{SE}\right] \quad (7)$$

where N_{SE} and N_{PR} are the number of solar cells connected in series ad parallel. Modeling of PV array is done based on data sheet parameters of SSI-3M6-250W poly-crystalline solar module at 25° C and 1000 W/m². Based on above parameters PV is modeled in Simulink model is developed under standard test conditions.

3. Type-2 Neuro Fuzzy Controller

In this section, the structure and mechanism of T2NFIS is presented. The structure of T2NFIS is shown in Fig. 2. It is a five layered network which uses type-2 neuro fuzzy sets in the antecedent and the consequent realizes the Takagi-Sugeno-Kang Type-0 fuzzy inference mechanism. Let assume the structure consists of q input features, n output features and has grown K rules after processing t-1 samples. Hereafter, we detail the function of each layer when the network is presented with the tth sample, x(t).

Layer 1 - Input layer
Each node in this layer passes the input data directly to the fuzzification layer. The output of ith node is given as in Eq. (8) and the diagram is shown in Fig. 2.

$$u_i(t) = x_i(t), \text{ where } i = 1, 2, \cdots, q \quad (8)$$
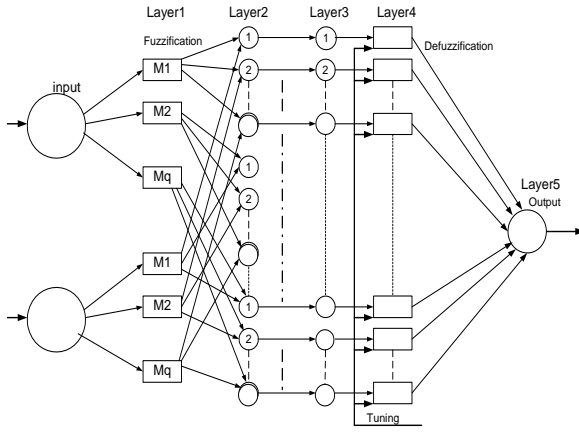
Fig. 2. Structure of five layered type-2 neuro-fuzzy system.

Layer 2 - Fuzzification layer

The function of this layer is to perform the fuzzification operation. Each node in this layer computes the Type-2 membership of the input with the rule antecedents. The membership of ith input feature with k^{th} rule is given by:

$$\emptyset_{ki}(t) = exp^{(-\frac{(u_i(t)-\mu_{ki})^2}{2\sigma_{ki}^2}\equiv\emptyset(\mu_{ki},\sigma_{ki},u_i(t))} \qquad (9)$$

where $\mu_{ki} \in [\mu_{ki}^l, \mu_{ki}^r]$ and $\sigma_{ki} \in [\sigma_{ki}^l, \sigma_{ki}^r]$. Are left and right limits of the center and width of kth rule's i^{th} feature respectively. The footprint of uncertainty of this membership function can be represented in terms of upper membership function φ_{up} and lower membership function φ_{lo} as given below

$$\emptyset_{ki}^{up}(t) = \begin{cases} \emptyset(\mu_{ki}^l, \sigma_{ki}^l, u_i(t)) \\ \emptyset(\mu_{ki}^r, \sigma_{ki}^r, u_i(t)) \end{cases} \qquad (10)$$

where $u_i(t) < \mu_{ki}^l, \mu_{ki}^l \leq u_i(t) \leq \mu_{ki}^r, u_i(t) > \mu_{ki}^r$

$$\emptyset_{ki}^{lo} = \begin{cases} \emptyset(\mu_{ki}^r, \sigma_{ki}^r, u_i(t)) \ u_i(t) \leq \frac{\mu_{ki}^l + \mu_{ki}^r}{2} \\ \emptyset(\mu_{ki}^l, \sigma_{ki}^l, u_i(t)) \ u_i(t) > \frac{\mu_{ki}^l + \mu_{ki}^r}{2} \end{cases} \qquad (11)$$

The output of each node can be represented as

$$\emptyset_{ki} = [\emptyset_{ki}^{lo}(t), \emptyset_{ki}^{up}(t)] \qquad (12)$$

Layer 3 - Firing layer

The firing layer consists of K nodes where each node represents the upper and lower antecedent part of a fuzzy rule. The function of this layer is to calculate the firing strength of each of the rules. The algebraic product operation is used to compute the firing strength of a rule and is given by

$$[F_k^{lo}(t), F_k^{up}(t)]; k = 1, ..., K \qquad (13)$$

$$[F_k^{lo}(t) = \prod_{i=1}^{m} \emptyset_{ik}^{lo} \ and \ F_k^{up}(t) = \prod_{i=1}^{m} \emptyset_{ik}^{up};$$

$$k = 1, ..., K \qquad (14)$$

Layer 4 - Interval-reduction layer

This layer contains K nodes. The function of each node is to perform the interval- reduction of Interval Type-1 fuzzy set to Type-1 fuzzy number. The computationally efficient algorithm is employed to reduce the interval and is given as

$$F_k(t) = \propto F_k^{lo}(t) + (1-\propto)F_k^{up}(t); k = 1, ..., K \qquad (15)$$

where α is the design vector. In our study α is chosen as 0.5.

Layer 5- Output layer

This layer computes the output of network by employing weighted average defuzzification technique and is given as

$$\hat{Y}_j(t) = \frac{\sum_{k=1}^{K} w_{jk}F_k(t)}{\sum_{p=1}^{K} F_p(t)}; j = 1, ..., n \qquad (16)$$

where w_{jk} is the output weight connecting the kth rule with the jth output node.

4. Novel Type-2 Neuro Fuzzy based MPPT Controller

TIFLCs are unable to handle rule uncertainties directly, because they will not use type-2 neuro fuzzy (T2NF) sets that are certain. On the other hand T2NFLC is very useful in uncertainties measurement with minimizing the effects of uncertainties in rule base. Because their use is not widespread yet. In this one should identify the main control variables and determine the sets that describe the values of each linguistic variable. This algorithm is designed to achieve the advantage of other MPPT algorithms to simplify and eliminate all aforementioned drawbacks. The change in PV array output and the change in PV array output voltage are the inputs of the T2NF. The increment of the reference voltage is the output of the T2NFLC where the increment is added to the previous reference voltage to produce the new reference voltage. The inputs and the outputs of the T2NFLC are shown in the equations from (17) to (19)

$$\Delta P = P(k) - P(k-1) \qquad (17)$$

$$\Delta V = V(k) - V(k-1) \qquad (18)$$

$$\Delta Vref = Vref(k) - Vref(k-1) \qquad (19)$$

The differential power dp can be calculated as

$$dP = Pmax - Pmin \qquad (20)$$

Flow chart of type-2 neuro fuzzy based MPPT algorithm is shown in Fig. 3.
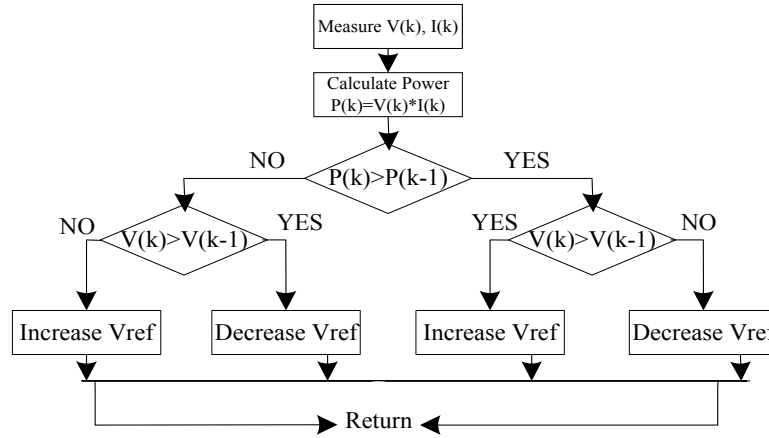
Fig. 3. Flowchart of type-2 neuro fuzzy based MPPT algorithm for power improvement.

The input variables of the T2NFLC are divided into 4 subsets as positive big (PB), positive small (PS), negative small (NS), negative big (NB). Also, the membership functions of the output variables are four fuzzy sets, where the maximum of minimum composition technique is used for the inference and the gravity method for defuzzification process to convert the fuzzy subset reference voltage changes to real members as presented in (21)

$$\Delta Vref = \frac{\sum_i^n \Delta Vrefi \, \mu(\Delta Vrefi)}{\sum_i^n \mu(\Delta Vrefi)} \qquad (21)$$

where $\Delta Vref$ is the fuzzy output and $\Delta Vrefi$ is the output membership functions of max-min interference composition. $\Delta Vref$ is the increasing function with respect Vref. The left most point VrefL and right most point VrefR can be obtained as follows

$$\Delta VrefL = \frac{\sum_i^n \Delta VrefLi \, \mu(\Delta VrefLi)}{\sum_i^n \mu(\Delta VrefLi)} \qquad (22)$$

$$\Delta VrefR = \frac{\sum_i^n \Delta VrefRi \, \mu(\Delta VrefRi)}{\sum_i^n \mu(\Delta VrefRi)} \qquad (23)$$

The defuzzified crisp output from the type-2 fuzzy system is the average of VrefL and VrefR as

$$\Delta Vref = \frac{\Delta VrefR + \Delta VrefL}{2} \qquad (24)$$

But from equations (17), (18) and (20) Pmax and Pmin we get as follows

$$Pmax = Vpv\_(k-1) * Ipv\_(k-1) \qquad (25)$$

$$Pmin = Vpv\_k * Ipv\_k \qquad (26)$$

This algorithm modifies the phase displacement between grid voltage and the converter voltage providing the voltage reference Vref. Furthermore, here an extra feature is added to monitor the maximum and minimum power oscillations on the PV side. In case of single-phase power systems, the instant power oscillates with the line frequency. If the system

operates in the area around MPP, the ripple of the power on the PV side is minimized. A flow chart of the MPPT explains how the angle of the reference voltage is modified in order to keep the operating point as close to MPP.

The phase displacement d$\delta mppt$ is provided by the controller. If that the operating in the area on the left side of the MPP then d$\delta mppt$ has to decrease. This decrement is indicated with side=-1. Moreover, if the operating in the area on the right side of the MPP then d$\delta mppt$ has to increase and it is indicated with side =+1. The increment size determines how fast the MPP is tracked. The measure of the power oscillations on the PV side is used to quantify the increment that is denoted.

5. Mathematical Modeling of Asynchronous Motor Drive

The mathematical modeling of a three-phase, squirrel-cage asynchronous motor drive can be described with stationary reference frame as

$$V_{qS} = (R_S + pL_S)I_{qS} + PL_M I_{qR} \qquad (27)$$

$$V_{dS} = (R_S + pL_S)I_{dS} + PL_M I_{dR} \qquad (28)$$

$$0 = pL_M I_{qS} - \omega_R L_M I_{dS} + (R_R + pL_R)i_{qR} - \omega_R L_R i_{dR} \qquad (29)$$

$$0 = \omega_R L_M i_{qS} + pL_M i_{dS} + \omega_R L_R i_{qR} + (R_R + pL_R)i_{dR}, \qquad (30)$$

where $\omega_R = \frac{d\theta}{dt}, p = \frac{d}{dt}$

Suffixes S and R represents stator and rotor respectively. V_{dS} and V_{qS} are d-q axis stator voltages respectively, i_{dS}, i_{qS} and i_{dR}, i_{qR} are d-q axis stator currents and rotor currents respectively. R_S and R_R are stator and rotor resistances per phase. L_S, L_R are self inductances of stator and rotor and L_M is mutual inductance. Stator and rotor flux linkages can be expressed as

$$\lambda_{qS} = L_S i_{qS} + L_M i_{qR} \qquad (31)$$
$$\lambda_{dS} = L_S i_{dS} + L_M i_{dR} \qquad (32)$$
$$\lambda_{qR} = L_R i_{qR} + L_M i_{qS} \qquad (33)$$
$$\lambda_{dR} = L_R i_{dR} + L_M i_{dS} \qquad (34)$$

From the above equations (27)-(30), Squirrel-cage asynchronous motor can described by following equations in stator reference frame as

$$\begin{bmatrix} V_{qS} \\ V_{dS} \\ 0 \\ 0 \end{bmatrix} = \begin{bmatrix} R_S + pL_S & 0 & pL_M & 0 \\ 0 & R_S + pL_S & 0 & pL_M \\ pL_M & -\omega_R L_R & R_R + pL_R & -\omega_R L_R \\ \omega_R L_M & pL_M & \omega_R L_R & R_R + pL_R \end{bmatrix} \begin{bmatrix} i_{qS} \\ i_{dS} \\ i_{qR} \\ i_{dR} \end{bmatrix}$$
$$(35)$$

The electromagnetic torque Te of the induction motor is given by

$$T_e = \frac{3}{2}\left(\frac{p}{2}\right)\left(\lambda_{qR} i_{dR} - \lambda_{dR} i_{qR}\right) \qquad (36)$$

From the dynamic model of asynchronous machine, the rotor flux is aligned along with the d-axis then the q-axis rotor flux λ_{qR}=0. So from the equations (33 and 36) described in the previous section and putting λ_{qR}=0, the electromagnetic torque of the motor in the vector control can be expressed as

$$T_e = \frac{3}{2}\left(\frac{p}{2}\right)\frac{L_M}{L_R}\left(\lambda_{dR} i_{qS}\right) \qquad (37)$$

If the rotor flux linkage λ_{dR} is not disturbed, the torque can be independently controlled by adjusting the stator q- component current i_{qS}. As the rotor flux aligned on d-axis, this leads to λ_{qR}=0 and λ_{dR}=λ_R, then

$$\omega_{sl} = \frac{L_M R_R}{\lambda_R L_R} i_{qS} \qquad (38)$$

6. Proposed SVM Technique for Two-Level Inverter

In this the space vector modulation algorithm for two level inverter is introduced for which the solar panels are connected to provide the dc supply. SVM basic principle and switching sequence is given in order to get symmetrical algorithm pulses and voltage balancing. This scheme is used to control the output voltage of the two level inverter with the T2NF based MPPT controller. In the SVM algorithm, the d-axis and q-axis voltages are converted into three-phase instantaneous reference voltages. Then the imaginary switching time periods proportional to the instantaneous values of the reference phase voltages. Which are defined as

$$T_{U1} = \left(\frac{T_S}{V_{DC}}\right)V_{U1}^*, T_{V1} = \left(\frac{T_S}{V_{DC}}\right)V_{V1}^*, T_{W1} = \left(\frac{T_S}{V_{DC}}\right)V_{W1}^*$$
$$(39)$$

where T_S and V_{DS} are the sampling interval time and dc link voltage respectively. Here the sampling frequency is the twice the carrier frequency.

Then the maximum (MAXI), middle (MID) and minimum (MINI) imaginary switching times can be in each sampling interval by using (40)-(42)

$$T_{MAXI} = MAXI(T_{U1}, T_{V1}, T_{W1}) \qquad (40)$$
$$T_{MINI} = MINI(T_{U1}, T_{V1}, T_{W1}) \qquad (41)$$
$$T_{MID} = MID(T_{U1}, T_{V1}, T_{W1}) \qquad (42)$$

The active voltage vector switching times T_1 and T_2 are calculated as

$$T_1 = T_{MAXI} - T_{MID} \text{ and } T_2 = T_{MID} - T_{MINI} \qquad (43)$$

The zero voltage vectors switching time is calculated as

$$T_Z = T_s - T_1 - T_2 \qquad (44)$$

The zero state time will be shared between two zero states as T_0 for V_0 and T_7 for V_7 respectively, and can be expressed as

$$T_0 = K_0 T_Z \qquad (45)$$
$$T_7 = (1 - K_0)T_Z \qquad (46)$$

Here K_0 is taken as 0.5 to obtain the SVM algorithm. The various SVM algorithms can be generated by changing K_0 between zero and one. However, in this SVM algorithm, the zero voltage vector time distributed equally among V_0 and V_7 as shown in Fig. 4.
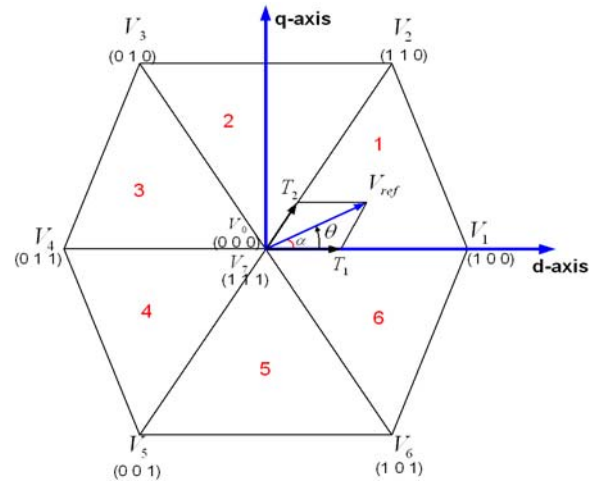
Fig. 4. Space vector diagram.

7. Proposed MPPT System with DC-DC Converter, Inverter and ASM Drive

The below system represents the proposed system structure with DC-DC converter. In this, PV array contains 6 PV modules with 250 Watts each; these modules are connected in series and parallel to yield better output voltage and current. The proposed type 2 neuro fuzzy (T2NF) based MPPT algorithm extracts the maximum power from solar PV array.

The point of operation of the PV array is adjusted by varying the duty cycle. DC-DC converter boosts the PV array voltage and also increases the maximum utilization of PV array by operating at MPP. Boost converter increases the array output voltage up to 400 Volts with the help of SVM based inverter. The minimum inductor value (L_{MIN}) is calculated from Eq. (47) to ensure the continuous inductor current.

$$L_{MIN} = \left(\frac{V_0(1-D)^2 \times D}{2}\right) \times f_S \times I_{AVG} \qquad (47)$$

where V_0 is the DC output voltage, D is the duty ratio, f_S is the switching frequency of the converter, I_{AVG} is the average output current. The minimum capacitance value (C_{MIN}) can be calculated using Eq. (48)

$$C_{MIN} = \frac{V_0 \times D}{R \times \Delta V_0 \times f_S} \qquad (48)$$

The switching frequency selection is trade-off between switching losses, cost of switch and the converter efficiency.

8. Results and Discussion

Simulation results are obtained under different operating conditions taking the reference value of speed as 1200 rpm. The results obtained with conventional MPPT and proposed type 2 neuro fuzzy (T2NF) based MPPT controller are given in Fig. 5-22.

8.1. Simulation Results of Asynchronous Motor Drive at starting

For the asynchronous motor drive the maximum current and the ripple content in the torque is reduced during starting in order to reach the early steady state. With the proposed type 2 neuro fuzzy (T2NF) based MPPT the maximum torque, stator phase current and the speed are obtained as 12.5 N-m, 20 Amps and 1200 RPM respectively. It is observed that the ripple content in the torque is reduced a lot compared to the other existed methods. Due to this better speed response is obtained. These results are presented in Figs. 5-7.
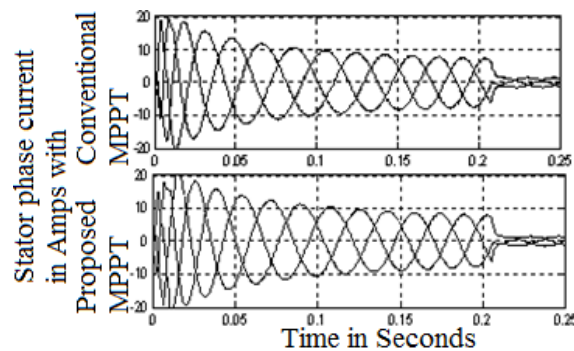
Fig. 5. Stator phase current responses with conventional and proposed T2NF based MPPT controller during starting.
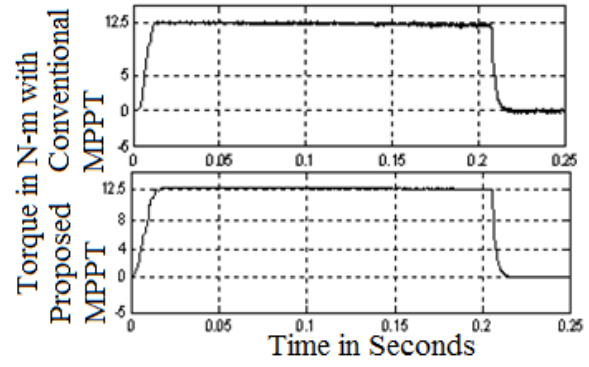
Fig. 6. Torque responses with conventional and proposed T2NF based MPPT controller during starting.
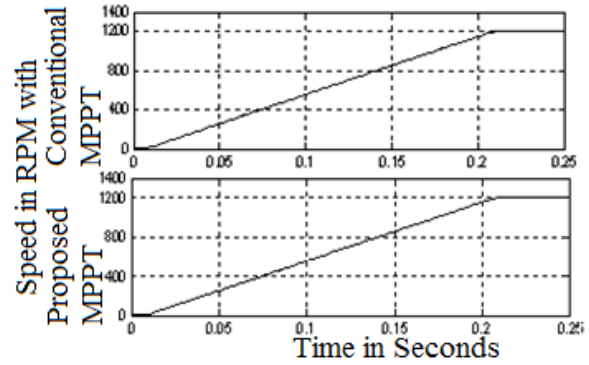
Fig. 7. Speed responses with conventional and proposed T2NF based MPPT controller during starting.

8.2. Simulation Results of Asynchronous Motor Drive at steady state condition

Here torque ripple with the proposed MPPT is reduced i.e. it is observed that the torque ripple with the conventional and proposed MPPT are 0.48 and 0.09 respectively. The better speed response is obtained with the proposed T2NF based MPPT controller. The steady state responses of the stator phase currents, torque and speed with conventional and proposed MPPT are observed in Figs. 8-10.
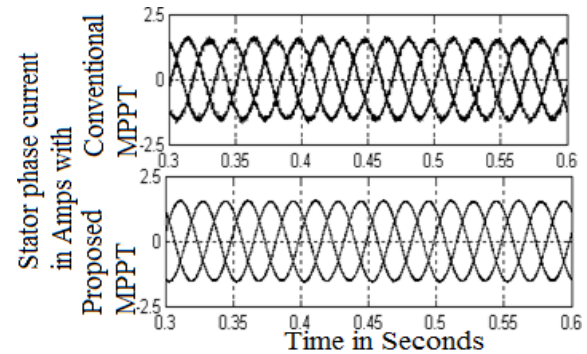
Fig. 8. Stator phase current responses with conventional and proposed T2NF based MPPT controller during steady state.
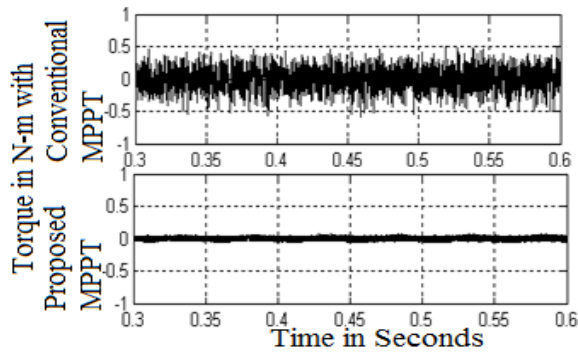
Fig. 9. Torque responses with conventional and proposed T2NF based MPPT controller during steady state.
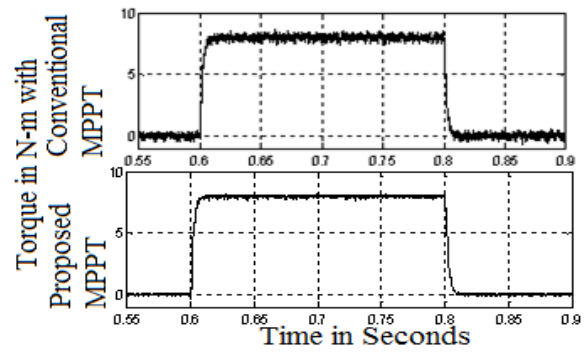
Fig. 12. Torque responses with conventional and proposed T2NF based MPPT controller during step change in load.
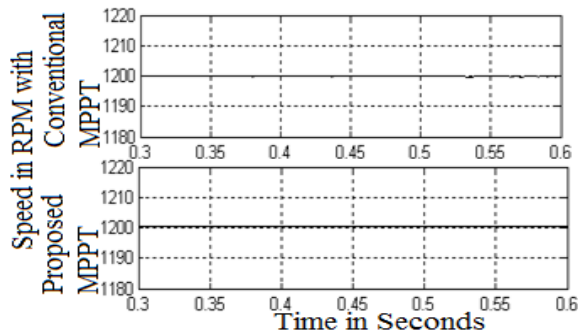
Fig. 10. Speed responses with conventional and proposed T2NF based MPPT controller during steady state.
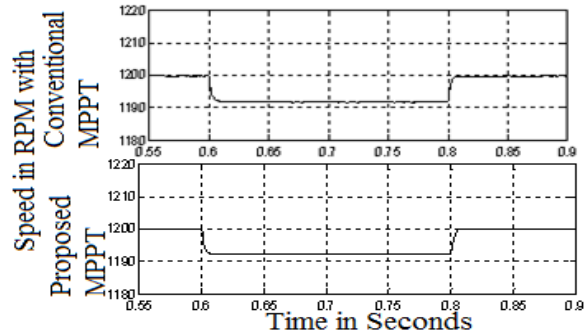
Fig. 13. Speed responses with conventional and proposed T2NF based MPPT controller during step change in load.

8.3. Simulation Results of Asynchronous Motor Drive at transients with step change in load

The ripple content in the current and torque is reduced with the proposed T2NF based MPPT. Also the speed decrement is little less with the proposed T2NF based MPPT during the load change. The response during the transients with step change in load torque of 8 N-m is applied at 0.6 sec and removed at 0.8 sec is shown in Figs. 11-13.
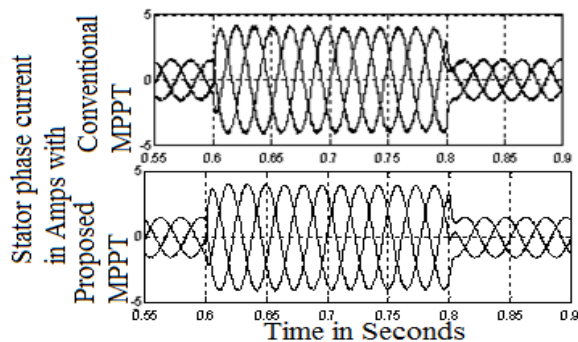
8.4. Simulation Results of Asynchronous Motor Drive at transients with the speed reversal operation from +1200 to -1200 RPM

The overall performance of the drive is improved with the proposed T2NF MPPT controller and the speed response reaches the reference value earlier compared to other existed methods. The results of the drive during speed reversals from +1200 to -1200 RPM are observed in Figs. 14-16.

Fig. 11. Stator phase current responses with conventional and proposed T2NF based MPPT controller during step change in load.
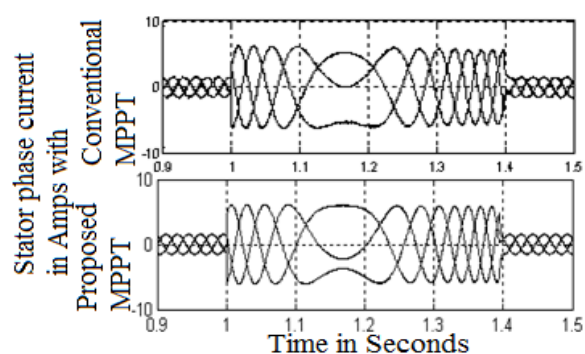
Fig. 14. Current responses with conventional and proposed T2NF based MPPT controller during transients at speed reversal from +1200 to -1200 RPM.
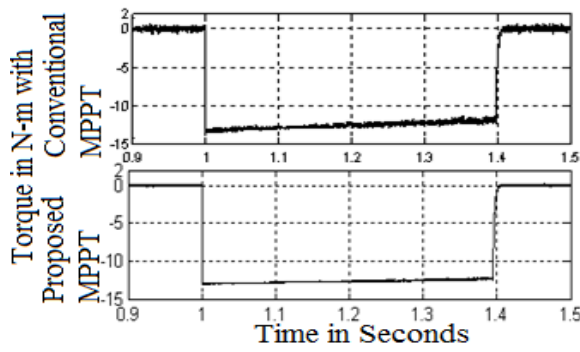
Fig. 15. Torque responses with conventional and proposed T2NF based MPPT controller during transients at speed reversal from +1200 to -1200 RPM.
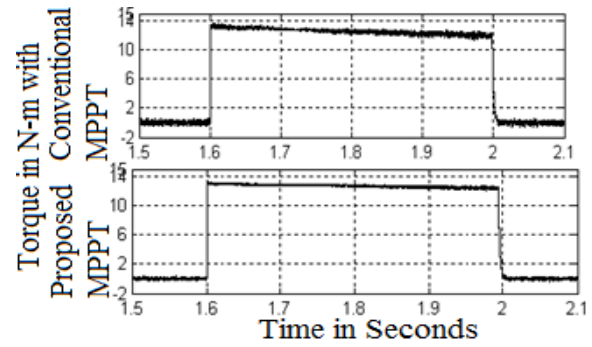
Fig. 18. Torque responses with conventional and proposed T2NF based MPPT controller during transients at speed reversal from -1200 to +1200 RPM.
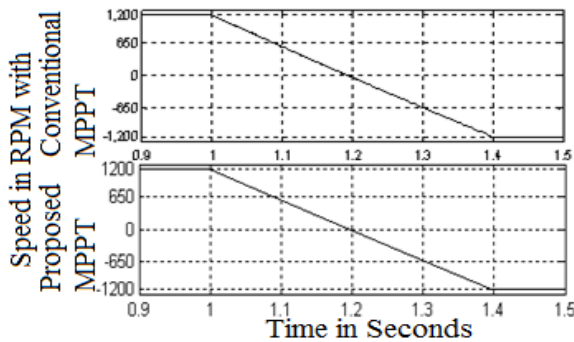
Fig. 16. Speed responses with conventional and proposed T2NF based MPPT controller during transients at speed reversal from +1200 to -1200 RPM.
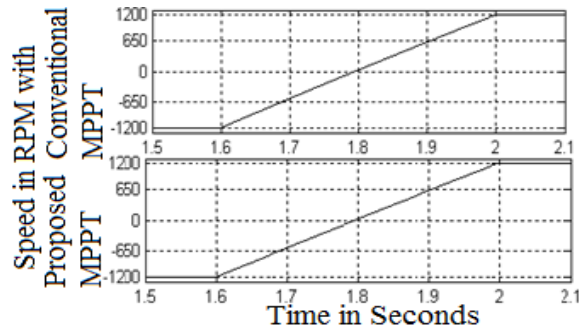
Fig. 19. Spedd responses with conventional and proposed T2NF based MPPT controller during transients at speed reversal from -1200 to +1200 RPM.

8.5. Simulation Results of Asynchronous Motor Drive at transients with the speed reversal operation from -1200 to +1200 RPM

The overall performance of the drive is improved with the proposed T2NF based MPPT controller and the speed response reaches the little earlier compared to conventional methods. The results of the drive during speed reversals from -1200 to +1200 RPM are observed in Figs. 17-19.
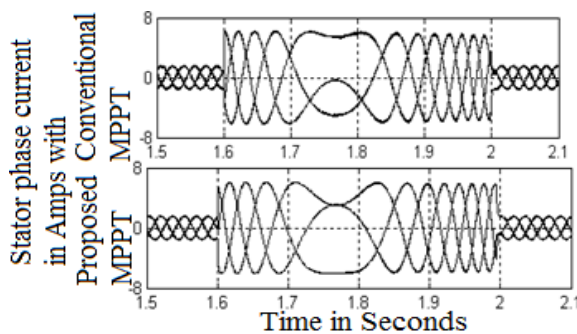
Fig. 17. Current responses with conventional and proposed T2NF based MPPT controller during transients at speed reversal from -1200 to +1200 RPM.

9. Conclusion

The PV array model with the type 2 neuro fuzzy (T2NF) based MPPT controller is tested. From this the performance of the asynchronous motor drive is analyzed with comparing the both conventional and proposed type 2 neuro fuzzy based MPPT controller results. Also the behavior of the proposed T2NF MPPT is observed with practical validations during a partially cloudy day. PV system with DC-DC boost converter and space vector modulation based technique inverter enhances the system performance even under abnormal weather conditions. The ripple contents in the torque and stator phase currents are reduced a lot with the proposed T2NF based MPPT controller. Here the early steady state response of the motor drive is reached along with attaining of better speed response. Thus the utilization and efficiency of the system is improved much with the proposed T2NF based MPPT controller.

Acknowledgement

References

[1]. O. Uncu and I. Turksen, Discrete interval type-2 fuzzy system models using unvertainty in learning raramenters, *IEEE Trans, Fuzzy Systems*, Vol. 15, No. 1, 2007, pp. 90-106.

[2]. L. Fangrui, D. Shanxu, L. Fei, L. Bangyin, and K. Yong, A variable step size INC MPPT method for PV systems, *IEEE Trans, Industrial Electronics*, Vol. 55, No. 7, 2008, pp. 2622–2628.

[3]. B. Pakkiraiah and G. Durga Sukumar, Research Survey on Various MPPT Performance Issues to Improve the Solar PV System Efficiency, *Journal of Solar Energy,* Vol. 2016, No. 2016, 2016, Article ID 8012432, pp. 1-20.

[4]. M. A. Masoum, H. Dehbonei, and E. F. Funchs, Theoretical and experimental analyses of photovoltaic systems with voltage and current-based maximum power point tracking, *Power Eng. Rev., IEEE*, Vol. 22, No. 8, 2002, pp. 62–62.

[5]. N. Femia, G. Petrone, G. Spagnuolo, and M. Vitelli, Optimizing duty cycle perturbation of P&O MPPT technique, in *Proceedings of the IEEE 35th Annu. Power Electron. Spec. Conf.,* Vol. 3, 2004, pp. 1939–1944.

[6]. B. Pakkiraiah and G. Durga Sukumar, A New Modified MPPT Controller for Solar Photovoltaic System, in *Proceedings of the IEEE International Conference on Research in Computational Intelligence and Communication Networks (ICRCICN)*, 2015, pp. 294-299.

[7]. M. F. Naguib and L. A. C. Lopes, Harmonics reduction in current source converter using fuzzy logic, *IEEE Transactions on Power Electronics*, Vol. 25, No. 1, 2010, pp. 158-167.

[8]. M. M. Rashid, N. A. Rahim, M. A. Hussain and M. A. Rahman, Analysis and experimental study of magnetorhological based damper for semiactive suspension system using fuzzy hybrids, *IEEE Transcations on Industrial Applications*, Vol. 47, No. 2, 2011, pp. 1051-1059.

[9]. M. Singh and A. Chandra, Appilcation of adaptive network- based fuzzy interface system for sensorless control of PMSG-based wind turbine with non linear load compensation capabilities, *IEEE Transactions on Power Electronics*, Vol. 26, No. 1, 2011, pp. 165-175.

[10]. B. N. Alajmi, K. H. Ahmed, S. J. Finney and B. W. Williams, Fuzzy-logic-control approach of a modified hill-climbing method for maximum power point in microgrid standalone system, *IEEE Transactions on Power Electronics*, Vol. 26, No. 4, 2011, pp. 1022-1030.

[11]. Alexis Kwasinski, Philip T. Krein, and Patrick L. Chapman, Time Domain Comparison of Pulse-Width Modulation Schemes, *IEEE Trans on Power Electronics*, Vol. 1, No. 3, 2003, pp. 64-68.

[12]. G. Narayanan, Di Zhao, Harish and K. Krishnamurthy, Space Vector Based Hybrid PWM Techniques for Reduced Current Ripple*, IEEE Trans. on Ind. Electron*, Vol. 55, No. 4, 2008, pp. 1614-1627.

[13]. I. Takahashi and T. Noguchi, A new quick-response and high- efficiency control strategy of an induction motor, *IEEE Trans. Ind. Appl.,* Vol. 22, No. 5, 1986, pp. 820–827.

[14]. Bimal K. Bose, Power Electronics and Motor Drives Advances and Trends, *Academic Press is an Imprint of Elsevier*, 2006.

[15]. B. Pakkiraiah and G. Durga Sukumar, A New Modified MPPT Controller for Improved Performance of an Asynchronous Motor Drive under Variable Irradiance and Variable Temperature, *International Journal of Computers and Applications-Taylor & Francis*, 2016, pp. 1-14.

[16]. Peter Vas, Sensor less Vector and Direct Torque Control, *Oxford University Press*, 1998.

[17]. D. Casadei, G. Serra, A. Tani, L. Zarri and F. Profumo, Performance analysis of a speed-sensor less induction motor drive based on a constant switching-frequency DTC scheme, *IEEE Trans. Ind. Appl.*, Vol. 39, No. 2, 2003, pp. 476–484.

[18]. N. N. Karnik, J. M. Mendel, and Q. Liang, Type-2 fuzzy logic systems, *IEEE Trans Fuzzy Systems*, Vol. 7, 1999, pp. 643-658.

[19]. J. M. Mendel and R. I. B. John, Type-2 fuzzy sets made simple, *IEEE Trans on Fuzzy System*, Vol. 10, 2002, pp. 117-127.

[20]. Q. Liang and J. M. Mendel, Interval type-2 fuzzy logic systems: Theory and design, *IEEE Trans on Fuzzy System*, Vol. 8, 2000, pp. 535 550.

[21]. Q. Liang, N. N. Karnik, and J. M. Mendel, Connection admission control in ATM networks using surveybased type-2 fuzzy logic systems, *IEEE Trans on Syst Man Cybern Part C*, Vol. 30, 2000, pp. 329-339.

[22]. Durga Sukumar, Jayachandranath Jitendranath and Suman Saranu, Three-level Inverter-fed Induction Motor Drive Performance Improvement with Neuro-fuzzy Space Vector Modulation, *Electrical Power Components and Systems-Taylor & Francis*, Vol. 42, No. 15, 2014, pp. 1633-1646.

[23]. B. Pakkiraiah and G. Durga Sukumar, A New Modified Adaptive Neuro Fuzzy Inference System Based MPPT Controller for the Enhanced Performance of an Asynchronous Motor Drive, in *Proceedings of the 1st International Conference on Advancement of Computer Communication & Electrical Technology (ACCET'16),* 21 – 22 October 2016.

—————————————

Harmonic Power Angle Monitoring for Unsymmetrical Fault Diagnosis in Distribution Network

**[1], * Debopoma KAR RAY, [2] Surajit CHATTOPADHYAY,
[3] Kaushik DAS SHARMA and [4] Samarjit SENGUPTA**

[1] EE Department, MCKVIE, 243, G.T. Road (N), Liluah, Howrah, 711204, India
[2] EE Department, GKCIET, TTC Campus, Maliha, Malda, W.B., 732102, India
[3, 4] Department of Applied Physics, University of Calcutta, 92, APC Road, Kolkata, 700009, India
* E-mail: debopoma86@gmail.com

Abstract: In this paper identification of a faulty load bus has been done in a multi-bus power system for double line fault, monitoring the feeder operating points and load angles in presence of various frequencies in harmonic P-δ plane. The usage of a new advanced variable slack bus incorporated converged power flow analysis determines the load angle, real power and feeder operating points for normal and fault in various load buses of the network in presence of some chosen harmonic frequencies in the system. The characteristic operating point shifting of the normal and fault operating points in normal and fault P-δ planes, determines the rule sets for identifying the fault buses in the grid system considered. This analysis can also be extended for other fault analysis in both online and offline conditions of the system.

Keywords: Fault detection, Harmonic power, Load angle, Line to line fault, Operating point, Stability zone.

1. Introduction

Interruption of supply systems is a common issue for industrial distribution networks, since the system is prone to various faults occurring in the grid system [1]. These faults have to be identified and mitigated far before the damage of a system, which requires the presence of fast fault detectors in the network. Least square error technique can be used for arcing fault detection and fault distance calculation, which can be tested on simulated as well as for laboratory experimental networks [2]. Symmetrical and Unsymmetrical fault assessment can be done in simulated systems by observing the voltage and current signatures of the load buses in the network [3]. An educational tool using FACTS devices, simulated in MATLAB, can be used for fault diagnosis, complex power flow studies [4]. Wavelet analysis can be done

for fault detection in single-core symmetrical phase shifting transformers [5]. A MATLAB based fault discrimination algorithm, based on Multi-Resolution analysis of discrete wavelet transform, can be used for fault detection in transmission systems [6]. Phasor Measurement units are suitable for fault detection and classification, using time synchronized values of current and voltage in digital form at normal and fault occurring in the system [7]. Single line to ground fault detection in wide area power system IEEE 14 bus network can be done using phasor data concentrator using WAMS technology [8]. A new relaying framework, using readings of the phase currents, during the first $1/4^{th}$ of a cycle in an integrated method combining symmetrical components with principle component analysis can be used for fault detection in a system [9]. Analysis shows the deviation in harmonic power, load angle and feeder operating

points at unsymmetrical fault in load bus of a system using a novel technique [10]. Identification of a faulty bus in a system can be done monitoring the operating points in P-delta plane [11]. None of the analysis, seen so far, deals with the double line (LL) fault identification, monitoring the load angle and feeder operating point shifting in harmonic P-δ plane to accurately depict which type of fault has actually occurred in the system at a specified bus.

In this work the technique proposed in [1] has been extended for double line fault identification in a multi-bus power system, monitoring the load angle and feeder operating point shifting in normal and harmonic P-δ planes. An advanced variable slack bus incorporated converged load flow solution is used for determination of the load angle and feeder operating points at normal and at LL fault, wherein the deviation of feeder operating points were assessed in normal and harmonic P-δ planes to depict the faulty bus in the network.

2. Fault Bus Identification Using Harmonic Power Versus Delta Plane

The fault bus identification technique has been implemented on a modeled IEEE 9 bus system with conventional line and bus data for acquiring the system data at line to line (LL) fault in a chosen load bus of the system, in presence of various harmonic frequencies in the network. The modeled network has been presented in Fig. 1.

However this analysis technique can also be implemented for other standard transmission and distribution systems, since this analysis technique has been checked with other standard bus systems for different unsymmetrical faults occurring in the network. In this analysis, the fault restoration time has not been considered.

Here 5th, 7th and 11th harmonic frequencies have been used to justify the effect of these frequencies in the detection of remote end faults in the system with the developed P-δ plane analysis technique. These frequencies were chosen since benchmark report, IEEE Std. 1459-2010 [12], uses some of these arbitrary frequency values for determining the performance of multi-bus power system networks.

The fault data obtained from the above analysis was used for building the harmonic P-δ planes at LL fault in buses 6 and 8 of the system in presence of certain harmonic frequencies in the system. The algorithm of the developed analysis technique has been shown in Fig. 2.

The real power, load angle and feeder operating points of 9-8 feeder has been analyzed at fault in buses 6 and 8, considered only one at a time, in presence of some chosen harmonic frequencies (5th, 7th and 11th). The data of the above analysis has been shown in Table 1- Table 2. In Table 1 - Table 2, "F" denotes the frequency values, "h" denotes the data at healthy condition of the system, "f_{LL6}" and "f_{LL8}" denotes the data of the system at fault in buses 6 and 8 considered one at a time.

From the data obtained in Table 1 - Table 2, harmonic P-δ curves have been developed (Fig. 3), wherein the feeder operating points have been placed.
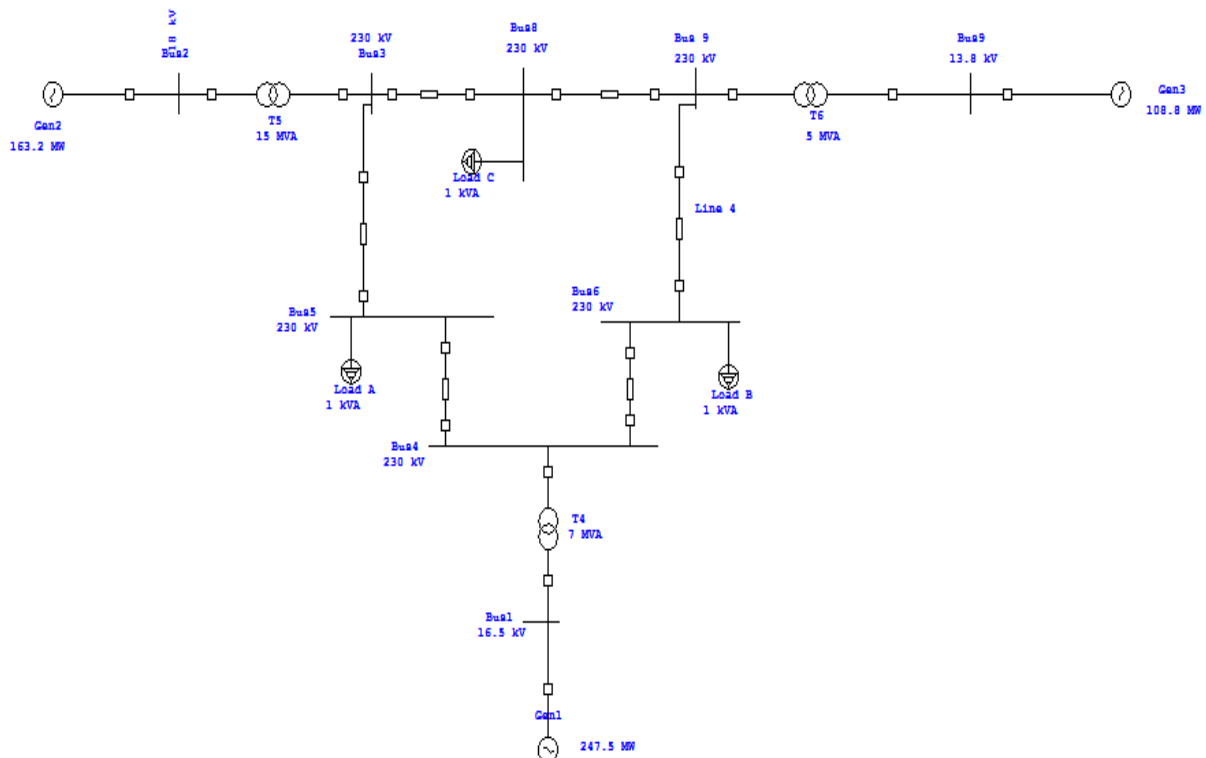
Fig. 1. IEEE 9 bus system model for analysis purpose.
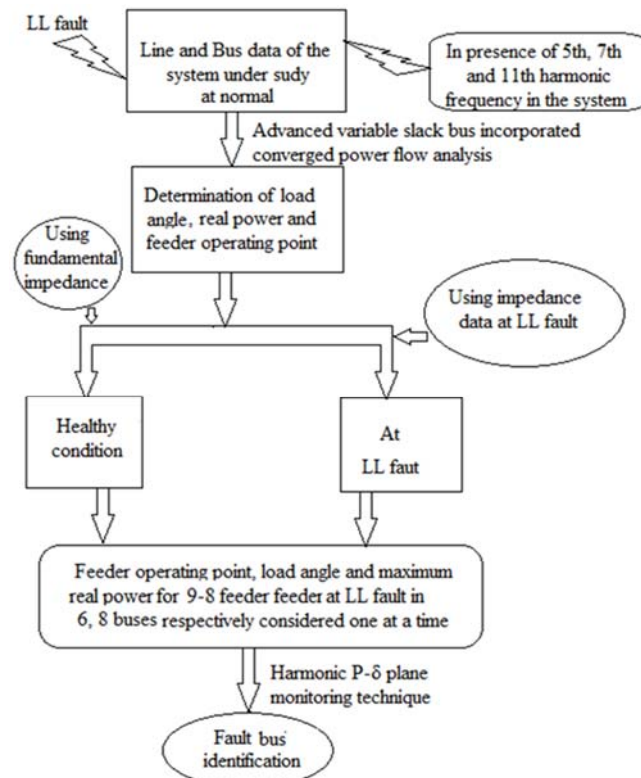
Fig. 2. LL fault analysis technique using harmonic P-δ plane.
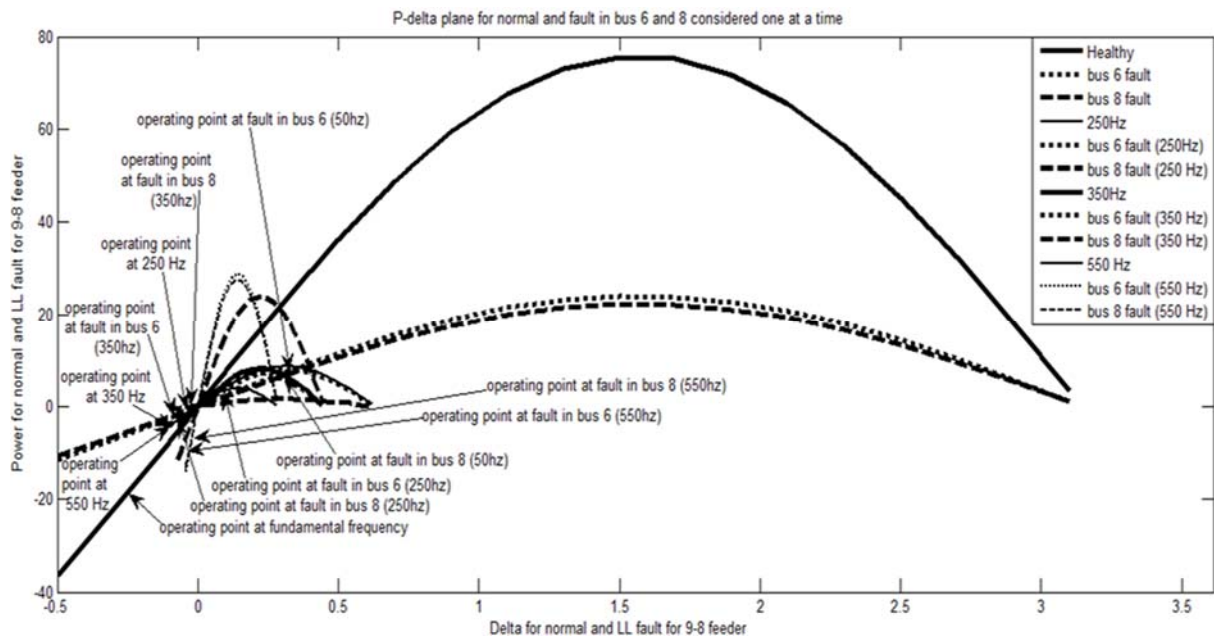
Fig. 3. Harmonic P-δ plane for 9-8 feeder at LL fault in Bus 6, 8 considered one at a time in presence of fundamental, 5th, 7th and 11th harmonic frequency.

Table 1. Study of maximum real power at LL fault in buses 6 and 8.

F (Hz)	Changes Observed		
	P_{max} (MW)		
	h	f_{LL6}	f_{LL8}
50	75.79	24	22.26
250	8.8	8	1.51
350	8.15	7	23.87
550	3.96	28.86	27.56

Table 2. Study of load angle and feeder operating points at LL fault in buses 6 and 8.

F (Hz)	Changes Observed					
	P (MW)			δ (radian)		
	h	f_LL6	f_LL8	h	f_LL6	f_LL8
50	-18.31	6.07	5.75	-0.5	0.7	0.8
250	0.948	4	-1.84	6.18	3.19	-3.19
350	-4.89	-3.41	-2.42	-6.18	-3.1	-3.18
550	-3.5	-15.12	-14.3	-3.26	-3.11	-3.2

The P-δ curves were plotted from the concept of occurrence of individual harmonic frequencies in a system [10-11]. The deviation of the feeder operating points and the change in direction of load angle of the feeders has been identified for depicting the faulty bus in the system. In this developed P-delta plane, the conventional positive P-delta curve was improvised and negative P-delta characteristics have been introduced, to detect the stable and unstable operating zones of the respective feeder under analysis.

3. Exact Fault Bus Identification and Related Stability Assessment

The data obtained from Table 1 - Table 2 and the Fig. 3 has been analyzed to extract some feature for depicting the fault bus in the system. Monitoring the operating points at normal and at fault, operating zone of the feeders were identified and depending on the changes obtained in the load angles at fault from normal rule sets have been developed for exact fault bus identification in the system, which has been presented in Table 3 - Table 4.

4. Specific Outcome of the Analysis

This analysis shows how a faulty load bus can be identified in a multi-bus power system, monitoring the feeder operating points and load angle change in normal and fault P-δ planes. Here, advanced variable slack bus incorporated converged power flow analysis has been used for finding the bus voltages, load angles and real powers at normal and at fault. Table 3 - Table 4, clearly shows that, for 9-8 feeder the power flow direction reverses from healthy condition both for fault in bus 6 and bus 8, but if the feeder operating point can be assessed in P-δ plane it can be seen that the deviation of feeder operating point at fault in bus 8 is much more that for fault in bus 6. Depending on the change in sign of load angle of the system a logic has been developed to clearly depict the LL fault bus in the system, which has been depicted in Table 4. In Table 4, 'N' denotes negative and 'P' denotes positive. Thus, code 'NPNN' denotes the system is healthy, 'PPNN' denotes LL fault in bus 6 and 'PNNN' denotes LL fault in bus 8.

Table 3. Stability assessment for the system at normal and at LL fault in buses 6, 8.

Frequency	Location of operating points		
	At healthy condition	At fault in bus 6	At fault in bus 8
50 Hz	Stable motoring zone	Stable generating zone	Stable generating zone
250 Hz	Stable generating zone	Stable generating zone	Stable motoring zone
350 Hz	Stable motoring zone	Stable motoring zone	Stable motoring zone
550 Hz	Stable motoring zone	Stable motoring zone	Stable motoring zone

Table 4. Identification of Exact Fault bus in the system.

Operating conditions	Changes in δ				Logic
	50 Hz	250 Hz	350 Hz	550 Hz	
Healthy system	-	+	-	-	[NPNN]
LL fault in bus 6	+	+	-	-	[PPNN]
LL fault in bus 8	+	-	-	-	[PNNN]

5. Conclusions

This paper presents a novel technique for identifying the faulty bus in a multi-bus power system, monitoring the deviation in the feeder operating points and corresponding load angles in normal and fault P-δ planes. Previously some analysis done [1] has been extended in this research and it has also been seen that for line to line fault, occurring in a load bus, the harmonic and fault power magnitudes sometimes becomes larger than fundamental power magnitudes in P-δ planes and there lies a wide range of variation of the feeder operating points in P-δ planes from -90° to +90° for LL fault in different load buses of the system.

Thus this analysis is well suitable for fault bus identification, monitoring the feeder operating points and the direction of power flow in a multi-bus power system in a specific zone of operation of the network.

Acknowledgements

References

[1]. D. Kar Ray, S. Chattopadhyay, K. Das Sharma, S. Sengupta, Line-to-Line Fault Detection in a Multi-Bus Power System by Harmonic Analysis, in *Proceedings of the Advancement of Computer Communication and Electrical Technology (ACCET'16)*, 2016, pp. 89-92.

[2]. M. B. Djuric, Z. M. Radojevic, V. V. Terzija, Arcing faults detection on transmission lines using least error squares technique*, International Transactions on Electrical Energy Systems*, Vol. 8, Issue 6, 1998, pp. 437-443.

[3]. P. Pooja, K. R. Preethi, H. R. Chetan, B. M. Nandish, Three phase transmission line fault analysis using MATLAB Simulink, *International Journal of Scientific Development and Research*, Vol. 1, Issue 5, 2016, pp. 376-378.

[4]. Tetiana Brockhoeft, Educational Modeling for FaultAnalysis of Power systems with STATCOM controllers using Simulink, *University of New Orleans Theses and Dissertations*, 2014.

[5]. Meenakshi Sahu, Rahul Rahangdale, Faults Detection in Single-Core symmetrical Phase shifting Transformers Based on Wavelets, *International Journal of Electrical, Electronics and Computer Systems*, Vol. 4, Issue 4, 2016, pp. 22-27.

[6]. P. Srinivasa Rao, B. Baddu Naik, Pattern Recognition Approach for Fault Identification in PowerTransmission Lines, *International Journal of Engineering Research and Applications,* Vol. 3, Issue 5, 2013, pp. 1051-1056.

[7]. C. Anil Kumar, K. Lakshmi, Monitoring and detectionof fault using phasor measurement units, *International Journal of Electrical, Electronics and Mechanical Controls,* Vol.3, Issue 2, 2014.

[8]. Surender Kumar, M. K. Soni, D. K. Jain, Monitoring of wide area power system network with phasor data concentrator, *International Journal of Information Engineering and Electronic Business,* Vol. 5, 2015, pp. 20-26.

[9]. Qais Alsafasfeh, Ikhlas Abdel-Qader, Ahmad Harb, Symmetrical pattern and PCS based framework for fault detection and classification in power systems, in *Proceedings of IEEE International Conference on Electro/Information Technology,* 2010, pp. 1-5.

[10]. D. Kar Ray, S. Chattopadhyay, K. Das Sharma, S. Sengupta, Assessment of Harmonic Voltage angles in a multi-bus power system during symmetrical fault at certain bus, in *Proceedings of the Michel Faraday IET International Summit (MFIIS'1*5), Kolkata, India, 2015, pp.243-248.

[11]. D. Kar Ray, S. Chattopadhyay, K. Das Sharma, S. Sengupta, Identification of Faulty Load bus in a Multi-Bus Power System,in *Proceedings of the 2nd International Conference on Control, Instrumentation, Energy & Communication (CIEC),*2016, pp. 289-293.

[12]. Standard Definitions for Measurement of Electric Power Quantities under Sinusoidal, Non-Sinusoidal, Balanced or Unbalanced Conditions, IEEE Standard 1459-2010.

_____

Generator Rescheduling under Congested Power System with Wind Integrated Competitive Power Market

*** Sadhan Gope, Arup Kumar Goswami and Prashant Kumar Tiwari**
National Institute of Technology, Silchar, Assam-788010, India
* Tel.: +91 9485074442, fax: 03892330834
* E-mail: sadhan.nit@gmail.com

Abstract: Integration of renewable energy like wind or solar energy creates a huge pressure to the system operator (SO) to ensure the congestion free transmission network under deregulated power market. Congestion Management (CM) with integration of wind farm in double auction electricity market are described in this work to minimize fuel cost, system losses and locational marginal price (LMP) of the system. Location of Wind Farm (WF) is identified based by using Bus sensitivity factor (BSF), which is also used for selection of load bus for double auction bidding (DAB). The impacts of wind farm in congested power system under deregulated environment have been investigated in this work. Modified 39-bus New England test system is used for demonstrate the effectiveness of the presented approach by using Sequential Quadratic Programming (SQP).

Keywords: Double auction bidding (DAB), Congestion Management (CM), Wind Farm (WF), Bus sensitivity factor (BSF), Locational marginal price (LMP), Sequential Quadratic program (SQP).

1. Introduction

The power transmission has been greatly affected after introduction of privatization and deregulation in power sector. The transaction in electricity has increased exponentially due to the competition in power market trading. GENCOs and DISCOS, in the deregulated power market, can independently or in pair transmit power. This may lead to a condition were an unanticipated direction, volume and length of power flow through the transmission networks. Such trade of power may not be accommodated by the present transmission network. As result congestion occurs in the system which may create violation of the system security also. Congestion is usually occurs in modern power system transmission line due to increase in electric power demand or line outage of the system [1].

In [2] optimal bidding strategy of a supplier has been discussed considering double sided bidding. It is very much essential to have maintained security of power system fairly for the continuity of power supply to the consumers with minimum price in deregulated market. Optimal bidding strategy for electricity suppliers under the congestion environment has been discussed in [3]. Bidding strategy is utilized to maximize the profit by using the Refined Immune Algorithm. Electrical market is settled based on the Locational marginal price (LMP) of the system. Optimal GENCOs bidding strategies of electricity market has been established by using Agent-based approach and numerical sensitivity analysis (NSA) technique [4].

The reference [5] describes the bidding strategy in a joint spinning reserve market and day-ahead energy market with integration of micro grid. The optimal cost of energy and spinning reserve bids are obtained by solving the bi-level bidding model using Interior point algorithm. The optimal bidding for the power market is depends on the bidding revenue, expected

imbalance and operation cost. Paper [6] presents an auction based market for consumer payment minimization under pool based day-a-head electricity market. A bi-level programming method has been used to characterize locational marginal price. Demand side bidding strategies are applied in electricity market to minimize the cost of purchasing power [7-8]. Flexible AC Transmission System (FACTS) devices like TCSC and SSSC are used to maximize the social welfare in double sided auction market [9].

Wind energy sources have become one of the rapid increasing energy sources in the world. Wind power heavily relies on the environmental conditions, therefore produce unpredictable output power. The reference [10-12] narrates wind and hydro power generation plays an important role in deregulated electricity market. Three bidding strategies are used to formulate the day-ahead bidding model. In the paper [13] author consider the wind energy for congestion management.

The main contribution of this paper is to integrate wind farm considering double auction bidding in power market to minimize the congestion as well as minimize the LMP of the system. With considering the cost function, GENCOs and DISCOs are participating in the pool market and they are maximizing their generation as well as minimizing the overall generation cost of the system. Wind Farm (WF) position in the bus is identified based on the BSF value. In this paper, modified 39-bus New England test system is used as a test system for solving the proposed method.

2. Problem Formulation

The objective function of this problem is to minimize the total fuel cost of thermal generating unit, minimize congestion cost and investment cost of WF connected to the system. Consider N numbers of WF are installed in existing power system network. As a result, the proposed objective function consists of three terms. Mathematically, the objective function of the presented approach is as follows:

$$OF = \sum_{i=1}^{NG} C_i(P_{Gi}) + \sum_{j=1}^{NG} C_j(\Delta P_G) + \sum_{k=1}^{N} C_{WF}(k), \quad (1)$$

where NG is equal to the number of generators, NL is equal to the number of loads, $C_i(P_{Gi})$ is equal to the generating cost of thermal unit, $C_j(\Delta P_G)$ is equal to the congestion cost, C_{WF} is equal to the installation cost of the wind farm.

2.1. Constraint

Following two types of constraints are used in Optimal Power Flow.

2.1.1. Equality Constraint

2.1.1.1. Real Power Balance Equations

$$\sum_{i=1}^{NG} P_{Gi} + P_{WF} - P_{loss} - P_D = 0, \quad (2)$$

$$\sum_{i=1}^{NG} \Delta P_{Gi} = 0, \quad (3)$$

$$P_{loss} = \sum_{J=1}^{TL} G_J \left[|V_i|^2 + |V_j|^2 - 2|V_i||V_j| Cos(\delta_i - \delta_j) \right], \quad (4)$$

where P_G is equal to the active power generation of thermal generating unit, P_{WF} is equal to the total wind power generation of wind farm, P_{loss} is equal to the transmission loss, P_D is equal to the total load, T_L is equal to the number of transmission lines, G_J is equal to the conductance of the line between buses i and j, $|V_i|$ is equal to the voltage magnitude, δ_i is equal to the voltage angle

2.1.1.2. Power Flow Equations

$$P_i - \sum_{k=1}^{BN} |V_i V_k Y_{ik}| Cos(\theta_{ik} - \delta_i + \delta_k) = 0, \quad (5)$$

$$Q_i + \sum_{k=1}^{BN} |V_i V_k Y_{ik}| Sin(\theta_{ik} - \delta_i + \delta_k) = 0, \quad (6)$$

where P_i and Q_i are the injected active and reactive power into the system, BN is equal to the number of buses, Y_{ik} is equal to the bus admittance matrix connected between i^{th} row and k^{th} column, θ_{ik} is equal to the bus admittance matrix connected between i^{th} row and k^{th} column.

2.1.2. Inequality Constraint

2.1.2.1. Bus Voltage Limits

$$V_i^{min} \le V_i \le V_i^{max} \qquad i = 1, 2, 3, ... N, \quad (7)$$

where V_i^{min} is equal to the lower limit of bus voltage, V_i^{max} is equal to the upper limit of bus voltage, N is equals the number of buses.

2.1.2.2. Power Limit of Generators

$$Q_{Gi}^{min} \le Q_{Gi} \le Q_{Gi}^{max} \qquad i = 1, 2, 3, ... N, \quad (8)$$

$$P_{Gi}^{min} \le P_{Gi} + \Delta P_{Gi} \le P_{Gi}^{max} \qquad i = 1, 2, 3, ... N, \quad (9)$$

where PG_i^{min}, PG_i^{max} is equal to the thermal unit minimum and maximum active power limit, QG_i^{min}, QG_i^{max} is equal to the thermal unit minimum and maximum reactive power limit.

2.1.2.3. Security Limit of Transmission Lines

$$\left| MVA\ flow_{i,j}^0 \right| \le MVA\ flow_{i,j}^0 \max_0 \quad MVA\ flow_{i,j}, i \ne j \text{，} \quad (10)$$

$$\left| MVA\ flow_{i,j}^k \right| \le MVA\ flow_{i,j}^k \max_k \quad MVA\ flow_{i,j}, i \ne j \text{，} \quad (11)$$

where MVA flow$_{ij}$ max$_0$ and MVA flow$_{ij}$ max$_k$ are represent the maximum power that can flow through the line connecting the buses i & j, during the pre-congestion and post congestion state.

2.1.2.4. Discrete Tap Setting of Transformer

$$T_i^{\min} \le T_i \le T_i^{\max} \qquad i = 1, 2, 3, ...N \qquad (12)$$

2.1.2.5. Ramp Limit of Generators

$$P_{Gi} - P_{Gi}^{\min} = \Delta P_{Gi}^{\min} \le \Delta P_{Gi} \le \Delta P_{Gi}^{\max} = P_{Gi}^{\max} - P_{Gi} \quad , \\ i = 1, 2, 3......N \qquad (13)$$

where $PG_i^{\min}$, $PG_i^{\max}$ is equal to the thermal unit minimum and maximum active power limit.

2.2. Bus Sensitivity Factor (BSF)

Bus sensitivity factor for a congested line is calculated by using following formula [13].

$$BSF_k^l = \frac{\Delta P_{ij}}{\Delta P_k}, \qquad (14)$$

where ΔP_{ij} is equals to the change in real power flow of line k, BSF_k^l is equals to the change in active power flow in the congested line *l* due to active power injection at bus k.

The details derivation of BSF is given in [14].

3. Result and Discussion

The proposed concept has been illustrated on modified 39 bus New England Test System which is having 10 generators and 29 load buses. The data for 39 bus New England system has taken from ref [15]. In the proposed method violation on line 15-16 has been created due to the 14-34 line outages in the system. In this presented approach 50MW of WF power is connected based on the BSF value. It has been found from the reference paper [16] that the investment cost of wind power generator (for 1 MW capacity) is 3.75 \$/hr (approx.). So for 50MW wind power cost 187.50 \$/hr has been added to the bidding

optimal cost of wind power condition. Two most sensitive bus i.e. one positive and one negative bus have been selected for analyzing the proposed method. Out of this two, one sensitive bus is selected for double auction bidding and another one is connected with wind farm. Congestion problem solves by using Sequential Quadratic programming (SQP) approach, which is also used for minimizing the fuel cost of the thermal generating unit.

Based on the bus sensitivity factor, here two cases are analyzed. Firstly, WF connected at bus number 14 and double auction bidding (DAB) at bus number 34 and secondly WF connected at bus number 34 and DAB at bus number 14.

In the present study, violation occurs in L 15-16 due to the line outage L14-34. So the line L15-16 is called congested line. Bus Sensitivity Factor (BSF) is calculated for congested line L 14-34 and some of the selected BSF value is shown in Table 1.

Table 1. Some selected BSF for congested line (15-16).

Bus No.	BSF	Bus No.	BSF
1	0	22	0.1543
2	-0.0334	24	0.1537
6	0.1547	26	0.0307
8	-0.0181	28	0.0325
9	0.0332	30	0.1539
12	-0.0379	33	0.2575
13	-0.0655	34	0.4196
14	-0.2536	35	0.2326
16	-0.0047	37	0.0796
20	0.1943	39	0.1538

Firstly, WF connected at bus number 14 and DAB has been done at bus number 34 with a load of 60MW and corresponding optimal power cost and losses are presented in Table 3.

Secondly, wind farm connected at bus number 34 and DAB has been done at bus number 14 with a load of 500MW and corresponding optimal cost and losses are presented in Table 5.

Table 2 shows the power flow through congested line before and after single auction bidding (SAB) and DAB with and without considering WF. From the result, it is seen that that after bidding active power flow through congested line (L 15-16) has reduced from the maximum level to reliable margin.

Table 2. Congested line power flow before and after bidding when WF is connected at bus No. 14.

Power Flow	Before SAB (MVA)	After SAB (MVA)	After SAB with WF (MVA)
L (15-16)	576.92	496.43	496.20
Power Flow	**Before DAB (MVA)**	**After DAB (MVA)**	**After DAB with WF (MVA)**
L (15-16)	576.92	496.43	496.93

Table 3 shows the optimal fuel cost of thermal generating unit with and without considering WF (bus No. 14) for SAB and DAB. From Table 3, it is seen that optimal generation cost with line outage using SAB is 42169.21 $/hr and losses is 54.715 MW, where as optimal generation cost with line outage by using DAB is 41399.62 $/hr and losses is 54.583 MW. From Table 3, it is also seen that optimal generation cost with line outage and with WF by using SAB is 41571.81 $/hr and losses is 52.586 MW, where as optimal generation cost with line outage and with WF by using DAB is 40798.26 $/hr and losses is 52.524 MW.

Fig. 1 shows the locational marginal price with and without considering WF at bus No. 14 and DAB at bus No. 34. It has been seen from Fig. 1 that LMP decreases with integration of WF compare to without WF in both SAB and DAB case.

Table 3. Optimal cost for SAB and DAB with and without presence of WF (bus No. 14) for 14-34 line outages.

Control Variable	Result reported [17]	SAB without line outage	SAB with line outage	SAB with WF and line outage	DAB with line outage	DAB with WF and line outage
PG1 (MW)	604.47	677.00	593.76	609.80	572.80	590.55
PG2 (MW)	646.00	689.42	737.20	715.24	733.09	711.74
PG3 (MW)	715.41	673.21	610.16	619.84	591.88	603.05
PG4 (MW)	652.00	646.73	652.00	648.04	651.41	641.23
PG5 (MW)	508.00	508.00	508.00	508.00	508.00	508.00
PG6 (MW)	687.00	657.45	670.48	658.63	662.30	651.55
PG7 (MW)	580.00	580.00	580.00	580.00	580.00	580.00
PG8 (MW)	564.00	564.00	564.00	564.00	564.00	564.00
PG9 (MW)	667.79	637.50	671.89	655.13	667.08	651.17
PG10 (MW)	674.44	669.10	721.46	698.14	718.26	695.48
Gen Cost ($/h)	41941.34	41932.73	42169.21	41571.81	41399.62	40798.26
Losses (MW)	44.88	48.180	54.715	52.586	54.583	52.524
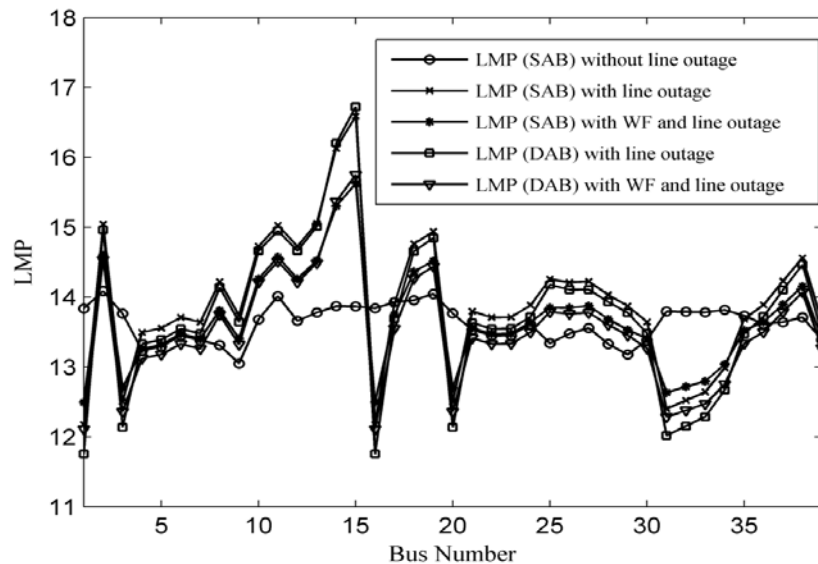
Fig. 1. Locational Marginal Price (LMP) with WF (bus No. 14).

Table 4 shows the power flow through congested line 15-16 before and after SAB and DAB with and without considering WF at bus No. 34. From this Table 4, it is observed that congested line power flow reaches very reliable margin with DAB case compare to SAB case.

Table 5 shows the optimal fuel cost of thermal generating unit with and without considering WF (bus No. 34) for SAB and DAB case. From Table 5, it is seen that optimal generation cost with line outage using SAB is 42169.21 $/hr and losses is 54.715 MW, where as optimal generation cost with line outage by

using DAB is 35396.39 $/hr and losses is 40.515 MW. From Table 5, it is also seen that optimal generation cost with line outage and with WF by using SAB is 41713.89 $/hr and losses is 54.647 MW, where as optimal generation cost with line outage and with WF by using DAB is 34975.52 $/hr and losses is 40.085 MW. From the Table 3 and Table 5, it is concluded that, with increasing DAB power, optimal generation cost and losses are reducing. Fig. 2 shows the locational marginal price with and without considering WF at bus No. 34 and DAB at bus No. 14. It has been seen from Fig. 2 that LMP decreases with integration of WF in DAB case compare to SAB case

Table 4. Congested line power flow before and after bidding when WF is connected at bus No. 34.

Power Flow	Before SAB (MVA)	After SAB (MVA)	After SAB with WF (MVA)
L (15-16)	576.92	496.43	496.38
Power Flow	Before DAB (MVA)	After DAB (MVA)	After DAB with WF (MVA)
L (15-16)	576.92	356.77	365.43

.

Table 5. Optimal cost for SAB and DAB with and without presence of WF (bus No. 34) for 14-34 line outages.

Control Variable	SAB with line outage	SAB with WF and line outage	DAB with line outage	DAB with WF and line outage
PG1(MW)	593.76	576.37	600.28	593.31
PG2(MW)	737.20	733.65	614.23	607.43
PG3(MW)	610.16	594.91	596.70	589.53
PG4(MW)	652.00	651.91	578.05	571.65
PG5(MW)	508.00	508.00	508.00	508.00
PG6(MW)	670.48	663.60	586.13	579.53
PG7(MW)	580.00	580.00	579.97	576.23
PG8(MW)	564.00	564.00	564.00	564.00
PG9(MW)	671.89	667.78	571.64	565.55
PG10(MW)	721.46	718.66	595.74	589.10
Gen Cost($/h)	42169.21	41713.89	35396.39	34975.52
Losses(MW)	54.715	54.647	40.515	40.085
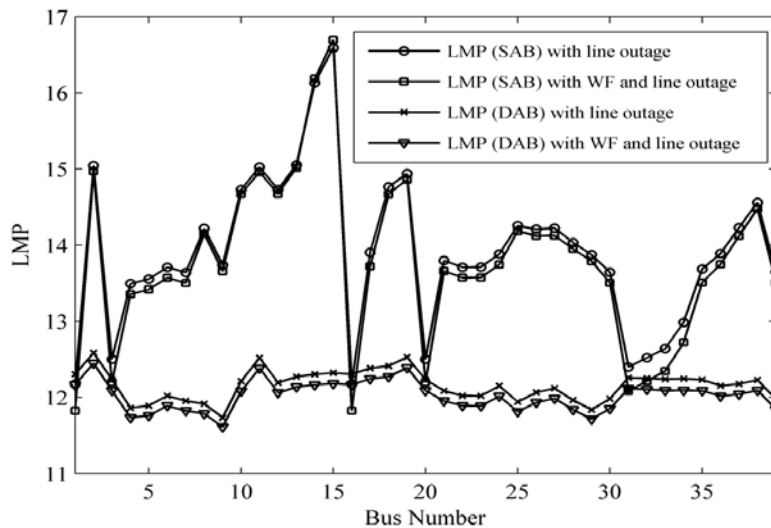
Fig. 2. Locational Marginal Price (LMP) with WF (bus No. 34).

4. Conclusion

The effectiveness of WF integrated competitive power market to alleviate transmission congestion has been investigated in this paper. To mitigate transmission congestion, optimal generation cost and losses are found minimum with DAB with WF integrated system compared to that of SAB with WF integrated system for mitigation transmission congestion. It is also investigates that LMP is minimum with presence of wind farm in the case DAB compared to SAB case. Sequential Quadratic programming (SQP) is used for implementing the proposed method and modified 39 bus New England test system is used for analysis of the proposed approach.

References

[1]. Sudipta Dutta, S. P Singh, Optimal rescheduling of generators for congestion management based on particle swarm optimization, *IEEE Transaction on Power System,* Vol. 23, Issue 4, 2008, pp. 1560-1569.

[2]. Arvind Kumar Jain, Suresh Chandra Srivastava, Niwas Singh, Laxmi Srivastava, Bacteria Foraging optmization based bidding strategy under transmission congestion, *IEEE System Journal*, Vol. 9, Issue 1, 2015, pp. 141-151.

[3]. Tengshum Peng, Kevin Tomsovic, Congestion influence on bidding strategies in an electricity market, *IEEE Transaction on Power System*, Vol. 18, Issue 3, 2003, pp. 1054-1061.

[4]. M. Mahvi, M. M Ardehali, Optimal bidding strategy in a competitive electricity market based on agent-based approach and numerical sensitivity analysis, *Energy*, Vol. 36, Issue 11, 2011, pp. 6367-6374.

[5]. L. Shi, Y. Luo, G. Y. Tu, Bidding strategy of micro grid with consideration of uncertainty for participating in power market, *Electrical Power and Energy Systems,* Vol. 59, 2014, pp. 1-13.

[6]. Ricardo Fernández-Blanco, José M. Arroyo, Natalia Alguacil, Network-Constrained Day-Ahead Auction for Consumer Payment Minimization, *IEEE Transactions on Power Systems*, Vol. 29, Issue 2, 2014, pp. 526-536.

[7]. Rico Herranz, Antonio Munoz San Roque, Jose Villar, Fco Alberto Campos, Optimal demand-side bidding strategies in Electricity spot market, *IEEE Transaction on Power System*, Vol. 27, Issue 3, 2012, pp. 1204-1213.

[8]. Faria Nassiri Mofakham, Mohammad Ali Namatbakhsh, Ahmad Baraani Dastjerdi, Nasser Ghasem Aghaee, Ryszard Kowalczyk, Bidding strategy for agent in multi-attribute combinational double auction, *Expert Systems with Application*, Vol. 42, Issue 6, 2015, pp. 3268-3295.

[9]. S. M. H. Nabavi, A. Kazemi, M. A. S. Masoum, Social welfare maximization with fuzzy based genetic algorithm by TCSC and SSSC in double-sided auction market, *Scientia Iranica, Computer Science & Engineering and Electrical Engineering*, Vol. 19, Issue 3, 2012, pp. 745-758.

[10]. Agustín A. Sánchez de la Nieta, Javier Contreras, José Ignacio Muñoz, Optimal Coordinated Wind-Hydro Bidding Strategies in Day-Ahead Markets, *IEEE Transactions on Power Systems*, Vol. 28, Issue 2, 2013, pp. 798-809.

[11]. Mahmoud Ghofrani, Amirsaman Arabali, Mehdi Etezadi-Amoli, Mohammed Sami Fadali, A Framework for Optimal Placement of Energy Storage Units Within a Power System with High Wind Penetration, *IEEE Transactions on Sustainable Energy*, Vol. 4, Issue 2, 2013, pp. 434-442.

[12]. Edgardo D. Castronuovo, J. A. Peças Lopes, On the Optimization of the Daily Operation of a Wind-Hydro Power Plant, *IEEE Transactions on Power Systems,* Vol. 19, Issue 3, 2004, pp. 1599-1606.

[13]. Subhasish Deb, Sadhan Gope, Arup Kumar Goswami, Congestion Management Considering Wind Energy Sources using Evolutionary Algorithm, *Electric Power Components and Systems*, Vol. 43, Issue 7, 2015, pp. 723-732.

[14]. Sadhan Gope, Arup Kumar Goswami, Prashant Kumar Tiwari, Congestion constraint corrective rescheduling in competitive power market with integration of wind farm, in *Proceedings of the International Conference on Advancement of Computer Communication and Electrical Technology (ACCET'16)*, 2016, pp. 45-49.

[15]. K. R. Padiyar, Power System Dynamics: Stability and Control, *John Wiley,* New York, 1996.

[16]. Subhojit Dawn, Prashant Kumar Tiwari, Improvement of economic profit by optimal allocation of TCSC & UPFC with wind power generators in double auction competitive power market, *Electrical Power and Energy Systems*, Vol. 80, 2016, pp. 191-201.

[17]. Lei Tang, James D. McCalley, An Efficient Transient Stability Constrained Optimal Power Flow using Trajectory Sensitivity, in *Proceedings of the IEEE North American Power Symposium (NAPS)*, 2012, pp. 1-6.

_____

Sensors & Transducers

Investigations on Evaluation of Some QoS Aspects of Service Oriented Computing System Based on Web Services

Subhash MEDHI, Abhijit BORA and Tulshi BEZBORUAH

Department of Electronics and Communication Technology, Gauhati University,
Assam, India, PIN-781014
Tel.: +91-361-2671262
E-mail: medhisubhash72@gmail.com, abhijit.bora0099@gmail.com, zbt_gu@yahoo.co.in

Abstract: Service Oriented Computing is a design paradigm that utilizes autonomous heterogeneous service applications as the fundamental elements to develop new composite functionalities at reduced cost and time. Web service is the standard way to implement the service oriented computing concepts in which business functions and resources are published, described, discovered, orchestrated and invoked using open standards and protocols. The web services emerged as an intelligent middleware web based technology for sharing business processes and resources amongst the disparate enterprises over the internet. Performance evaluation of service is an important criterion to be assessed by end users and service providers before adopting web services to deal with the challenging global markets. In this perspective, we propose to implement a composite ATM services using. Net technology to evaluate trustworthiness of web services in dealing with massive users. The uniqueness of our proposed system is the hierarchically designed parent and child services where the parent service authenticates a user to access resources and redirects the user's query for executing child service for adequate solutions. The industry standard testing software tool, Mercury LoadRunner was deployed to test our proposed e-ATM system and record the performance metrics to analyse the quality aspects of the service. The outcome of the experiment will help in adoption and usage of the web services in diverse business enterprises. We present here the architecture, framework of testing, transaction status and reliability estimation of web services under massive stress of service users.

Keywords: SOC, Web Services, SOA, SOAP, QoS, Reliability, ATM, e-ATM.

1. Introduction

The rapid development of Internet brought more people to familiar with computer and mobiles and people embraced it for better communication, services and resource sharing. With the advent of Web Services (WS), the Internet has been changed from information repository to service repository. WS is a software component designed to support interoperability within machines over a network and public interfaces are described in a process able format termed as Web Service Description Language (WSDL) [1]. The WS technology implements Service Oriented Computing (SOC) design paradigm to develop and integrate heterogeneous services by using open standards and protocols. SOC is a resource and business

functionalities in open environments [2]. The SOC system concentrated on composing autonomous services by using mutually agreed standards and protocols. Service Oriented Architecture (SOA) is an architectural design paradigm to organize and utilize distributed applications deployed in disparate environments that can be controlled by different owners [3]. The WS supports communications with other services and clients using technologies such as Extensible Markup Language (XML), Simple Object Access Protocol (SOAP), WSDL, Universal Description Discovery Integration (UDDI) and internet protocols, such as, hyper text transfer protocol (HTTP) and hyper text transfer protocol secure (HTTPS) [4]. Once the WS is deployed, various heterogeneous organizations that are running on diverse networks can be interconnected for business processes. WS transactions are used for efficient and reliable communication of web applications across the internet where multiple users can access resources simultaneously [5]. It is an important issue to assess the trustworthiness of composite WS built on different networks and languages [6]. The ever growing reliance on the data and services provided by various WS vendors consent these services be superior in performance and reliable, as these services offered over the internet have rapidly permeates our lives due to the convenience and low cost factors [7]. In widespread application of internet technology, WS applications such as online shopping, banking, travel booking, stock trading have been adopted and developed tremendously [8]. WS is becoming more familiar to the people due to the recent development and applications over the internet, as many top companies such as Microsoft, IBM, Oracle and SUN have launched supports for technologies related to WS [9]. An important quality of software is the capability to which it can perform to its intended operation. The reliability is an important factor that represents the quality service delivery of WS system. Thus the reliability of WS system plays an important role in an organization as unreliable service system may lead to economic loss as well as reputation of stakeholders. The software failure is attributed to the quality of software, hardware and human intervention; hence it is essential to analyse the quality of software, hardware and principle of application before implementing in to an existing system. The software reliability is a probabilistic assessment which can be defined as the probability function that the software works failure free within a specified environment and a given amount of time [10]. Many software tools have been developed to estimate the reliability of software that helps to tracks the quality of software product right from the development processes, concept to commissioning. In this study we present a heuristic approach to investigate the quality of service properties in a composite e-ATM service delivery system. The Mercury LoadRunner performance testing tool is deployed to test the proposed model. The statistical analysis of the recorded data for reliability aspects of the WS is presented here.

2. Related Work

In the year 2006, Abdelkarim, *et al.* had addressed the requirements of reliability and fault tolerance of service delivery system and proposed some recovery policies to handle and recover from faults during the composition of WS [11].

In the year 2014, Shangguang Wang *et al.* had proposed a framework for solving multi user WS selection problem by predicting missing QoS values based on the historical QoS values of multi users. The authors stated that this prediction algorithm can predict the multi-QoS values more precisely at same time for different users [12].

In the year 2007, Pat, *et al.* had identified some parameters that can impact the WS dependability. They had elaborated the methods of dependability enhancement by redundancy in space and time [13].

In the year 2007, Michael P., *et al.* had proposed a business aware WSs transaction model and support mechanism. The proposed model allows business functions such as payment, delivery conditions, and dispute resolution policies and blends these functions with QoS criteria [14].

In the year 2010, Huiyuan Zheng, *et al.* had proposed an approach to calculate the QoS for composite services with complex structures. Using the proposed approach, users can explicitly specify their requirement on the mean path, the maximum and minimum value of Quality of Service (QoS) [15].

In the year 2014, Bora, *et al.* had presented an empirical study on hierarchical SOAP based WS implementing WS Security policy. The authors had observed that the WS response time with security incorporation is more than the time without security policy [16].

In the year 2014, Medhi, *et al.* had performed empirical and statistical analysis of hierarchical WS performance by implementing a financial model [17].

In the year 2014, Maurizio Gabbrielli, *et al.* had proposed a methodology which maps Coloured Petri nets-modelled SOAs in to Jolie SOA by exploiting some workflow patterns [18].

In the year 2015, Bezboruah, *et al.* had performed an evaluation of performance of hierarchical WSs using a cluster and non cluster web server [19].

In the year 2015, Bora A., *et al.* had carried out a study on the quality evaluation of interoperability for multi service multifunctional SOC system [20].

In the year 2016, Medhi, *et al.* had implemented a service model e-ATM system using WCF technology incorporating a message level security. The authors had observed that the security policy incorporation in service system influences the performances of WS system [21].

In the year 2017, Medhi, *et al.* had performed investigations on reliability of WCF system implemented in a prototype financial service model. The authors experimentally proved in the proposed model that the reliability of WS remains strong up to 600 virtual users (VU) and degrades with the higher levels of service consumers [22].

This work is an extended version of our study of a series of test conducted randomly by using different levels of VU such as 30, 50, 100, 300, 500, 800, 1000, 1400, 1500, 1900, 2000, 2200 and 2500 [23]. For statistical analysis and evaluation of the service quality of WSs, we have recorded the fault count (FC) for 30 times at 1500 VU. We have improved the average connection refusal to 1.07 % and also extended the test up to 2500 VU.

In this study we have performed the investigations on user perspective evaluation of some QoS characteristics of SOC system based on WS. The novelty of this work is that we have done a series of test randomly at different levels of VU by using an industry standard software testing tool, recorded some quality attributes, failure count and prepared a framework for reliability analysis for predicting the nature of WSs under massive stress of concurrent users.

3. Proposed Work and Methodology

The objective of the proposed work is to implement a prototype electronic automated teller machine (e-ATM) service delivery system using .NET technology to study some QoS attributes of WSs. The prototype service model has three components as presented in Fig. 1:

1) A Service Consumer;

2) Parent ATM service where the consumers identities are authenticated and,

3) Child ATM service to execute Business Processes. The authenticated users are authorised to access the resources that is users queries are served by the Child ATM service application.

To evaluate the availability and scalability of the service model, the software testing tool, Mercury LoadRunner was deployed and recorded some quality of service characteristics of the system. The prototype e-service system was designed to provide all the facilities of commercial bank ATM facilitates to a consumer. A service consumer was developed to invoke the services using the same design and development environment of the service applications. A database of size 15,000 is prepared for testing the proposed service. The service application has been tested at different levels of VU to evaluate the quality of the WSs. The statistical analysis is done on the recorded QoS attributes to estimate the availability, scalability and reliability of the services.

4. Software and Hardware Specification

The software used to develop the service applications at server system are:

a) IIS 7.5;

b) MS SQL Server;

c) Microsoft Visual Studio, 2012;

d) Internet Explorer;

e) Windows Server 2008 and the software supporting tools such as Microsoft SDK version 7.1.

The hardware components in the server includes Intel(R) Xenon(R) CPU E5620 processor with 2.4 GHz speed, 8 GB RAM and 600 GB hard drive. The software testing tool Mercury LoadRunner, Windows XP(OS), Internet Explorer, EasyFit5.6 were used by the load generator machine to generate the load on the services. We have created the script by capturing the VU's queries using the tool and replayed to test the service under higher level of loads. The load was given on the WS from a remote windows XP machine. The hardware components in the windows XP machine consists of:

1) Intel (R) Pentium (R) Dual CPUE2200;

2) Processor Speed- 2.2 GHz;

3) RAM- 1GB;

4) Hard Disk- 150 GB.
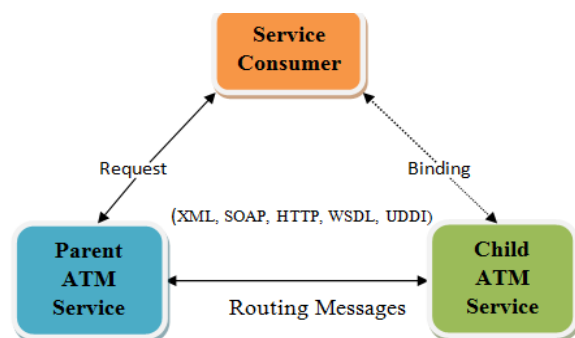
Fig. 1. Proposed E-ATM service architecture.

5. Automated Testing Tool

We have tested our proposed e-ATM service by using Mercury LoadRunner under stress of simulated VUs. Mercury LoadRunner is an industry standard performance and load testing tool for testing system behaviour and performance under stress of simulated users. The Mercury LoadRunner can simulate thousands of users using application software and users are allowed to access resources, record and latter analyse the performance of the system components [24].

5.1. Configuration of the Testing Tool

Before starting the performance test, we had configured the following parameter to emulate real like user activity and behaviour during testing.

1) Run Logic: The number of iterations.

2) Pacing: This is the controlling time between successive iterations of VU activities.

3) Think Time: The time that a user waits for performing successive operations [25].

4) Bandwidth (BW): The capacity of network that supports the transactions of VU.

5.2. Testing Parameter

We have recorded the Response Time (s), Hits/s, Throughput (byte/s), and CPU utilization which measures the quality of the system under workloads of concurrent VUs. During the load test, a user was scheduled to start in every 15 seconds and run for 300 s after completion of the ram up time. A think time of 10 s was set for every VU to pause to interact with the system.

The simulated users were used to load the system to observe the behaviour of the service applications at different loads and to measure the stress limit of the system. In this load test, the successful and failure transactions were recorded to analysis and predict reliability aspects of the system at higher loads.

6. Results and Analysis

We have conducted a series of test randomly at different stress level of VU, such as, 30, 50, 100, 300, 500, 800, 1000, 1400, 1500, 2000, 2200 and 2500 with maximum utilization of BW over the network. A test case for select operation has been prepared for accessing the service. The statistical analysis is carried out over the recorded performance attributes of the service. The different transaction status against massive stress level is presented in Table 1. For statistical analysis the test was conducted for 30 times repeatedly at 1500 VU by using the database of 15000 VUs. It has been observed that the system is responding well up to 1400 VU and consistently serving well with little refusal at larger number of workloads of VU. The average number of refusal at 1500 VU is calculated to be 1.07 %. As seen in the frequency Table 2 and Histogram in Fig. 2, the Histogram is right skewed, which is the feature of a specific distribution of data, so that we can assume that the data distribution is a Weibull distribution. The computed Bin and Frequency of QoS metrics Response Time(s), Throughput (byte/s) and Hits/s are presented in Table 3 and plotted in the Histogram as in Fig. 3, Fig. 4 and Fig. 5 respectively. Here, it is observed that the histograms for Hits/s and Throughput are left skewed and histograms for Response Time is right skewed. It predicts that the distributions of data are normal. From Fig. 6, Fig. 7 and Fig. 8 it is seen that the Throughput, Response time and Hits/s are rising with the higher number of VU. In Fig. 9 and Fig. 10 it is observed that the Response Time and Throughput are gradually rising with the higher number of Hits/s. In Fig. 10, the throughput is gradually rising against the Response Time. From these patterns of graphs we can infer that there is a close influences among the Reponses Time, Throughput and Hits/s. The parameter values are scaled up along with the progression of VU. A series of responses is recorded and shown in Table 4. Here, the Hits/s is increasing and the Response Time is very consistent and well acceptable up to 2500 VU. The throughput is increasing as expected against the larger

values of VU. The CPU Time and Disk Time utilization are less than 1 % up to 2500 VU. From these out comes we can conclude that our proposed WCF based e-ATM system is quite scalable and robust against massive number of real like VU.

Table 1. The e-ATM service transactions at different VU.

Operation	VU	Pass	Fail	Total
SQL Select Operation	30	308	0	308
	50	638	0	638
	100	1897	0	1897
	300	13200	0	13200
	500	34500	0	34500
	800	85200	0	85200
	1000	131518	0	131518
	1400	254213	0	254213
	1500	267183	7884	275067
	1900	462236	1682	463918
	2000	511478	1843	513321
	2200	614424	2221	616645
	2500	774218	8148	782366

Table 2. Bin and Frequency of Failure Count.

Failure Ranges	Frequency
0-3	1
3-3757	22
3757-7511	2
7511-11265	3
11265-15019	1
>15019	1

Table 3. Bin and Frequency of QoS Metrics.

Response Time		Throughput		Hits/s	
Bin	Fre	Bin	Fre	Bin	Fre
0.039	3	48750.07	1	29.923	1
0.145	11	55263.86	3	33.869	2
0.251	9	61777.65	9	37.815	8
0.356	5	68291.43	2	41.761	3
0.462	1	74805.22	5	45.708	6
>0.462	1	>74805.22	10	>45.708	10

Table 4. QoS Parameter for the e-ATM Service.

VU	Hits/s	ResT	ThrPut	CPU-Time	Disk-Time
30	1.537	0.043	2519.825	0.139	0.011
50	2.279	0.042	3727.144	0.105	0.010
100	4.054	0.048	6630.339	0.369	0.010
300	10.595	0.040	17385.96	0.144	0.008
500	16.71	0.038	27361.17	0.302	0.011
800	26.745	0.042	43778.66	0.180	0.009
1000	31.771	0.117	51981.78	0.125	0.014
1400	46.287	0.051	75746.08	0.099	0.007
1500	49.607	0.112	81153.09	0.138	0.189
1900	61.712	0.079	100943.6	0.591	0.293
2000	61.841	0.059	101171.3	0.300	0.010
2200	68.282	1.213	111938.9	0.309	0.013
2500	77.884	2.692	127329.84	0.348	0.009
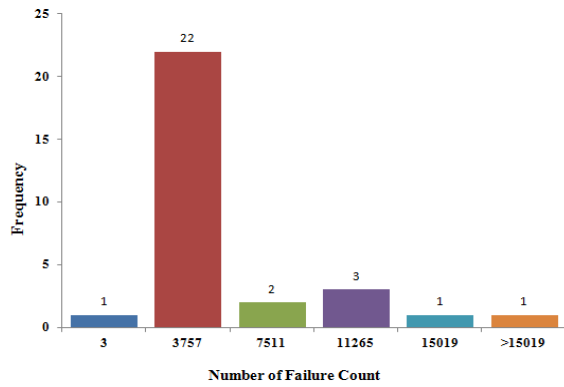
Fig. 2. Histogram for Failure Count.
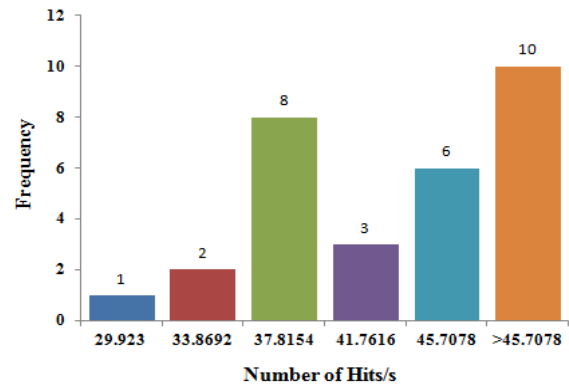
Fig. 3. Histogram for Number of Hits/s.
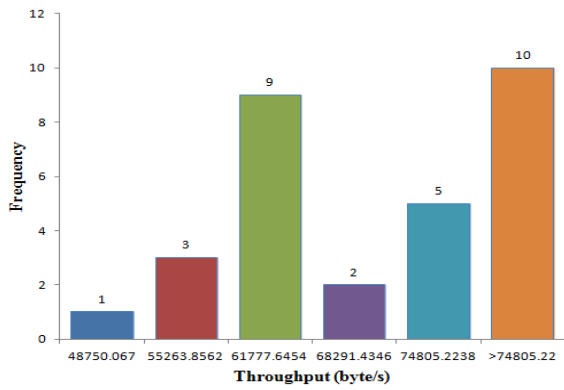
Fig. 4. Histogram for Throughput (byte/s).
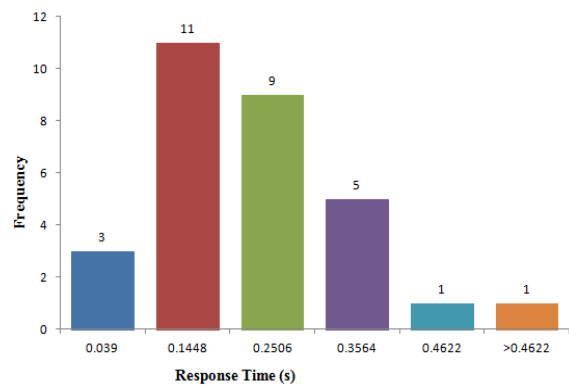
Fig. 5. Histogram for ResponseTime (s).
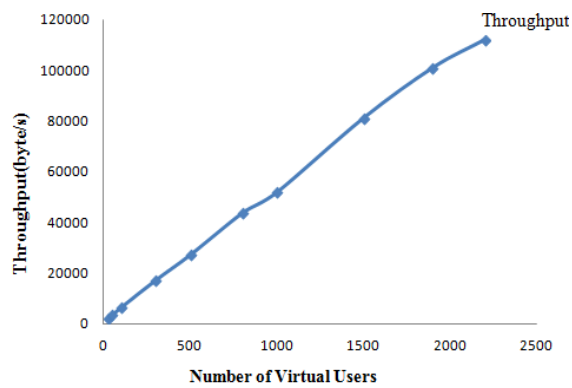
Fig. 6. Throughput (byte/s) VS Virtual Users.
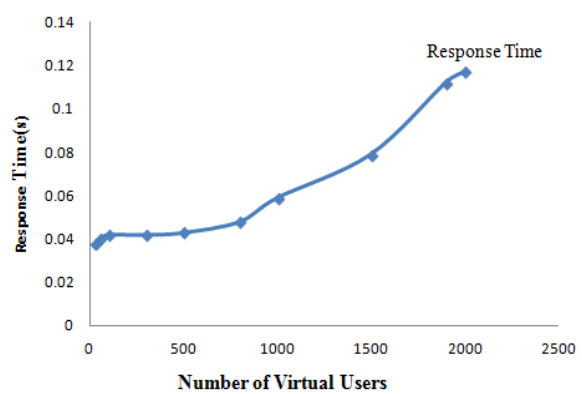
Fig. 7. Response time (s) VS Virtual Users.
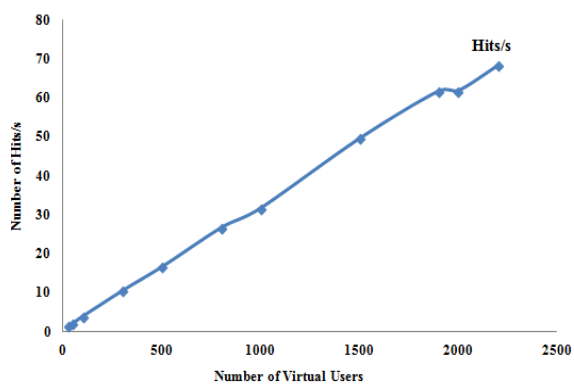
Fig. 8. Number Hits/s VS Virtual Users.
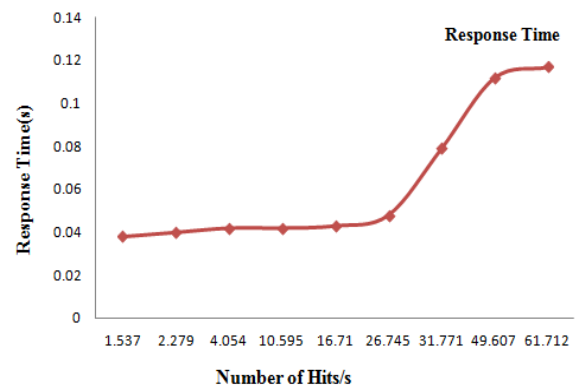
Fig. 9. Response Time (s) VS Hits/s.
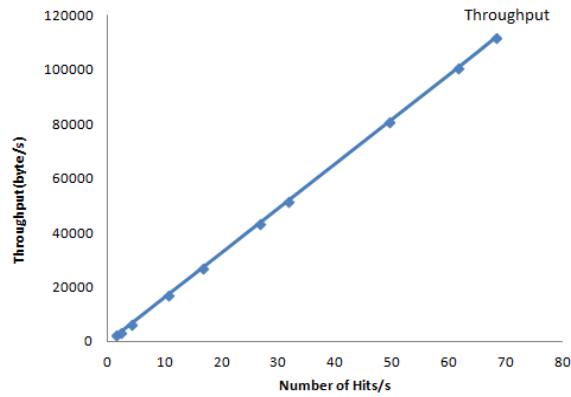
Fig. 10. Throughput (byte/s) VS Hits/s.
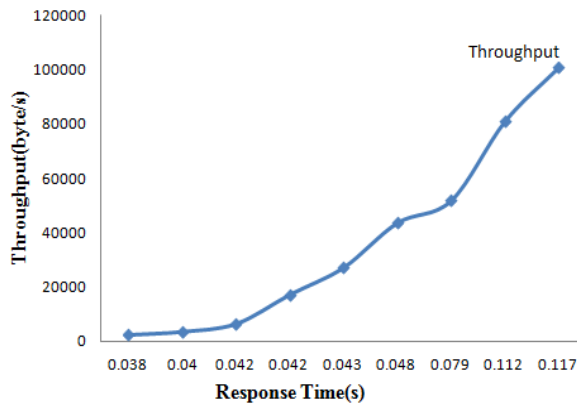
Fig. 11. Throughput (byte/s) VS Response Time (s).

To further study the distribution of data, we have used the EasyFit, a statistical software tool to estimate the values of shape (α) and scale parameter (β) which are found as $\alpha = 0.62606$ and $\beta = 2157.7$ [26]. The Weibull cumulative distribution function (CDF) can be calculated by using the Equation (1) for the FC values [27].

$$CDF = 1 - \exp \{-(FC/ \beta)^{\alpha}\} \qquad (1)$$

7. Goodness of Fit (GoF) Evaluation Using Kolmogorov-Smirnov Test

The Kolmogorov Smirnov (KS) GoF test is used to test whether a data sample comes from a population with a specific distribution. In the distance test, the assumed distribution is correct, if the maximum departure between the observed CDF (F_o) and the expected CDF (F_n) distributions are minimum. We have calculated the intermediate values for KS GoF test for Weibull distribution and is given in Table 5. It is seen that the KS GoF test statistic value Dmax (0.1783) is smaller than the KS table critical value (0.24) for $\alpha=0.05$ and a sample of size n=30. Based on these outcome, we do not reject the hypothesis that the obtained CDF of the FC is distributed Weibull ($\alpha=0.6261$, $\beta=2157.7$). Hence the population from

where these data were obtained is distributed Weibully.

Table 5. Intermediate Values for K-S GoF Test.

Sl	Fo	Fn	Fn-1	D+	D-
1	0.0161	0.0333	0.00000	0.0172	-0.0161
2	0.0504	0.0667	0.0333	0.0163	-0.0170
3	0.1414	0.1000	0.0667	-0.0414	-0.0748
4	0.2014	0.1333	0.1000	-0.0681	-0.1014
5	0.2893	0.1667	0.1333	-0.1227	-0.1560
6	0.3982	0.2000	0.1667	-0.1982	-0.2315
7	0.4029	0.2333	0.2000	-0.1695	-0.2029
8	0.4039	0.2667	0.2333	-0.1372	-0.1706
9	0.4039	0.3000	0.2667	-0.1039	-0.1372
10	0.4130	0.3333	0.3000	-0.0796	-0.1130
11	0.4354	0.3667	0.3333	-0.0687	-0.1020
12	0.4408	0.4000	0.3667	-0.0408	-0.0741
13	0.4490	0.4333	0.4000	-0.0156	-0.0490
14	0.4599	0.4667	0.4333	0.0068	-0.0265
15	0.4787	0.5000	0.4667	0.0213	-0.0120
16	0.4814	0.5333	0.5000	0.0519	0.0186
17	0.4869	0.5667	0.5333	0.0797	0.0464
18	0.5054	0.6000	0.5667	0.0946	0.0612
19	0.5112	0.6333	0.6000	0.1221	0.0888
20	0.5182	0.6667	0.6333	0.1484	0.1151
21	0.5217	0.7000	0.6667	0.1783	0.1449
22	0.6340	0.7333	0.7000	0.0994	0.0660
23	0.6526	0.7667	0.7333	0.1141	0.0808
24	0.6889	0.8000	0.7667	0.1111	0.0777
25	0.8000	0.8333	0.8000	0.0333	0.0000
26	0.8866	0.8667	0.8333	-0.0200	-0.0533
27	0.8947	0.9000	0.8667	0.0053	-0.0280
28	0.8980	0.9333	0.9000	0.0354	0.0020
29	0.9035	0.9667	0.9333	0.0632	0.0298
30	0.9792	1.0000	0.9667	0.0208	-0.0126
			Dmax	**0.1783**	0.1449

7.1. Confidence Interval of CDF

The mean value for CDF is estimated at 95% confidence interval for 1500 VU. The populations mean values μ can be calculated by using the equation as in (2) [28].

$$\mu = \bar{x} \pm t_c SD/\sqrt{N} \qquad (2)$$

We consider the mean value of CDF as $\bar{x}$, the critical value from $t_c(0.05,29)$, the standard deviation as SD, sample size as N and the margin of error as $t_c SD/\sqrt{N}$. The estimated population mean μ is calculated and presented in Table 6. At 95 % confidence interval, the mean value of CDF lies between 0.51 ± 0.09, i.e. 0.60 and 0.42.

Table 6. Estimated values for μ.

N	tc(0.05,29)	Parameter	$\bar{x}$	SD	tcSD/√N
30	2.045	CDF	0.51	0.25	0.09

7.2. Reliability Estimation

Reliability of a system is evaluated over phases of time and environment that the system executes without failure in the specified period. We have calculated the reliability of our proposed system by using average FC and HTTP transactions from 30 sample data i.e. FC = 2507.57, HTTP transaction = 225239.5. The probability of failure (P_f) is calculated as FC/Total HTTP transaction, i.e. 2507.57/225239.5, P_f = 0.01. The probability of success is the reliability and can be calculated as reliability (R) = 1-P_f = 98.89 % [29]. Thus the reliability can be defined as the probability of no failure within a specified period of time and stated environment. Reliability can also be estimated by using Equation (3) as in [30].

$$R=e^{-\lambda t} \qquad (3)$$

Here the λ is the transactional failure rate. It is a probability density function for operational time λ (t). The execution time unit is considered as 1, so we set t=1, the reliability becomes $R=e^{-\lambda}$. In practice reliability can be estimated by using the Equation (4).

$$R=1-\lambda \qquad (4)$$

Thus we obtained the following reliabilities at incremented values of VU: R(1500) = 98.89 %, R(1900) = 99.64 %, R(2000) = 99.64 %, R(2200) =99.64 %, and R(2500)=91.52 %. It is noticed that the reliability is consistent against the escalated number of VUs which indicates that the system is fairly scalable at the higher number of VUs. We performed the test at different values of VU randomly and observed that the reliability at 30, 50, 100, 300, 500, 800, 1000 and 1400 VU is 100 %. For the different level of service loads, the system will be serving as expected to the user's request. However, in higher load levels such as 1500, 1900, 2000, 2200 and 2500; the reliabilities estimated are 98.89 %, 99.64 %, 99.64 %, 99.64 % and 91.52 % respectively, i.e. more than 90 % request is served successfully. Thus, we can conclude that the reliability is quite stable and more than 90 % queries are served well in the VU range from 1500 to 2500 that is the users will get most expected responses with little refusals from the WCF service as the web server refuses at massive concurrent request.

The overall reliability evaluation framework with reliability assessment is presented in Table 7. In the FC histogram, it is observed that the highest density of FC is 22 and is occurred in the range from 3-3757 transactions. The histogram for FC follows right skewed. So, we can conclude that our FC distribution is a Weibull distribution.

Using CDF values we have computed the KS statistic by using EasyFit statistical software. It is a tool for statistical data analysis and simulation that allows for fitting probability distributions to make better decisions. From the analysis, it is revealed that the statistics value obtained (0.178) is smaller than the

critical value (0.2417) at α =0.05 which indicates that the assumed samples were from a population of Weibull distribution. Based on the analysis results we can conclude that the observed data adequately fits in the Weibull distribution. We have evaluated the reliability of our proposed system by increasing VU. In lower number of VU, the reliability estimated to be 100 % and the reliability decreases at escalated number of VU.

Table 7. The reliability evaluation framework.

Parameter	Remarks
Transactions at VU 30, 50, 100, 300, 500, 800, 1000, 1400	100 % success
Transactions at VU 1500, 1900, 2000, 2200, 2500	Failures observed and increases gradually
FC Histogram at 1500 VU	Right skewed with highest failure density 22 in the range from 3-3757
GoF test using K-S at 95 % confidence level for 1500 VU	Failure data distribution qualified in the Weibull distribution
CDF	Mean CDF is 0.51 and lies in between 0.60 and 0.42
Reliability up to 1400 VU	R=100 %. Consumer will get expected services
Reliability for 1500 VU	R=98.89 %, acceptable reliability with probability of failure occurrences
Reliability more than 1500 VU	Service quality degrades gradually

8. Conclusion and Future Work

In this paper we have conducted a series of test at different levels of simulated users that accessed concurrently in the proposed e-ATM model and carried out a statistical analysis of some QoS attributes of WS. We have recorded some performance metrics which measures the quality of the system and plotted the quality metrics in histograms to see the behavior of the service under stress of higher loads. From the Table 4, it is observed that the average Hits/s is gradually increased from 1.537 at 30 VU to 60.138 at 2500 VU. The Response Time (s) was very consistent though the VU was increased gradually from 30 to 2500. The response time is recorded to be less than 1 second up to 2000 VU with a maximum of 2.69 second at 2500 VU. The Throughput is gradually increased with the progression of VU as expected, the minimum value of 2519 byte/s is observed at 30 VU. The maximum value of throughput is recorded to be 127329.84 at 2500 VU. The CPU Time and Disk Time utilization are showing the consistency over the growing limit of VU and the utilization is less than 1 % which indicates that our proposed WCF based e-ATM system is capable to handle large number of consumers on the available BW.

Using FC record and analysis approach, we have computed the reliability of our system at different levels of VU and are observed to be quite strong up to 1400 VU and slightly degraded with the progress of VU. More than 90 % services were successful up to 2500 VU. This occurrence of service failures may be attributed to database server or system resources. The experimental study revealed the strong evidence of availability, scalability and reliability of the proposed service to communicate with massive number of VU.

As part of the future work we propose to investigate some QoS aspects of WCF and webAPI Restful service which may highlight the reliability of service system based on different techniques.

Acknowledgement

References

[1]. W.W.W. Consortium http://www.w3.org/TR/ws-gloss

[2]. Lina Barakat, Simon Miles, Michael Luck, Efficient adaptive QoS-based service selection, *SOCA,* Vol. 8, 2014, pp. 261-275.

[3]. Marc N. Haines, William Haseman, Service Oriented Architecture Adoption Patterns, in *Proceedings of the IEEE 42nd Hawaii International Conference on System Sciences*, 2009, pp. 1-9.

[4]. Kenedy Mutange Senagi, George Okeyo, Wilson Cheruiyot, An aggregated technique for optimization of SOAP performance communication in Web services, *SOCA,* Vol. 10, Issue 3, 2016, pp. 273-278.

[5]. Ruben Casado, Javier Tuya, Muhmmad Younas, A family of Test Criteria for web services Transactions, in *Proceedings of the International Symposium on Advances in Transaction Processing*, Vol. 10, 2012, pp. 880-887.

[6]. Duhang Zhong, Zhichang Qi, A Petri Net Based Approach for Reliability Prediction of Web services, in *Lecture Notes in Computer Science*, Vol. 4277, 2006, pp. 116-125.

[7]. Gokhale Swapna S., Paul J. Vndal, Jijun Lu, Performance and Reliability analysis of web server Software Architectures, in *Proceedings of the 12th Pacific Rim International Symposium on Dependable Computing (PRDC'06)*, 2006, pp. 351-358.

[8]. Wang Haiyan, Wang Suichang, Ding Fei, Reliability Prediction–based Web Service Selection, *Advances in Information Sciences & Service Sciences*, Vol. 5, Issue 9, May 2013, pp. 391.

[9]. Hou Zhai-Wei, Zhai Hai-Xia, Gao Guo-Hong, A Study on Web Services Performance Optimization, in *Proceedings of the Third International Symposium on Electronic Commerce and Security Workshops*, 2010, pp.184-188.

[10]. Goel A. L., Software reliability Models: Assumptions, Limitations, and Applicability, *IEEE Transactions on Software Engineering*, Vol. SE 11, No. 12, 1985, pp. 1411-1423.

[11]. Abdelkarim E., Maheswary P., Vladimir T., Recovery Policies for Enhancing Web service Reliability, in *Proceedings of the IEE International Conference on Web Services (ICWS'06)*, 2006, pp. 189-196.

[12]. Shangguang Wang, Ching–Hsien Hsu, Zhongjun Liang, Multi-user web service selection based on multi-QoS prediction, *Inf. Syst. Front*, 16, 2014, pp. 143-152.

[13]. Pat P. W. Chan, Michael R. Lyu, Miroslaw Malek, Reliable Web Services: Methodology, Experiment and Modeling, in *Proceedings of the IEEE International Conference on Web Services*, USA, 2007, pp. 679-687.

[14]. Michael P. Papazoglow, Benedikt Kratz, Web services technology in support of business transactions, *SOCA,* Vol. 1, 2007, pp. 51-63.

[15]. Huiyuan Zheng, Jian Yang, Weiliang Zhao, QoS Analysis and Service Selection for Composite Services, in *Proceedings of the IEEE International Conference of Services Computing*, 2010, pp. 122-129.

[16]. Bora A., Bezboruah T., Investigation on Security Implementation and performance Aspects of MedWS: a Hierarchical SOAP based Web Service, *International Journal of Database Theory and Application*, Vol. 7, No. 4, 2014, pp. 169-188.

[17]. Medhi S., Bezboruah T., Investigations on implementation of e-ATM Web services based on .NET technique, *International Journal of Information Retrieval Research*, Vol. 4, No. 2, April-June 2014, pp. 41-56.

[18]. Maurizio Gabbrielli, Saverio Giallorenzo, Fabrizio Montesi, Service-Oriented Architectures: From Design to Production Exploiting Workflow Patterns, in *Proceedings of the 11th International Symposium on Distributed Computing and Artificial Intelligence*, Salamanca, Spain, Vol. 290, Jun. 2014, pp. 131-139.

[19]. Bezboruah T., Bora A., Performance Evaluation of Hierachical SOAP Based Web Service in Load Balncing Cluster-Based and Non-Cluster Based Web Server, *International Journal of Information Retrieval Research*, Vol. 5, Issue 4, 2015, pp. 20-31.

[20]. Bora A., Bezboruah T., Some aspects of QoS for Interoperability of Multi Service Multifunctional Service Oriented Computing, in *Proceedings of the IEEE International Conference on Research in Computational Intelligence and Communication Network*, India, 2015, pp. 363-368.

[21]. Subhash Medhi, Abhijit Bora, Tulshi Bezboruah, Security Impact on e-ATM Windows Communication Foundation Services using Certificate based Authentication and Protection: An implementation of Message Level Security based on .NET Technique, *International Journal of Information Retrieval Research*, Vol. 6, Issue 3, July-September, 2016, pp. 1-15.

[22]. Subhash Medhi, Abhijit Bora, Tulshi Bezboruah, Investigations On Some Aspects of Reliability of Content Based Routing SOAP based Windows Communication Foundation Services, *International Journal of Information Retrieval Research*, Vol. 7, Issue 1, January-March 2017, pp. 17-31.

[23]. Subhash Medhi, Abhijit Bora, Tulshi Bezboruah, Investigations on user perspective evaluation of some reliability aspects of web services, in *Proceedings of the 1st International Conference on Advancement of Computer Communication & Electrical Technology (ACCET'16)*, 21-22 October 2016, pp. 65-69.

[24]. Retrieved at http://genesis.co.kr/image/product/pds/ LoadRunner/Manual/LoadRunner_Generator.pdf

[25]. Loadrunner, retrieved from http://www.en. wikipedia.org/wiki/HP_LoadRunner, 2017.

[26]. EasyFit Distribution tools at http://www.mathwave.com/easyfit-distribution-fitting.html, Retrieved on 2017.

[27]. Chandra M., Singpurwala N. D., Stephen M. A., Kolmogorov Statistics for Test of Fit for the Extreme Value and Weibull distribution, *Journal of the American Statistical Association*, Vol. 76, No. 375, 1981, pp. 729-731.

[28]. Speigel M. R., Theory and problems of probability and Statistics (Schaum's Outline Series), 2 ed., *Schaum's Outlines,* 2000.

[29]. Shooman M. L., Reliability of Computer Systems and Networks: Fault Tolerance, Analysis, and Design, *John Wiley & Sons, Inc.*, 2002.

[30]. Lijun Wang, Xiaoying Bai, Lizhu Zhou, Yinong Chen, A Hierarchical Reliability Model of Services Based Software System, in *Proceedings of the 33rd Annual IEEE International Computer Software and Applications Conference*, Vol. 1, 2009, pp. 199-208.

Sensors & Transducers

An Ideal Multi-Secret Sharing Scheme with Verification

[1,] [*] **Arup Kumar CHATTOPADHYAY,** [2] **Amitava NAG**
and [3] **Koushik MAJUMDER**

[1] Department of Computer Science and Engineering, Academy of Technology,
Hooghly, 712121, India
[2] Department of Information Technology, Academy of Technology, Hooghly, 712121, India
[3] Department of Computer Science and Engineering, Maulana Abul Kalam Azad
University of Technology, Kolkata, West Bengal, 700064, India
[*] Tel.: 9339770502
[*] E-mail: ardent.arup@gmail.com

Abstract: The (t,n) - threshold secret sharing scheme proposed by Shamir (1979) encodes the secret key into n shares and those shares are distributed among the participants. Each share incorporates an *x*-value uniquely designated for every single participant. If the shares are distributed on insecure (or public) channels, malicious users may acquire a few (or all) shares. If the number of shares obtained by the malicious users is t or more ($\leq n$), then malicious users can reconstruct the secret. Chattopadhyay, *et al.* (2016) proposed a scheme for the distribution of shares with RSA to encrypt the *x*-values at insecure channel along with verification, such that the secrecy of shares and secret both are maintained. A verifiable $(t,k,n)-$ threshold multi-secret sharing scheme is proposed in this paper which extends the work proposed by Chattopadhyay, *et al.* (2016). The proposed scheme is ideal as the sizes of the shares are of same as that of the secrets.

Keywords: Secret sharing, Multi-secret sharing, Verifiable, Hash function, RSA.

1. Introduction

A secret sharing schemes (SSS) are defined to share a secret among a group of participants and protect the secret from disloyal access by unauthorized groups. In a (t,n) - threshold secret sharing scheme, a secret S is encoded into n shadows or shares and distributed among n participants or players (a Dealer is responsible for construction and distribution of the shares). If any t or more ($\leq n$) shares are submitted by participants, then the full secret S can be reconstructed (reconstruction can be also done by a special entity called Combiner). Otherwise, no less than t shares can reconstruct the secret or expose any

information about the secret. So, any group with $< t$ members constitutes a disloyal group.

Secret sharing was first introduced independently by two authors - Shamir and Blakley in the year of 1979. Shamir's scheme [3] was based on Lagrange's interpolation and Blakley's scheme [7] was based on hyperplane geometry. Mignotte proposed secret sharing scheme [17] based on Chinese Reminder Theorem (CRT) and it was improved by Asmuth-Blooms [4].

The scheme proposed by Shamir [3] is extended by many researchers in different scenarios. Thien and Lin proposed secret image sharing (SIS) scheme in [5] based on Shamir's scheme. If the shares generated by Shamir's scheme, are distributed on insecure channels,

the confidentiality of shares becomes volatile and the shares can be misused by malicious users. Hence, Zhao, *et al.* has proposed a method in [21] to ensure the confidentiality of the shares on insecure channels. The secure key distribution method used in [21] is extended for secure distribution of shares of medical images by Ulutas, *et al.* in [18] and the authors also used the Shamir's framework with better authenticity and confidentiality properties.

During the reconstruction of secret phase, when the shareholders present their shares, dishonest shareholder(s) called cheater(s) can present faked share(s) and thus deceive the other honest shareholders as they obtain a faked secret as result. So, cheater detection and identification are essential properties of an efficient secret sharing scheme. Harn and Lin [11] defined a method for cheater detection and identification for Shamir's secret sharing scheme. Authors in [11] assume a situation where more than t shares are presented for reconstruction of the secret and the redundant shares are used to identify the cheaters. A variety of secret sharing schemes were proposed that can verify whether the shares received by shareholders are consistent under the condition the secrecy of shares and secret both are maintained. Harn, *et al.* [12] proposed a verifiable secret sharing scheme based on the CRT and extension of Asmuth-Bloom's scheme [4]. Another efficient scheme [22] based on Asmuth-Blooms scheme is proposed by Liu, *et al.* Liu & Chang had proposed an integrable mechanism for verification in [23] with generalized Chinese Reminder Theorem, Shamir's Secret sharing and Asmuth-Bloom's secret sharing and it improvise the verification method proposed by Harn, *et al.* in [12] by using one way hash function.

In multi-secret sharing (MSS) schemes, several secrets can be shared during a single secret sharing process. In 2004, Yang, Chang and Hwang (YCH scheme in [6]) proposed an efficient MSS, which is based on the two-variable one-way function. But the scheme doesn't have the property of verification. Based on YCH scheme, a number of MSS schemes are proposed to realize the property of verification and also do not need a security channel for delivering shares to the participants. Shao and Cao (SC scheme in [10]) proposed an efficient verifiable multi-secret sharing (in 2005) based on YCH scheme, but in the scheme as the shadows are chosen by the dealer, even if the dealer is honest, the system also needs a secure channel between the dealer and the participants so that the dealer can distribute the shadows to the participants safely. In 2007, Zhao, *et al.* presented a new practical verifiable MSS scheme (ZZZ scheme in [8]) based on YCH scheme and the intractability of the discrete logarithm [19] which ensures the verifiability of shares and secrets both and do not require a secret channel for distribution of shares. In the same year, Dehkordi and Mashhadi presented another MSS scheme [15] based on based on- YCH scheme, the intractability of Discrete Logarithm and RSA cryptosystem. The scheme needs no secure channel and at the same time verifiable property is more

efficient than defined in [10]. The same authors, in 2008 presented another MSS scheme [16] based on YCH and homogeneous linear recursion, which is performance wise better than SC and ZZZ schemes. Shao (2014) presented another MSS scheme [9] based on Shamir's scheme and a hash function. The scheme, in [9] is computationally efficient and holds all the properties of MSS.

In our proposed multi secret scheme we ensure that it holds cheating prevention – shares are secure even distributed on public channels and also the shares and the secrets both are verifiable. Moreover, the proposed scheme is ideal as the shares are of the same size as that of the secret. The rest of the of the paper is arranged as follows – in Section 2 the important entities of threshold secret sharing are briefed; we have discussed about the related schemes and algorithms in Section 3; our proposed scheme is presented in Section 4; in Section 5 we have discussed about the performance of our scheme and Section 6 concludes the paper.

2. Preliminaries

The important entities used in a threshold secret sharing scheme are briefed as follow:

Secret: A secret S is the confidential information need to be secured from unauthorized users or unauthorized groups.

Shares: The secret S is encoded into n shares or shadows, say $s_1, s_2, ..., s_n$, such that none of them individually reveals any information about the secret.

Dealer: Dealer or distributor (D) is the data owner or trusted-third party, mainly responsible to encode the secret into n shares and to distribute them to the participants.

Participants: Participants or players are represented as $P_1, P_2, ..., P_n$ and they are the users seeking for the secrets.

Combiner: A combiner (C), one of the participants or trusted-third party, mainly responsible to decode the secret if threshold number (t) or more shares are obtained from the participants.

In a (t, n)-threshold secret sharing scheme, the D generates n *shares* and distributes it among n *participants*. If any t or more *participants* submit their *shares* to the C, then the secret can be retrieved in full. If any less than t *shares* are submitted then no part of the secret will be revealed.

3. Related Study

3.1. Review of Shamir's Secret Sharing Scheme (1979)

Shamir proposed a (t, n) – threshold secret sharing scheme [3] based on Lagrange's interpolation. For

given t points (x_i, y_i), where $i = 1, 2, ..., t$ in the 2D-plane, the Lagrange's interpolation polynomial $f'(x)$ can be constructed using:

$$f'(x) = \sum_{i=1}^{t} y_i \prod_{j=1, j \neq i}^{t} \frac{x - x_j}{x_i - x_j}.$$

Consider the secret is S and the dealer has to generate n shares as - $s_1, s_2, ..., s_n$. It allows t or more $(\leq n)$ shares to reconstruct the secret. The solution requires a random $(t-1)^{th}$ degree polynomial:

$$F(x) = \left(S + a_1 x + a_2 x^2 + ... + a_{t-1} x^{t-1}\right) \bmod p,$$

in which p is the large prime number and the coefficient of polynomial $a_1, a_2, ..., a_{t-1}$ are randomly selected within the range $\left[0, (p-1)\right]$. Dealer computes the shares as follows:

$$s_1 = (1, F(1)), s_2 = (2, F(2)), ..., s_n = (n, F(n)).$$

If t or more $(\leq n)$ shares are obtained then the polynomial $F(x)$ can be regenerated by Lagrange interpolation as:

$$F(x) = \sum_{i=1}^{t} S_i \prod_{j=1, j \neq i}^{t} \frac{x - j}{i - j}$$

The secret will retrieved as $S = F(0)$.

3.2. Threats in Distribution of Shares in Shamir's Secret Sharing

Each share generated by Shamir's scheme, is distributed as pair of two integers $(x_i, F(x_i))$, where $x_i \neq 0$. But in this scheme the x-values are easy to predict. So x-values can be considered as random numbers. But still, if the shares are distributed on insecure channels, any knowledge of t or more $(\leq n)$ shares were gathered by malicious users are enough to reconstruct the polynomial - $F(x)$. The value of the polynomial at position $x_i = 0$ is the secret $S = F(x_i = 0)$.

For example, we consider $(3, 10)$ – threshold secret sharing $(n = 10, t = 3)$ and a 2nd order polynomial as:

$$F(x) = \left(9 + 13x + 5x^2\right) \bmod 37$$

All the coefficients are assumed within [0-36], secret $S = 9$ and $p = 37$. The polynomial can be reconstructed (as shown in Fig. 1) if 3 or more shares

are known. The secret will be recovered where the polynomial intersects Y-axis that is at point $\left(0, F(0)\right)$. In our example secret is $S = F(0) = 9$.
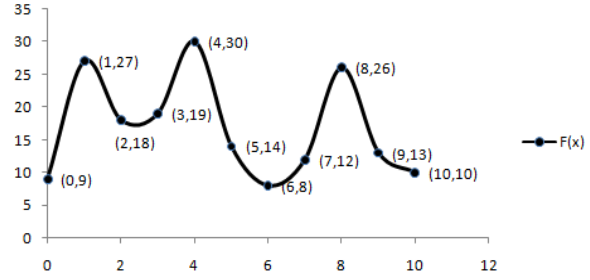
Fig. 1. Example of $(3, 10)$-threshold SSS.

3.3. Review of the YCH Scheme (2004)

C.-C. Yang, T.-Y. Chang and M.-S. Hwang proposed a (t, n)-threshold multi-secret sharing scheme [6] which is based on Shamir's secret sharing. It assumes a two-variable, one-way function $f(r, s)$ and k secrets - $S_1, S_2, ..., S_n$.

Initialization Phase:
The dealer (D) randomly chooses n secret shadows - $s_1, s_2, ..., s_n$ and delivers them to the participants $P_1, P_2, ..., P_n$ secretly. Then, D chooses a value r randomly and computes $f(r, s_i)$ for $i = 1, 2, ..., n$.

Construction Phase:
$if\ (k \leq t)$
   1. Choose a polynomial of degree $(t-1)$

$$g(x) = S_1 + S_2 x^2 + ... + S_k x^{k-1} + a_1 x^k + a_2 x^{k+1}$$
$$+ ... + a_{t-k} x^{t-1} \bmod q,$$

where q is the large prime and $0 < S_1, S_2, ..., S_k, a_1, a_2, ..., a_{t-k} < q$.
   2. D computes $y_i = g(f(r, s_i)) \bmod q$ for $i = 1, 2, ..., n$.
   3. D publishes $(r, y_1, y_2, ..., y_n)$.

$if\ (k > t)$
   1. Choose a polynomial of degree $(k-1)$

$$g(x) = S_1 + S_2 x + ... + S_k x^{k-1} \bmod q;\ ,$$

where q is a large prime and $0 < S_1, S_2, ..., S_k$.
   2. D computes $y_i = g(f(r, s_i)) \bmod q$ for $i = 1, 2, ..., n$. D also computes $g(i) \bmod q$ for $i = 1, 2, ..., k - t$.

3. *D* publishes

$$\left(r, y_1, y_2, ..., y_n, g(1), g(2), ..., g(k-t)\right).$$

Recovery Phase:

Let, any t participants submit their shares $f(r, s_i) \bmod q$ for $i = 1, 2, ..., t$. Then the polynomial $g(x)$ can be uniquely determined as follows:

$$if\left(k \le t\right)$$

$$g(x) = \sum_{i=1}^{t} y_i \prod_{j=1, j \ne i}^{t} \frac{x - f(r, s_j)}{f(r, s_i) - f(r, s_j)} \bmod q$$

$$= S_1 + S_2 x + ... + S_k x^{k-1} + a_1 x^k + a_2 x^{k+1} + ...$$

$$+ a_{t-k} x^{t-1} \bmod q;$$

$$if\left(k > t\right)$$

$$g(x) = \sum_{i=1}^{t} y_i \prod_{j=1, j \ne i}^{t} \frac{x - f(r, s_j)}{f(r, s_i) - f(r, s_j)} \bmod q$$

$$+ \sum_{i=1}^{k-t} g(i) \prod_{j=1, j \ne i}^{k-t} \frac{x - j}{i - j} \bmod q$$

$$= S_1 + S_2 x + ... + S_k x^{k-1} \bmod q;$$

But, as in this scheme shadows are chosen by the dealer, even if the dealer is honest, the system also needs a secure channel between the dealer and the participants so that the dealer can distribute the shadows to the participants safely. Hence, it increases the cost of distribution. In 2009, Zhao, *et al.* proposed a scheme [21] which do not require secret channel (for Shamir's secret sharing). In the next subsection, we review only the initialization and sharing phase of it.

3.4. Scheme Proposed by Zhao, *et al.* (2009)

The intercommunication between dealer and participants to distribute the shares on an insecure channel was made secure (confidentiality of the shares is not lost) by the cheating proof secret image sharing scheme [21] proposed by Zhao, *et al.* It ensures the confidentiality of *x*-values are protected as the *x*-values are calculated independently by both dealer and participant before distribution begins. Even if intruders able to gather the information about any t or more ($\le n$) shares (only the values of $F(x)$), they must also have to accrue the *x*-values to apply Lagrange's interpolation to recover the secret. Thus, even an insecure channel is sufficient to keep the confidentiality of the secret. The process of initialization and sharing phase of the scheme are as follow:

1. The dealer chooses two large integer numbers *p* and *q*. Computes $N = pq$ such that $p \equiv 3 \bmod 4$ and $q \equiv 3 \bmod 4$.

2. Dealer selects an integer $g \in \left[N^{\frac{1}{2}}, N\right]$ such that g is relatively prime to *p, q* and publishes $\{g, N\}$.

3. Each participant chooses his/her secret shadow as $s_i \in [2, N]$ and computes $R_i = g^{s_i} \bmod N$.

4. Each participant sends his/her R_i to the dealer. Dealer ensures each R_i is unique, otherwise demands a new secret shadow from that participant.

5. Then, the dealer randomly chooses $s_0 \in [2, N]$ such that it is relatively prime to $(p-1)$ and $(q-1)$. Dealer also computes $R_0 = g^{s_0} \bmod N$ and publishes R_0.

6. Dealer computes $x_i = R_i^{s_0} \bmod N$ for each participant.

The dealer assigns a x_i - value for each participant. The participant can calculate his own x_i independently from secret shadow from publicly known value R_0 as

$$x_i = R_0^{s_i} \bmod N$$

Zhao, *et al.* (2007) also used the similar algorithm for secure distribution in their proposed multi-secret sharing scheme [8].

In our scheme, RSA (by Rivest, *et al.* 1978) algorithm [20] is used such that dealer encrypt each *x*-value by the public key of the participant and the *x*-value can be decoded by the corresponding participant (private key holder) only. The plain-text message (here the *x*-value) need to be preprocessed so that security can be ensured by random oracle model [13].

Random oracle model [13] was first established in 1993 by M. Bellare and P. Rogaway. In this paradigm, the authors stated that a practical protocol is produced by first devising and providing a protocol for the random oracle model; and then replacing the random oracle by appropriate hash function. The authors argued that this paradigm yields protocols those are much more efficient than standard ones and the paradigm applicable for encryption, signatures and zero-knowledge proof.

Bellare, & Rogaway (1995) proposed Optimal Asymmetric Encryption Protocol (OAEP) [14] for RSA, which is proven in the random oracle model. The OAEP algorithm uses a pair of random oracle *G* and *H* to preprocess the pain text before asymmetric encryption applied. The pair of oracle combined with trapdoor one way permutation function is semantically secure under plain-text attack (IND-CPA). If the scheme further can be combined with trapdoor function like RSA is also proven secure against chosen cipher attack (NM-CPA). The instantiation of G-Oracle for IND-CCA attack and instantiation of H-Oracle and use trapdoor permutation (trapdoor function) for NM-CPA attack are discussed by

Boldyreva and Fischlin (2006) in [1]. The authors also provided a detail security analysis of OAEP with random oracle model.

OAEP Algorithm for Preprocessing the Pain-text

Consider the following:

- f is a k-bits to k-bits trapdoor function (in our scheme RSA).

- k_0 is chosen such that adversary running time is significantly smaller than s^{k_0}.

- Length of the message x is $k - k_0$ (if the message is smaller then has to be padded with zeros).

- G is a "generator" such that $G : \{0,1\}^{k_0} \rightarrow \{0,1\}^n$ and H is the hash function $H : \{0,1\}^n \rightarrow \{0,1\}^{k_0}$.

Encoding:

1. Chose a random $r = \{0,1\}^{k_0}$.

2. Generate the encoded stream $E = \left(x \oplus G(r) \right) \| \left(r \oplus H \left(x \oplus G(r) \right) \right)$, where $\|$ is concatenation operator. We can also represent the equation as $E = X \| Y$ where and $Y = r \oplus H \left(x \oplus G(r) \right)$.

Decoding:

1. Extract X and Y parts from encoded message E and recover r as $r = Y \oplus H(X)$.

2. Recover the padded message $x = X \oplus G(r)$.

In proposed model, we use RSA as trapdoor function.

4. Proposed Scheme

We first present the secure and verifiable version of Shamir's (t, n)- threshold secret sharing as proposed in [2].

The objectives are defined as follows:

1. In the proposed version the *x*-values should not be predictable by the malicious users.

2. The shares can be distributed on insecure or public channels, but it can only be used by authorized users.

3. The shares are submitted by the participants must be verifiable, such that any fake share(s) submitted can be easily identified by the combiner.

4. The scheme should also identify if the dealer himself is dishonest and supplied fake shares to one or more participants.

The different phases of the model are as follows:

Initialization Phase

1. Each participant $P_i, i = 1, 2, ..., n$ considers two large primes p_i, q_i and computes the following:

$$N_i = p_i q_i \text{ and } \varphi_i = (p_i - 1)(q_i - 1).$$

2. The participant $P_i, i = 1, 2, ..., n$ chooses an integer $e_i, 1 \le e_i \le \varphi$, such that $\gcd(e_i, \varphi_i) = 1$.

3. Each participant also computes the secret exponent $d_i, 1 \le d_i \le \varphi_i$, such that $e_i d_i \equiv 1 \bmod \varphi$.

The public keys are $Kpu_i = (e, N_i)$ and private keys are $Kpr_i = (d_i, p_i, q_i)$. Participant keeps d_i, p_i, q_i and φ_i secret.

4. Participants share the public keys - $Kpu_1, Kpu_2, ..., Kpu_n$ with the dealer and combiner.

Let, H is a suitable collision resistance one-way hash function, which takes an input as a binary string of variable length and outputs a hash-code which is a binary string with fixed length.

Construction of Shares

1. Dealer (*D*) uses a suitable random number generation function to generate n distinct random integers - $r_1, r_2, ..., r_n$.

2. *D* considers a polynomial function of Shamir's (t, n)-threshold secret sharing is in following form

$$F(x) = \left(S + a_1 x + a_2 x^2 + ... + a_{t-1} x^{t-1} \right) \bmod p$$

Then, the intermediate shares are computed as
$$s_1 = (r_1, F(r_1)), s_2 = (r_2, F(r_2)), ..., s_n = (r_n, F(r_n))$$

3. *D* encrypts the random numbers r_i with the public keys Kpu_i as follows:

$$Er_i = r_i^{e_i} \bmod N \text{ for } i = 1, 2, ..., n$$

4. *D* applies hash function *H* to generate hash code h_i for each $(Er_i, F(r_i))$ as

$$h_i = H \left(Er_i, F(r_i) \right) \text{ for } i = 1, 2, ..., n$$

5. *D* distributes the shares as follows:

$$sh_i = \left(Er_i, F(r_i) \right) \text{ for } i = 1, 2, ..., n$$

6. *D* also applies the hash-function *H* on the secret *S* as - $h_s = H(S)$. Dealer publishes h_s.

7. *D* also publishes $h_1, h_2, ..., h_n$.

Recovery of Secret

1. The participant - P_i extracts Er_i out of his/her sh_i and decrypts it as

$$r_i = Er_i^{d_i} \bmod N.$$

2. P_i submits $sh_i = (r_i, F(r_i))$ to the combiner.

3. If combiner (C) obtains t or more $(\leq n)$ shares in form of $(r_i, F(r_i))$, he/she can applies Shamir's secret sharing to interpolate the value of secret $S = F(0)$.

Verifications

1. After receiving the share from D, each participant - P_i can verify if the obtained share has been modified by any intruder at the public channel. Participant P_i applies the hash-function to his/her share sh_i to obtain the hash-code h_i^* and confirms $h_i^* \overset{?}{=} h_i$. If $h_i^* \neq h_i$, then sh_i has been modified.

2. The combiner or participants can regenerate the hash-code for the obtained secret S^* as - $h_s^* = H(S^*)$ and verify with h_s as $h_s^* \overset{?}{=} h_s$ to confirm that it is the actual secret. If it does not match, then either one or more participants has supplied faked shares or the dealer is the dishonest (has supplied false share(s)). To verify the shares, combiner (C) can regenerate $sh_i = (Er_i, F(r_i))$ from $(r_i, F(r_i))$ using the corresponding public key (Kpu_i). C applies hash function H to obtain the hash-code h_i^*. If $h_i^* \neq h_i$ then the S_i share is faked and P_i is the identified cheater. If none of the shares is faked, then the dealer is identified as dishonest.

Proposed Model for Multi-Secret Sharing

Our $(t, k, n)-$ threshold multi-secret sharing scheme assumes the following:

- The k secrets are - $S_1, S_2, ..., S_k$.
- The n participants are - $P_1, P_2, ..., P_n$.
- H is a suitable, collision resistant, one-way hash function.

Initialization Phase

1. Each participant P_i, ($i = 1, 2, ..., n$) considers two large prime p_i, q_i and computes the following:

$$N_i = p_i q_i \text{ and } \varphi_i = (p_i - 1)(q_i - 1).$$

2. Each P_i chooses an integer $e_i, 1 \leq e_i \leq \varphi$, such that $\gcd(e_i, \varphi_i) = 1$.

3. Each P_i also computes the secret exponent $d_i, 1 \leq d_i \leq \varphi_i$, such that $e_i d_i \equiv 1 \bmod \varphi$.
The public keys are $Kpu_i = (e, N_i)$ and private keys are $Kpr_i = (d_i, p_i, q_i)$ for $i = 1, 2, ..., n$. P_i keeps $d_i, p_{i,}, q_i$ and φ_i secret.

4. Participants $P_i, i = 1, 2, ..., n$ share the public keys - $Kpu_1, Kpu_2, ..., Kpu_n$ with the dealer (D) and

combiner (C). D ensures the public keys are unique otherwise demand a new public key.

Construction Phase

1. Dealer D chooses a suitable random number generator and generates random numbers $r_1, r_2, ..., r_n$.

2. D applies the hash-function H on the secrets as

$$h_{s_i} = H(S_i) \text{ for } i = 1, 2, ..., k$$

Concatenate all h_{s_i} to compute h_s as

$$h_s = \left(h_{s_1} \| h_{s_2} \| ... \| h_{s_k} \right);$$

3. Consider the polynomial as follow

$$if\ (k \leq t)$$

3.1. Construct a polynomial $F(x)$ of degree $(t-1)$:

$$F(x) = S_1 + S_2 x + ... + S_k x^{k-1} + a_1 x^k + a_2 x^{k+1}$$
$$+ ... + a_{t-k} x^{t-1} \bmod p;$$

where p is the large prime number and $0 < S_1, S_2, ..., S_k, a_1, a_2, ..., a_{t-k} < p$.

3.2. D computes $y_i = F(r_i) \bmod p$ for $i = 1, 2, ..., n$.

$$if\ (k > t)$$

3.3. Construct a polynomial $F(x)$ of degree $(k-1)$:

$$F(x) = S_1 + S_2 x + ... + S_k x^{k-1} \bmod p;\ ,$$

where p is a large prime and $0 < S_1, S_2, ..., S_k < p$.

3.4. D computes $y_i = F(r_i) \bmod p$ for $i = 1, 2, ..., n$ and also computes $F(i) \bmod p$ for $i = 1, 2, ..., k-t$.

3.5. D publishes $F(i) \bmod p$ for $i = 1, 2, ..., k-t$.

4. Dealer encrypts the random numbers r_i with the public keys Kpu_i as follows:

$$Er_i = r_i^{e_i} \bmod N \text{ for } i = 1, 2, ..., n$$

5. Use hash function H to generate hash code h_i for each (Er_i, y_i).

$$h_i = H(Er_i, y_i) \text{ for } i = 1, 2, ..., n$$

6. D publishes $(h_s, h_1, h_2, ..., h_n)$.

7. *D* distributes the shares as follows:

$$sh_i = \left(Er_i, y_i \right) \text{ for } i = 1, 2, ..., n$$

Recovery Phase

1. Participant (P_i) extracts Er_i from sh_i and decrypts it as

$$r_i = Er_i^{d_i} \bmod N.$$

2. Submit $\left(r_i, y_i \right)$ to the combiner (*C*).

3. If combiner (*C*) obtains all t or more ($\leq n$) shares in form of $\left(r_i, y_i \right)$, then the k secrets can be revealed by the reconstructing the unique polynomial $F(x)$ as follows:

$$if \left(k \leq t \right)$$

$$F(x) = \sum_{i=1}^{t} y_i \prod_{j=1, j \neq i}^{t} \frac{x - r_j}{r_i - r_j} \bmod p$$

$$= S_1 + S_2 x + ... + S_k x^{k-1} + a_1 x^k + a_2 x^{k+1} + ...$$

$$+ a_{t-k} x^{t-1} \bmod p$$

$$if \left(k > t \right)$$

$$F(x) = \sum_{i=1}^{t} y_i \prod_{j=1, j \neq i}^{t} \frac{x - r_j}{r_i - r_j} \bmod p$$

$$+ \sum_{i=1}^{k-t} F(i) \prod_{j=1, j \neq i}^{k-t} \frac{x - j}{i - j} \bmod p$$

$$= S_1 + S_2 x + ... + S_k x^{k-1} \bmod p$$

Verifications

1. After receiving the share (sh_i^*) from the dealer, each participant (P_i) can verify $H\left(sh_i^* \right) \overset{?}{=} h_i$ to satisfy that the share is not modified or corrupted on the channel.

2. As t or more ($\leq n$) shares (sh_i^*) are pooled by the combiner (*C*). *C* can reconstruct the k secrets as $S_1^*, S_2^*, ..., S_k^*$ and also calculates $h_s^* = H\left(S_1^* \right) \| H\left(S_2^* \right) \| ... \| H\left(S_k^* \right)$. Thus, *C* can verify that the obtained secrets are the actual secrets or not by examining $h_s^* \overset{?}{=} h_s$.

If the obtained secrets are not true secrets ($h_s^* \neq h_s$), then either a few participants are cheaters or the dealer (*D*) is dishonest. The combiner can verify $H\left(sh_i^* \right) \overset{?}{=} h_i$ (as *C* possesses the public key Kpu_i for P_i, so *C* can recalculate sh_i^* from obtained $\left(r_i^*, F(r_i)_i^* \right)$) to ensure that the shares submitted by the participants are not faked. If $H\left(sh_i^* \right) \neq h_i$, then sh_i is faked and P_i is the cheater. But in the case

$H\left(sh_i^* \right) = h_i$ for all $i = 1, 2, ..., t$, then the dealer (*D*) must be the dishonest and provided fake shares to one or more participants.

5. Performance

The performance features for the scheme proposed in [2] are as follow:

Robustness – A $\left(t, n \right)$ – threshold secret sharing scheme is called robust if any t or more ($\leq n$) participants can reconstruct the full secret information. Shamir's secret sharing already holds this property.

Confidentiality - A $\left(t, n \right)$ – threshold secret sharing scheme holds confidentiality, if no information about the secret can be obtained if less than t shares are pooled.

Shamir's secret sharing already holds the property, along with that, the proposed scheme also promises that any malicious user learned the encrypted shares on the public channel had no clue about the *x*-values. Hence, malicious users or intruders cannot obtain a useful share.

Traceability - A $\left(t, n \right)$ – threshold secret sharing holds traceability, if it is able to detect any participant P_i who sends a fake share $S_i^* \neq S_i$ to the combiner. The proposed method utilizes hash function to make the shares verifiable.

Participant authentication and verification of shares – In the proposed scheme only a legal participant holds the legal private key to access his/her share (as the share is encrypted by corresponding public key by the dealer).

No need to have a secure channel for distribution – as the *x*-values are encrypted with the pubic keys before distribution, only the legal participants (the one possess the private key) can receive the *x*-values.

Verifiable secret – Hash-function ensures the correctness of the secret, obtained from the shares.

Comparisons between different secret sharing schemes based on verifiability of shares and secrets are shown in Table 1.

Our proposed verifiable $\left(t, k, n \right)$ – threshold multi-secret sharing scheme supports all the above mentioned attributes. As the MSS scheme is also based on Lagrange Interpolation, *robustness* and *confidentiality* are assured. If t or more ($\leq n$) shares are obtained the all k secrets can be revealed. Otherwise (with the number of shares $< t$) none of the secrets can be achieved.

The traceability property is assured by use of hash-function.

The proposed scheme is also *t-consistent*, i.e. if the share s_i^* received by participant P_i passes the validity checking, it is guaranteed to be the valid ith share ($s_i^* = s_i$) for the k given secrets. The *t-consistent* property also assured by use of hash-function.

Table 1. Comparison between secret sharing schemes.

Scheme by	Secure distribution	Verification of shares	Verification of secret
Zhao, *et al.* in [21] (2009)	Yes	No	No
Harn, *et al.* in [11] (2009)	No	Yes	No
Ulutas, *et al.* in [18] (2011)	Yes	Yes	No
Harn, *et al.* in [12] (2014)	No	Yes	Yes
Liu, *et al.* in [22] (2015)	No	Yes	Yes
Liu, *et al.* in [23] (2016)	No	Yes	Yes
Our proposed scheme	Yes	Yes	Yes

6. Conclusions

Shamir's secret sharing scheme requires a secure channel to deliver the shares to the participants because it cannot resist attacks on the distribution channel. If the shares are communicated through insecure channel, then malicious users may learn the shares and with sufficient shares may reconstruct the secret. The same is true for any multi-secret sharing scheme which is based on Shamir's secret sharing scheme. In our proposed multi-secret sharing scheme, we have employed a method where some parts of the shares are communicated in encrypted form over a public channel. The shares only can be decrypted by authorized participants. Our proposed scheme also possesses properties to verify, whether the shares received by shareholders are consistent under the condition the secrecy of shares and secret both are maintained.

References

[1]. A. Boldyreva, M. Fischlin, On the Security of OAEP, in *Proceedings of the Advances in Cryptology – ASIACRYPT'06*, Vol. 4284, 2006, pp. 210-225.

[2]. A. K. Chattopadhyay, A. Nag, K. Majumder, A Verifiable and Cheating Resistant Secret Sharing Scheme, in *Proceedings of the International Conference on Advancement of Computer Communication & Electrical Technology (ACCET'16)*, Berhampore, India, October, 2016, pp. 264-268.

[3]. A. Shamir, How to Share a Secret, *Communications of the ACM*, Vol. 22, Issue 11, 1979, pp. 612-613.

[4]. C. Asmuth, J. Bloom, A Modular Approach to Key Safeguarding, *IEEE Transactions on Information Theory*, Vol. 29, Issue 2, 1983, pp. 208-210.

[5]. C.-C. Thien, J.-C. Lin, Secret image sharing, *Computers and Graphics*, Vol. 26, Issue. 5, 2002, pp. 765-770.

[6]. C.-C. Yang, T.-Y. Chang, M.-S. Hwang, A *(t, n)* multi-secret sharing scheme, *Applied Mathematics and Computation*, Vol. 151, Issue 2, 2004, pp. 483-490.

[7]. G. R. Blakley, Safeguarding cryptographic keys, in *Proceedings of the International Workshop on Managing Requirements Knowledge*, New York, June, 1979, pp. 313-317.

[8]. J. Zhao, J. Zhang, R. Zhao, A practical verifiable multi-secret sharing scheme, *Computer Standards & Interfaces*, Vol. 29, Issue 1, 2007, pp. 138-141.

[9]. J. Shao, Efficient verifiable multi-secret sharing scheme based on hash function, *Information Sciences*, Vol. 278, 2014, pp. 104-109.

[10]. J. Shao, Z. Cao, A new efficient *(t, n)* verifiable multi-secret sharing (VMSS) based on YCH scheme, *Applied Mathematics and Computation*, Vol. 168, Issue 1, 2005, pp. 135-140.

[11]. L. Harn, C. Lin, Detection and identification of cheaters in *(t, n)* secret sharing scheme, *Designs, Codes and Cryptography,* Vol. 52, No. 1, 2009, pp. 15-24.

[12]. L. Harn, M. Fuyou, C-C. Chang, Verifiable secret sharing based on the Chinese remainder theorem, *Security and Communication Networks*, Vol. 7, Issue 6, 2014, pp. 950-957.

[13]. M. Bellare, P. Rogaway, Random Oracles are Practical: A Paradigm for Designing Efficient Protocols, in *Proceedings of the 1st ACM Conference on Computer and Communications Security (CSS'93),* New York, NY, USA, 1993, pp. 62-73.

[14]. M. Bellare, P. Rogaway, Optimal Asymmetric Encryption - How to Encrypt with RSA, in *Proceedings of the Eurocrypt'94,* 1995, pp. 1-19.

[15]. M. H. Dehkordi, S. Mashhadi, An efficient threshold verifiable multi-secret sharing, *Computer Standards & Interfaces*, Vol. 30, Issue 3, 2008, pp. 187-190.

[16]. M. H. Dehkordi, S. Mashhadi, New efficient and practical verifiable multi-secret sharing schemes, *Information Sciences*, Vol. 178, Issue 9, 2008, pp. 2262-2274.

[17]. M. Mignotte, How to share a secret, in *Proceedings of the Workshop on Cryptography*, Burg Feuerstein, Germany, March-April, 1982, pp. 371-375.

[18]. M. Ulutas, G. Ulutas, V. V. Nabiyev, Medical image security and EPR hiding using Shamir's secret sharing scheme, *Journal of Systems and Software*, Vol. 84, No. 3, 2011, pp. 341-353.

[19]. R.-J. Hwang, C.-C. Chang, An on-line secret sharing scheme for multi-secrets, *Computer Communications*, Vol. 21, Issue 13, 1998, pp. 1170-1176.

[20]. R. L. Rivest, A. Shamir, L. Adleman, A method for obtaining digital signatures and public key cryptosystems, *Communications of the ACM*, Vol. 21, No. 2, 1978, pp. 120-126.

[21]. R. Zhao, J.-J. Zhao, F. Dai, F-Q, Zhao, A new image secret sharing scheme to identify cheaters, *Computer Standards & Interfaces*, Vol. 31, Issue 1, 2009, pp. 252-257.

[22]. Y. Liu, L. Harn, C.-C. Chang, A novel verifiable secret sharing mechanism using theory of numbers and a method for sharing secrets, *International Journal of Communication Systems*, Vol. 28, No. 7, 2015, pp. 1282-1292.

[23]. Y. Liu, C. Chang, An Integratable Verifiable Secret Sharing Mechanism, *International Journal of Network Security*, Vol. 18, No. 4, 2016, pp. 617-624.

Convergence Property of Relaxation Rabling Under Two-Way Sinkhon Normalization

Jong-Ha Lee

Dept. of Biomedical Engineering, Keimyung University, Daegu, South Korea
E-mail: segeberg@gmail.com

Abstract: This article describes the convergence property of relaxation Rabling under two-way Sinkhon normalization. This method can be used in non-rigid image registration and point matching. In this article, we have used Shinkon normalization to prove it.

Keywords: Point matching, Relaxation, Normalization, Medical imaging.

1. Introduction

The point matching is widely used in computer vision and pattern recognition because point representations are generally easy to extract. Point matching can be categorized as rigid matching and non-rigid matching based on the deformation of objects captured in the image. Compare with the rigid case, non-rigid matching is more complicated. Generally, there are two unknown operations: correspondence and transformation. Most non-rigid point matching approaches use an iterated estimation framework to find appropriate correspondence and transformation [1]. The Iterated Closest Point (ICP) algorithm is one of the most well known heuristic approaches. It utilizes the relationship by assigning the correspondence with binary values zero and one. However, this binary assumption is no longer valid in the case of non-rigid transformation, especially when the deformations are large [2]. The Thin Plate Spline Robust Point Matching (TPS-RPM) algorithm is an Expectation Maximization (EM) algorithm to jointly solve for the feature correspondence as well as the geometric transformation. The cost function that is being minimized is the sum of Euclidean distances between points. In the TPS-RPM, the binary correspondence value of the ICP is relaxed to the

continuous value between zero and one. This soft-assign method improves the matching performance because the correspondences are able to improve gradually and continuously without jumping around in the space of binary permutation matrices [3-4]. The algorithm is robust compared to the ICP in the non-rigid case, but the joint estimation of correspondences and transformation increases complexity. In addition, the Euclidean distance makes sense only when there are at least rough initial alignments of the shapes. If the initialization is not aligned well, the matching result is poor. Recently, the Shape Context (SC) algorithm has been proposed. It is an object recognizer based on the shape. For each point, the distribution of the distance and orientation are estimated to the neighboring points through a histogram [5]. This distribution is used as the attribute relations for the points. The correspondences can be decided by comparing each point's attributes in one set with the attributes of the other. Because only the attributes are compared, the searching for the correspondences can be conducted more easily compared to the ICP and the TPS-RPM. Generally, the SC performs better in handling complex patterns than the TPS-RPM. Another interesting approach of point matching is a kernel correlation-based point matching. The cost function is proportional to the correlation of two

kernel density estimates. The work was extended by using the L2 distance between mixtures of Gaussian representing the point set data in. The Coherent Point Drift (CPD) algorithm is another probabilistic algorithm [6]. They proposed to use the displacement filed between the point sets following the motion coherence theory. They also successfully extend the general non-rigid registration framework, and show that TPS-RPM is its special case [7]. The Robust Point Matching by preserving Local Neighborhood Structures (RPM-LNS) introduces the notion of a neighborhood structure for the general point matching problem. The RPM-LNS uses a relaxation labeling method with binary value coefficient. This approach is based on the assumption that although the absolute distance between two points may change significantly under non-rigid deformation, the neighborhood structure of a point is generally well preserved. The cost function is formulated as an optimization problem to preserve local neighborhood relations. This research shows the convergence property of relaxation Rabling under two-way Sinkhon normalization. This method can be used in non-rigid image registration and point matching. In this paper, we used Shinkon normalization to prove it.

2. Problem Definition

Let $S = \{s_1, s_2, ..., s_M\}$ be a set of points in a model shape and $T = \{t_1, t_2, ..., t_N\}$ be a set of points in the target shape. In a point matching problem, one-to-one matching is desired, but in general, one-to-one matching is not possible because of outliers. To handle this problem, two point sets are augmented to $S' = \{s_1, s_2, ..., s_M, nil\}$ and $T' = \{t_1, t_2, ..., t_N, nil\}$ by introducing a dummy point *nil*. Then a match between shapes S and T is $f: S' \Leftrightarrow T'$ and common points can be matched one-to-one and outliers can be matched to a dummy point *nil*. Under a rigid transformation (transformation and rotation), the distance between any pair of points is preserved. Therefore, the optimal match $\hat{f}$ is

$$\hat{f} = arg \min_{f} C(S, T, f),$$

where

$$C(T, D, f) = \sum_{m=1}^{M} \sum_{i=1}^{M} (\|s_m - s_i\| - \|f(s_m) - f(s_i)\|)^2$$
$$+ \sum_{n=1}^{N} \sum_{j=1}^{N} (\|t_n - t_j\| - \|f(t_n) - f(t_j)\|)^2.$$

If a non-rigid transformation is present, the distance between a pair of points will not be preserved, especially for points which are far apart. On the other hand, due to physical constraints, and in order to

preserve the rough structure, the local neighborhood of a point may not change freely. We therefore define the local neighborhood of a point. For a given point, $s_m \in S'$, a neighbor point is $\mathcal{N}_i^{s_m}$, $i = 1, 2, ..., I$. Similarly, for a given point, $t_n \in T'$, a neighbor point is $\mathcal{N}_j^{t_n}$, $j = 1, 2, ..., J$. Since the only distance of neighboring point pairs are preserved, (2) becomes

$$C(T, D, f) = \sum_{m=1}^{M} \sum_{i=1}^{I} (\|s_m - \mathcal{N}_i^{s_m}\| - \|f(s_m) - f(\mathcal{N}_i^{s_m})\|)^2$$
$$+ \sum_{n=1}^{N} \sum_{j=1}^{J} (\|t_n - \mathcal{N}_j^{t_n}\| - \|f(t_n) - f(\mathcal{N}_j^{t_n})\|)^2$$

We quantize the distance to two levels as

$$\| s_m - \mathcal{N}_i^{s_m} \| = \begin{cases} 1 \text{ if } s_m \in \mathcal{N}_i^{s_m} \\ 0 \text{ if } s_m \notin \mathcal{N}_i^{s_m} \end{cases},$$

$$\| f(s_m) - f(\mathcal{N}_i^{s_m}) \| = \begin{cases} 1 \text{ if } f(s_m) \in \mathcal{N}_i^{f(s_m)} \\ 0 \text{ if } f(s_m) \notin \mathcal{N}_i^{f(s_m)} \end{cases},$$

$$\| t_n - \mathcal{N}_j^{t_n} \| = \begin{cases} 1 \text{ if } t_n \in \mathcal{N}_j^{t_n} \\ 0 \text{ if } t_n \notin \mathcal{N}_j^{t_n} \end{cases},$$

$$\| f(t_n) - f(\mathcal{N}_j^{t_n}) \| = \begin{cases} 1 \text{ if } f(t_n) \in \mathcal{N}_j^{f(t_n)} \\ 0 \text{ if } f(t_n) \notin \mathcal{N}_j^{f(t_n)} \end{cases}.$$

Equation ( ) then is simplified to

$$C(T, D, f) = \sum_{m=1}^{M} \sum_{i=1}^{I} d(s_m, \mathcal{N}_i^{s_m})$$
$$+ \sum_{n=1}^{N} \sum_{j=1}^{J} d(t_n, \mathcal{N}_j^{t_n}),$$

where

$$d(s_m, \mathbb{N}_i^{s_m}) \in \begin{cases} 1 \text{ if } s_m \notin \mathbb{N}_i^{s_m} \text{ or } f(s_m) \notin \mathbb{N}_i^{f(s_m)} \\ 0 \text{ if } s_m \in \mathbb{N}_i^{s_m} \text{ and } f(s_m) \in \mathbb{N}_i^{f(s_m)} \end{cases}$$

and

$$d(t_n, \mathcal{N}_j^{t_n}) \in \begin{cases} 1 \text{ if } t_m \notin \mathcal{N}_j^{t_m} \text{ or } f(t_m) \notin \mathcal{N}_j^{f(t_m)} \\ 0 \text{ if } t_m \in \mathcal{N}_j^{t_m} \text{ and } f(t_m) \in \mathcal{N}_j^{f(t_m)} \end{cases}.$$

Simple deduction makes to convert the above minimization problem to a maximization problem.

$$\hat{f} = arg \max_{f} K(S, T, f),$$

$$K(T,D,f) = \sum_{m=1}^{M} \sum_{i=1}^{I} \delta(s_m, \mathcal{N}_i^{s_m})$$
$$+ \sum_{n=1}^{N} \sum_{j=1}^{J} \delta(t_n, \mathcal{N}_j^{t_n}) \ ,$$

where $\delta(i,j) = 1 - d(i,j)$.

In this paper, the point matching problem is restated as the graph isomorphism problem [12]. The optimal solution of ( ) is the one that maximizes the number of matched edges of two graphs. Each point is a node of a graph, and a point and its adjacent point constitute the edges of the graph. Then the problem is to maximize the number of matched edges between two graphs. For this purpose, we determine the fuzzy correspondence matrix P with dimension $(M+1) \times (N+1)$. Each entry of P has continuous value between [0,1] that indicates the weight of the correspondence between s_m and t_n. The optimal match $\hat{P}$ is found by maximizing the energy function as follows.

$$\hat{P} = arg \max_P E(P),$$

where

$$E(P) = \sum_{m=1}^{M} \sum_{i=1}^{I} \sum_{n=1}^{N} \sum_{j=1}^{J} P_{mn} P_{ij}.$$

subject to

$$\sum_{m=1}^{M+1} P_{mn} = 1, \ \forall n, \ \sum_{n=1}^{N+1} P_{mn} = 1, \ \forall m, \ P_{mn} \in [0,1].$$

3. Relaxation Labeling

Start with a set of nodes i and a set of labels λ. Derive a set of compatibility coefficients r for each problem of interest and then apply the basic recipe of relaxation labeling for updating the node-label assignments:

$$q_i(\lambda) = \sum_{j=1} \sum_{\mu=1} r_{ij}(\lambda, \mu) p_j(\mu),$$

$$p_i(\lambda)^{(n+1)} = \frac{p_i(\lambda)^{(n)}(1 + \alpha q_i(\lambda)^{(n)})}{\sum_{\mu=1} p_i(\mu)^{(n)}(1 + \alpha q_i(\mu)^{(n)})}$$

Now, we prove that the relaxation labeling process always converges with two way constraints ( ). The common framework of prediction algorithm is as follows.

$$F(p, \sigma) = E(p) + \frac{1}{\alpha} d(p, \sigma),$$

where $d(p, \sigma)$ is a distance measure between p and an "old" value σ.

Examine the following objective function using the generalized KL divergence as the distance measure:

$$E(M, \sigma, \mu, v, \alpha) = -\sum_{i=1}^{I} \sum_{b=1}^{B} \sum_{j=1}^{J} \sum_{a=1}^{A} M_{p_i q_j} M_{\mathcal{N}_a^{p_i} \mathcal{N}_b^{q_j}}$$
$$+ \frac{1}{\alpha} \sum_{i=1}^{I} \sum_{j=1}^{J} (M_{p_i q_j} \log \frac{M_{p_i q_j}}{\sigma_{p_i q_j}}$$
$$- M_{p_i q_j} + \sigma_{p_i q_j})$$
$$+ \sum_{i=1}^{I+1} \mu_i (\sum_{j=1}^{J+1} M_{p_i q_j} - 1)$$
$$+ \sum_{j=1}^{J+1} v_j (\sum_{i=1}^{I+1} M_{p_i q_j} - 1)$$

Instead of solving for the Lagrange parameter vectors μ and V, we use Sinkorn's theorem instead to ensure that the row and column constrains satisfied. From our assumption of exact convergence of Sinkorn, it follows that the Lagrange parameter vectors μ and V can be dropped from the energy function.

We first formalize a few definitions.

Algorithm 1: (Shinkhorn Scaling Algorithm)

Given a nonnegative, $m \times n$ matrix A, and specified vectors of the row sums ($r \in \mathbb{R}^m$) and column sums ($c \in \mathbb{R}^m$), we iterate the following until convergence, with initial values $a_{ij}^{(0)} = a_{ij}$, and $k = 1$:

1) Multiple every element $a_{ij}^{(k-1)}$ by the ratio of the desired row sum r_i to the actual row sum

$$\sum_{j=1}^{n} a_{ij}^{(k-1)} \ , \ a_{ij}^{(k)} = r_i a_{ij}^{(k-1)} / (\sum_{j=1}^{n} a_{ij}^{(k-1)})$$

2) Multiple every element $a_{ij}^{(k)}$ of the matrix from (1) by the ratio of the desired column sum c_j to the actual column sum $\sum_{i=1}^{m} a_{ij}^{(k)} \ , \ a_{ij}^{(k^*)} = c_j a_{ij}^{(k)} / (\sum_{i=1}^{m} a_{ij}^{(k)})$.

It can be shown that with any given matrix A, Sinkorn scaling process will converge to a unique matrix B that satisties the row and column sum constraints. The following theorem is a unified statement of the convergence of the Sinkorn scaling process, from various previous results in the literature.

Theorem 1: Consider $A \in \mathbb{R}^{m \times n}$, a nonnegative matrix, and desired row sums $r \in \mathbb{R}^m$ and column sums $c \in \mathbb{R}^n$. Then there exists a unique matrix

$B \in \mathbb{R}^{m \times n}$ which satisties these prescribed row and column sums, where $B = D_1 A D_2$ for $D_1 \in \mathbb{R}^{m \times m}$ and $D_2 \in \mathbb{R}^{n \times n}$, D_1 and D_2 both diagonal, positive definite matrices.

If we assume that Sinkhorn procedure always returns a doubly stochastic matrix.

Then we have used the generalized KL divergence which is guaranteed to be greater than or equal to zero without requiring the usual constraints

$$\Delta F \overset{def}{=} F(M^{(t)}) - F(M^{(t+1)})$$

$$= -\sum_{i=1}^{I}\sum_{b=1}^{B}\sum_{j=1}^{J}\sum_{a=1}^{A} M^{(t)}_{p_i q_j} M^{(t)}_{\mathcal{N}_a^{p_i}\mathcal{N}_b^{q_j}}$$

$$+\frac{1}{\alpha}\sum_{i=1}^{I}\sum_{j=1}^{J}(M^{(t)}_{p_i q_j}\log\frac{M^{(t)}_{p_i q_j}}{\sigma_{p_i q_j}} - M^{(t)}_{p_i q_j} + \sigma_{p_i q_j})$$

$$+\sum_{i=1}^{I}\sum_{b=1}^{B}\sum_{j=1}^{J}\sum_{a=1}^{A} M^{(t+1)}_{p_i q_j} M^{(t+1)}_{\mathcal{N}_a^{p_i}\mathcal{N}_b^{q_j}}$$

$$-\frac{1}{\alpha}\sum_{i=1}^{I}\sum_{j=1}^{J}(M^{(t+1)}_{p_i q_j}\log\frac{M^{(t+1)}_{p_i q_j}}{\sigma_{p_i q_j}}$$

$$- M^{(t+1)}_{p_i q_j} + \sigma_{p_i q_j})$$

$$E(M,\sigma,\mu,\nu,\alpha) = -\sum_{i=1}^{I}\sum_{b=1}^{B}\sum_{j=1}^{J}\sum_{a=1}^{A} M_{p_i q_j} M_{\mathcal{N}_a^{p_i}\mathcal{N}_b^{q_j}}$$

$$+\frac{1}{\alpha}\sum_{i=1}^{I}\sum_{j=1}^{J}(M_{p_i q_j}\log\frac{M_{p_i q_j}}{\sigma_{p_i q_j}} - M_{p_i q_j} + \sigma_{p_i q_j})$$

$$+\sum_{i=1}^{I+1}\mu_i(\sum_{j=1}^{J+1} M_{p_i q_j} - 1)$$

$$+\sum_{j=1}^{J+1}\nu_j(\sum_{i=1}^{I+1} M_{p_i q_j} - 1)$$

$$\Delta F \overset{def}{=} \sum_{i=1}^{I}\sum_{b=1}^{B}\sum_{j=1}^{J}\sum_{a=1}^{A}\Delta M_{p_i q_j}\Delta M_{\mathcal{N}_a^{p_i}\mathcal{N}_b^{q_j}}$$

$$+\frac{1}{\alpha}\sum_{i=1}^{I}\sum_{j=1}^{J} M^{(t)}_{p_i q_j}\log\frac{M^{(t)}_{p_i q_j}}{M^{(t+1)}_{p_i q_j}} \geq 0$$

$$\Delta F \overset{def}{=} F(M^{(t)}) - F(M^{(t+1)})$$

$$= -\sum_{i=1}^{I}\sum_{b=1}^{B}\sum_{j=1}^{J}\sum_{a=1}^{A} M^{(t)}_{p_i q_j} M^{(t)}_{\mathcal{N}_a^{p_i}\mathcal{N}_b^{q_j}}$$

$$+\frac{1}{\alpha}\sum_{i=1}^{I}\sum_{j=1}^{J}(M^{(t)}_{p_i q_j}\log\frac{M^{(t)}_{p_i q_j}}{\sigma_{p_i q_j}} - M^{(t)}_{p_i q_j} + \sigma_{p_i q_j})$$

$$+\sum_{i=1}^{I}\sum_{b=1}^{B}\sum_{j=1}^{J}\sum_{a=1}^{A} M^{(t+1)}_{p_i q_j} M^{(t+1)}_{\mathcal{N}_a^{p_i}\mathcal{N}_b^{q_j}}$$

$$-\frac{1}{\alpha}\sum_{i=1}^{I}\sum_{j=1}^{J}(M^{(t+1)}_{p_i q_j}\log\frac{M^{(t+1)}_{p_i q_j}}{\sigma_{p_i q_j}} - M^{(t+1)}_{p_i q_j} + \sigma_{p_i q_j}),$$

where $\Delta M_{p_i q_j} \overset{def}{=} \Delta M^{(t+1)}_{p_i q_j} - \Delta M^{(t)}_{p_i q_j}$ and $\Delta M_{\mathcal{N}_a^{p_i}\mathcal{N}_b^{q_j}} \overset{def}{=} \Delta M^{(t+1)}_{\mathcal{N}_a^{p_i}\mathcal{N}_b^{q_j}} - \Delta M^{(t)}_{\mathcal{N}_a^{p_i}\mathcal{N}_b^{q_j}}$. The first term is nonnegative due to the positive definiteness in the subspace spanned by the row and column constraints. The second term is non-negative by virtue of being a KL distance measure. We have shown the convergence to a fixed point of the relaxation labeling under Sinkhorn scaling.

This is a consequence of the following extension to the well-known Birkoff-von Neumann theorem: the set of doubly stochastic matrices is the convex hull of the set of permutation matrices and outliers. So it can be ensured that we will always achieve one-to-one correspondence.

Complexity and Convergence of Sinkhorn Scaling

The Sinkhorn iterations are a natural way of scaling a matrix to achieve prescribed row and column sums. While Sinkorn proved that the iterative procedure converges for appropriate matrices, it could take a very long time to reach a desired accuracy ($b_{ij} < \varepsilon$). In our algorithm, however, we set $b_{ij} < 0.95$ as an outlier by matching them a dummy point and set as 0. This way improves the rate of convergence of Sinkorn process significantly.

4. Transformation Function

Given a finite set of correspondences between, one can proceed to estimate a plane transformation. $f : \mathfrak{R}^2 \to \mathfrak{R}^2$ or $f : \mathfrak{R}^3 \to \mathfrak{R}^3$ that may be used to map arbitrary points from one image to the other. In this study, we mostly use the thin plate spline (TPS) model, which is commonly used for representing flexible coordinate transformations. Bookstein found it to be highly effective for modeling changes in biological forms. Powell applied the TPS model to recover transformations between curves. The thin plate spline is the 2D generalization of the cubic spline. In its regularized form, which is discussed below, the TPS model includes the affine model as a special case.

Let v_i denote the target function values at corresponding locations $p_i = (x_i, y_i)$ in the plane, with $i = 1, 2, ..., n$. In particular, we will set v_i equal to x_i' and y_i' in turn to obtain one continuous transformation for each coordinate. We assume that the locations (x_i, y_i) are all different and are not collinear. In 2-D interpolation problem, the TPS interpolant $f(x, y)$ minimizes the bending energy

$$I_f = \int\int_{\mathbb{R}^2}\left[\left(\frac{\partial^2 f}{\partial x^2}\right)^2 + 2\left(\frac{\partial^2 f}{\partial x \partial y}\right)^2 + \left(\frac{\partial^2 f}{\partial y^2}\right)^2\right]dxdy$$

and has the form

$$f(x,y) = a_1 + a_x x + a_y y + \sum_{i=1}^{n} w_i U(\|(x_i, y_i) - (x, y)\|)$$

If the problem is 3-D interpolation, the bending energy is

$$I_f = \iiint_{\mathbb{R}^3} \left[\begin{array}{c} \left(\dfrac{\partial^2 f}{\partial x^2}\right)^2 + \left(\dfrac{\partial^2 f}{\partial y^2}\right)^2 + \left(\dfrac{\partial^2 f}{\partial z^2}\right)^2 \\ + 2\left(\left(\dfrac{\partial^2 f}{\partial x \partial y}\right)^2 + \left(\dfrac{\partial^2 f}{\partial x \partial z}\right)^2 + \left(\dfrac{\partial^2 f}{\partial y \partial z}\right)^2\right) \end{array} \right] dxdydz$$

and the interpolant form is

$$f(x,y,z) = a_1 + a_x x + a_y y + a_z z$$
$$+ \sum_{i=1}^{n} w_i U(\|(x_i, y_i, z_i) - (x, y, z)\|)$$

The kernel function $U(r)$ is defined by $U(r) = r^2 \log r^2$ and $U(0) = 0$ as usual. In order for $f(x,y)$ to have square integrable second derivatives, we require the boundary condition as

$$\sum_{i=1}^{n} w_i = 0 \text{ and } \sum_{i=1}^{n} w_i x_i = \sum_{i=1}^{n} w_i y_i = 0.$$

A special characteristic of the thin-plate spline is that the resulting transformation is always decomposed into a global transformation and a local non-affine warping component. The first three terms in 2-D and four terms in 3-D case describes global affine transform and rest terms describe non-linear (nonglobal) transformation.

Together with the interpolation conditions, $f(x_i, y_i) = v_i$, this yields a linear system for the TPS coefficients:

$$\begin{pmatrix} K & P \\ P^T & 0 \end{pmatrix} \begin{pmatrix} W \\ A \end{pmatrix} = \begin{pmatrix} V \\ 0 \end{pmatrix},$$

where $K = \begin{bmatrix} 0 & U(r_{12}) & \cdots & U(r_{1n}) \\ U(r_{21}) & 0 & \cdots & U(r_{2n}) \\ \cdots & \cdots & \cdots & \cdots \\ U(r_{n1}) & U(r_{n2}) & \cdots & 0 \end{bmatrix}$

and $P = \begin{bmatrix} 1 & x_1 & y_1 \\ 1 & x_2 & y_2 \\ \cdots & \cdots & \cdots \\ 1 & x_n & y_n \end{bmatrix}$.

Here, $r_{ij} = \| P_i - P_j \|$ is the distance between points P_i and P_j. W and A is column vectors formed from $W = (w_1, w_2, ..., w_n)$ and $A = (a_1, a_x, a_y)$, respectively.

$V = (v_1, v_2, ..., v_n)$ is any n-vector. We will denote the $(n+3) \times (n+3)$ matrix $\begin{pmatrix} K & P \\ P^T & 0 \end{pmatrix}$ by L. Since L is nonsingular, we can find the solution by inverting L [Powell 1995]. Define the vector $Y = (V \mid 0 \;\; 0 \;\; 0)^T$, then $(W \mid a_1 \;\; a_x \;\; a_y)^T = L^{-1} Y$. If we denote the upper left $n \times n$ block of L^{-1} by L_p^{-1}, then it can be shown that $I_f \propto v^T L_p^{-1} v = w^T K w$.

When there is noise in the specified value v_i, one may wish to relax the exact interpolation requirement by means of regularization. This is accomplished by minimizing

$$H[f] = \sum_{i=1}^{n} (v_i - f(x_i, y_i))^2 + \lambda I_f$$

The regularization parameter λ, a positive scalar, controls the amount of smoothing; the limiting case of $\lambda = 0$ reduces to exact interpolation. As demonstrated in [ ], we can solve for the TPS coefficients in the regularized case by replacing the matrix K by $K + \lambda I$.

In the application we take the points (x_i, y_i) to be landmarks and V to be $n \times 2$ matrix,

$V = \begin{bmatrix} x_1' & x_2' & \cdots & x_n' \\ y_1' & y_2' & \cdots & y_n' \end{bmatrix}^T$ Y to be $(n+3) \times 2$ matrix,

$Y = \begin{bmatrix} x_1' & x_2' & \cdots & x_n' & | & 0 & 0 & 0 \\ y_1' & y_2' & \cdots & y_n' & | & 0 & 0 & 0 \end{bmatrix}^T$ where each (x_i', y_i')

is the control points homologous to (x_i, y_i) in another copy of $\Re^2$. The application of L^{-1} to the first column of V^T specifies the coefficient of 1, x, y, and the U's for $f_x(x, y)$, the x - coordinate of the image of (x, y). The application of L^{-1} to the second column of V^T does the same for the y - coordinate $f_x(x, y)$. The resulting function $f(x, y) = [f_x(x, y), f_y(x, y)]$ is nor vector-valued and it maps each point (x_i, y_i) to its homolog (x_i', y_i') and is least bent of all such functions. These vector valued functions $f(x, y)$ are the thin-plate spline mappings.

5. 3-D Point Context

We treat an object as a point set and we assume that the shape of an object is essentially captured by a finite subset of its points. For each point on the first shape, we want to find the best matching point. We propose a 3-D novel descriptor, the 3-D point context, which could play such a role in shape matching. Consider the set of vectors originating from a point to all other sample points on a shape. These vectors express the configuration of the entire shape relative to the reference point.

The full set of vectors as a shape descriptor is much too detailed since shapes and their sampled representation may vary of one instance to another in a category. We identify the distribution over relative points as a more robust and compact, yet highly discriminative descriptor. For a point p_i on the shape, we compute a coarse histogram h_i of the relative coordinates of the remaining $n-1$ points,

$$h_i(k) = \#\{q \neq p_i : (q - p_i) \in \text{bin}(k)\}.$$

The histogram is defined to be the shape context of p_i. We use bins that are uniform in log-polar space, making the descriptor more sensitive to positions of nearby sample points than to those of points farther away.

The log-polar geometry was first motivated by its resemblance with the structure of the retina of some biological vision systems and by its data compression qualities. The log-polar transformation is a conformal mapping from the points on the Cartesian plane (x, y) to points in the log-polar plane (ξ, η).

The mapping is described by

$$\xi = \log \sqrt{x^2 + y^2}$$
$$\eta = a \tan(y / x)$$

Consider a point p_i on the first shape and a point q_j on the second shape. Let $C_{ij} = C(p_i, q_j)$ denote the cost of matching these two points. As shape contexts are distributions represented as histograms, it is natural to use the chi-square test statistics:

$$C_{ij} \equiv C(p_i, q_j) = \frac{1}{2} \sum_{k=1}^{K} \frac{[h_i(k) - h_j(k)]^2}{h_i(k) + h_j(k)},$$

where $h_i(k)$ and $h_j(k)$ denote the K-bin normalized histogram at p_i and q_j, respectively.

6. The Background of Nystrom Approximation

The computation cost of TPS becomes prohibitive when the number of samples is large. Let n be the number of samples of a deformation map. TPS require the solution of a $n \times n$ dense system with $O(n^3)$ complexity for determining interpolation coefficients.

One drawback of the TPS model is that its solution requires the inversion of a large dense matrix of size $n \times n$, where n is the number of points in the data set. In this section, the approximation method that addresses this computational problem is discussed.

Since inverting L is an $O(n+3)^3$ operation, solving for the TPS coefficients can be very expensive when n is very large. We will now discuss the

Nystrom approximation method that reduces this computational burdon. The Nystrom method is a technique for finding numerical approximations to eigenfunction problems of the form:

$$\int_a^b K(x, y)\phi(y)dy = \lambda\phi(x)$$

We can approximate this integral equation by evaluating it as a set of evenly spaced points $\xi_1, \xi_2, ..., \xi_n$ on the interval $[a, b]$ and employing a simple quadrature rule,

$$\frac{(b-a)}{n} \sum_{j=1}^{n} K(x, \xi_j)\hat{\phi}(\xi_j) = \lambda\hat{\phi}(x),$$

where $\hat{\phi}(x)$ is the approximation to the true $\phi(x)$. To solve the above, we set $x = \zeta_i$ yielding the system of equations

$$\frac{(b-a)}{n} \sum_{j=1}^{n} K(\xi_i, \xi_j)\hat{\phi}(\xi_j) = \lambda\hat{\phi}(\xi_i) \quad \forall i \in \{1, 2, ..., n\}$$

Without loss of generality, we let $[a, b]$ be $[0,1]$ and the structure the system as the matrix eigenvalue problem:

$$K\hat{\Phi} = n\hat{\Phi}\Lambda,$$

where $K_{ij} = k(y_i, y_j)$ is the Gram matrix and $\Phi = [\phi_1 \ \phi_2 \ ... \ \phi_n]$ are n approximate eigenvectors with corresponding eigenvalues $\lambda_1, \lambda_2, ..., \lambda_n$. Substituting back into equation yields Nystrom extension for each $\hat{\phi}_i$

$$\hat{\phi}_i(x) = \frac{1}{n\lambda_i} \sum_{j=1}^{n} K(x, \zeta_j)\hat{\phi}_i(\zeta_j)$$

7. Approximating the Eigenvectors of Affinity Matrices

The preceding analysis suggests that it should be possible to find approximate eigenvectors of a large Gram matrix by solving a much smaller eigenproblem using only a subset of the entries and employing the Nystrom extension to fill in the rest.

Consider a Gram matrix $K \in \mathbb{R}^{p \times p}$ partitioned as follows $K = \begin{bmatrix} A & B \\ B^T & C \end{bmatrix}$ with $A \in \mathbb{R}^{n \times n}$, $B \in \mathbb{R}^{n \times m}$, and $C \in \mathbb{R}^{m \times m}$, where $p = n + m$ and we will take n to be much smaller than m. Since K is positive definite, we can write it as the inner product of a matrix Z with itself: $K = Z^T Z$. If K is of rank n and the rows of the submatrix $[A, B]$ are linearly independent, Z can be written using only A and B as follows. Let Z be

partitioned $Z = [X \ Y]$ with $X \in \mathbb{R}^{p \times n}$ and $Y \in \mathbb{R}^{p \times m}$. Rewriting K we have:

$$K = Z^T Z = \begin{bmatrix} X^T X & X^T Y \\ Y^T X & Y^T Y \end{bmatrix}$$

Then $A = X^T X$ and $B = X^T Y$. Using the diagonalization $A = U \Lambda U^T$, where $U^T U = I$ we obtain

$$X = \Lambda^{1/2} U^T$$
$$\hat{Y} = (X^T)^{-1} B = (\Lambda^{1/2} U^T)^{-1} B = \Lambda^{-1/2} U^T B$$

Combining the two into $\hat{Z} = [X \ \hat{Y}] \in \mathbb{R}^{P \times P}$ gives us

$$
\begin{aligned}
K &= \begin{bmatrix} X^T X & X^T \hat{Y} \\ \hat{Y}^T X & \hat{Y}^T \hat{Y} \end{bmatrix} \\
&= \begin{bmatrix} X^T X & (\Lambda^{1/2} U^T)^T \Lambda^{-1/2} U^T B \\ (\Lambda^{-1/2} U^T B)^T \Lambda^{1/2} U^T & (\Lambda^{-1/2} U^T B)^T \Lambda^{-1/2} U^T B \end{bmatrix} \\
&= \begin{bmatrix} A & B \\ B^T & B^T A^{-1} B \end{bmatrix} \\
&= \begin{bmatrix} A \\ B^T \end{bmatrix} A^{-1} [A \ B]
\end{aligned}
$$

Again $A = U \Lambda U^T$ be its eigendecomposition where U has orthonormal columns and Λ is diagonal. Letting $\tilde{U}$ denote the approximate eigenvectors of K, the Nystrom extension gives

$$\tilde{U} = \begin{bmatrix} U \\ B^T U \Lambda^{-1} \end{bmatrix}$$

And the associated approximation of K, which we denote $\hat{K}$, then takes the form

$$
\begin{aligned}
\hat{K} = \tilde{U} \Lambda \tilde{U}^T &= \begin{bmatrix} U \\ B^T U \Lambda^{-1} \end{bmatrix} \Lambda [U^T \ \Lambda^{-1} U^T B^T] \\
&= \begin{bmatrix} U \Lambda U^T & B \\ B^T & B^T \Lambda B \end{bmatrix} = \begin{bmatrix} A & B \\ B^T & B^T \Lambda B \end{bmatrix} \\
&= \begin{bmatrix} A \\ B^T \end{bmatrix} A^{-1} [A \ B]
\end{aligned}
$$

Note that in general the columns of $\tilde{U}$ are not orthogonal.

This is addressed as follows. If A is positive definite, then we can solve the orthogonalized approximate eigenvectors. Let $A^{1/2}$ denote the symmetric positive definite square root of A, define $S = A + A^{-1/2} BB^T A^{-1/2}$ and diagonalize it as $S = U_S \Lambda_S U_S^T$. If the matrix V is defined as

$$V = \begin{bmatrix} A \\ B^T \end{bmatrix} A^{-1/2} U_S \Lambda_S^{-1/2}$$

Then one can show that $\hat{W}$ is diagonalized by V and Λ_S, i.e. $\hat{K} = V \Lambda_S V^T$ and $V^T V = I$.

$$
\begin{aligned}
\hat{K} &= \{ \begin{bmatrix} A \\ B^T \end{bmatrix} A^{-1/2} U_S \Lambda_S^{-1/2} \} \Lambda \{ \Lambda_S^{-1/2} U_S A^{-1/2} [A \ B] \} \\
&= V \Lambda V^T
\end{aligned}
$$

$$
\begin{aligned}
I &= V^T V \\
&= \{ \Lambda_S^{-1/2} U_S^T A^{-1/2} [A \ B] \} \{ \begin{bmatrix} A \\ B^T \end{bmatrix} A^{-1/2} U_S \Lambda_S^{-1/2} \}
\end{aligned}
$$

By multiplying from the left by

$$
\begin{aligned}
U_S \Lambda_S U_S^T &= A^{-1/2} [A \ B] \begin{bmatrix} A \\ B^T \end{bmatrix} A^{-1/2} \\
&= A + A^{-1/2} BB^T A^{-1/2} = S
\end{aligned}
$$

From the standard formula for the partitioned inverse of L, we have

$$
\begin{aligned}
L^{-1} &= \begin{bmatrix} K & P \\ P^T & 0 \end{bmatrix}^{-1} \\
&= \begin{bmatrix} (K^{-1} + K^{-1} P Q^{-1} P^T K^{-1} & -K^{-1} P Q^{-1} \\ -Q^{-1} P^T K^{-1} & Q^{-1} \end{bmatrix}
\end{aligned}
$$

with $Q = -P^T K^{-1} P$.

Thus

$$
\begin{aligned}
\begin{bmatrix} W \\ A \end{bmatrix} &= \begin{bmatrix} K & P \\ P^T & 0 \end{bmatrix}^{-1} \begin{bmatrix} V \\ 0 \end{bmatrix} \\
&= \begin{bmatrix} (K^{-1} + K^{-1} P Q^{-1} P^T K^{-1} & -K^{-1} P Q^{-1} \\ -Q^{-1} P^T K^{-1} & Q^{-1} \end{bmatrix} \begin{bmatrix} V \\ 0 \end{bmatrix} \\
&= \begin{bmatrix} (K^{-1} + K^{-1} P Q^{-1} P^T K^{-1}) V \\ -Q^{-1} P^T K^{-1} V \end{bmatrix}
\end{aligned}
$$

$$
\begin{aligned}
\begin{bmatrix} W \\ A \end{bmatrix} &= \begin{bmatrix} K & P \\ P^T & 0 \end{bmatrix}^{-1} \begin{bmatrix} V \\ 0 \end{bmatrix} \\
&= \begin{bmatrix} (K^{-1} + K^{-1} P Q^{-1} P^T K^{-1} & -K^{-1} P Q^{-1} \\ -Q^{-1} P^T K^{-1} & Q^{-1} \end{bmatrix} \begin{bmatrix} V \\ 0 \end{bmatrix} \\
&= \begin{bmatrix} (K^{-1} + K^{-1} P Q^{-1} P^T K^{-1}) V \\ -Q^{-1} P^T K^{-1} V \end{bmatrix}
\end{aligned}
$$

Using the Nystrom approximation to K, we have $\hat{K} = V \Lambda_S V^T$ and $\hat{K}^{-1} = V \Lambda_S^{-1} V^T$

$$\hat{W} = (I + \hat{K}^{-1}P\hat{Q}^{-1}P^T)\hat{K}^{-1}V$$
$$= (I + V\Lambda_S^{-1}V^T P\hat{Q}^{-1}P^T)V\Lambda_S^{-1}V^T V$$
$$\hat{A} = -\hat{Q}^{-1}P^T\hat{K}^{-1}V = -\hat{Q}^{-1}P^T V\Lambda_S^{-1}V^T V$$

with $\hat{Q} = -P^T\hat{K}^{-1}P = -P^T V\Lambda_S^{-1}V^T P$ with is 3×3. Therefore, by computing matrix vector products in the appropriate order, we can obtain estimates to the TPS coefficients without having to invert or store a large $(n+3)\times(n+3)$ matrix. For the regularized case, one can proceed in the same manner, using

$$(\hat{K} + \lambda I)^{-1} = (V\Lambda_S V^T + \lambda I)^{-1} = V(\Lambda_S + \lambda I)^{-1}V^T$$

Finally, the approximate bending energy is given by

$$I_f = w^T\hat{K}w = w^T V\Lambda_S V^T w = (V^T w)^T \Lambda_S (V^T w)$$

Note that this bending energy is the average of the energies associated to the x and y components.

7. Conclusions

This research shows the convergence property of relaxation Rabling under two-way Sinkhon normalization. This method can be used in non-rigid image registration and point matching. In this paper, we used Shinkon normalization to prove it.

Acknowledgements

References

[1]. D. S. Coming, O. G. Staadt, Velocity-Aligned Discrete Oriented Polytopes for Dynamic Collision Detection, *IEEE Trans. Visualization and Computer Graphics*, Vol. 14, No. 1, Jan./Feb. 2008, pp. 1-12.

[2]. J. Clerk Maxwell, A Treatise on Electricity and Magnetism, 3rd ed., *Oxford, Clarendon,* Vol. 2, 1892, pp. 68-73.

[3]. I. S. Jacobs, C. P. Bean, Fine Particles, Thin Films and Exchange Anisotropy, in Magnetism, G. T. Rado and H. Suhl, (Eds.), Vol. III, *Academic Press,* 1963, pp. 271-350.

[4]. C. J. Kaufman, Rocky Mountain Research Laboratories, Boulder, CO, Personal Communication, 1992.

[5]. H. Goto, Y. Hasegawa, M. Tanaka, Efficient Scheduling Focusing on the Duality of MPL Representation, in *Proceedings of the IEEE Symposium Computational Intelligence in Scheduling (SCIS'07)*, Apr. 2007, pp. 57-64.

[6]. M. Young, The Technical Writer's Handbook, *University Science,* Mill Valley, CA, 1989.

[7]. J. M. P. Martínez, R. B. Llavori, M. J. A. Cabo, T. B. Pedersen, Integrating Data Warehouses with Web Data: A Survey, *IEEE Transactions on Knowledge and Data Engineering*, Vol. 20, No. 7, 2008, pp. 940-955.

———————————————

Sensors & Transducers

Performance Evaluation of a System to Detect Awakening Behavior of Bedridden Patients with a Quilt Using a Depth Sensor

Geer Cheng and Hideo Furuhashi
1247, Yachigusa, Yakusa-cho, Toyota, 470-0392, Japan
Tel.: +81-565-48-8121
E-mail: chenggeer2008@yahoo.co.jp

Abstract: We evaluate a system that monitors bedridden patients covered by different types of quilts by utilizing a proximity depth sensor with an infrared projector (Kinect). This system is capable of detecting people as they wake up. We believe that this system could be useful for monitoring patients in hospitals or private homes who must occasionally be left unsupervised. The system, which utilizes an optimal linear discriminant function, is demonstrated with subjects covered by quilts of different thicknesses. The detection rate of a basic system using height and space data for four cases - lying on the back, lying on the side, sitting up, and no longer in bed—was 99.2 % when a thin quilt was used and 80.4 % when a thick quilt was used. The detection rate was also low (80.8 %) when two variables were used for the cases using either thin or thick quilts. The rate improved to 96.3 % using the data of the initial condition of the subject. Good performance was obtained regardless of the thickness of the quilt.

Keywords: Kinect, Depth sensor, Awakening behavior detection, Optimal linear discrimination.

1. Introduction

Many clinics and healthcare providers worldwide are urgently seeking accurate, low-cost, and easy-to-use technological solutions for predicting risks owing to a patient's frailty and falling, which are the most common causes of unintentional injury and death. The demand for methods of monitoring patients in hospitals and private homes is increasing. In hospitals, if a patient awakens, it is important that the responsible healthcare professionals are cautioned because the patient might fall out of bed and suffer severe injuries. Older people being cared for by family members at home can be similarly injured. Furthermore, the wandering of older people suffering

from dementia is a serious social problem. However, providing complete 24-h supervision is difficult.

We herein describe a system that monitors bedridden patients who are in a coma or sleeping due to anesthesia and detects awakening behaviors. Numerous types of monitoring systems for patients or older people are available or have been proposed [1-8]. These include passive camera-based image-processing systems, mat sensors, and ultrasonic sensors. However, the recognition rates of passive camera-based systems and ultrasonic systems are low, and mat sensors are subject to mechanical failure. Some investigations have been reported on the measurement of human activities or the monitoring of patients or older adults using a depth sensor [9-18].

However, such systems monitor active people who can move about within the room and detect the action of falling down on the floor or falling out of a bed. For monitoring comatose patients or patients who are sleeping due to anesthesia, detection of the patient waking up is important to prevent them from falling out of the bed. Such patients may be groggy, and this comes with a high risk. Therefore, immediate support of caregivers is required when the patients wake up.

Some systems detecting awakening behavior have been reported. H. Satoh et al. proposed a system using an RGB camera and neural network [19, 20]. Takeda proposed a system for medical use using a Kinect depth sensor and neural networks [21]. They placed the RGB camera or Kinect sensor besides the bed. They classified the behavior into two classes: (a) safety action (lying, being sitting up, or sitting) and (b) dangerous action (almost falling). However, it is sometimes too late if the caregivers are called when the dangerous action occurs. Ni et.al proposed a get-up event detection for hospital fall prevention using the Kinect RGB-D sensor and multi-kernel learning framework [22]. In their study, the sensor was located beside the bed. We have also reported a system that uses a depth sensor and optimal linear discriminant analysis (OLDA) with future amounts of the height, space, and volume above the bed to detect the awakening behavior of subject [23]. The depth sensor was mounted on the ceiling. They are classified in four cases: (a) lying on the back (b) lying on the side (c) sitting up, and (d) no longer in bed; the caregiver is called in the case of occurrence of b, c, and d. A high detection rate was obtained. However, patients are generally covered by many types of quilts, and the shape of the subject on the bed is blurry. The previous studies did not focus on the influence of the quilt.

Herein, we discuss the performance of that depth sensor for monitoring situations wherein the subjects are covered by quilts of different thicknesses. The discrimination was performed by considering the quilt thickness and the subject size.

2. Experimental Setup

Fig. 1 shows the experimental setup. We mounted a depth sensor, Kinect (Microsoft Corp), on the ceiling at a height of 240 cm above the floor. The bed height was 30 cm. A subject covered with a quilt lay on the bed. Two quilts of thicknesses 5.5 and 38.5 mm were used for the experiments. The data measured by the depth sensor were fed into a computer and analyzed.

Fig. 2 shows the measurement process used for data analysis. Initially, depth data were acquired in the area of the bed without a subject or a quilt on the bed. The area of the bed was 215 cm × 290 cm. Next, depth data were acquired in the same area with a subject and a quilt on the bed and was subtracted from the depth data of empty bed. Therefore, the subtracted data were based on the height from the bed. Next, the volume, maximum height, and area with height above a threshold value were calculated. Data were acquired

for four cases a subject: (1) lying on the back, (2) lying on the side, (3) sitting up, and (4) no longer in bed. Finally, we calculated the volume, maximum height, and space above a threshold value and then analyzed the data using optimal linear discriminant analysis (OLDA).
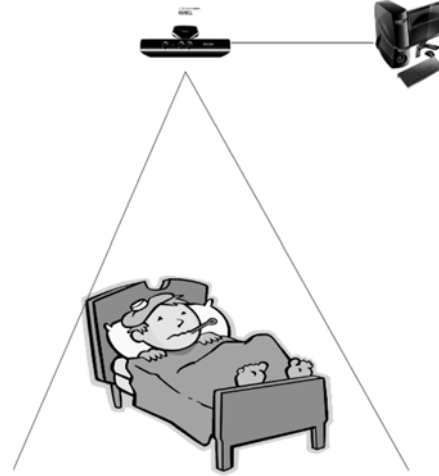

Fig. 1. Experimental setup showing the monitoring sensor on the ceiling and a subject on the bed covered with a quilt.
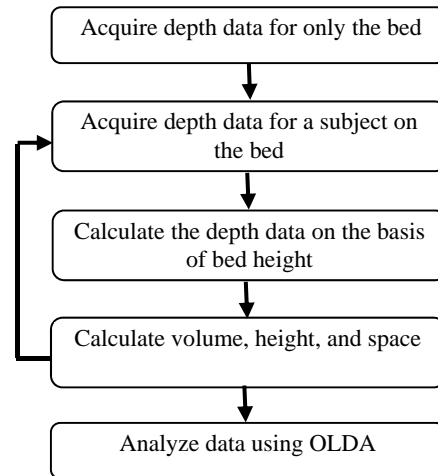

Fig. 2. Measurement flowchart for data analysis.

The bed area volume V, maximum height H_{max}, and the space S_{area} for which the height from the bed is higher than a threshold value h_{thres} are calculated by the following equations. x and y represent position coordinates of a pixel in the depth image.

$$h_0 = f_0(x, y) \tag{1}$$

$$h = f(x, y) \tag{2}$$

$$V = \int_S (h - h_0) dS \tag{3}$$

$$H_{max} = Max_s(h - h_0) \qquad (4)$$

$$S_{area} = \int_{(h-h_0)>h_{thres}} dS, \qquad (5)$$

where h_0 and h are the heights of the bed without and with a subject, respectively. f_0 and f represent the functions giving h_0 and h, respectively, for position (x, y).

Ten sets of data for experiments with six subjects (60 sets of data) were collected, and then such data sets were collected for all four cases for each of the six subjects (24 experiments and 240 sets of data) with a thin or thick quilt. The subjects' heights were 165–178 cm and their weights were 52–83 kg.

3. Data Analysis

3.1. Thin Quilt

Fig. 3 shows examples of the height data for the four cases with a thin quilt covering the subject. Table 1 shows the calculated volumes, maximum heights, and spaces. The volume characteristics are similar in the four cases. However, the space and maximum height characteristics show differences. The space values were smaller for the case wherein the subject was no longer in bed than for other cases. The maximum height values were larger for the case wherein the subject was sitting up than for other cases.
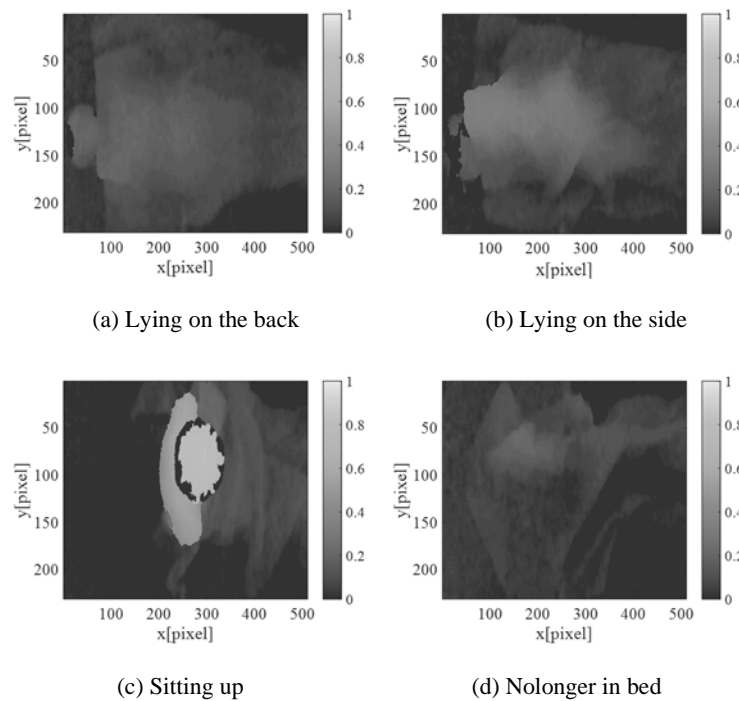

(a) Lying on the back

(b) Lying on the side

(c) Sitting up

(d) Nolonger in bed

Fig. 3. Examples of height data for the four cases with a thin quilt covering the subject. One pixle equals 4.5 mm and the color bar unit is meters.

Table 1. Calculated volumes, maximum heights, and spaces for the four cases with a thin quilt covering the subject.

		Mean	Standard deviation	Minimum value	Maximum value
Volume ($\times 20.25 \cdot 10^3 mm^3$)	Lying on back	9511	1553	7355	13734
	Lying on side	10485	1329	7980	13319
	Sitting up	13080	1819	10979	17344
	On longer in bed	4880	1127	2722	6395
Space ($\times 20.25 mm^2$)	Lying on back	40719	10957	25780	61276
	Lying on side	41783	8312	30183	57494
	Sitting up	38579	6296	24418	49843
	On longer in bed	5085	3679	1196	12529
Maximum height ($\times 10^3 mm$)	Lying on back	0.152	0.0347	0.115	0.216
	Lying on side	0.2377	0.0241	0.157	0.281
	Sitting up	0.7304	0.0287	0.682	0.808
	On longer in bed	0.1021	0.021	0.071	0.157

Table 2 shows the Wilks coefficients for the case of a thin quilt covering the subject.

Table 2. Wilks coefficient for each combination in the case of a thin quilt.

	Volume	Space	Maximum height
Volume			
Space	0.07820		
Maximum height	0.00385	0.00176	

The lowest coefficient was obtained for the combination of maximum height and space. Therefore, optimal linear discriminant functions (OLDFs) were made with these data.

3.2. Thick Quilt

Fig. 4 shows examples of the height data for the four cases with a thick quilt covering the subject. Table 3 shows the calculated volumes, maximum heights, and spaces. Although the data show similar behavior as the thin quilt case, some differences were noted. In the thin quilt case, the maximum heights for the case with the subject no longer in bed were smaller than those for other cases, whereas in the thick quilt case, the maximum heights for the case with the subject no longer in bed sometimes became larger than those for the cases with the subject lying on the back and lying on the side. This is because the thick quilt left on the bed has a large volume itself.
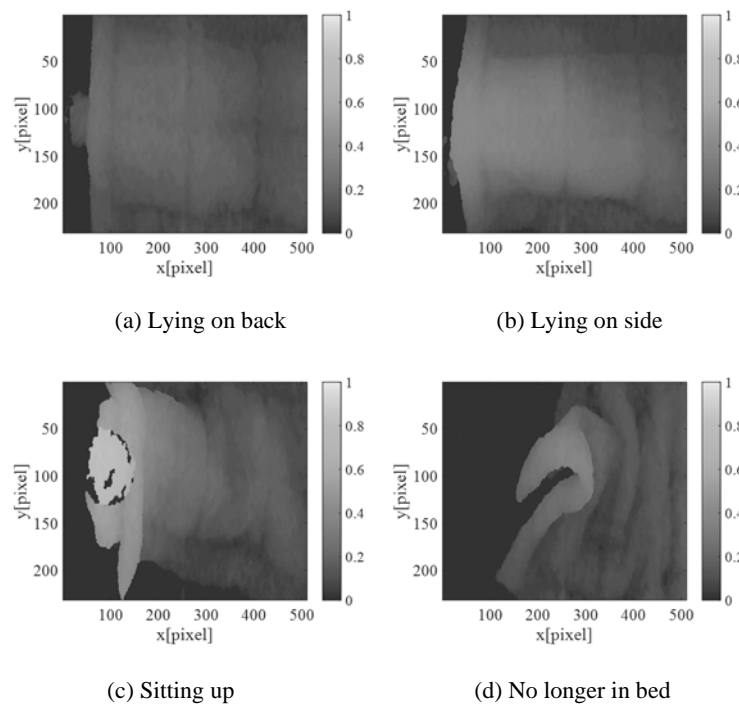

(a) Lying on back

(b) Lying on side

(c) Sitting up

(d) No longer in bed

Fig. 4. Examples of height data for the four cases with a thick quilt covering the subject. One pixel equals 4.5 mm and the color bar unit is meters.

Table 3. Calculated volumes, maximum heights, and spaces for the four cases with a thick quilt covering the subject.

		Mean	Standard deviation	Minimum value	Maximum value
Volume ($\times 20.25 \cdot 10^3 mm^3$)	Lying on back	20682	3201	15862	27076
	Lying on side	23811	3639	20043	31391
	Sitting up	23168	4745	16318	30149
	No longer in bed	13401	1223	10650	14772
Space ($\times 20.25 mm^2$)	Lying on back	17892	15502	0	41430
	Lying on side	42728	10448	27794	63198
	Sitting up	36267	12185	16579	56404
	No longer in bed	6273	4467	2750	14231
Maximum height ($\times 10^3 mm$)	Lying on back	0.0173	0.0418	0.136	0.263
	Lying on side	0.3125	0.0725	0.245	0.521
	Sitting up	0.7233	0.0333	0.661	0.786
	No longer in bed	0.2137	0.0489	0.167	0.308

Table 4 shows the Wilks coefficients for the thick quilt case. The lowest coefficient was obtained for the combination of maximum height and space. Therefore, OLDFs were made with these data.

Table 4. Wilks coefficient for each combination in the case of a thick quilt.

	Volume	Space	Maximum height
Volume			
Space	0.22658		
Maximum height	0.01975	0.01531	

4. Discrimination

First, the depth data was captured by the depth sensor. Second, the maximum height and space (volume) were calculated. Third, the discriminant functions were calculated. Finally, the conditions of the subjects were determined.

Table 5 shows the results of the OLDA judgment for experiments conducted using a thin quilt. For the cases with the subject lying on the back or lying on the side, good judgments were obtained; however, some judgments were incorrect.

Fig. 5 shows the depth image where the subject was lying on the back but judged as lying on the side. Such results are due to the space being increased as the quilt was spread wide.

Table 5. Confusion matrix for the thin quilt case (%).

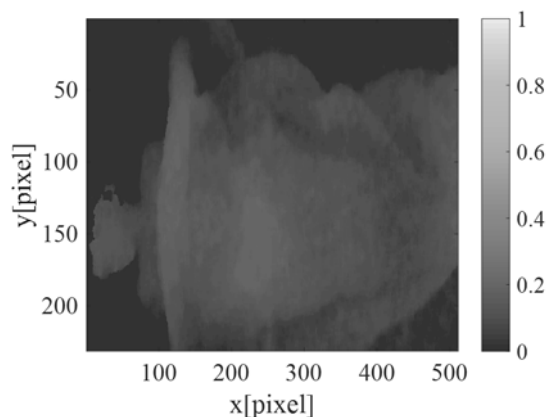|	Lying on back	Lying on side	Sitting up	No longer in bed
Lying on back	98.33	1.67	0.00	0.00
Lying on side	1.67	98.33	0.00	0.00
Sitting up	0.00	0.00	100.00	0.00
No longer in bed	0.00	0.00	0.00	100.00

Fig. 5. Depth image of a subject lying on the back and covered with a thin quilt, which was misjudged as a subject lying on the side. One pixle equals 4.5 mm and the color bar unit is meters.

Fig. 6 shows the depth image where the subject was lying on the side but judged as lying on the back. Such results are due to the space being decreased as the quilt was narrowed. The judgement accuracy was 100 % for the cases with the subject sitting up or no longer in bed. Therefore, the system performed well when detecting the situations wherein the subject is sitting up or no longer in bed.
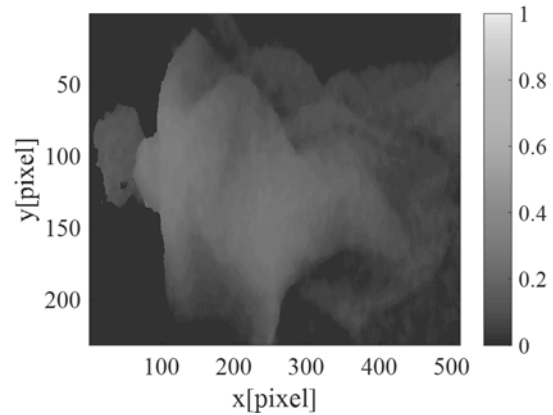

Fig. 6. Depth image of a subject lying on the side and covered with a thin quilt, which was misjudged as a subject lying on the back. One pixle equals 4.5 mm and the color bar unit is meters.

Table 6 shows the results of OLDA judgment in the thick quilt case. Some cases of the subject lying on the back were misjudged as the subject no longer in bed. Comparing with the case of thin quilt, accuracy decreased for the cases of the subject lying on the side, and the incidences of misjudgments that indicated the subject was lying on the back increased.

Table 6. Confusion matrix for the thick quilt case (%).

	Lying on back	Lying on side	Sitting up	No longer in bed
Lying on back	43.33	18.33	0.00	38.33
Lying on side	21.67	78.33	0.00	0.00
Sitting up	0.00	0.00	100.00	0.00
No longer in bed	0.00	0.00	0.00	100.00

Fig. 7 shows the depth image where the subject was lying on the back but judged as no longer in bed. Such results occurred because the quilt narrowed and the space decreased. Fig. 8 shows the depth image where the subject was lying on the side but judged as lying on the back. Such results occurred because the quilt narrowed and the space decreased. The judgement accuracy was 100 % for cases with the subject sitting up or no longer in bed. Therefore, this system performs well when detecting the situations

wherein the subject is sitting up or no longer in bed. The error rate for the thick quilt case is higher than that for the thin quilt case. When a thick quilt is used, judgement becomes difficult, because the differences in the space and height become small between the three cases of the subject lying on back, lying on the side, and no longer in bed.
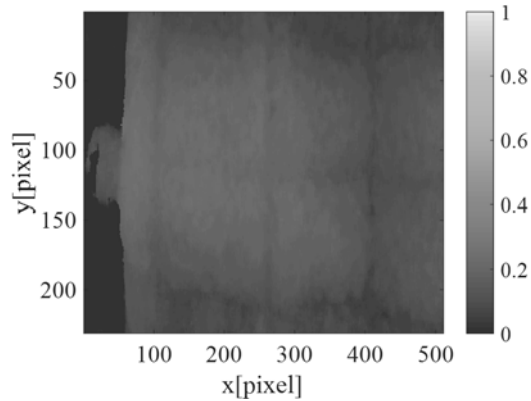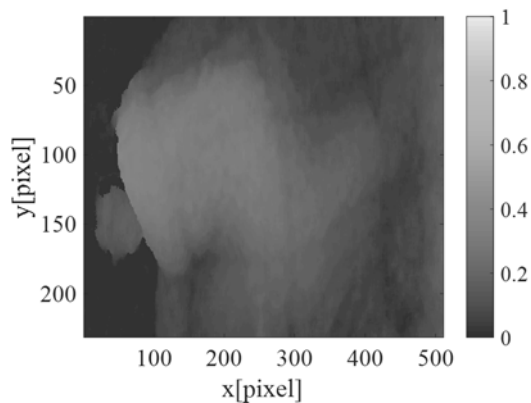

Fig. 7. Depth image of a subject lying on the back and covered with a thick quilt, which was misjudged as a subject on longer in bed. One pixle equals 4.5 mm and the color bar unit is meters.

Fig. 8. Depth image of a subject lying on the side and covered with a thick quilt, which was misjudged as a subject lying on the back. One pixle equals 4.5 mm and the color bar unit is meters.

5. Judgment of Using a Combination of a Thin Quilt and a Thick Quilt

5.1. Judgement Using Two Variables

Different quilts are used depending on the season or climate. Therefore, we next considered whether the system could perform well independent of the quilt thickness with one discrimination function. Table 7 shows the Wilks coefficients for the cases using a combination of a thin quilt and a thick quilt. The lowest coefficient was obtained for the combination of maximum height and space.

Table 7. Wilks coefficient for each combination in the case of a combination of thin and thick quilts.

	Volume	Space	Maximum height
Voluem			
Space	0.34977		
Maximum height	0.02913	0.02251	

Table 8 shows the judgement results for cases using a thin and thick quilt combination. The judgment accuracy decreased compared with the accuracy of using only a thin or a thick quilt. In particular, cases of the subject lying on the side were misjudged as the subject sitting up. Fig. 9 shows the depth image when the subject was lying on the side but was judged as sitting up. Such results occurred because the subject was overweight and the height increased when the subject was lying on the side.

Table 8. Confusion matrix for a combination of thin and thick quilts (%).

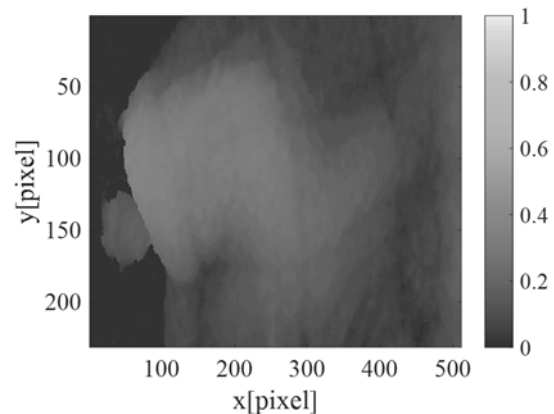|	Lying on back	Lying on side	Sitting up	No longer in bed
Lying on back	48.33	26.67	0.00	25.00
Lying on side	21.67	78.33	0.00	0.00
Sitting up	0.00	0.00	100.00	0.00
No longer in bed	0.00	0.00	0.00	100.00

Fig. 9. Depth image of a subject lying on the side and covered with a thick quilt, which was misjudged as a subject sitting up. One pixle equals 4.5 mm and the color bar unit is meters.

5.2. Judgement Using Three Variables

As shown above, the judgment is affected by subject size and quilt thickness. Therefore, we introduced the data of the initial condition (the subjects lying on back first)—volume, maximum height, and space. These were measured only once,

when the subject or the quilt was changed. The data for the three variables were analyzed using OLDFs. The smallest coefficient was obtained for space, maximum height, and initial volume.

Table 9 shows the judgment results using three variables. The judgment accuracy significantly improved. This system performed well when used to detect situations wherein the subjects were sitting up or no longer in bed. Although, the data for four variables were also analyzed, better results were not obtained.

Table 9. Confusion matrix using three variables (%).

	Lying on back	Lying on side	Sitting up	No longer in bed
Lying on back	94.17	5.83	0.00	0.00
Lying on side	9.17	90.83	0.00	0.00
Sitting up	0.00	0.00	100.00	0.00
No longer in bed	0.00	0.00	0.00	100.00

The reported detection rate of the dangerous action (almost falling) using neural networks is 84 % [21]. The detection rate of the dangerous action (lying on side, sitting up, and no longer in bed) in this system is 97 %. Although the situations of the dangerous action differ, a better detection rate is obtained in this system. The reported detection rate for the get-up event using the multi-kernel learning framework is 98.76 %, and the frame rate is 10 fps [22]. A same level of the detective rate is obtained by OLDA. The frame rate of this system is 30 fps, which is limited by the frame rate of the Kinect sensor. Our system enables high-speed operation

6. Conclusions

In this paper, we proposed a system for monitoring patients in a coma. The system uses a depth sensor with an infrared projector and the discrimination results are based on simple OLDA. The system is capable of detecting the behaviors of a person awakening and a person no longer in bed. The obtained data were analyzed by OLDFs. The detection rate when the subject was covered by a thin quilt and was lying on the back, lying on the side, sitting up, or no longer in bed was 99.2 %; thus, the system has high reliability and practicality. The detection rate was 80.4 % when using a thick quilt and 80.8 % when using a combination of a thin and a thick quilt. However, the rate improved to 96.3 % using the data of the initial condition of the subject.

We believe that the system will be useful for monitoring patients in a coma or patients who are sleeping due to anesthesia who must occasionally be left unsupervised. This technique has higher accuracy than passive camera-based image-processing systems and is more durable than mat sensors. Although, its

accuracy depends on the subjects' physique and quilt thickness, accurate results are obtained by measuring these values. For further verification, investigation using more samples is required.
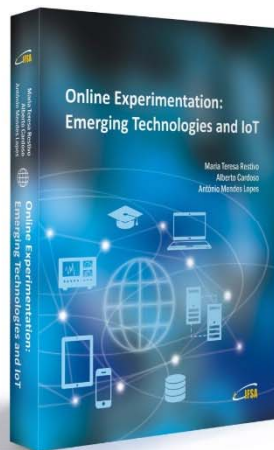
References

[1]. P. Rashidi, A. Mihailidis. A Survey on Ambient-Assisted Living Tools for Older Adults, *IEEE Journal of Biomedical and Health Informatics,* Vol. 17, No. 3, 2013, pp. 579-590.

[2]. K. Ozcan, A. K. Mahabalagiri, M. Casares, and S. Velipasalar. Automatic Fall Detection and Activity Classification by a Wearable Embedded Smart Camera. *IEEE Journal on Emerging and Selected Topics in Circuits and Systems,* Vol. 3, No. 2, 2013, pp. 125-136.

[3]. L. Yun, K. C. Ho, and M. Popescu, A Microphone Array System for Automatic Fall Detection, *IEEE Transactions on Biomedical Engineering,* Vol. 59, No. 5, 2012, pp. 1291-1301.

[4]. C. Rougier, J. Meunier, A. St-Arnaud, and J. Rousseau. Robust Video Surveillance for Fall Detection Based on Human Shape Deformation, *IEEE Transactions on Circuits and Systems for Video Technology,* Vol. 21, No. 5, 2011, pp. 611-622.

[5]. F. Zhengming, T. Delbruck, P. Lichtsteiner, and E. Culurciello. An Address-Event Fall Detector for Assisted Living Applications, *IEEE Transactions on Biomedical Circuits and Systems,* Vol. 2, No. 2, 2008, pp. 88-96.

[6]. M. Alwan, P. J. Rajendran, S. Kell, D. Mack, S. Dalal, M. Wolfe, and R. Felder, A Smart and Passive Floor-Vibration Based Fall Detector for Elderly, *Information and Communication Technologies,* Vol. 1, 2006, pp. 1003-1007.

[7]. A. Staranowicz, G. R. Brown, and G.-L. Mariottini. Evaluating the Accuracy of a Mobile Kinect-based Gait-Monitoring System for Fall Prediction, *in Proceedings of the 6th International Conference on Pervasive Technologies Related to Assistive Environments (PETRA '13),* 2013.

[8]. A. Dubois, F. Charpillet, Human activities recognition with RGB-Depth camera using HMM, in *Proceedings of the International Conference of the IEEE Engineering in Medicine & Biology Society,* 2013, pp. 4666-4669.

[9]. C. Chen, R. Jafari, and N. Kehtarnavaz. A survey of depth and inertial sensor fusion for human action recognition, *Multimedia Tools & Applications,* 2015, pp. 1-21.

[10]. Z. Yang, Z. Liu, and H. Cheng, RGB-Depth Feature for 3D Human Activity Recognition, *Communications China,* Vol. 10, No. 7, 2013, pp. 93-103.

[11]. L. Lin, K. Wang, W. Zuo, M. Wang, J. Luo, and L. Zhang. A Deep Structured Model with Radius–Margin Bound for 3D Human Activity Recognition. *International Journal of Computer Vision,* Vol. 118, No. 2, 2016, pp. 256-273.

[12]. D. R. Faria, C. Premebida, and U. Nunes. A probabilistic approach for human everyday activities recognition using body motion from RGB-D images, in *Proceedings of the IEEE International Symposium on Robot and Human Interactive Communication (Ro-Man),* 2014, pp. 732-737.

[13]. Z. Cai, J. Han, L. Liu., and L. Shao, RGB-D datasets using Microsoft Kinect or similar sensors: a survey. *Multimedia Tools and Applications*, 2016*, pp.* 1-43.

[14]. L. Xia, J. K. Aggarwal, Spatio-temporal Depth Cuboid Similarity Feature for Activity Recognition Using Depth Camera, in *Proceedings of the IEEE Conference on Computer Vision and Pattern Recognition (CVPR)*, 2013, pp. 2834-2841.

[15]. J. K. Aggarwal, L. Xia, Human activity recognition from 3D data: A review, *Pattern Recognition Letters,* Vol. 48, 2014, pp. 70-80.

[16]. I. Raul, C. Medrano, and I. Plaza. Challenges, issues and trends in fall detection systems, *Biomedical Engineering*, 2013*, pp.* 1-24.

[17]. T. Shuai, K. Mineichi, and N. Hidetoshi. Privacy-Preserved Behavior Analysis and Fall Detection by an Infrared Ceiling Sensor Network, *Sensor Journal*, 2012*,* pp. 16920-16936.

[18]. E. E. Stone, M. Skubic. Fall Detection in Homes of Older Adults Using the Microsoft Kinect, *IEEE Journal of Biomedical and Health Informatics*, 2015*,* pp. 290-301.

[19]. H. Satoh, F. Takeda, Y. Saeki, R. Ikeda, and Y. Shiraishi, Proposal of Awakening Behavior Detection System using Neural Network, in *Proceedings of the Computational Intelligence*, 2006, p. 523.

[20]. H. Satoh, T. Ohkura, and F. Takeda, Proposal for the awakening behavior detection system using images and adaptation for fluctuation of brightness quantity in the captured image, in *Proceedings of the 4th International Conference on Modeling, Simulation and Applied Optimization (ICMSAO)*, 2011*,* pp. 1-7.

[21]. N. Bingbing, N. C. Dat, and P. Moulin, RGBD-camera based get-up event detection for hospital fall prevention, in *Proceedings of the IEEE International Conference on Acoustics, Speech and Signal Processing*, 2012, pp. 1405-1408.

[22]. F. Takeda, Proposal of an Awakening Behavior Detection System for Medical Use and Adaptation for Fluctuation of the Brightness Quantity, *Signal-Image Technology Internet-Based Systems*, 2013, pp. 714-719.

[23]. G. Cheng, S. Kida, and H. Furuhashi, Detection of a Person Awaking or Falling Out of Bed Using a Range Sensor, in *Proceedings of the Information Systems International Conference (ISICO)*, 2013, pp. 503-508.

_____

Estimation of Human Heart Activity Using Ensemble Kalman Filter

Pradhnya Arun Priyadarshi and Surender Kannaiyan

Department of Communication System Engineering,
Visvesvaraya National Institute of Technology, Nagpur - 440010, India
Tel.: (+91) - 9130225990, (+91) - 9168931539
E-mail: priyadarshipradhnya06@gmail.com, ksurender@ece.vnit.ac.in

---

Abstract: Heart beat measurement techniques come across various challenges. Electrocardiogram (ECG) obtained sometimes does not reveal complete information about electrochemical activity of human heart, because of which functioning of heart cannot be studied properly. In this paper Ensemble Kalman Filter (EnKF) is used to generate ECG signal efficiently with better accuracy such that the drawbacks of current techniques are eliminated. Here EnKF is applied to second order mathematical model of human heart, input applied to this mathematical model is a pacemaker signal. The initial values of heart muscle movements and electrochemical activity as a discrete data set are used and prediction steps are commenced. EnKF uses ensemble integration technique to model error statistics which helps obtaining more precise output. The results are obtained with negligible sum squared error, therefore the ECG obtained using EnKF can diagnose the disease related to heart with better accuracy.

Keywords: Heart model, Ensemble Kalman filter, Electrocardiogram, Non-linear systems, State estimation techniques.

---

1. Introduction

The existing heart beat prediction techniques has various drawbacks since the additive noise present in the measured input signal given to the electrocardiogram (ECG) machine is not properly modeled and is not completely eliminated. Presence of noise results into noticeable variations in readings from the desired output and large value of sum squared error, which has to be reduced. ECG is a time varying signals which represents the electrical activity of cardiac tissues. A single cycle of ECG reflects systole and diastole of heart. ECG is recorded by placing electrode on the skin. ECG is used to indicate the cardiac health such that heart problems can be detected.

The drawbacks of current heart model estimation systems are such that the recorded signal sometimes

may not reflect the symptoms of heart diseases, that is sometimes ECG does not reflects any abnormality at all. In some instances, the ECG may be entirely normal despite the presence of an underlying cardiac conditions, this is because the systems estimation about the heart movements is not proper. Improper estimation is one of the cause of improper diagnosis of diseases related to heart.

Heart beat estimation models are proposed prior with different estimation techniques. Extended Kalman Filter (EKF) is one of the estimation techniques. The existing models for heart beat with different algorithms are given in [4, 6] and [9, 10]. EKF is used to reduce the noise in the ECG signal [3] but the EKF requires large dimensional space for matrix computation. The technique of estimation of EnKF circumvents the high computational cost of storing and propagating the background error

covariance for a large model dimension but EKF technique cannot circumvents the high computational cost since it does not propagates an ensemble of state from which the required covariance information is obtained at the time of update.

In this paper the EnKF [7] is used for state estimation. The major difference in the output of Extended Kalman Filter and Ensemble Kalman Filter is that the approximation of states of model in EnKF [1, 2 and 7] is more proper as compared to EKF since the EKF uses a linearized equation for the error covariance propagation while the EnKF nonlinearly propagates a finite ensemble of model trajectories. The EKF cannot account for the wider range of model errors as well as it cannot account for the horizontal error correlations in large systems for computational reasons. All these drawbacks of EKF are eliminated by EnKF [2, 8].

In this paper second order heart beat model is used which is given in section II, to estimate the state of heart muscle movements and electrochemical activity of human heart. Which includes the pacemaker signal, which is acting as an input to the model. The model used here has been developed as a mathematical differential equation which expresses three main processes of heart muscle movements (a) stable equilibrium point, (b) threshold for triggering muscle movement and (c) coming back to initial position.

The heart model shows the nonlinear behavior therefore the EnKF is applied in section III, as for nonlinear systems results obtained with EnKF are more accurate. The EnKF uses ensemble of output of forecasted steps for the estimation of current state, it keeps updating the ensemble values for upcoming states and it updates its covariance matrix also. The approximation converges faster with EnKF [1]. The improper noisy estimation is improved using EnKF.

The output waveform is used to analyze the behavior of heart muscles and electrochemical activity of human heart. With EnKF the quality of estimation is enhanced. The MATLAB simulation is carried out in section IV. For this system, the results are obtained with small value of sum squared error. The output waveforms are given in section IV. Estimated values of length of muscle fiber and electrochemical activity are plotted against the true signal values. From the plots it can be observed that how the muscle fiber length varies with the change in the value of electrochemical activity with respect to time in presence of noise as well as in absence of noise along with the presence of sufficient deviation between the heart model considered for human body and heart model in EnKF. It is observed that the results obtained with the help of EnKF are more precise.

2. Mathematical Model of Human Heart Beat

Human heart pumps blood throughout the body. The electrical impulse is responsible for producing

heartbeat. The sinus node produces this electrical impulse, therefore the sinus node acts as natural pacemaker of heart. The sinus node is located at the top of the right atrium. The electrical signal produced travels through the heart tissue due to which atria and ventricles get contracted and relaxed, then blood gets pumped towards the body, this act as orderly progression of depolarization. At the time of depolarization right atrium and right ventricle pumps oxygen-poor blood returning from body towards the lungs, so that blood will get re-oxygenated. The left atrium and left ventricle pumps this oxygenated blood throughout the body. The back flow of the blood is prevented by heart valves. The systemic circuit helps spreading blood in whole body.

The orderly pattern of depolarization gives rise to the characteristic ECG tracing. ECG conveys a large amount of information about the structure of the heart and the function of its electrical conduction system. The ECG is used to measure the rate and rhythm of heart beats, the size and position of the heart chambers, the presence of any damage to the heart's muscle cells or conduction system, the effects of cardiac drugs and the function of implanted pacemakers if any. The heart model [4, 6] and [9, 10] is developed as second order heart beat differential equation such that using it ECG can be traced

$$\epsilon * \dot{x}_1 = -(x_1^3 - Tx_1 + x_2), \qquad (1)$$

$$\dot{x}_2 = (x_1 - x_d) + (x_d - x_s) * u, \qquad (2)$$

where x_1 represents the length of muscle fiber of heart, x_2 representsthe electrochemical activity, x_2 is the one of those factors which are responsible for producing heart muscle movements. ϵ represents the small positive constant, T represents the tension in muscle fiber, x_d represents the length of muscle fiber in diastole, x_s represents the length of muscle fiber in systole and u represents the pacemaker signal applied as the input signal. The model is developed such that it should satisfy the three main properties which are (a) the model exhibits the equilibrium state corresponding to diastole, (b) it also contains a threshold for triggering the electrochemical wave emanating from the pacemaker causing the heart to contract into systole and (c) it reflects the rapid return to the equilibrium state.

The first property is proved by taking general equations

$$\frac{dx_1}{dt} = f(x_1, x_2) \qquad (3)$$

$$\frac{dx_2}{dt} = g(x_1, x_2) \qquad (4)$$

This system is linearized around the initial values x_{10}, x_{20} and it is observed that for stability and to make the system free from undesired oscillations the Eigen values should be negative and real [6]. The

another important point taken into consideration is that the rate of change of muscle fiber contraction depends at any particular instant on tension of the fiber and the chemical control changes at the rate directly proportional to the muscle fiber tension, this is proved by modifying the system as given

$$\epsilon * \frac{dx_1}{dt} = -T(x_1 - x_{10}) - (x_2 - x_{20}) \qquad (5)$$

$$\frac{dx_2}{dt} = (x_1 - x_{10}) \qquad (6)$$

The second property is proved by considering that the threshold is responsible for triggering the muscle movements. There are always two equilibrium states for the heart i.e. diastole and systole. An equation (5, 6) represents only one equilibrium state that is diastole. For systole the pacemaker input is considered as a threshold and given to the system of equation (5) and (6) therefore the system is modified [4, 6] as

$$\epsilon * \frac{dx_1}{dt} = -T(x_1 - x_{10}) - (x_2 - x_{20}) \\ - (x_1 - x_{10})^3 \\ - 3x_{10}(x_1 - x_{10})^2 \qquad (7)$$

$$\frac{dx_2}{dt} = x_1 - x_{10} \qquad (8)$$

and above two equations for convenience are written as

$$\epsilon * \frac{dx_1}{dt} = -(x_1{}^3 - Tx_1 + x_2), \qquad (9)$$

where equation (9) is valid only for T > 0,

$$\frac{dx_2}{dt} = x_1 - x_{10} \qquad (10)$$

The above model does not reflects the third essential property observed from the phase portraits [6], to satisfy the third property the equation is finally modeled as

$$\epsilon * \frac{dx_1}{dt} = -(x_1^3 - Tx_1 + x_2) \qquad (11)$$

$$\frac{dx_2}{dt} = (x_1 - x_d) + (x_d - x_s) * u, \qquad (12)$$

where u [6] is the control variable associated with the pacemaker which is defined as $u = 1$ for $x_{20} \leq x_2 \leq x_{21}$ and for those values of x_1 for which

$$(x_1^3 - Tx_1 + x_2) > 0 \qquad (13)$$

and all values of x_1 and $u = 0$ otherwise, where x_{21} is the first value of x_2 obtained after x_{20}, which is the final second order equation to which the EnKF is applied. Here the pacemaker signal is acting as input

signal u, which is generated either by natural pacemaker or by artificial cardiac pacemaker attached with unhealthy heart.

3. Ensemble Kalman Filter Applied to Heart Model

The Ensemble Kalman Filter [2] is an estimator to predict the statistics of noise in system and for predicting the system's state by using ensemble integration. EnKF is used for those systems which shows nonlinear behavior. EnKF is used for the system which has large data samples obtained after discretization of partial differential equation, therefore EnKF uses sample covariance instead of covariance matrix. EnKF always assumes the probability distributions involved are Gaussian. Ensemble is a sample which is independent identically distributed random variables and its probability distribution is represented by the mean and covariance, therefore it is assumed that the ensemble is normally distributed. The ensemble covariance is computed from all ensemble members together, which introduces dependence and the EnKF formula [8] is a nonlinear function of the ensemble, which destroys the normality of the ensemble distribution.

For finding the error statistics and state estimate for current time t_n where n represents the time instant, EnKF uses the ensemble of previous states and corresponding outputs. If it is assumed that there are q forecasted state estimates at n sec, this initial or forecasted states are used to estimate the output at n^{th} state and then ensemble matrix gets updated which is then used to calculate the output and next state. The ensemble [7] is written as

$$x_n^f \triangleq (x_n^{f_1}), (x_n^{f_2}), \ldots., (x_n^{f_q}), \qquad (14)$$

where f indicates the ensemble member number, $x_n^{f_i}$ is obtained after applying $x_{n-1}^{f_i}$ to the system model where $x_{n-1}^{f_i}$ is calculated as

$$(initial\ true\ state\ value) + f_0, \qquad (15)$$

where initial value matrix has initial values of x_1 and x_2. Where f_0 represents deviation from true state values.

In this paper the ensemble size that is forecasted estimates states is chosen as q = 40. Initially these 40 values are applied to system model which considers those values as initial state and then for each such value current states are calculated, which acts as modified ensemble whose mean is calculated. The ensemble mean [1, 2] and [5] is calculated using all these values

$$\bar{x}_n^f \triangleq \frac{1}{q}\sum_{i=1}^{q} x_n^{f_i}, \qquad (16)$$

which is denoted as

$$\bar{x}_n^f \in R^{m \times q} \tag{17}$$

therefore 40 different values of output will get generated after processing it as per EnKF algorithm, average of this output values gives the current estimate.

The estimated state value for current state using Ensemble Kalman Filter algorithm is given by

$$\bar{x}_n^a = \frac{1}{q} \sum_{i=1}^{q} x_n^{a_i} \tag{18}$$

$$x_n^{a_i} = x_n^{f_i} + \widehat{K}_n \left[ym_n - h\left(x_n^{f_i} \right) \right] \tag{19}$$

and i varies from 1 to q, where $\widehat{K}_n$ is filter gain calculated as ratio of error covariance matrices,

$$\widehat{K}_n = \hat{P}_{xy_n}^f (\hat{P}_{yy_n}^f)^{-1} \tag{20}$$

Further the elements of sample covariance matrix are found out, Ensemble Kalman Filter's state error covariance matrix is given by

$$E_n^f \in R^{m \times q} \tag{21}$$

with ensemble error matrix as

$$E_n^f \triangleq \left[x_n^{f_1} - \bar{x}_n^f, \ldots \ldots, x_n^{f_q} - \bar{x}_n^f \right] \tag{22}$$

and the output error matrix is given by

$$E_{y_n}^a \triangleq \left[y_n^{f_1} - \bar{y}_n^f, \ldots \ldots, y_n^{f_q} - \bar{y}_n^f \right], \tag{23}$$

where output matrix is calculated for one of the values out of two states i.e. x_1 or x_2, which is getting estimated in correspondence with measured signal. For n^{th} state ensemble of estimated states at $(n-1)^{th}$ state is used for calculations. The approximated values [2] are

$$\hat{P}_n^f \triangleq \frac{1}{q-1} E_n^f * \left[E_n^f \right]^T \tag{24}$$

$$\hat{P}_{xy_n}^f \triangleq \frac{1}{q-1} E_n^f * \left[E_{y_n}^f \right]^T \tag{25}$$

$$\hat{P}_{yy_n}^f \triangleq \frac{1}{q-1} E_{y_n}^f * [E_{y_n}^f]^T \tag{26}$$

from equations (25) and (26) EnKF gain is obtained. The approximated error covariance matrix is

$$\hat{P}_n^a \triangleq \frac{1}{q-1} E_n^a * (E_n^a)^T \tag{27}$$

Perturbed measured value is obtained as given below, when true state values are applied to heart model then the output gets generated which has processed values of x_1 and x_2. The processed values then gets added with the state noise w_n [7]. w_n is sampled from a normal distribution with zero average and covariance Q_n. The sample error covariance matrix calculated from w_n converges to Q_n as $q \to \infty$.

$$y1_n = y(output\ at\ nth\ state) + w_n \tag{28}$$

Therefore $y1_n$ contains the processed values of x_1 and x_2. At the time of measurement if any one value out of this two state values is measured then in that value measurement noise v_n [7] gets added.

$$ym_n = y1_n + v_n, \tag{29}$$

where v_n is a zero mean random variable which has normal distribution and covariance R_n. The sample error covariance matrix obtained from v_n converges to R_n as $q \to \infty$.

Substituting all computed values in equation (19) the estimated value at n^{th} state is found out. The current state value is given as

$$x_n^{a_i} = x_n^{f_i} + \widehat{K}_n \left[y1_n + v_n - h\left(x_n^{f_i} \right) \right] \tag{30}$$

for all i varies from 1 to q and finally current output [1, 2] and [5] is estimated as

$$\bar{x}_n^a = \frac{1}{q} \sum_{i=1}^{q} x_n^{a_i} \tag{31}$$

The computation burden in case of EKF due to approximation of the nonlinearity $f(x, u)$ and $h(x)$ [7] in evaluation of the filter gain $\widehat{K}_n$ is reduced in EnKF, therefore no need to calculate the Jacobian of $f(x, u)$ and $h(x)$ thus EnKF has less numbers of computations.

4. Matlab Simulation and Discussion

Performance of the proposed EnKF after applying it to the heart model is observed using MATLAB simulation. The parameters estimated through this simulation are length of muscle fiber of heart (x_1) and electrochemical activity (x_2). The model of heart given in equations (1, 2) is chosen for analysis. Estimator is tracking the true value of parameters efficiently, is observed from the results of different case studies. The value of sum squared error obtained between true value and estimated value of the parameters is very small, sum squared error for different case studies is given in Table 2.

Table 1 shows the values [10] used for MATLAB simulation of heart model. The pacemaker signal [10] is used as input signal u. Initial true state values given to model are considered as -0.3 for x_1 and 0.01 for x_2.

The set of differential equations (1, 2) is solved in MATLAB using values as per Table 1. The solution of this equation gives true state values, which further gets added with the state noise w_n and measurement noise v_n due external environmental factors affecting. Noise values are given as

$$w_n = \begin{bmatrix} c1 \\ c2 \end{bmatrix} * random\ noise \qquad (32)$$

$$v_n = c3 * random\ noise \qquad (33)$$

Table 1. Set Parameters for Heart Model.

Parameters	Values
T	1 mg
(x_d)	1.024 micrometer
(x_s)	-1.3804 micrometer
ϵ	0.2
x_1 (initial)	-0.3
x_2 (initial)	0.01
Ensemble size	EnKF members ≥ twice the number of states

The constants $c1$, $c2$ and $c3$ show the amplitude of respective noise levels. ($c1 * random\ noise$) gets added in x_1 and ($c2 * random\ noise$) gets added in x_2. The solution of equations (1, 2) which is added with state noise is known as true value, this true value gets added with measurement noise, this sum is known as measured value which act as input to EnKF. This measured value is estimated by EnKF.

EnKF always have number of members greater than or equal to twice the number of states. Initial EnKF members are formed as true initial value added with deviation, given by

$$EnKF(member) = \begin{bmatrix} -0.3 \\ 0.01 \end{bmatrix} + f_0, \qquad (34)$$

where f_0 is the deviation, here deviation value used for simulation are

$$f_0 = \begin{bmatrix} -0.4 \\ -0.01 \end{bmatrix} \qquad (35)$$

This forecasted ensemble member is considered as initial estimation of parameters. Here second order differential equation is used therefore it has two states to be found, so the ensemble of size greater than or equal to twice the number of states is used for estimation. If EnKF is considered with more than two members then those members are declared as given in equation (14).

Following case studies are done after simulation of heart model with EnKF in absence of noise as well as in presence of noise. The graphs are plotted between true value against estimated value.

- Case study 1: The state noise and measurement noise values are assumed negligible. The ensemble size is considered 40. Time steps are considered as 0.01 sec and graph is plotted for 1 sec. The result is shown in Fig. 1.
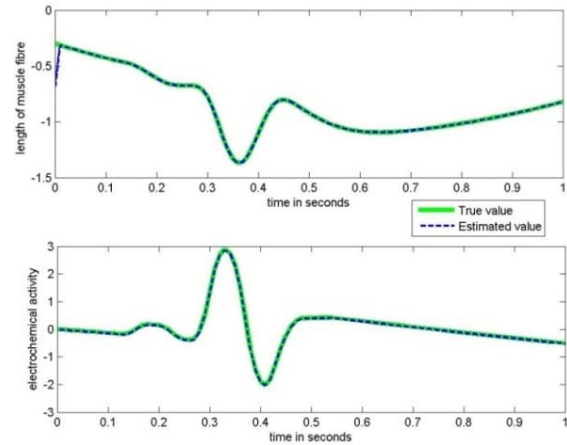

Fig. 1. Simulation result for case study 1.

- Case study 2: The state noise and measurement noise values are assumed negligible. The ensemble size is considered with 80 members. Time steps are considered as 0.01 sec and graph is plotted for 1 sec. The result is shown in Fig. 2.
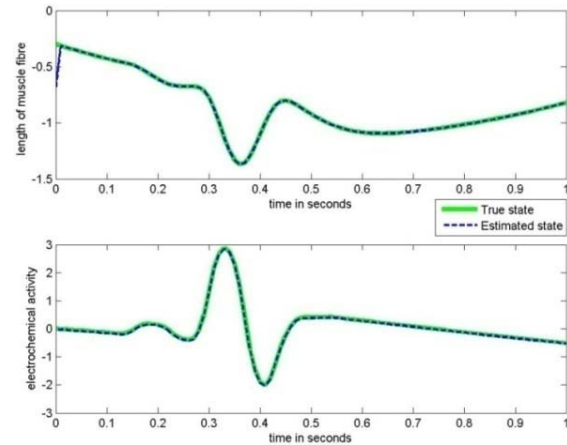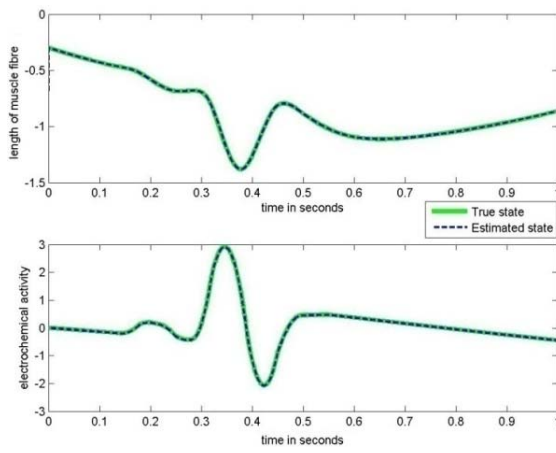

Fig. 2. Simulation result for case study 2.

- Case study 3: The state noise and measurement noise values are assumed negligible. The ensemble size is considered with 40 members. Time steps are considered as 0.0001 sec and graph is plotted for 1 sec. The result is shown in Fig. 3.
- Case study 4: The small amount of state noise and measurement noise values are added. The ensemble size is considered with 40 members. Time steps are considered as 0.01 sec and graph is plotted for 1 sec. The result is shown in Fig. 4.
- Case study 5: The large amount of state noise and Same measurement noise values as used in case study 4 are added. The ensemble size is considered with 40 members. Time steps are considered as 0.01 sec and graph is plotted for 1 sec. The result is shown in Fig. 5.

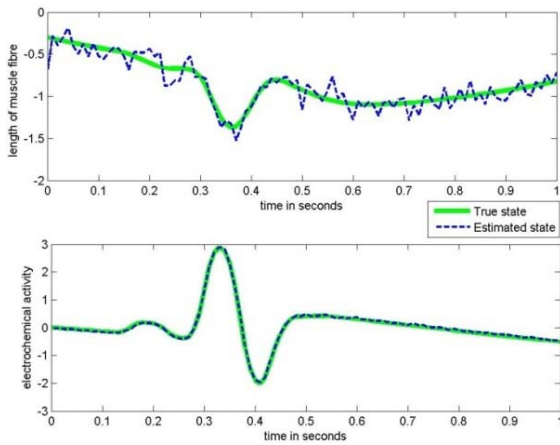**Fig. 3.** Simulation result for case study 3.

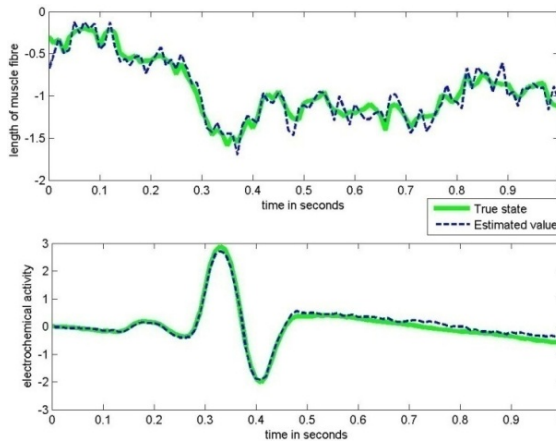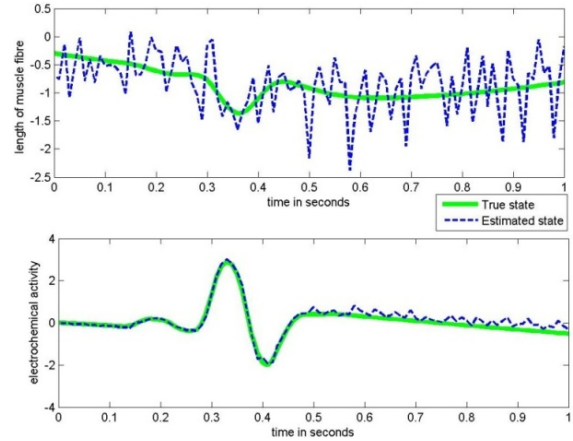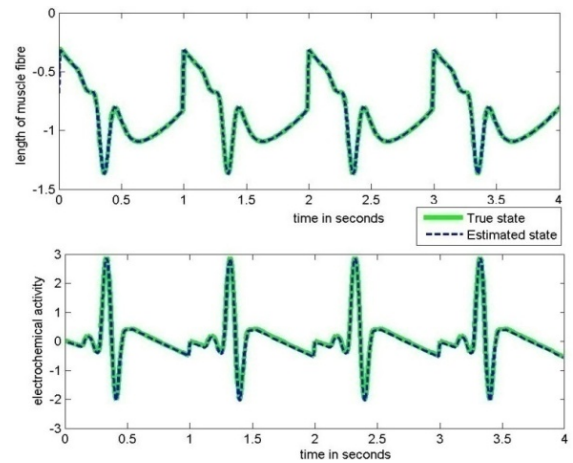**Fig. 4.** Simulation result for case study 4.

Fig. 5. Simulation result for case study 5.

- Case study 6: The small amount of state noise and large amount of measurement noise values are added. The ensemble size is considered with 40 members. Time steps are considered as 0.01 sec and graph is plotted for 1 sec. The result is shown in Fig. 6.

- Case study 7: Negligible amount of state noise and measurement noise values are added. The ensemble size is considered with 40 members. Time

steps are considered as 0.01 sec and graph is plotted for 4 sec. The result is shown in Fig. 7.

- Case study 8: The small amount of state noise and measurement noise values are added. The ensemble size is considered with 40 members. Time steps are considered as 0.01 sec and graph is plotted for 4 sec. The result is shown in Fig. 8.

Fig. 6. Simulation result for case study 6.
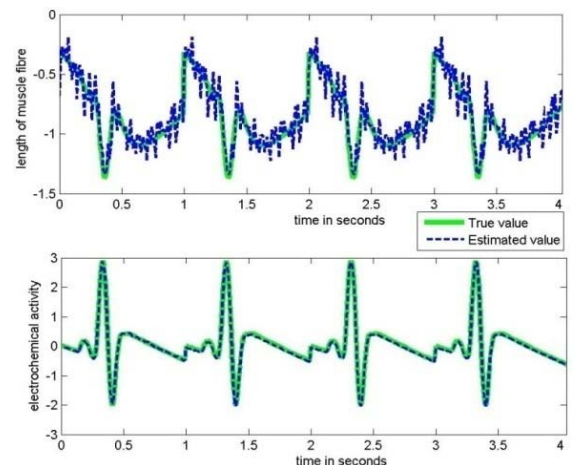

Fig. 7. Simulation result for case study 7.

Fig. 8. Simulation result for case study 8.

The values of constants c1, c2 and c3 in presence and absence of noise along with sum squared error obtained for all this case studies are given in Table 2. The sum squared error (SSE) is calculated as,

$$SSE = \sum_{i=1}^{n}(y1_i - \bar{x}_i)^2 , \qquad (36)$$

where i represents the time instant.

Table 2. Values Used for Simulation.

Case study number	C1	C2	C3	Sum squared error
1	0	0	0	0.0307
2	0	0	0	0.0491
3	0	0	0	0.7871
4	10^{-3}	10^{-4}	0.1	1.1787
5	10^{-1}	10^{-2}	0.1	2.0054
6	10^{-3}	10^{-4}	0.5	31.7522
7	0	0	0	0.0017
8	10^{-3}	10^{-4}	0.1	0.0049

5. Conclusion

The observation of case studies 1, 2 and 3 reveals that in absence of noise EnKF is tracking the true values very efficiently with sum squared error approximately zero. In case study 2 the size of ensemble is increased but with increased size sum squared error is also got sufficient increment thus ensemble size should not be increased a lot. For case studies 4 and 5 measurements noise is kept constant and state noise is varied, with increased value of state noise small increment in sum squared error is observed.

In case study 6 the measurement noise is further increased. From case studies 6, 4 it is noted that when state noise is constant and measurement noise is increased the increment in sum squared error is very large. Therefore it is concluded that sum squared error is influenced more by the value of measurement noise as compared to state noise. For multiple cycles case studies 7, 8 are done and corresponding sum squared error are noted. From case studies it is concluded that EnKF is estimating the parameters successfully in absence of noise as well as in presence of noise within the proper noise bounds. Therefore EnKF applied to heart model can be used to diagnose the disease related to heart with better accuracy.

References

[1]. A. J. Krener and A. Duarte, A Hybrid Computational Approach to Nonlinear Estimation, in *Proceedings of the 35th Conference on Decision and Control*, Kobe, Japan, December 1996, pp. 1815-1819,

[2]. B. D. O. Anderson and J. B. Moore, Optimal Filtering, *Prentice-Hall,* 1979.

[3]. Babak Yazdanpanah, Dr. G. S. N. Raju and K. Sravan Kumar, Reduction Noise of ECG Signal Using Extended Kalman Filter, *International Journal of Advanced Research in Electronics and Communication Engineering (IJARECE),* Vol. 3, 9, 2014, pp. 1029-1033.

[4]. E. C. Zeeman, Differential equations for the heartbeat and nerve impulse, *Towards a Theoretical Biology,* Vol. 4, 1972, pp. 8-67.

[5]. F. E. Daum, Exact Finite Dimensional Nonlinear Filters, *IEEE Trans. Automatic Control,* Vol. AC-31, No. 7, July 1986, pp. 616-622.

[6]. D. S. Jones, B. D. Sleeman, Michael Plank, Differential Equations and Mathematical Biology, Mathematical Biology and Medicine Series, *CRC Press,* 2009.

[7]. S. Gillijns, O. Barrero Mendoza, J. Chandrasekar, B. L. R. DeMoor, D. S. Bernstein and A. Ridley, What Is the Ensemble Kalman Filter and How Well Does it Work, in *Proceedings of the American Control Conference,* Minneapolis, Minnesota, USA, June 14-16, 2006, pp. 4448-4453.

[8]. V. E. Benes, Exact Finite-Dimensional Filters For Certain Diffusions with Nonlinear Drift, *Stochastics*, Vol. 5, 1981, pp. 65-92.

[9]. Witt Thanmon, Robert N. K. Loh, Nonlinear Control of Heart Beat Models, Systemics, *Cybernetics and Informatics,* Vol. 9, No. 1, 2011, pp. 21-27.

[10]. Witt Thanmon, Robert N. K. Loh, Observer Based Nonlinear Feedback Controls for Heartbeat ECG Tracking System, *Intelligent Control and Automation,* 3, 2012, pp. 251-261.
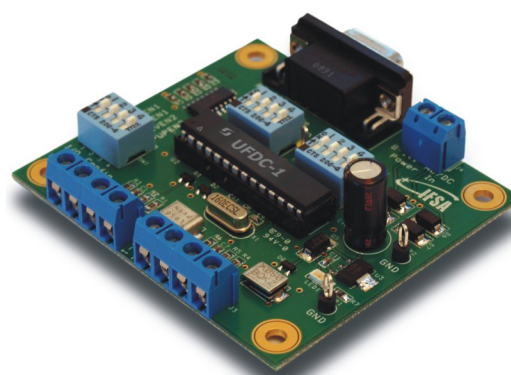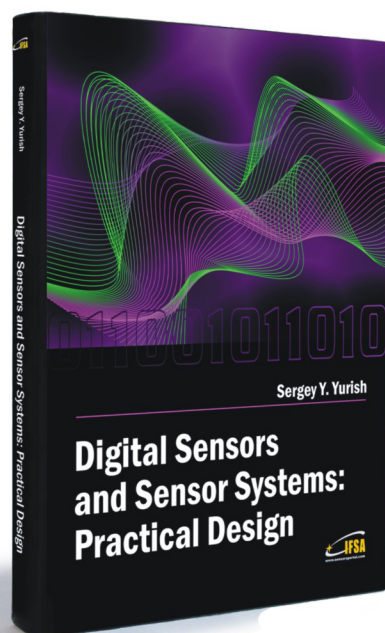

Theory:

Digital Sensors and Sensor Systems: Practical Design

and

Practice:

Development Board EVAL UFDC-1/UFDC-1M-16

Sergey Y. Yurish

Digital Sensors and Sensor Systems: Practical Design

IFSA

+

Buy book and Evaluation board together. **Save 30.00 EUR**

IFSA

ISSN 1726- 5479

9 771726 547001

www.sensorsportal.com

International Frequency Sensor Association Publishing